Orbital stability in a classical pilot-wave system

by

Nicholas Z. Liu

B.Sc. Physics, Faculty of Science, The University of Melbourne, 2016
M.Sc. Department of Mathematics and Statistics, The University of Melbourne, 2018

Submitted to the Department of Mathematics
in partial fulfillment of the requirements for the degree of

DOCTOR OF PHILOSOPHY IN MATHEMATICS

at the

MASSACHUSETTS INSTITUTE OF TECHNOLOGY

September 2024

Authored by: Nicholas Z. Liu
                  Department of Mathematics
                  August 9, 2024

Certified by: John W. M. Bush
                  Professor of Applied Mathematics, Thesis Supervisor

Accepted by: Jonathan Kelner
                  Professor Mathematics
                  Chair of Applied Mathematics

Orbital stability in a classical pilot-wave system

by

Nicholas Z. Liu

Submitted to the Department of Mathematics
on August 9, 2024 in partial fulfillment of the requirements for the degree of

DOCTOR OF PHILOSOPHY IN MATHEMATICS

ABSTRACT

The hydrodynamic bouncing droplet system, consisting of millimetric droplets bouncing on a vibrating fluid bath, displays many quantum mechanical phenomena on a macroscopic scale. These phenomena include tunnelling, diffraction and wave-like statistics. This thesis focuses on the features responsible for the quantisation of orbital radii, and rationalises this quantisation in terms of the stability of circular orbits arising in the presence of a rotating frame and a central force. We find that orbital quantisation is most pronounced when the waves generated by each bounce decay slowly. The wave decay rate, in turn, is related to the concept of path memory, the number of prior impacts with the bath that affect the droplet's future dynamics. We conduct an analytical investigation into the stability of circular orbits using a generalised theoretical framework that allows for an exploration of classical pilot-wave dynamics both inside and outside the experimentally accessible parameter regime. The exploration of parameter regimes beyond those accessible with the hydrodynamic system reveals much richer orbital dynamics. Our novel mathematical approach allows for evaluation of the integrals appearing in the stability problem in terms of Bessel functions of complex order, and thus facilitates asymptotic expansions of the stability problem in various limits. Within the experimental parameter regime, we demonstrate that in a rotating frame, circular orbits destabilise only via resonant instabilities, for which the growing perturbations oscillate at a frequency that is an integer multiple of the orbital frequency. Conversely, in a central force, non-resonant instabilities arise, for reasons detailed herein. Outside the experimental parameter regime, we show how the non-resonant instability leads to counter-intuitive scenarios; for example, circular orbits that are stabilised by increasing memory. In the limit of vanishing particle inertia, infinite path memory and a linear spring force, we demonstrate the intriguing possibility of infinitely many sharply quantised orbital states, where the allowed orbital radii exist in vanishingly thin intervals, and are stabilised by the combined influence of the time-averaged wave field and spring force. We demonstrate that these sharply quantised orbital states are only stable for higher memory. We then consider the effect of weak external forces on spin states, circular orbits arising in the absence of external forces, and show that the destabilisation of spin states depends in a complex manner on the type of external force applied. Finally, we show that the instability of large circular orbits is related to the in-line speed oscillations of free walking droplets in a manner that is independent of the external force.

Thesis supervisor: John W. M. Bush
Title: Professor of Applied Mathematics

Acknowledgments

First and foremost, I would like to thank my advisor, Professor John Bush, for his support and unique perspectives throughout my PhD. I became interested in this field during the MIT Department of Mathematics Open House in March 2019, and was never going to consider working in other areas. Even within the field of bouncing droplets, however, John has a very different set of interests to me; ever since he suggested I work on orbital stability, I would become very obsessed with gathering more data, refining my algorithms, and performing more and more esoteric asymptotic expansions. John would constantly ask me about the physical meaning of all of the calculations, before I got too carried away. While I was not always successful in identifying said physical meaning, my ability to glean physical insights from my work significantly improved. John also has very high standards for his plots and for his writing, and, despite my constant complaining about the writing, I must admit that my writing ability and willingness have improved immensely over the years. Thus, I thank John for forcing me to improve in many areas I would not have, without his pushing. Outside of research, John is a very friendly person, always willing to joke with the group, treat us with food during group meetings, and even hold BBQs at his place. John's standards for writing are only matched by his standards for food, and I must say that I've never been disappointed by his cooking.

Secondly, I would like to thank Matthew Durey, for also helping me with all the writing, and with all of the mathematical discussions over the years. Matt has been an invaluable resource throughout my PhD, constantly making sure that my mathematical arguments are sound and always asking questions about my work and the assumptions I've made. He has spent an incredible amount of time listening to my mathematical ramblings, often enthusiastically participating himself too, and is certainly a big reason why my asymptotic analysis was so successful. Many of the interesting ideas in my thesis can be directly attributed to our conversations. In addition, Matt has also been very helpful in improving my paper writing, often helping to refine my word choice and to communicate more clearly. I am especially appreciative of both John and Matt for all of the time they have spent helping me prepare this thesis, doubly so given the time of day they have sometimes worked at.

Thirdly, I would like to thank Rodolfo (Ruben) Rosales for the chats that we have had about mathematics, about the state of the world, about academic writing, and about different careers. I have always enjoyed chatting with Ruben, and hearing his perspective. One conversation that I am particularly fond of was about an issue that I had about my complex order Bessel function implementation. We had a three-hour long conversation, after which I was quickly able to find the bug in my implementation.

Fourthly, I would like to thank my parents for their behind-the-scenes support. I am in a

very privileged position to not have to worry about financial problems, as a graduate student, and my parents have provided me with the foundation to pursue my dreams, whatever they are. As I am well aware that not every graduate student is as fortunate as I am, I am very grateful for their love and support.

Finally, I would like to thank my girlfriend, Lily (Xinming) Liu, who I met at the start of my PhD, during the pandemic. Lily has been a constant source of joy in my life, and was instrumental in helping me navigate PhD life during the pandemic. She has also heard far too much about bouncing droplets when I get stuck. She has been very happy to help provide an outsider's perspective on the clarity of my writing, and is always there to make me feel better when writing becomes challenging, or when I am just tired. Outside academics, she also introduced me to the Sidney Pacific Graduate Community, with which I have become quite close, and met many wonderful people. It is hard to imagine that I would be able to accomplish what I had without her.

Contents

List of Figures

11

List of Tables

Chapter 1

Introduction

In 2005, the seminal experiments of Couder and Fort uncovered a fluid system that has since exhibited many features previously thought to be exclusive to quantum mechanics [15, 21]. In their experiments, millimetric droplets bounce over the surface of a vibrating fluid bath, generating surface waves. Droplet propulsion arises from landing on the sloped surface of the superposition of the surface waves generated by prior impacts with the fluid bath. By associating particle behaviour with the motion of the droplets and wave behaviour with the evolution of the wave field, it is evident how the fluid system provides a tangible macroscopic realisation of wave-particle duality and a foundation upon which a trajectory-based quantum theory may be formulated.

The experiments consist of placing a drop of silicone oil on the surface of a vertically vibrating bath of the same liquid [20, 21, 85]. Faraday waves arise at the free surface of a vibrating bath when the vibrational acceleration of the bath exceeds a critical value, known as the Faraday threshold [6]. Right below this threshold, any disturbances to the free surface decay. A key feature of the walking droplet system is that the droplets bounce at half the frequency of the bath's vibrational forcing, equivalently the frequency of the bath's most unstable Faraday waves. This resonance between the droplet's bouncing motion and the accompanying wave field leads to a quasi-monochromatic pilot-wave field, with a single dominant wavelength equal to the Faraday wavelength. Droplets interact with the slope of the local wave field; as the wave field consists of waves generated by previous impacts with the bath, the drop dynamics are non-Markovian, and depending on the droplet's previous history. The extent to which past bounces affect the droplet's future trajectory is prescribed by the path memory, which depends on the decay rate of disturbances, and thus the proximity of the vibrational acceleration to the Faraday threshold [38]. The quantum features of the hydrodynamic system are most pronounced in the high-memory limit, when the vibrational acceleration approaches the Faraday threshold, and when the wave field is most persistent[14].

Inspired by the wave-particle duality inherent in the droplet system, Couder and Fort [18, 19] experimentally realised the first hydrodynamic quantum analog: deflection of a single walking droplet by a gap between submerged barriers, where the statistics of the scattering angle resembled that of single-slit diffraction of photons [95] and electrons [23]. The authors explain that the deviations occur because, during the approach of a droplet near a barrier, the local wave field includes the effects of waves reflected from the barriers. When a walker passes through a pair of slits, although the droplet only ever walks through one

slit, its accompanying wave field passes through both slits, and the resulting interference is responsible for the trajectory of the droplet. The experiments were revisited by Pucci et al. [86], who observed that while walkers do not pass straight through the slits, it nevertheless most commonly does so at a single preferred angle. The authors observed that similar deflection angles resulted from reflection with a planar wall, deflection past an edge and deflection by a slit, and thus argued that walker-boundary interactions dominate. Thus, the authors did not report statistical patterns corresponding to the diffraction pattern of a plane wave. They also concluded that Couder and Fort's original experiments were probably affected by walker boundary interactions due to the small size of the experimental apparatus. Ellegaard and Levinsen [40] argued that the root cause of the observed interference arising in the double-slit experiment is the back-scattering of the wave on the slit unused by the droplet, and suggests that the slit dynamics are not chaotic, merely sensitive to the experimental parameters.

In an analog of quantum tunnelling, Eddi et al. [36] experimentally considered a walking droplet colliding with barriers of various thicknesses. They demonstrated that a walking droplet can reflect or transmit through a barrier unpredictably, in a manner analogous to quantum tunnelling. The crossing probability was found to decay exponentially with the barrier width, whereas quantum probabilities vary exponentially with the energy difference with the potential barrier. Hubert et al. [55] proposed a model of self-propulsion, considering a particle in 2D immersed in a force field of limited extent, self-propelled via a velocity-dependent Rayleigh-type friction force [63]. The authors demonstrated that randomised initial incident angles upon the force field result in a Boltzmann-like probability distribution for the crossing probability as a function of barrier length. However, the model does not describe the effect of wave field memory on the tunnelling probability, and ascribes the stochasticity of the tunnelling event to the initial conditions. Nachbin et al. [73] presented a one-dimensional hydrodynamic model for walker tunnelling, and also observed an exponential decay of the tunnelling probability on the barrier length. Furthermore, the authors noted the influence of blocker waves on the tunnelling event for large path memory. By controlling for variations in the initial walking speed and fluctuations during the experiment, Tadrist et al. [92] argued that the unpredictability of the tunnelling events was due to chaos in the walking droplet system due to variations in the vertical dynamics. Their experimental setup was designed to eliminate the possibility of lack of precise knowledge of initial conditions and unpredictability resulting from the fast bouncing time scale.

A bouncing droplet moving in a rotating frame was first considered experimentally by Fort et al. [43]. The authors found that at low memory, droplets executed inertial orbits, where the Coriolis force balances the centrifugal force, and thus the orbital radius decreased continuously with the bath rotation rate. At higher memory, the authors reported quantisation of the orbital radii, which was reminiscent of the Landau levels in quantum mechanics for a charge moving in a circular trajectory in a uniform magnetic field. In the hydrodynamic system, the Faraday wavelength would play the part of the quantum-mechanical de Broglie wavelength. Further experiments of droplets in a rotating frame were performed by Harris et al. [53]. The authors characterised the emergence of orbital quantisation at high memory, and presented a menagerie of the nonlinear states resulting from the destabilisation of the circular orbits. The authors also noted that oscillatory destabilisations of the circular orbits gave rise to wobbling states, with a fixed orbital centre, and the wobbling frequency tended

to be twice the orbital frequency. Further increases in memory led to a drifting orbital centre. Thereafter, orbital motion with a fixed orbital centre arose with sporadic jump motion of the orbital centre. Finally, at even higher memory, the walker was no longer confined to any orbital motion and exhibited chaotic behaviour. The wobbling frequencies were characterised as twice the orbital angular frequency, which we explain in chapter 2. The erratic unconfined states were characterised by a multimodal histogram of the radius of curvature of trajectory, where the peaks of the distribution were related to the zeros of the J_0 Bessel function.

Perrard et al. [83] developed an experimental procedure to study walking droplets in a simple harmonic potential, by magnetising a droplet with ferrofluid and subjecting the droplet to a magnetic field. The resulting force on the droplet was approximately a linear central force. As in the rotating frame experiments [43, 52], the authors demonstrated that at low memory, the orbital radii were continuous in the external forcing, satisfying a relationship similar to the force balance between the magnetic and centrifugal forces. At high memory, the authors noted that the radii of circular orbits were quantised, as in the experiments of Fort et al. [43]. However, Perrard et al. noticed that, at increased memory, the frequency of the ensuing wobbling instabilities were approximately $\sqrt{2}$ times the orbital frequency, and were thus non-resonant, a marked departure from the behaviour in the rotating frame. Further increase of the memory led to progressively more diverse periodic trajectories, including ellipses, lemniscates and trefoils. The authors recognised that these periodic trajectories satisfied a double quantisation in angular momentum and mean spatial radial position, and classified many trajectories by their angular momentum and spatial quantum numbers. They pointed out that the additional quantisation arose from the breaking of translational symmetry. Finally, at even higher memory, the authors demonstrated that the resulting chaotic trajectories could be decomposed into smaller unstable periodic segments.

The dynamics of walkers inside corrals has also been the focus of experimental studies at MIT [22, 53, 87]. Harris et al. [53] created a bath with a deep layer surrounded by a relatively shallow layer, and thus confined a droplet to walk above the deep layer. Circular orbits were observed at low memory, but as memory was progressively increased, more complex trajectories appeared. Cristea-Platon et al. [22] observed that as memory increases, stable circular orbits gave way to successively more complex periodic trajectories, and demonstrated a double-quantisation in angular momentum and radial position, very similar to walker dynamics in a linear central force, and hypothesised that the double quantisation arises from the effective confining potential induced by the corral walls. In the chaotic regime, a histogram of the droplet's radial position was found to match quite well with the amplitude of the linear Faraday wave mode of the corral, as in quantum mechanics. Sanz [90] demonstrated an analog of the Kondo effect [59], which describes the scattering of electrons in a metal due to magnetic impurities, and leads to a minimum in electrical resistivity with temperature. In experiments, Manoharan and workers [71] studied an elliptical corral, a ring of atoms on a substrate, whose arrangement causes a particular distribution of electrons inside the corral. They showed that individual atoms, playing the part of magnetic impurities in the corral, can be used to control the relevant weights of individual cavity modes, allowing for the generation of arbitrary superpositions of quantum eigenstates. When placed at one focus, the magnetic impurity excites a particular elliptical eigenmode with extrema near that focus. Similarly, Saenz and coworkers were able to drastically vary the proportion of excited corral

modes by moving the submerged circular wells. As in the experiments of Manoharan, when the circular well was placed at one focus of the elliptical corral, one particular corral mode, with maxima at the foci, dominated the statistical behaviour of the walker. This was a hydrodynamic analog of statistical projection.

Sáenz et al. [88] presented an analog of Friedel oscillations, using walker dynamics around a submerged cylindrical well. Friedel oscillations [42, 44, 58] arise from perturbations in the wavefunction and density of states of a free electron gas on the surface of a metal in the presence of a defect, or inhomogeneity. In the quantum system, no interaction mechanism between the electron gas and the inhomogeneity has been put forth; instead, the inhomogeneities are described in terms of scattering potentials [42]. In the hydrodynamic system, however, the reflection of the waves from the well causes droplets incident upon the well to scatter. During the interaction with the well, the walker resonates with the wave-mode of the well, and generates a standing wave field that lasts even after the walker leaves the well. This standing wave field leads to concentric oscillations in droplet speed, where the wavelength of oscillations corresponds closely to the Faraday wavelength. The authors relate these speed oscillations to the emergent quantum-like statistics.

These experiments highlight how the walker system is a macroscopic realisation of a pilot-wave system first proposed by de Broglie as a realist model of quantum mechanics [3, 24, 26], where particles can be described as having trajectories. He postulated that quantum particles move in response to a guiding pilot wave, itself generated by the particle's vibration. However, the theory was incomplete, and no mechanism of wave generation was specified. In 1952, David Bohm proposed an alternate pilot-wave theory [10, 11], where quantum particles move under the influence of the quantum potential, a non-local potential constructed from the Schrodinger wavefunction. By construction, while quantum particles do not generate the pilot-wave, their statistics are equivalent to those derived from classical non-relativistic quantum mechanics. The principle objection to Bohmian mechanics is its non-locality; as the quantum potential, at any point in space, evolves instantaneously with the motion of the quantum particle, it is necessarily incompatible with special relativity.

One of the earliest models of bouncing droplets was due to Molaćek and Bush [69, 70], who considered the pilot-wave as a superposition of wave fields generated by prior impacts. In analytically deriving a model for the wave field generated by a bouncer, and prescribing the interactions with the bath, Molaćek and Bush were successful in describing the different bouncing and walking regimes, including different bouncing modes, walking thresholds and walking speeds. To simplify the model, Oza et al. [78] assumed that bouncing droplets bounce resonantly at exactly twice the vibrational frequency, which was one of the bouncing modes identified by Molaćek and Bush, and averaged over the periodic motion (strobing), thereby eliminating consideration of the vertical dynamics. Oza also modelled the droplets as a continuous source of monochromatic waves, which converted the sum over past impacts to an integral over past time, and led to a more analytically tractable model. This stroboscopic model has been used successfully to rationalise many features in the hydrodynamic system, such as the appearance of the walking state as a supercritical pitchfork bifurcation [78] and orbital quantisation of circular orbits in the presence of an applied rotation [79, 80].

Some models of bouncing droplets proceed directly from the Navier-Stokes equations. Milewski et al. [68] decomposed the velocity field by a Helmholtz equation, and assumed that the vortical component was small, to develop a linearised quasi-potential model of the

fluid behaviour. While they were able to predict the Faraday threshold, they needed to use an effective viscosity of $\nu_{\mathrm{eff}} = 0.8025\nu$ to correctly predict the experimental Faraday threshold. Nevertheless, this model represented the first model of bouncing droplets derived from purely fluid-mechanical considerations. This numerical model for bouncing droplets was expanded upon by Durey and Milewski [32], who modelled droplet impacts as point forcings, expanded the wave field in terms of the system's wave modes, and developed a discrete-time map for the expansion coefficients Durey used this model to numerically demonstrate the Doppler effect [38], and the exponential spatial damping of wave fields, effects not captured by stroboscopic models. Galeano-Rios [45, 47] extended the quasi-potential model by developing a kinematic matching model for the droplet's impacts with the fluid surface, where the surface deformation was assumed to match the shape of the droplet. By explicitly modelling the droplet-bath interaction, Galeano-Rios was successful in describing bouncing modes and impact phases. The main disadvantage of this method, however, was its computational complexity [14]. Various authors extended the quasi-potential model to include variable topography. Faria [41] accounted for variable topography by treating them as changes in wave speed, instead of boundaries. Nachbin *et al.*[72, 73] reduced the quasi-potential model to a one-dimensional model to numerically study tunnelling.

The first theoretical analysis of the stroboscopic model in a rotating frame was performed by Oza et al. [79], who developed a framework for understanding stability of circular orbits, a framework that we develop further in this thesis. The authors theoretically derived the relationship, at low memory, between the orbital radius, orbital speed and rotation rate, which differs from that obtained from balancing Coriolis and centrifugal forces by a multiplicative factor. This multiplicative factor was later explained by Bush et al. [15] as a wave-induced added mass. At high memory, the authors demonstrate that orbital quantisation can be partially explained through the relationship between the orbital radius, r_0, and the required rotation rate to sustain circular orbits of radius r_0, and that significant portions of solution branches of the rotation rate, as a function of the orbital radius, are unstable. The quantised orbital radii were then rationalised as the stable orbital solutions among neighbouring unstable circular orbits. They also present a hydrodynamic analog of Zeeman splitting Eddi et al. [39], by showing that the presence of the frame rotation causes the breaking of degeneracy of circular orbits with the same orbital radius and frequency, but travelling in opposite directions. The authors hint at the possibility of hydrodynamic spin states, orbital states in the absence of external rotation, but did not find any stable spin states in the experimental parameter regime. This work was expanded upon by Oza et al. [80], who numerically determined the types of nonlinear states possible when circular orbits destabilise, in agreement with the experiments of Harris [52]. The dependence of the frequency and amplitude of stable wobbling orbits on the memory were consistent with the experimental data of Harris et al. [53]. Also in agreement with the work of Harris et al. [53] was the prevalence of wobbling states with the wobbling frequency twice that of the orbital frequency, which we explain in chapter 2. At higher memory, they observed chaotic dynamics, where peaks in the histogram of the instantaneous radius of curvature were identified as occurring near zeros of Bessel functions, and concluded that the chaotic trajectories consisted of switching between the least unstable periodic orbits.

Various authors have studied the wave-induced added mass [9, 15], motivated by noticing the similarity between low-memory pilot-wave hydrodynamics, and the dynamics in the

21

absence of the pilot-wave. Bush et al. [15] demonstrated that, at low memory, the pilot-wave has two effects: a hydrodynamic boost factor, which increases the effective mass of the droplet, and a speed-dependent nonlinear drag, which selects a preferred walking speed. This model both rationalises the low-memory relationships between the orbital radius and the rotation rate for orbital motion in a Coriolis force, as observed by Fort [43] and Oza [79], and explains the preferred orbital speed in a Coriolis force [79], and is easily extended to central force systems. Blitstein [9] extends the boost model by decomposing the stroboscopic wave force into the local hydrodynamic boost force, and an additional spatiotemporal non-local force, a superposition of waves generated by secondary sources at points along the droplet's past trajectory for which the distance to the orbital centre is instantaneously stationary. The authors then distinguish between the physical effects of the two forces, and argue that it is the non-local force that is responsible for orbital quantisation.

Stability analysis of circular orbits using the stroboscopic model was also performed by Labousse et al. [64] in a linear central force, using a similar formalism to that of Oza et al. [79]. The authors demonstrated that the most unstable orbital radii appeared to correspond to zeros of Bessel functions of different orders, and sought to rationalise this behaviour in terms of the energy of the modes of the wave field. The authors also showed that the predicted orbital stability sometimes did not agree with the experimental results of Perrard et al. [84]. Some suggested reasons for the discrepancies included experimental difficulties in detecting differences between slightly wobbling and stable circular orbits, breakdown of the droplet and wave synchronisation at high memory and non-constancy of the impact phase. However, the predicted stability behaviour of circular orbits was found to be inconsistent with the theoretical developments of Tambasco et al. [94], whose stability diagrams for the linear central force deviate significantly from that of Labousse et al. [64]. This matter will be settled in chapter 3 of this thesis. Finally, Tambasco also investigated the stability of circular orbits when subject to a two-dimensional Coulomb force, a physical system also considered in this thesis in chapter 3.

Kurianski et al. [60] performed numerical simulations of walking droplets in a simple harmonic potential using the stroboscopic model. They reproduced many of the periodic trajectories found experimentally by Perrard et al. [84], such as circular orbits, trefoils and lemniscates. The authors also recovered a double quantisation in angular momentum and mean radius and found that chaotic trajectories could be viewed as transitioning between various unstable periodic states, in agreement with Perrard et al. [84] and Durey and Milewski [32]. Differences, however, were observed at high memory, where the assumptions behind the theoretical model may break down experimentally. The authors noted that the potential in the experiments of Perrard et al. [84] was only approximately harmonic to three Faraday wavelengths, which may have led to discrepancies in the behaviour at large distances from the centre of force.

Durey et al. [33] considered the effect of the time-averaged mean wave field on the long-term statistics. Assuming ergodicity of the underlying dynamics, and thus the equivalence of time-averaging with spatially averaging the wave field, Durey *et al.*showed that the mean wave field can be obtained by convolving the wave field of a bouncer with the probability density function of the particle, thereby providing a direct link between the mean wave field and the long-term statistics. The authors then demonstrated that the mean wave field acted as an effective potential in the chaotic regime. Tambasco and Bush [93] demonstrates rapid
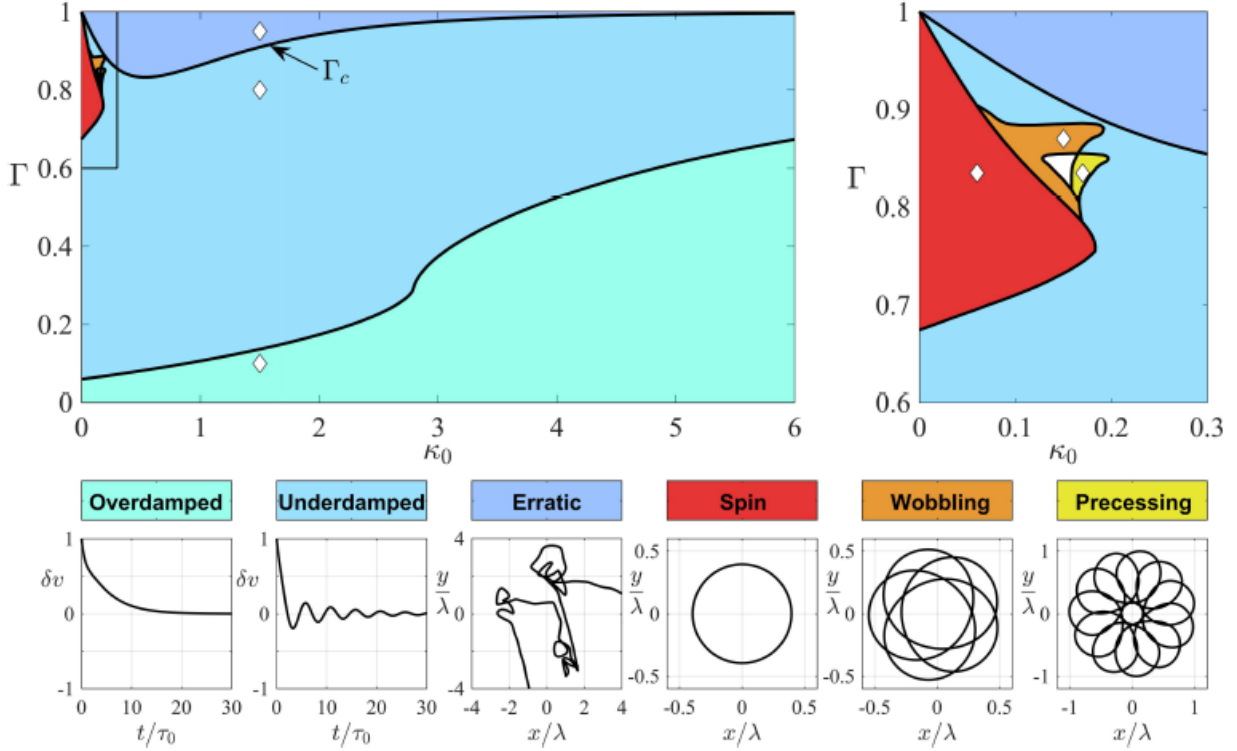
Figure 1.1: The regime diagram of the free particle in the GPWF, illustrating the particle behaviour as a function of the memory parameter, Γ, and the non-dimensional mass, κ_0. At low memory and Γ, inline perturbations to free rectilinear trajectories decay via underdamped oscillations. As Γ is increased, the perturbations decay via overdamped oscillations instead, and at sufficiently high memory, rectilinear trajectories destabilise. In chapter 6, we investigate the effect of applied forces on the spin state stability boundary (boundary of red region), and in 7, we show that large circular orbits destabilise via an instability similar to that of free rectilinear trajectories, marked here as Γ_c.

convergence of the wave field convolution to the mean wave field, even when the particle has only explored a small region of the physical space. In chapter 5, we demonstrate how the wave field converges to the mean wave field in the limit of high memory. Treating the wave field as a self-induced potential, we are able to describe the stabilisation of circular orbits at high memory, and the thinness of the intervals of permissible orbital radii.

There have been many connections between stability and system energy identified in the hydrodynamic pilot-wave system through various experiments and theoretical developments. Some investigations have suggested that the onset of instability is accompanied by a decrease in wave field energy at the onset of several instabilities, including the transition from bouncing to walking states [32], the transition from parallel walkers to promenading pairs [12, 32], and the destabilisation of periodic orbits in a harmonic potential [28, 33]. In addition, the stability of droplet lattices appears to be related to the height of the local wave field averaged across all droplets in the lattice, itself related to the mean droplet gravitational potential energy [16, 96]. Finally, it has been suggested that the onset of orbital instability

in a harmonic potential is controlled by the relative energy contribution of a small number of wave modes [64]. In chapter 2, we assess the value of these energy-based arguments for predicting the instability of orbital walker motion on a rotating bath.

The generalised pilot-wave framework [13, 82] (GPWF) is a parametric generalisation of the stroboscopic model of Oza et al. [78], in which the relative magnitudes of particle inertia, drag and wave force may assume any values. It was introduced by Bush [13] to facilitate explorations in classical pilot-wave theory in parameter regimes inaccessible to the walker system. By postulating that a particle acts as a continuous source of quasi-monochromatic but exponentially decaying waves, the GPWF dispenses with many of the complications of the hydrodynamic system, such as the far-field decay of the wave field [38], variable bouncing phases [17] and nonlinear effects near the Faraday threshold. The purpose of the GPWF is thus to explore the conditions and parameter regimes under which quantum-like behaviour may be observed, using the core ingredients of the hydrodynamic system. In chapter 4 onwards, we consider different parameter regimes in the GPWF in search of novel dynamical features.

Of particular interest is the existence of hydrodynamic spin states, in which a droplet is confined by its own wave field to a stable circular orbit in the absence of any external forcings. Stable spin states have not been found experimentally as they are predicted to exist in currently experimentally inaccessible parameter regions [82]. Bernard-Bernardet et al. [7], however, discovered drifting spin states, where droplets executed circular orbits about a moving orbital centre. Oza et al. [82] used the generalised pilot-wave framework to characterise the stability of spin states, arising when a particle is confined by its own wave field to a stable circular orbit in the absence of any external forces, and demonstrated that although many spin state solutions exist, only the smallest radius spin states are ever stable, in a parameter regime outside experimentally accessible ranges. Durey et al. [33] demonstrated the instability of the steady rectilinear propulsion state to in-line oscillations [4] with oscillation amplitudes comparable in size to the wavelength of the pilot wave, a feature not reported by Oza et al. [78] in their examination of the walker system. In chapter 7, we investigate how these in-line oscillations are related to the end of quantisation of circular orbits for very large orbital radii, and demonstrate that this quantisation termination mechanism is a universal property of the GPWF, independent of the external force. In further study of the dynamics of the free particle, Durey and Bush [31] present a comprehensive treatment of two-dimensional free-particle motion in the GPWF, and delineated distinct regimes marked by spin states, rectilinear motion with over- and under-damped in-line oscillations, and erratic particle motion. They also observed wobbling and precessing states just outside the spin state stability region, features previously only seen before in the presence of external forces. In contrast, Bernard-Bernardet et al. [7] discovered drifting spin states, where droplets executed circular orbits about a moving orbital centre, as they used droplets corresponding to parameter values just outside the stability region described by Oza et al. [82], and very similar to the drifting states identified by Oza et al. [80]. In chapter 6, we study the effect of external forces on the stability of spin states, and show that drifting instabilities may appear in the absence of translational invariance. We thus attribute the drifting spin states discovered by Bernard-Bernardet et al. [7] to the breakdown of translational invariance due to the finite size of their experimental apparatus.

The generalised pilot-wave framework has been generalised further to include different

wave kernels. Valani et al. [99] demonstrates that the stability region of the steady rectilinear walking state, in one dimension, increases with the decay rate of the wave field by investigating Bessel, sinusoidal and Gaussian wave kernels. Durey [29] and Valani et al. [99] also demonstrate the possibility of reducing the 1D generalised pilot-wave framework to a form similar to the Lorenz system. This reduction raises the possibility of studying the 1D generalised pilot-wave framework using low-dimensional dynamical systems theory. Throughout this thesis, we consider the possibility of observing similar quantum-like behaviour in pilot-wave systems with different kernels.

This thesis is motivated by the following questions:

1. What factors cause, or terminate, orbital quantisation?

2. How is the stability of circular orbits impacted by the type of external force?

3. Can we use the GPWF find a sharper analog of orbital quantisation, closer to quantum mechanics, where the orbital radius may only take values in a disjoint union of very narrow intervals?

4. In what parameter regimes do we expect to see quantum-like behaviours, and what other novel dynamical features can we find?

In chapter 2, we present the results of asymptotic analyses of the stability of circular orbits in the experimental regime in a rotating frame. We build upon the stability framework outlined by Oza et al. [79], and analytically evaluate the integrals appearing in the stability problem to simplify asymptotic analysis. This simplification of the stability problem allows us to determine analytical approximations of the stability boundaries, which verify that the only instability mechanisms at the onset of instability are monotonic instabilities, and wobbling instabilities with the wobbling frequency close to twice that of the orbital frequency, hence called 2ω instabilities. In addition, the stability boundaries of both wobbling and monotonic instabilities are quasi-periodic with the same period. We show that 2ω instabilities are enhanced when the destabilisation frequencies are exactly twice the orbital frequency. We then use our asymptotic results to compare various energy-based heuristics for the most unstable orbital radii, and suggest a heuristic based upon the gradient of the mean wave force. Chapter 2 appears as published in: Pilot-wave dynamics in a rotating frame: the onset of orbital instability. Liu, N., Durey, M. and Bush, J. W. M. *Journal of Fluid Mechanics* **973** (2023).

In chapter 3, we contrast the stability of circular orbits in a rotating frame with that in a central force. We first consider the related classical orbital mechanics problem of a satellite orbiting a central object under the influence of a general central force, and show the presence of a new fundamental instability mechanism associated with the form of the central force. We then leverage the relative constancy of orbital speeds in the hydrodynamic pilot-wave system [15] to distinguish the pilot-wave system from classical orbital mechanics, and heuristically explain the instability frequency of this new non-resonant instability. The asymptotic analysis introduced in chapter 2 is then employed to mathematically analyse the stability boundaries in a general central force. Specifically, we demonstrate how the new non-resonant instability dominates the monotonic instabilities in convex radial potentials,

or when the attractive force increases with radial position, and how the non-resonant instability dominates the 2ω instabilities in concave radial potentials. We also prove, in more generality, a theorem first proved by Oza et al. [79] for a general class of external forces, which demonstrates that monotonic instabilities arise when the net radial force pushes outwards perturbations further outwards. This theorem allows us to rationalise the increased prevalence of monotonic instabilities in external forces that decay too rapidly with radial position. Chapter 3 is in preparation for submission to publication in the Journal of Fluid Mechanics.

In chapters 4 and 5, we use the generalised pilot-wave framework to consider parameter regimes outside of the experimental regime. In chapter 4, we observe that the non-resonant instability can behave very counter-intuitively outside the experimental regime. Specifically, one expects large circular orbits to destabilise like the in-line speed oscillations of free walkers [31, 35, 77, 79]. Indeed, for large orbital radius, the critical memory of instability approaches a constant value. However, we show that, for low inertia and large orbital radius in the presence of central forces, circular orbits may still destabilise via the non-resonant instability, via a completely different instability mechanism. For higher memory, we observe that circular orbits may re-stabilise, the first time that increasing memory has been observed to stabilise circular orbits, and this phenomenon leads to a new type of orbital quantisation. We show that these new non-resonant quantised islands occur when the the non-resonant instability dominates all the other instabilities, and when its critical memory of instability varies slowly with the orbital radius. We call the parameter regime when this occurs the plateau regime, and extend Oza's mathematical framework [77, 79] to study the onset of these non-resonant instability plateaus. In addition, we show that, for lower orbital radii, the critical memory of instability predicted by the non-resonant instability is quasi-periodic in the orbital radius, with a period different to that of the resonant stability boundaries. We demonstrate how this behaviour paves the way for the appearance of higher order resonant instabilities at the onset of instability, like 4ω instabilities.

In chapter 5, we consider the high memory and zero inertia limit of particle motion in a linear central force, using the GPWF. In this limit, we show that stable circular orbits exist for very narrow ranges of the orbital radius. Specifically, stable circular orbits only exist near the Faraday threshold if the orbital radius takes values between the neighbouring zeros of J_0 and J_2, where J is the Bessel function of the first kind; thus, for large orbital radius, the set of stable orbital radii shrinks to zero. We show that this phenomenon arises due to the limited ability of the mean wave field and central force to stability circular orbits at high memory. However, we also show that these sharply quantised orbits destabilise as memory is lowered, due to the deviations from the mean wave field. We thus demonstrate the physical mechanisms behind this sharp quantisation, and explain why it only arises in the high memory and low inertia limit. Curiously, we find that these sharply quantised orbits destabilise via a dual resonance: the instability frequency is approximately an integer multiple of the orbital frequency, but the oscillation amplitude is approximately equal to the Faraday wavelength.

In chapter 6, we consider the effect of weak Coriolis and central forces on the stability of spin states. We show that while stable spin states exist in the limit of zero inertia and infinite memory, frame rotation will destabilise all circular orbits at sufficiently high memory. Our analysis provides further evidence of Zeeman splitting, where the Coriolis force

splits the degeneracy of anticlockwise and clockwise orbits into anticyclonic and cyclonic states, which are orbital states moving in the opposite and same direction as the frame rotation, respectively. While we show the existence of cyclonic orbital states, we demonstrate that these orbital states are destabilised by rotation rate, and that for sufficiently large rotation rate, all cyclonic states are unstable. We show that the stability boundaries change discontinuously as a central force is added, because the central force causes the loss of translational symmetry, and thus previously trivial eigenvalues destabilise, allowing for the onset of drifting instabilities. This leads to the paradoxical scenario where, at sufficiently low memory, stable spin states that remain stable in the presence of an infinitesimal repulsive central force may be destabilised in the presence of an infinitesimal attractive central force.

In chapter 7, we investigate a mechanism that universally terminates orbital quantisation. Specifically, we show that, for sufficiently large orbital radii, circular orbits destabilise via the quasi-rectilinear instability, the orbital analogue of the in-line speed oscillations of rectilinear states first studied by Durey [33, 35]. For very large values of the orbital radius, the quasi-rectilinear instability can be studied as a perturbation of the instability of free walkers. We observe that, for smaller values of the orbital radius, the critical memory of instability decreases with increasing orbital radius, as the curvature of the circular orbit decreases, facilitating in-line perturbations to circular orbits. However, for intermediate values of the orbital radius, we demonstrate that a near-resonance between the amplitude of these speed oscillations and the pilot-wave wavelength appears, which causes the critical memory of instability to increase with increasing orbital radius, and requires a new set of asymptotic expansions. We provide metrics to quantify when the instability is 'near-resonant', and develop an asymptotic expansion that is uniformly valid for when the quasi-rectilinear is near-resonant, and when it is not. This approach allows us to quantify the orbital radius at which many quantised phenomena end, such as the non-resonant quantised islands of chapter 4, or the sharply quantised states of chapter 5. We show that the behaviour of this instability is independent of the external forcing, and is thus a fundamental feature of orbital pilot-wave dynamics.

In chapter 8, we conclude our study of the generalised pilot-wave framework. We discuss the results and limitations of our work, and propose some future research directions.

Chapter 2

Pilot-wave dynamics in a rotating frame: the onset of orbital instability

2.1   Introduction

Millimetric droplets may bounce and self-propel along the surface of a vertically vibrating liquid bath [20, 21]. These walking droplets, or 'walkers', provide a tangible macroscopic example of wave-particle duality and represent a classical realisation of a pilot-wave system of the form envisaged by de Broglie [24, 25] in the 1920s. Since its discovery in 2005, the hydrodynamic pilot-wave system has provided the basis for an unexpectedly long list of hydrodynamic quantum analogs [13, 14]. Notable examples include single-particle diffraction and interference [18, 40, 86], unpredictable tunneling [37, 92], Friedel oscillations [88], spin lattices [89], and quantum-like statistics in corrals [53, 87]. Of particular interest here are the quantised orbits emerging when a droplet walks in the presence of an imposed force [43, 84].

Faraday waves are generated at the free surface of a vibrating liquid bath when the bath's vibrational acceleration exceeds a critical value known as the Faraday threshold [6, 67]. Walking droplets arise just below this threshold, and so respond only to the waves generated by their own bouncing. A key feature of the walker system is that the droplets bounce at the frequency of the bath's most unstable Faraday waves, specifically half the frequency of the bath's vibrational forcing. The resulting resonance between the bouncing droplet and the bath insures that the pilot-wave field be quasi-monochromatic, with a dominant wavelength prescribed by the Faraday wavelength. The dynamics is local in that the droplet responds to the local slope of its guiding wave; however, as the slope is determined by the droplet's past trajectory, the droplet dynamics are non-Markovian. The path memory of the system determines the mean number of prior impacts that contribute to the wave force acting on the droplet, and is prescribed by the proximity of the vibrational acceleration to the Faraday threshold [38]. The quantum features of the pilot-wave hydrodynamic system emerge in the high-memory limit arising when the vibrational acceleration approaches the Faraday threshold, and the pilot-wave is most persistent.

Orbital quantisation is a canonical feature of the hydrodynamic pilot-wave system, and one of its most compelling as a quantum analog. At sufficiently high memory, the quasi-monochromatic form of the guiding or 'pilot' wave constrains the droplet to quantised dy-
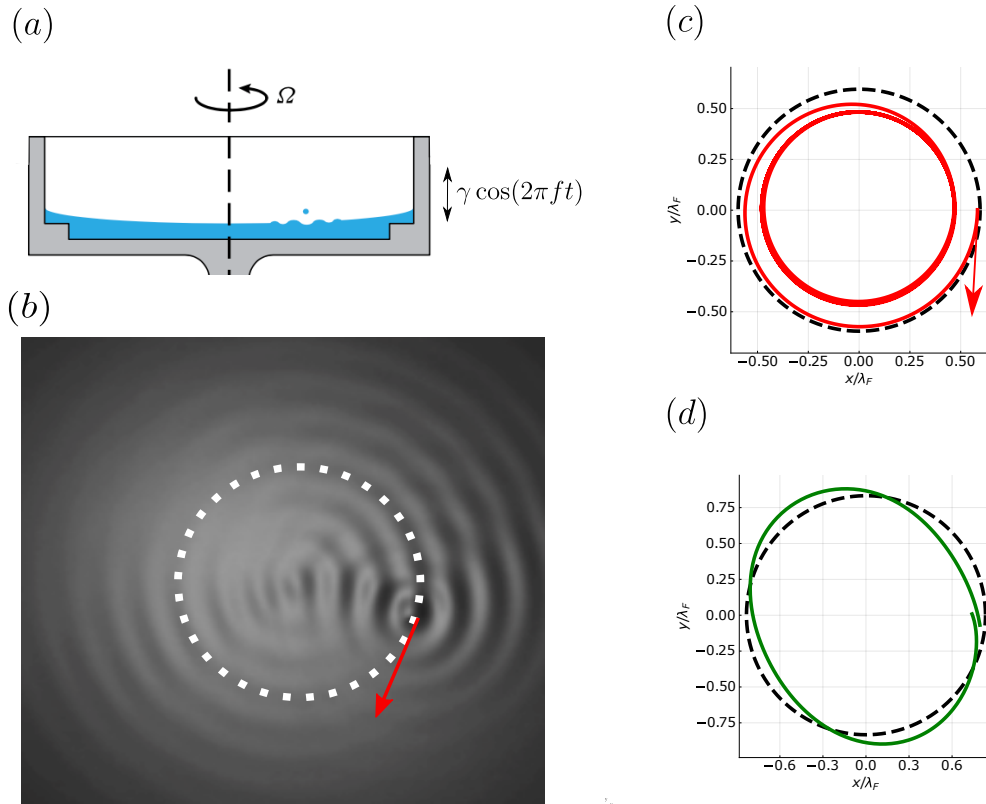
Figure 2.1: (a) A schematic illustration of the physical system of interest, millimetric droplets walking on the surface of a liquid bath vibrating vertically with acceleration $\gamma \cos(2\pi f t)$ and rotating about the vertical axis with angular frequency Ω. (b) In the rotating frame, the droplets may execute anticyclonic inertial circular orbits, in which the dominant force balance is between the outwards inertial force and the inward Coriolis force. This force balance is augmented by the wave force, which at high memory may give rise to orbits that are quantised in radius [43, 52, 79]. The wave field generated by the walking droplet has a characteristic wavelength corresponding to the Faraday wavelength, λ_F. As the memory is increased progressively, these orbits may go unstable via one of two mechanisms. (c) A circular orbit (black dashed circle) of radius $r_0/\lambda_F = 0.60$ destabilises by a monotonic instability (red) characterised by initially exponential monotonic divergence from the circular path, the result being an orbit of smaller radius. (d) A circular orbit (black dashed circle) of radius $r_0/\lambda_F = 0.83$ destabilises into a wobbling orbit (green), characterised by a wobbling frequency of approximately twice the orbital frequency, known as a 2-wobble. In (c, d), the dimensionless vibration parameter, $\Gamma = (\gamma - \gamma_W)/(\gamma_F - \gamma_W)$, takes values (c) $\Gamma = 0.7$ and (d) $\Gamma = 0.8$, where γ_W and γ_F are the walking and Faraday thresholds, respectively. Figures 2.1(a, b) are adapted from Harris and Bush [52].

namical states [43, 64, 79, 84]. Orbital quantisation has been shown to arise for walkers in a rotating frame [43, 52, 79], a simple harmonic potential [32, 64, 83, 84], and confinement to a submerged well [22, 34, 53]. In the former, quantised states consist of circular orbits [43]. In the latter two systems, more complex orbits may arise, including lemniscates and trefoils [22, 34], and orbits are quantised in both energy and angular momentum [84]. In all three systems, in the high-memory limit the quantised orbits destabilise, and the droplet switches intermittently between the accessible orbits, giving rise to statistics reminiscent of their quantum counterpart [22, 53, 64, 79, 80].

The first investigation of droplets walking in a rotating frame was that of Fort et al. [43], who observed that the droplets move in circular orbits (see figure 2.1). At lower path memory, the orbital radius depends continuously on the bath rotation rate in a manner expected to arise for inertial orbits, from a balance between centripetal and Coriolis forces. At higher memory, the geometric constraint imposed by the monochromatic Faraday wave field restricts the permissible stable orbital radii, giving rise to an effective quantisation in orbital radii. The authors noted that the Coriolis force takes the same form as the Lorentz force on a moving charged particle and so drew the analogy between the quantised inertial orbits arising in their system and the Landau levels arising when a charged quantum particle moves in a uniform magnetic field. The observed orbital quantisation was captured in their accompanying simulations [43].

Harris and Bush [52] revisited droplets walking in a rotating frame experimentally, and focused on the destabilisation of the quantised orbits and the onset of chaos as the memory is increased progressively. They demonstrated the emergence of wobbling (see figure 2.1(d)), drifting, wobble-and-leap motions and erratic trajectories at high path memory. In the long-path-memory limit, all circular orbits are unstable, and the droplet transitions intermittently between different quantised circular orbits; thus, the histogram of the droplet's radius of curvature is multimodal, with peaks at the orbital radii of the quantised circular orbits. The emerging physical picture in this and other pilot-wave hydrodynamic systems is one of a droplet exciting then navigating its own potential [14].

The theoretical modeling of the walking droplet system developed by Moláček and Bush [69, 70] formed the basis of the stroboscopic model [78, 79], in which the walking droplet is treated as a continuous source of monochromatic waves. The stroboscopic model has been successful in rationalising a number of features of the hydrodynamic pilot-wave system, including the destabilisation of a bouncing droplet into a walker, and the stability of various static and dynamic bound states [14]. Oza et al. [79] used the stroboscopic model to analyse droplets walking in a rotating frame, and rationalised the onset of orbital quantisation in terms of orbital instability at certain radii. Moreover, simulation of the stroboscopic model in a rotating frame revealed a variety of wobbling, drifting and quasi-periodic trajectories [80] consistent with experimental observations reported by Harris and Bush [52]. Both experimental and theoretical studies report that at the onset of wobbling, the wobbling frequency is approximately twice the orbital frequency [52, 80]. We rationalise such resonant instabilities herein.

Several connections between stability and system energy have been proposed in the context of pilot-wave hydrodynamics. In particular, several investigations have suggested that the wave field energy is decreased at the onset of several instabilities, including the transition from bouncing to walking states [32], the transition from parallel walkers to promenading

pairs [12, 32], and the destabilisation of periodic orbits in a harmonic potential [28, 33]. Moreover, the stability of droplet lattices appears to be related to the height of the local wave field averaged across all droplets in the lattice, a proxy for the mean droplet gravitational potential energy [16, 96]. Finally, it has been suggested that the onset of orbital instability in a harmonic potential is controlled by the relative energy contribution of a small number of wave modes [64]. We here assess the value of these energy-based arguments for predicting the instability of orbital walker motion on a rotating bath.

The mean wave field in pilot-wave hydrodynamics has proven to be a useful diagnostic for interpreting both the dynamical and statistical behaviour of walking droplets; moreover, it is of particular interest given its proposed relation to the quantum potential in Bohmian mechanics [14]. The influence of the mean pilot wave on the droplet dynamics has been explored in a number of settings, including the quantisation of circular and exotic orbits arising in a harmonic potential [61, 84]. The connection between the mean pilot wave and the emergent droplet statistics was first reported in an experimental study of walker motion in an elliptical corral [87], and a mathematical link between the two developed by Durey et al. [33, 34]. We here demonstrate the utility of the mean pilot-wave field as a diagnostic for orbital stability in a rotating frame.

We present herein a theoretical investigation of the orbital instability of a droplet walking in a rotating frame. We introduce the stroboscopic pilot-wave model in §2.2, and determine an alternative formulation for the orbital stability problem in terms of various integrals that specify the influence of the system's path memory. In §2.3, we deduce analytical expressions for the critical memory at the onset of orbital instability, and also rationalise the form of instability. For the case of wobbling instabilities, the associated wobbling frequency is deduced. In §2.4, we compare the efficacy of various heuristic arguments for the onset of orbital instability and introduce a more insightful heuristic based on consideration of the mean wave field. Finally, in §2.5, we discuss the implications of our findings for a broader class of orbital pilot-wave systems.

2.2 Pilot-wave hydrodynamics

We consider the motion of a millimetric drop of mass m self-propelling along the surface of a liquid bath vibrating vertically with frequency f and acceleration $\gamma \cos(2\pi f t)$ (see figure 2.1(a)). The system is subject to a vertical gravitational acceleration $-g\boldsymbol{e}_z$ and rotates about a vertical axis with angular velocity $\boldsymbol{\Omega} = \Omega \boldsymbol{e}_z$, where $\boldsymbol{e}_z$ is the vertical unit vector. When the vibrational acceleration exceeds the Faraday threshold, $\gamma > \gamma_F$, the bath spontaneously destabilises to subharmonic Faraday waves with period $T_F = 2/f$ and wavelength $\lambda_F = 2\pi/k_F$ prescribed by the water-wave dispersion relation [6]. The parameter regime of interest is $\gamma < \gamma_F$, where the fluid bath would remain quiescent in the absence of the droplet. For vibrational acceleration beneath the bouncing threshold, $\gamma < \gamma_B$, the droplet coalesces into the bath; however, for $\gamma > \gamma_B$, it bounces in place on the free surface. As γ is increased further, the drop achieves resonance with the bath, bouncing at the Faraday frequency. Beyond the walking threshold, $\gamma > \gamma_W$, this resonant bouncing state destabilises into a dynamic walking state, and the walking droplet generates a quasi-monochromatic wave field with the Faraday wavelength. The wave decay time, T_M, depends on the proximity to the

Faraday threshold, specifically $T_M = T_d/(1 - \gamma/\gamma_F)$, where T_d is the viscous decay in the absence of vibrational forcing [70]. The memory parameter, $M_e = T_M/T_F$, prescribes the number of prior impacts relevant to the dynamics. In the absence of system rotation, the droplet follows a rectilinear path at constant speed, u_0. In the rotating frame, the droplet instead executes anticyclonic inertial orbits with radius r_0 and angular frequency ω.

A key notion in our study is that of orbital memory, M_e^O, the ratio of the memory time, T_M, to the orbital period, $2\pi/\omega$, as prescribes the extent to which the orbiting drop interacts with its own wake [79]. When $M_e^O \gg 1$, the pilot wave decays over several orbital periods, the droplet interacts significantly with its own wake, and its trajectory is strongly influenced by its history. It is in the regime of intermediate orbital memory, $M_e^O \sim O(1)$, that orbital instability first arises, and so will be a focus of our study. When $M_e^O \ll 1$, the droplet is unperturbed by its wake and instability emerges in the form of in-line speed oscillations that may arise for the rectilinear trajectory of a free walker [4, 35, 56].

We root our discussion in the parameter regime explored by Harris and Bush [52], who used a fluid of density 949 kg m^{-3}, kinematic viscosity 20 cSt, surface tension 0.0206 N m^{-1}, and depth 4 mm, with a vibrational frequency $f = 80$ Hz and a droplet of radius 0.4 mm whose free walking speed was approximately $u_0 = 11$ mm s^{-1}.

2.2.1 Governing equations

To model the horizontal motion of the walker, we utilise the stroboscopic trajectory equation developed by Oza et al. [78, 79], whereby the pilot-wave system is time-averaged over one bouncing period, $T_F = 2/f$ [70]. The droplet's horizontal position, $\boldsymbol{x}_p(t)$, thus evolves over time, t, according to [78–80]

$$m\ddot{\boldsymbol{x}}_p + D\dot{\boldsymbol{x}}_p = -mg\nabla h(\boldsymbol{x}_p(t), t) - 2m\boldsymbol{\Omega} \times \dot{\boldsymbol{x}}_p. \tag{2.1a}$$

The drop is propelled by the wave force, $-mg\nabla h(\boldsymbol{x}_p(t), t)$, and also responds to the linear drag force, $-D\dot{\boldsymbol{x}}_p$, and the Coriolis force, $-2m\boldsymbol{\Omega} \times \dot{\boldsymbol{x}}_p$. The accompanying pilot wave,

$$h(\boldsymbol{x}, t) = \frac{A}{T_F} \int_{-\infty}^{t} \mathrm{J}_0(k_F|\boldsymbol{x} - \boldsymbol{x}_p(s)|)\mathrm{e}^{-(t-s)/T_M} \, \mathrm{d}s, \tag{2.1b}$$

is modelled as a continuous superposition of axisymmetric waves of amplitude A centred along the droplet's path, decaying exponentially in time over the memory time scale, T_M. The quasi-monochromatic form of the pilot wave field imposes a geometric constraint on the droplet's motion whose effects are most pronounced at high memory, where the Faraday waves are most persistent. The Faraday wavenumber, drag and wave amplitude parameters, respectively k_F, D and A, are defined in terms of physical quantities in appendix A.1.

We project the pilot wave onto the droplet's path to yield an integro-differential trajectory equation for the droplet [78] that may be expressed in dimensionless variables as [79, 82]

$$\kappa_0 \ddot{\hat{\boldsymbol{x}}}_p + \dot{\hat{\boldsymbol{x}}}_p = 2\int_{-\infty}^{\hat{t}} \frac{\mathrm{J}_1(|\hat{\boldsymbol{x}}_p(\hat{t}) - \hat{\boldsymbol{x}}_p(s)|)}{|\hat{\boldsymbol{x}}_p(\hat{t}) - \hat{\boldsymbol{x}}_p(s)|}(\hat{\boldsymbol{x}}_p(\hat{t}) - \hat{\boldsymbol{x}}_p(s))\mathrm{e}^{-\mu(\hat{t}-s)} \, \mathrm{d}s - \hat{\boldsymbol{\Omega}} \times \dot{\hat{\boldsymbol{x}}}_p, \tag{2.2}$$

where $\hat{\boldsymbol{x}}_p = k_F\boldsymbol{x}_p$, $\hat{t} = t/T_W$ and $T_W = \sqrt{2DT_F/mgAk_F^2}$ is the memory time at the onset of walking, $\gamma = \gamma_W$ [35, 78]. The dimensionless parameters $\mu = T_W/T_M > 0$ and $\kappa_0 =$

Dimensionless parameters	Definition
$\kappa_0 = m/(DT_W)$	Inertia-to-drag ratio
$\hat{\boldsymbol{\Omega}} = 2m\boldsymbol{\Omega}/D$	Dimensionless rotation vector
$\mu = T_W/T_M$	Wave decay rate
$\Gamma = (\gamma - \gamma_W)/(\gamma_F - \gamma_W)$	Vibration parameter
r_0	Orbital radius, normalised by k_F^{-1}
ω	Orbital angular frequency
$\omega_{\text{orb}} = \omega/\mu$	Orbital memory parameter
$\beta = \mu/\omega = \omega_{\text{orb}}^{-1}$	Inverse orbital memory parameter
$U = r_0\omega$	Orbital speed
s	Asymptotic complex growth rate of perturbations
$S = \text{Im}(s)$	Destabilisation frequency
$\xi = S/\omega$	Destabilisation frequency relative to orbital frequency

Table 2.1: The dimensionless parameters appearing in the pilot-wave system (2.2) and subsequent analysis.

m/DT_W describe the wave decay rate and the relative importance of inertial and drag forces, respectively, and $\hat{\boldsymbol{\Omega}} = 2m\boldsymbol{\Omega}/D = \hat{\Omega}\boldsymbol{e}_z$ is the dimensionless rotation vector.

We characterise the pilot-wave dynamics in terms of the dimensionless vibration parameter $\Gamma = (\gamma - \gamma_W)/(\gamma_F - \gamma_W) = 1 - \mu$ [13, 35, 82], which increases with increasing path memory. We note that $\Gamma = 0$ corresponds to the walking threshold in the absence of a Coriolis force ($\gamma = \gamma_W$), while $\Gamma = 1$ corresponds to the Faraday threshold ($\gamma = \gamma_F$), and thus infinite path memory [13]. The experimental parameter regime of Harris and Bush [52] corresponds to $\kappa_0 \approx 1.6$. We note that κ_0 typically takes values in the range $0.8 \lesssim \kappa_0 \lesssim 1.6$ in the laboratory; likewise, the dimensionless rotation rate, $\hat{\Omega}$, is restricted to the interval $0 \leq |\hat{\Omega}| \lesssim 1.3$ [52, 79, 82]. Henceforth, we thus treat κ_0 and $\hat{\Omega}$ as $O(1)$ quantities, whose influence on the pilot-wave dynamics we characterise through systematic asymptotic analysis.

2.2.2 Orbital dynamics

We characterise orbits in terms of their radius, r_0, and angular frequency, $\omega > 0$. By omitting hats and substituting $\boldsymbol{x}_p(t) = r_0(\cos(\omega t), \sin(\omega t))$ into the trajectory equation (2.2), we express the radial and tangential force balances as [79]

$$-\kappa_0 r_0 \omega^2 = 2 \int_0^\infty \text{J}_1\left(2r_0 \sin\left(\frac{\omega t}{2}\right)\right) \sin\left(\frac{\omega t}{2}\right) \text{e}^{-\mu t}\, \text{d}t + \Omega r_0 \omega, \qquad (2.3a)$$

$$r_0 \omega = 2 \int_0^\infty \text{J}_1\left(2r_0 \sin\left(\frac{\omega t}{2}\right)\right) \cos\left(\frac{\omega t}{2}\right) \text{e}^{-\mu t}\, \text{d}t, \qquad (2.3b)$$

which may be solved for r_0 and ω given κ_0, μ and Ω.

In our dimensionless notation, a suitable proxy for the orbital memory, M_e^O, is $\omega_{\text{orb}} = \omega/\mu$, which is the ratio of the wave decay time scale, μ^{-1}, to the orbital time scale, $\omega^{-1} \sim r_0/u_0$, where u_0 is the steady walking speed in the absence of bath rotation [35, 78]. The orbital

speed, $U = r_0\omega$, typically remains close to the free walking speed, u_0, and satisfies $U < \sqrt{2}$ for all parameter values (see §2.4.1). As U depends only weakly on the orbital radius at fixed memory, we note that $\omega_{\text{orb}} = U/(r_0\mu)$ decreases with increasing r_0.

2.2.3 Orbital stability

In order to characterise the droplet's response to perturbations from a circular orbit, we apply linear stability analysis. Following the framework developed by Oza et al. [79], we linearise the trajectory equation (2.2) about the orbital solution expressed by equation (2.3). Specifically, we write

$$\boldsymbol{x}_p(t) = r_p(t)\left(\cos\theta_p(t), \sin\theta_p(t)\right), \tag{2.4a}$$

where $r_p(t)$ and $\theta_p(t)$ are the time-varying radial and angular polar coordinates of the droplet's position, respectively. For a small perturbation from an orbital trajectory, we consider solutions of the form

$$r_p(t) = r_0 + \epsilon r_1(t) \quad \text{and} \quad \theta_p(t) = \omega t + \epsilon\theta_1(t), \tag{2.4b}$$

where r_0 and ω satisfy the orbital equations (2.3), and $\epsilon \ll 1$ is a small parameter. We substitute equations (2.4) into (2.2), retain terms to $O(\epsilon)$, and then take the Laplace transform of the resultant linear equations. It follows that the perturbed trajectory's asymptotic complex growth rates, s, satisfy $F(s) = 0$, where

$$F(s) = \mathscr{A}(s)\mathscr{D}(s) + \mathscr{B}(s)\mathscr{C}(s),$$

and the stability coefficients are defined (in a form equivalent to Oza et al. [79, 82])

$$\mathscr{A}(s) = \kappa_0(s^2 - 2\omega^2) + \mu + s - 2\Omega\omega + \mathcal{C}_0(s) + \mathcal{I}_1(s) - 2\mathcal{I}_0(0), \tag{2.5a}$$

$$\mathscr{B}(s) = 2\kappa_0\omega s + \Omega s - \mu\left(\kappa_0\omega + \Omega\right) - \mathcal{S}_0(s), \tag{2.5b}$$

$$\mathscr{C}(s) = 2\kappa_0\omega s + 2\omega + \Omega s + \mu\left(\kappa_0\omega + \Omega\right) - \mathcal{S}_0(s), \tag{2.5c}$$

$$\mathscr{D}(s) = \kappa_0 s^2 + s - \mu + \mathcal{C}_0(s) - \mathcal{I}_1(s). \tag{2.5d}$$

Of particular interest in our investigation are the integrals (defined for $\text{Re}(s) > -\mu$ and any integer $m \geq 0$)

$$\mathcal{I}_m(s) = \int_0^\infty \mathrm{J}_{2m}\left(2r_0\sin\left(\frac{\omega t}{2}\right)\right) e^{-(\mu+s)t}\,\mathrm{d}t, \tag{2.6a}$$

$$\mathcal{C}_m(s) = \int_0^\infty \mathrm{J}_{2m}\left(2r_0\sin\left(\frac{\omega t}{2}\right)\right) \cos(\omega t)e^{-(\mu+s)t}\,\mathrm{d}t, \tag{2.6b}$$

$$\text{and} \quad \mathcal{S}_m(s) = \int_0^\infty \mathrm{J}_{2m}\left(2r_0\sin\left(\frac{\omega t}{2}\right)\right) \sin(\omega t)e^{-(\mu+s)t}\,\mathrm{d}t, \tag{2.6c}$$

which encode the effects of memory on the stability problem, and present most of the difficulty in solving the stability problem analytically. One important contribution of our study

is the exact analytical evaluation of the stability integrals (2.6) in terms of Bessel functions of complex order. Specifically, we derive in appendix A.2 the closed form expression

$$\mathcal{I}_m(s) = \frac{\pi}{\omega} \mathrm{J}_{m+\mathrm{i}\eta}(r_0) \mathrm{J}_{m-\mathrm{i}\eta}(r_0) \operatorname{csch}(\pi\eta), \tag{2.7}$$

where $\eta = (\mu + s)/\omega$. Moreover, by representing $\cos(\omega t)$ and $\sin(\omega t)$ in terms of complex exponential functions, we deduce that

$$\mathcal{C}_m(s) = \frac{1}{2}\Big(\mathcal{I}_m(s + \mathrm{i}\omega) + \mathcal{I}_m(s - \mathrm{i}\omega)\Big) \text{ and } \mathcal{S}_m(s) = \frac{1}{2\mathrm{i}}\Big(\mathcal{I}_m(s - \mathrm{i}\omega) - \mathcal{I}_m(s + \mathrm{i}\omega)\Big), \quad (2.8)$$

which we use to derive similar closed form formulae for $\mathcal{C}_m$ and $\mathcal{S}_m$. Using (2.7)–(2.8), we derive in appendix A.2 simplified expressions for each of the stability integrals appearing in (2.5) in terms of products of Bessel functions of the first kind, $\mathrm{J}_\nu(r_0)$, and its derivative, $\mathrm{J}'_\nu(r_0)$, where the complex order, ν, takes values $\nu \in \{\pm\mathrm{i}(\mu + s)/\omega\}$. We then utilise asymptotic expansions of each integral evaluation to characterise orbital instability (§2.3).

Motivated by our exact analytical evaluation of the stability integrals, we seek to recast the force balance equations (2.3) in a similar manner. To simplify our investigation, we parameterise the orbital dynamics entirely in terms of the radius, r_0 [77], thereby effectively eliminating Ω from the stability problem. This elimination process is achieved by first recasting the radial force balance (2.3a) as

$$\Omega = -\kappa_0\omega - \frac{2}{r_0\omega} \int_0^\infty \mathrm{J}_1\left(2r_0 \sin\left(\frac{\omega t}{2}\right)\right) \sin\left(\frac{\omega t}{2}\right) \mathrm{e}^{-\mu t} \, \mathrm{d}t, \tag{2.9}$$

where we observe that the integral in equation (2.9) may be expressed as

$$\int_0^\infty \mathrm{J}_1\left(2r_0 \sin\left(\frac{\omega t}{2}\right)\right) \sin\left(\frac{\omega t}{2}\right) \mathrm{e}^{-\mu t} \, \mathrm{d}t = -\frac{1}{2}\frac{\partial \mathcal{I}_0(0)}{\partial r_0}. \tag{2.10}$$

By combining equations (2.9) and (2.10), we eliminate Ω in the stability coefficients (2.5), yielding

$$\mathscr{A}(s) = \kappa_0 s^2 - \frac{2}{r_0}\frac{\partial \mathcal{I}_0(0)}{\partial r_0} - 2I_0(0) + \mu + s + \mathcal{C}_0(s) + \mathcal{I}_1(s), \tag{2.11a}$$

$$\mathscr{B}(s) = \kappa_0\omega s - \frac{(\mu - s)}{r_0\omega}\frac{\partial \mathcal{I}_0(0)}{\partial r_0} - \mathcal{S}_0(s), \tag{2.11b}$$

$$\mathscr{C}(s) = \kappa_0\omega s + 2\omega + \frac{(\mu + s)}{r_0\omega}\frac{\partial \mathcal{I}_0(0)}{\partial r_0} - \mathcal{S}_0(s), \tag{2.11c}$$

$$\mathscr{D}(s) = \kappa_0 s^2 + s - \mu + \mathcal{C}_0(s) - \mathcal{I}_1(s). \tag{2.11d}$$

Finally, we reduce the tangential force balance by integrating (2.3b) by parts, from which it follows that the orbital speed, $U = r_0\omega$, satisfies [79]

$$\mathcal{I}_0(0) = \frac{1}{\mu}\left(1 - \frac{r_0^2\omega^2}{2}\right). \tag{2.12}$$

36

For any given $r_0 > 0$, the orbital stability problem may be expressed solely in terms of the reduced tangential force balance (2.12) and the stability condition $F(s) = 0$, both of which are defined in terms of the stability integrals (2.6).

The orbital solution is unstable if there are any roots, s, of F satisfying $\text{Re}(s) > 0$. By denoting s_* as the unstable root with largest real part, the instability is monotonic if $\text{Im}(s_*) = 0$ and oscillatory otherwise. The stability function, F, has trivial eigenvalues at 0 and $\pm i\omega$, corresponding to rotational and translational invariance of the orbital motion, respectively [79]. It follows, therefore, that the nontrivial roots of the stability problem satisfy $G(s) = 0$, where

$$G(s) = \frac{\mathscr{A}(s)\mathscr{D}(s) + \mathscr{B}(s)\mathscr{C}(s)}{s(s^2 + \omega^2)}. \tag{2.13}$$

We apply the method of Delves and Lyness [27] to find the roots of G in the domain over which G is analytic, i.e. $\text{Re}(s) > -\mu$. To ascertain whether a particular orbital state is stable or unstable, we typically utilise a rectangular integration contour spanning the domain $\text{Re}(s) \in [0, 20]$ and $\text{Im}(s) \in [0, 5]$, which we find to be sufficient for identifying all roots with a positive real part across the experimentally-based parameter regime considered in this study ($0 \leq \Gamma \leq 0.99$). This approach differs from that of Oza et al. [82], who instead applied the methodology of Delves and Lyness [27] to F, integrating F'/F over a deformed contour specifically chosen to avoid the trivial zeros at $s = 0$ and $s = \pm i\omega$. The method presented here instead removes the singularities analytically, thereby avoiding contour deformations near the trivial zeros of F; however, local Taylor series approximations are necessary to avoid numerical difficulties arising sufficiently close to the removable singularities of G.

In figure 2.2(a), we follow Oza et al. [79, 82] in presenting the dependence of the orbital radius on the bath rotation rate for $\Gamma = 0.8$. In figure 2.2(b), we summarise the stability behaviour for all Γ. As path memory is increased progressively, stable circular orbits (blue) destabilise via either a monotonic (red, see figure 2.1(c)) or oscillatory (green, see figure 2.1(d)) instability mechanism. Associated monotonic (red) and oscillatory (green) instability 'tongues' emerge in the stability diagram, with the tip of each tongue corresponding to the onset of a new instability. The blue regions between the instability tongues correspond to regions of orbital quantisation. Notably, as memory is increased beyond the tip of an oscillatory instability tongue, the orbital instability typically manifests as a wobbling orbit, in which the orbital centre remains roughly constant, but the radius of curvature exhibits small-amplitude oscillations with a frequency approximately twice that of the orbital frequency, as reported in the experiments of Harris and Bush [52] and the numerical simulations of Oza et al. [80] (see figure 2.1(d)). Furthermore, the instability tongues appear to have a periodic structure, with the critical memory increasing with increasing orbital radius. We observe that the monotonic and wobbling instability tongues are nested, with monotonic instability tongues forming at lower memory than the neighbouring wobbling instability tongues.

2.2.4 The onset of instability: asymptotic scaling relationships

Although the stability integrals (2.6) may be evaluated analytically (see (2.7)–(2.8)), the purpose of this section is to motivate the asymptotic scaling relationships arising near the
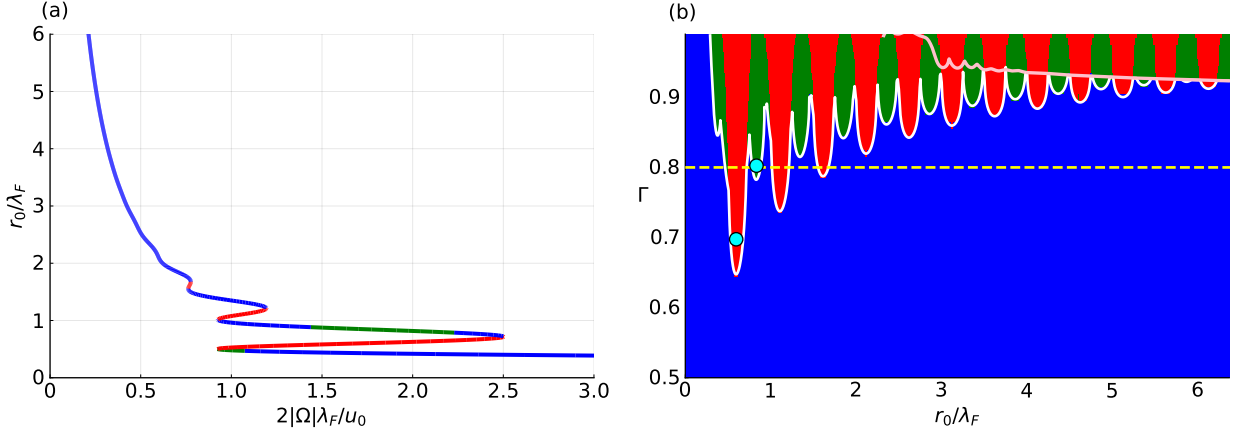
Figure 2.2: Orbital stability and the onset of quantisation for $\kappa_0 = 1.6$, where $\kappa_0 = m/(DT_W)$ is the inertial coefficient appearing in equation (2.2). (a) The dependence of orbital radius on bath rotation rate for $\Gamma = 0.8$, where $\Gamma = (\gamma - \gamma_W)/(\gamma_F - \gamma_W)$ is the dimensionless vibration parameter. (b) The delineation of orbital stability for any given radius and memory. The stability boundary is highlighted in white and the yellow line at $\Gamma = 0.8$ corresponds to the curve in panel (a). In both panels, stable orbital states are indicated in blue, while oscillatory and monotonic instabilities are highlighted in green and red, respectively. We note that in (b), the instability tongues alternate between monotonic and wobbling as the orbital radius is increased progressively. The cyan dots in the red and green regions denote the parameters corresponding to the monotonic and wobbling trajectories presented in figure 2.1(c,d). The pink curve denotes an instability related to in-line speed oscillations on the order of the Faraday wavelength [35], which is subdominant for $r_0/\lambda_F \lesssim 4$, and truncates the instability tongues for $r_0/\lambda_F \gtrsim 4$.

tip of each instability tongue. In particular, we determine the main contributions to each stability integral arising along a stability boundary ($s = \mathrm{i}S$ with S real) for large orbital radius ($r_0 \gg 1$), for which each integrand is highly oscillatory. Using (2.8) to express $\mathcal{C}_m$ and $\mathcal{S}_m$ in terms of $\mathcal{I}_m$, we henceforth focus our attention on the study of $\mathcal{I}_m$. Furthermore, by recognising that $\mathcal{I}_m$ is a Laplace transform of a periodic function, we reduce the integral (2.6a) to

$$\mathcal{I}_m(\mathrm{i}S) = \frac{\mathcal{L}_m(\xi)}{\omega\left(1 - \mathrm{e}^{-2\pi(\beta+\mathrm{i}\xi)}\right)}, \quad \text{where} \quad \mathcal{L}_m(\xi) = \int_0^{2\pi} \mathrm{J}_{2m}\left(2r_0 \sin\left(\frac{\theta}{2}\right)\right) \mathrm{e}^{-(\beta+\mathrm{i}\xi)\theta}\,\mathrm{d}\theta, \quad (2.14)$$

$\beta = \mu/\omega$ is the inverse orbital memory and $\xi = S/\omega$ is the scaled destabilisation frequency (see table 2.1). Based on experimental and numerical observations of monotonic and wobbling instabilities [52, 80], we assume henceforth that the destabilisation frequency is comparable to the orbital frequency (i.e. $\xi = O(1)$). Notably, our analysis does not account for the instability associated with in-line speed oscillations arising at larger orbital radii (denoted by the pink curve in figure 2.2(b)), for which $S \sim U$, or $\xi \sim r_0$ [35]. Finally, by writing $\beta = \mu r_0/U$ and noting that μ at the tip of successive wobbling (or successive monotonic) instability tongues decreases with increasing orbital radius (see figure 2.2(b)), we deduce that the magnitude of β is at most of $O(r_0)$ when the orbital radius is large (since $U = O(1)$ for all orbital radii). Our analysis in this section determines the precise scaling relationship between β and r_0, namely $\beta = O(\ln r_0)$, where ln denotes the natural logarithm.

Before proceeding with the asymptotic expansions, we provide a physical interpretation for the integral $\mathcal{L}_m(\xi)$. The argument $2r_0 \sin\left(\frac{\theta}{2}\right) \geq 0$ is the length of the chord spanning two points lying an angle θ apart on a circle of radius r_0. This distance reflects the influence of the droplet's path memory on the evolution of the perturbed trajectory, where the extent of the path memory is controlled by the damping rate $\beta > 0$. Notably, $\mathrm{e}^{-\pi\beta}$ is the wave damping factor over half an orbital period, as accounts for the contribution of waves generated when the droplet was last diametrically opposite its current position; likewise, $\mathrm{e}^{-2\pi\beta}$ determines the wave damping factor over a complete orbital period. Finally, the factor $\mathrm{e}^{-\mathrm{i}\xi\theta}$ accounts for oscillations in the perturbed droplet trajectory. For large r_0, the integrand of $\mathcal{L}_m(\xi)$ is generally highly oscillatory, with dominant contributions arising over non-oscillatory intervals centred about critical points; these critical points are either internal points of stationary phase, or boundary points arising when the argument of J_{2m} vanishes, i.e. at $\theta = 0$ and $\theta = 2\pi$ [8]. The internal points of stationary phase arise when the argument of the Bessel function is stationary, i.e. at $\theta = \pi$. We now proceed to determine the magnitude of the contribution made by each critical point.

We first examine the contributions to $\mathcal{L}_m$ arising about $\theta = 0$ and $\theta = 2\pi$, which we denote by $\mathcal{L}_{m,0}$ and $\mathcal{L}_{m,2\pi}$, respectively. We derive in appendix A.3 the leading-order contribution $\mathcal{L}_{m,0} = O(r_0^{-1})$, which is valid when $\xi = O(1)$ and β is of maximum size $O(r_0)$: both of these conditions are met near the tip of each instability tongue. Using the structure of the integrand of $\mathcal{L}_m(\xi)$, we similarly determine that the leading-order contribution about $\theta = 2\pi$ satisfies $\mathcal{L}_{m,2\pi}(\xi) = \mathrm{e}^{-2\pi(\beta+\mathrm{i}\xi)}\mathcal{L}_{m,0}(\xi)$; thus, the relative size of $\mathcal{L}_{m,0}(\xi)$ and $\mathcal{L}_{m,2\pi}(\xi)$ is controlled by the orbital damping factor $\mathrm{e}^{-2\pi\beta}$. Finally, we use the method of stationary phase (see appendix A.3) to determine that the interior point contribution to $\mathcal{L}_m$ at π has
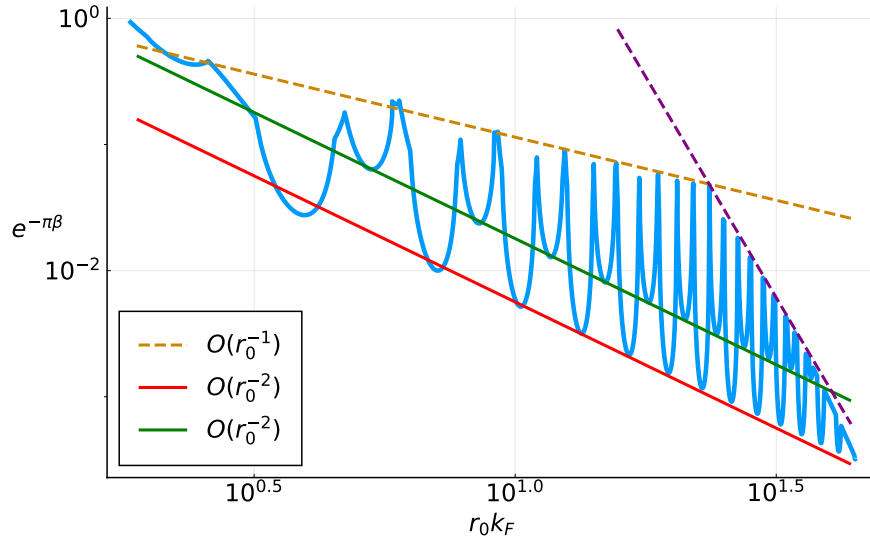
Figure 2.3: Envelopes of the stability boundary, the scalings of which are deduced from our stationary phase analysis (see §2.2.4). The blue curve corresponds to the white stability boundary in figure 2.2(b). The green and red lines correspond to the wobbling and monotonic instability envelopes. The gold and purple dashed lines denote the upper bounds on the existence of stable circular orbits, corresponding to the transition from wobbling to monotonic instabilities, and the onset of in-line speed oscillations (pink curve in figure 2.2(b)), respectively. The half-orbit wave damping factor, $\mathrm{e}^{-\pi\beta}$, scales as $(r_0 k_F)^{-2}$ for the green and red lines, and as $(r_0 k_F)^{-1}$ for the gold line.

magnitude

$$\mathcal{L}_{m,\pi} = O\left(\frac{\mathrm{e}^{-\pi\beta}}{r_0}\right).$$

The relative weight of the integral contributions about $\theta = 0$, π and 2π seemingly decreases consecutively by a factor $\mathrm{e}^{-\pi\beta}$. However, the contribution about $\theta = \pi$ becomes significant when $\mathrm{e}^{\pi\beta}$ scales algebraically with r_0, corresponding to a strong influence of the waves generated diametrically opposite the droplet's current position, as is characteristic of high orbital memory [43]. Indeed, as is evident in figure 2.3, the tips of each instability tongue, both monotonic (red line) and oscillatory (green line), satisfy the asymptotic scaling relationship $\mathrm{e}^{\pi\beta} = O(r_0^2)$, which motivates the asymptotic scaling relationships utilised in the forthcoming analysis (§2.3). In fact, we observe that each instability tongue is bounded above in memory by either the oscillatory instability threshold satisfying $\mathrm{e}^{\pi\beta} = O(r_0)$ (gold dashed line), or the in-line speed oscillation instability threshold (purple dashed line) arising for free walkers [4, 35, 56]. Detailing the latter instability (denoted by the pink curve in figure 2.2(b)), which manifests as in-line speed oscillations along the circular orbit with amplitudes on the order of the Faraday wavelength and arises for orbits so large as to be inaccessible within the laboratory, will be the subject of a future investigation.

2.3   The onset of instability

In figure 2.4, we compare the scaled destabilisation frequency, $\xi = S/\omega$, computed along the stability boundary for the first wobbling instability tongue (see figure 2.2(b)) to that of nonlinear wobbling states arising just beyond the instability threshold (see figure 2.1(d)), as reported in the experimental study of [52] and the numerical simulations of [80]. The nonlinear wobbling frequency remains close to that predicted by the linear stability analysis, with the two coinciding in the small-wobbling-amplitude limit. Furthermore, both frequencies remain close to twice the orbital frequency, which serves to further motivate our analysis of resonant wobbling instabilities. We proceed to elucidate these observations by means of systematic asymptotic analysis performed along the stability boundary. Our analysis will also rationalise the quasi-periodicity and envelopes of the instability tongues, and the influence of the inertial coefficient, κ_0, on orbital stability.

We characterise the onset and form of each instability tongue using asymptotic analysis valid when $r_0 \gg 1$. For wobbling instabilities, the destabilisation frequency, S, is comparable to the orbital frequency, ω; thus, we assume that the dimensionless wobbling frequency $\xi = S/\omega = O(1)$. Moreover, the dimensionless orbital speed, $U = r_0\omega$, typically remains close to the free walking speed, $u_0 = O(1)$ [35]. We thus replace ω with U/r_0 in the stability equations (2.11) and tangential force balance (2.12), and henceforth assume $U = O(1)$. The dependence of the orbital memory, ω_{orb}, on the orbital radius is more subtle. As motivated in §2.2.4 and evidenced in figure 2.3, the tip of each instability tongue is characterised by the scaling relationship $\mathrm{e}^{\pi\beta} = O(r_0^2)$ (where $\beta = \omega_{\mathrm{orb}}^{-1}$), which represents the key dominant balance underpinning our asymptotic analysis. Notably, this dominant balance implies that the orbital memory generally decreases with increasing orbital radius, such that $\omega_{\mathrm{orb}} \sim (\ln(r_0))^{-1}$ when $r_0 \gg 1$.
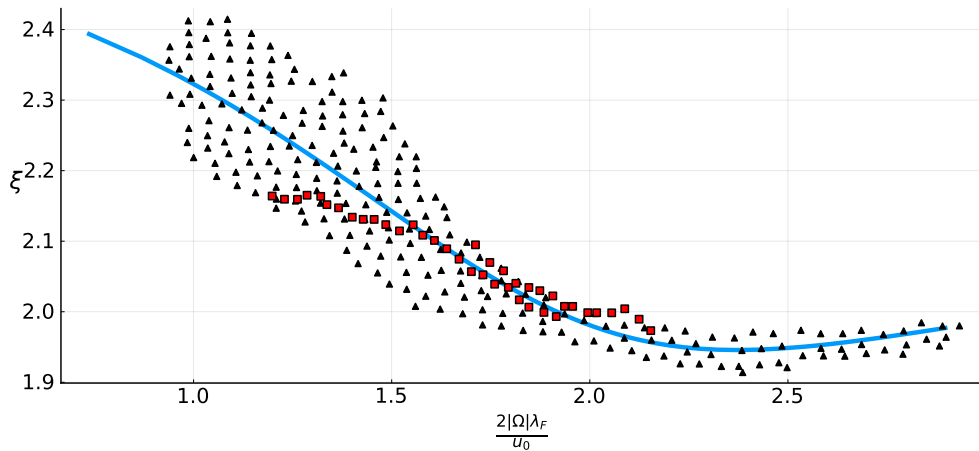
Figure 2.4: The dependence of the ratio of the wobbling frequency to the orbital frequency, ξ, on the bath rotation rate, Ω, just beyond the onset of instability for the first wobbling tongue in figure 2.2(b). Data indicating the wobbling frequencies reported in the experimental study of Harris and Bush [52, figure 7(b)] (red squares, $0.961 \leq \gamma/\gamma_F \leq 0.978$) and the numerical simulations of Oza et al. [80, figure 2 (c,d)] (black triangles, $0.952 \leq \gamma/\gamma_F \leq 0.967$), corresponding to $\kappa_0 = 1.6$, where $\kappa_0 = m/DT_W$. The blue curve indicates our prediction for the wobbling frequency along the stability boundary (white curve in figure 2.2(b)), corresponding to the small-wobbling-amplitude limit.

2.3.1 Asymptotic expansion

We proceed by using the asymptotic expansions of the integrals in equations (2.11) to identify the imaginary roots of the stability function G defined in equation (2.13) when $r_0 \gg 1$. Specifically, we seek the roots that minimise the critical memory of instability, as arise along the stability boundary in figure 2.2(b). We utilise asymptotic expansions for the closed form expressions of the stability integrals (see appendix A.2), which involve Bessel functions, $J_\nu(r_0)$, of the first kind with complex order ν, and their derivatives with respect to argument, $J_\nu'(r_0)$ (see equation (A.6)). As the complex order takes values in the set $\nu \in \{\pm i\beta, \pm i(\beta \pm i\xi)\}$ along the stability boundary, where $\beta = O(\ln(r_0))$ and $\xi = O(1)$ for $r_0 \gg 1$, the argument of each Bessel function is asymptotically large relative to its order. We may thus expand each of the stability coefficients in equation (2.11) when $r_0 \gg 1$, utilising the dominant balance $e^{\pi\beta} = O(r_0^2)$, with details presented in appendix A.4. Likewise, we use the large-argument expansions of the Bessel functions, valid when $\beta = O(\ln(r_0)) \ll \sqrt{r_0}$, to deduce that

$$U^2 = 2\left(1 - \frac{\beta}{r_0}\right) + O\left(\frac{1}{r_0^3}\right), \tag{2.15}$$

which will be utilised throughout the following analysis.

As our aim is to identify the imaginary roots of the equation $G(s) = 0$, we proceed by substituting the asymptotic approximations expressed in equations (A.9) into equation (2.13). Moreover, we determine the orbital speed, U, scaled destabilisation frequency, ξ, and inverse orbital memory, β, by means of an asymptotic expansion in terms of the small parameter r_0^{-1}, namely

$$U = U_0 + \frac{U_1}{r_0} + O\left(\frac{1}{r_0^2}\right), \quad \xi = \xi_0 + \frac{\xi_1}{r_0} + O\left(\frac{1}{r_0^2}\right), \quad \beta = \beta_0 + \frac{\beta_1}{r_0} + O\left(\frac{1}{r_0^2}\right). \tag{2.16}$$

In §2.3.2, we present the solution to the leading-order problem, for which we systematically demonstrate that $\xi = 2 + O(r_0^{-2})$ at the tip of each wobbling instability tongue, corresponding to a wobbling instability with wobbling angular frequency 2ω, the so-called 2-wobble [52, 80] (see figure 2.2) and find the critical memory for wobbling and monotonic instabilities. To determine how the scaled destabilisation frequency varies away from the tip of each wobbling instability tongue, we extend the asymptotic procedure to incorporate higher-order corrections in §2.3.3.

2.3.2 Leading-order solution

We proceed to determine the leading-order solution, corresponding to the values of U_0, ξ_0 and β_0. By using the asymptotic relationship $\mathscr{D} = i\xi\mathscr{C} + O(r_0^{-3})$ deduced in equation (A.9), we find that the stability condition (2.13) satisfies

$$\frac{\mathscr{C}\left(i\xi\mathscr{A} + \mathscr{B}\right)}{i\xi(\xi^2 - 1)} = O\left(\frac{1}{r_0^4}\right), \tag{2.17}$$

whereupon substituting the leading-order expressions for $\mathscr{A}$, $\mathscr{B}$, U, ξ and β from equations (A.9) and (2.16) results in

$$\frac{\mathscr{C}}{U_0}\left[\frac{2\sin(2r_0)}{\xi_0^2-1}\Big(\operatorname{csch}(\pi(\beta_0+\mathrm{i}\xi_0))+\operatorname{csch}(\pi\beta_0)\Big)+\frac{\kappa_0 U_0^3+1}{r_0^2}\right]=O\left(\frac{1}{r_0^3}\right). \qquad (2.18)$$

As $\mathscr{C}=2U_0/r_0+O\left(r_0^{-2}\right)$ is nonzero to leading order (see equation (A.9)), the leading-order solution to (2.18) may be found by setting the term in square brackets equal to zero. Furthermore, the imaginary part of equation (2.18) can only be satisfied when the destabilisation frequency, ξ_0, is an integer, whose possible values will be the focus of the remainder of this section. We proceed to eliminate possible integer values for ξ_0 by looking for the solutions to the stability problem that occur at the highest possible value of β_0, as these solutions correspond to the instabilities arising at lowest memory for a given orbital radius. Our analysis will show that only two solutions are possible: (i) $\xi_0=0$, corresponding to a monotonic instability; and (ii) $\xi_0=2$, corresponding to a 2ω instability.

To explore the possibility of ξ_0 being odd, we first consider the limit $\xi_0\to 1$ in equation (2.18). By applying L'Hôpital's rule, we find that the leading-order stability condition reduces to

$$1+\kappa_0 U_0^3+\mathrm{i}\pi r_0^2\sin(2r_0)\coth(\pi\beta_0)\operatorname{csch}(\pi\beta_0)=0.$$

As the real parts cannot be balanced (since $U_0>0$), there are no solutions to this equation. Similarly, if ξ_0 were odd and not equal to 1, the leading-order stability condition (2.18) would become

$$1+\kappa_0 U_0^3=0,$$

which is also impossible to satisfy. We thus conclude that ξ_0 cannot be odd, meaning that the destabilisation frequency must be an even multiple of the orbital frequency.

To explore the possible even values of ξ_0, we denote $\xi_0=2n$ (where n is an integer) and use the approximation $\sinh(x)\approx\cosh(x)\approx\frac{1}{2}\mathrm{e}^x$ for $x\gg 1$; as such, the leading-order stability condition (2.18) reduces to

$$\mathrm{e}^{\pi\beta_0}=\frac{8r_0^2\sin(2r_0)}{(1-4n^2)(1+\kappa_0 U_0^3)}. \qquad (2.19)$$

To be consistent with the assumed scaling of $\mathrm{e}^{\pi\beta_0}=O(r_0^2)$, we require $\sin(2r_0)=O(1)$. As $\sin(2r_0)$ can be either positive or negative, the lowest memory (or largest β_0) condition requires maximising the magnitude of the right-hand side of (2.19). In the case of $n=0$, we have a monotonic instability: by noting that $U_0=\sqrt{2}$ from equations (2.15) and (2.16), we thus arrive at the monotonic stability boundary

$$\mu_{\mathrm{mon}}=\frac{\sqrt{2}}{\pi r_0}\ln\left(\frac{8r_0^2\sin(2r_0)}{1+2\sqrt{2}\kappa_0}\right), \qquad (2.20)$$

which is valid when $\sin(2r_0)>0$ and $\sin(2r_0)=O(1)$. For the case $n\neq 0$, we observe that $1-4n^2<0$; we thus deduce the requirement $\sin(2r_0)<0$. The magnitude of the

right-hand side of equation (2.19) is then minimised at $n = 1$, which corresponds to $\xi = 2$, or $s = 2i\omega$. We have thus demonstrated that the destabilisation frequency along wobbling stability boundaries is approximately twice the orbital angular frequency. By substituting $n = 1$ into (2.19) and rearranging, we deduce that the corresponding critical wave decay rate for a wobbling instability is

$$\mu_{\text{wob}} = \frac{\sqrt{2}}{\pi r_0} \ln\left(-\frac{8r_0^2 \sin(2r_0)}{3(1 + 2\sqrt{2}\kappa_0)}\right), \tag{2.21}$$

which is valid when $\sin(2r_0) < 0$ and $\sin(2r_0) = O(1)$.

The asymptotic expressions (2.20)–(2.21) for the instability memory give rise to alternation between wobbling ($\sin(2r_0) < 0$) and monotonic ($\sin(2r_0) > 0$) instabilities with increasing orbital radius. In addition, μ_{mon} and μ_{wob} are maximised (corresponding to the tip of each instability tongue) when, to leading order for large orbital radius, $\sin(2r_0) = 1$ and $\sin(2r_0) = -1$, respectively. These extrema thus determine the wobbling and monotonic envelopes

$$\mu_{\text{wob}}^{\text{env}} = \frac{\sqrt{2}}{\pi r_0} \ln\left(\frac{8r_0^2}{3(2\sqrt{2}\kappa_0 + 1)}\right) \quad \text{and} \quad \mu_{\text{mon}}^{\text{env}} = \frac{\sqrt{2}}{\pi r_0} \ln\left(\frac{8r_0^2}{2\sqrt{2}\kappa_0 + 1}\right), \tag{2.22}$$

which are represented in figure 2.5(a) by the green and red dashed curves, respectively. Notably, increasing κ_0 increases the critical memory of wobbling and monotonic instabilities. Furthermore, since $\mu_{\text{mon}}^{\text{env}} - \mu_{\text{wob}}^{\text{env}} = \sqrt{2}\ln(3)/(\pi r_0) > 0$, we conclude that the envelope of the monotonic instabilities arises at a lower memory than that of wobbling instabilities, as evident from the red and green lines in figure 2.3.

2.3.3 First-order wobbling and monotonic solutions

The leading-order analysis presented in §2.3.2 determined approximations for the wobbling frequency and the critical memory at onset of instability, from which we deduced the most unstable orbital radii. However, the leading-order analysis did not provide insight into the behaviour of the instability frequency along each wobbling tongue, specifically the extent to which wobbling instabilities are approximated by a 2-wobble. So as to investigate this behaviour and so determine U_1, ξ_1 and β_1, we proceed to solve the tangential force balance and the stability problem in equations (2.15) and (2.17) to next order by using the expansions in equation (2.16). The expanded tangential force balance equation (A.9) shows that $U_1 = -\beta_0/U_0$. By substituting into the stability condition $i\xi\mathscr{A} + \mathscr{B} = 0$, using equations (A.9) and (2.16), retaining next-order terms and solving for the real and imaginary parts, we deduce that wobbling instabilities ($\xi_0 \neq 0$) have the first-order correction

$$\xi_1 = -\frac{4\beta_0}{\pi}\cot(2r_0) \quad \text{and} \quad \beta_1 = \frac{3\sqrt{2}\kappa_0\beta_0}{\pi(2\sqrt{2}\kappa_0 + 1)} + \left(\frac{64\beta_0 + 27\pi}{12\pi^2} - \frac{\beta_0^2}{\pi}\right)\cot(2r_0). \tag{2.23}$$

Similarly, for the monotonic instability ($\xi_0 = 0$), one may deduce that $\xi_1 = 0$ and

$$\beta_1 = \frac{3\sqrt{2}\kappa_0\beta_0}{\pi(2\sqrt{2}\kappa_0 + 1)} + \left(\frac{2\pi\beta_0 + 1}{4\pi} - \frac{\beta_0^2}{\pi}\right)\cot(2r_0). \tag{2.24}$$

We recall that the asymptotic solution is valid when $\sin(2r_0) = O(1)$. Notably, ξ_1 vanishes for wobbling instabilities when $\cos(2r_0) = 0$, corresponding to $s = i\omega \left(2 + O\left(r_0^{-2}\right)\right)$ at the most unstable orbital radii (see §2.3.2). Wobbling instabilities are thus driven by a resonance between the destabilisation frequency and the orbital frequency, with a larger critical memory necessary to destabilise orbits whose instability frequency deviates from twice the orbital frequency.

2.3.4 Comparison to the numerical instability tongues

To buttress our asymptotic developments, we compare the numerically deduced instability tongues to our asymptotic formulae in figure 2.5, with leading-order results presented in figure 2.5(a,c) and first-order corrections in figure 2.5(b,d). Notably, our asymptotic results are valid when $r_0 \gg 1$, $\sin(2r_0) = O(1)$ and either $\xi = 0$ (corresponding to monotonic instabilities) or $\xi \approx 2$ (corresponding to wobbling instabilities). Despite these restrictions, the leading-order memory captures the main features of the stability tongues, and the asymptotic instability frequency closely matches the numerical behaviour for $\xi = 0$ or $\xi \approx 2$. The success of our asymptotic results even for orbits of moderate radius is rooted in the choice of expansion parameter, namely $k_F r_0$ in dimensional variables, which is assumed to be large. We note that all orbits presented in figure 2.5 satisfy $k_F r_0 \geq 2\pi$ (or $r_0/\lambda_F \geq 1$), which is evidently sufficiently large for our asymptotic results to yield reasonable agreement. Finally, we note that a similarly favourable agreement between our asymptotic and numerical results was obtained across a wide range of κ_0 values, including for those inaccessible in the laboratory (see figure 2.4.1).

In summary, our asymptotic results explain the preponderance of 2-wobbles, with an exact resonance arising at the most unstable radius of each wobbling instability tongue. Moreover, we quantify the detuning from an exact resonance and the corresponding increase in the critical memory for nearby orbital radii. Finally, our asymptotic results demonstrate that the instability tongues alternate between wobbling and monotonic instabilities as the orbital radius is progressively increased, with the envelope of the monotonic instabilities arising at a lower memory than that of wobbling instabilities (figure 2.3).

2.4 Physical interpretations of the wobbling and monotonic instability tongues

Having established concise asymptotic formulae describing the onset of wobbling and monotonic instabilities, we now deepen our physical understanding by comparing the efficacy of different heuristic arguments for the critical radii at the onset of instability. Specifically, we first compare the predictions of several energy-based heuristics suggested in prior investigations to those of our numerical and asymptotic results (§2.4.1). We then propose a new heuristic based on the form of the mean pilot wave (§2.4.2), which we show to be more fruitful than prior heuristics.
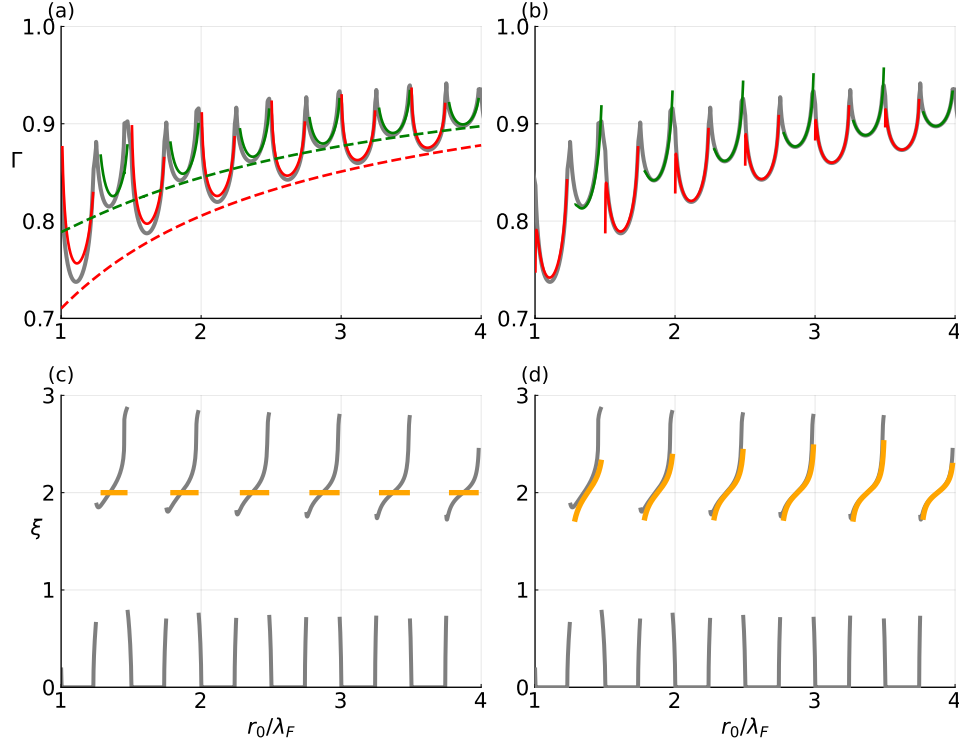
Figure 2.5: Comparison of the numerical solution and asymptotic approximations to the wobbling and monotonic stability boundaries. (a,b) The critical dimensionless vibration parameter at onset, $\Gamma = (\gamma - \gamma_W)/(\gamma_F - \gamma_W)$, and (c,d) the instability frequency relative to the orbital frequency, $\xi = S/\omega$, for $\kappa_0 = 1.6$. We compare the numerical solution (grey) with (a,c) the leading-order (equations (2.20)–(2.21)) and (b,d) the first-order (equations (2.23)–(2.24)) asymptotic results. (a,b) the critical memory compared to the asymptotic wobbling (green) and monotonic (red) instability boundaries. In (a), the leading-order envelopes (equation (2.22)) are denoted by dashed curves. (c,d) The critical wobbling frequency and its asymptotic counterpart (orange). All the asymptotic results presented in (a)-(d) are valid when $\sin(2k_F r_0) = O(1)$, $k_F r_0$ is large, and $\xi = 0$ (monotonic instabilities) or $\xi \approx 2$ (2-wobbles). Discontinuities in the grey curves (c,d) reflect transitions between monotonic ($\xi = 0$) and wobbling ($\xi \approx 2$) instabilities.

2.4.1 Energy-like heuristics

The hydrodynamic pilot-wave system is a driven-dissipative system: energy is supplied by the system vibration and ultimately lost through viscous dissipation. Nevertheless, quasi-steady and periodic dynamical states arise in which the energy input precisely balances that lost through dissipation, and energy is exchanged primarily between the bouncing drop and the Faraday wave field excited by its impact [69, 70]. For inviscid gravity-capillary waves, kinetic energy is exchanged with gravitational potential and surface energies. For our investigation, it thus suffices to characterise the system energetics in terms of the wave energy, which is readily computed from our model.

Owing to the slow spatial decay of the walker wave field (2.1b), the standard wave energy integral diverges when integrating over the plane. Instead, we adopt the notion of *wave intensity*, E, as coined by Hubert et al. [57], which acts as a suitable proxy for the sum of the wave field gravitational potential and surface energies. In dimensional units, we thus define

$$E = \lim_{R \to \infty} \frac{1}{R} \left[\int_{|\boldsymbol{x}| \leq R} \frac{1}{2} \rho g h^2 \, \mathrm{d}\boldsymbol{x} + \int_{|\boldsymbol{x}| \leq R} \sigma \left(\sqrt{1 + |\nabla h|^2} - 1 \right) \mathrm{d}\boldsymbol{x} \right], \tag{2.25}$$

where σ and ρ are the fluid surface tension coefficient and density, respectively, and E has units of energy per unit length. For small wave slope, we henceforth approximate the bracketed term in the second integral by $\frac{1}{2} |\nabla h|^2$. By applying the divergence theorem to the surface energy contribution and exploiting the fact that the wave field is monochromatic with wavenumber, k_F, we demonstrate in appendix A.5.1 that the contributions from gravitational and surface energies are proportional to each other, and equation (2.25) reduces to

$$E = (\rho g + \sigma k_F^2) \lim_{R \to \infty} \frac{1}{2R} \int_{|\boldsymbol{x}| \leq R} h^2(\boldsymbol{x}, t) \, \mathrm{d}\boldsymbol{x}, \tag{2.26}$$

an expression proportional to that obtained by Labousse et al. [65] and Hubert et al. [57], who neglected the contribution of surface tension.

To analyse the wave intensity, we transform (2.26) to dimensionless variables by defining $\hat{h} = h/h_0$ and $\hat{E} = E/E_0$, where $h_0 = AT_W/T_F$ and $E_0 = h_0^2 k_F^{-1}(\rho g + \sigma k_F^2)$ are the characteristic wave height and intensity. By once again taking k_F^{-1} and T_W as the units of length and time (see §2.2.1), we define the dimensionless wave intensity by

$$\hat{E} = \lim_{R \to \infty} \frac{1}{2R} \int_{|\boldsymbol{x}| \leq R} \hat{h}^2(\boldsymbol{x}, t) \, \mathrm{d}\boldsymbol{x}, \tag{2.27}$$

where

$$\hat{h}(\boldsymbol{x}, t) = \int_{-\infty}^{t} \mathrm{J}_0(|\boldsymbol{x} - \boldsymbol{x}_p(s)|) \mathrm{e}^{-\mu(t-s)} \, \mathrm{d}s, \tag{2.28}$$

is the dimensionless form of the pilot wave.

For circular orbital motion, the dimensionless wave intensity takes the remarkably simple form (see appendix A.5.2)

$$\hat{E} = \frac{1}{\mu} \mathcal{I}_0(0), \tag{2.29}$$
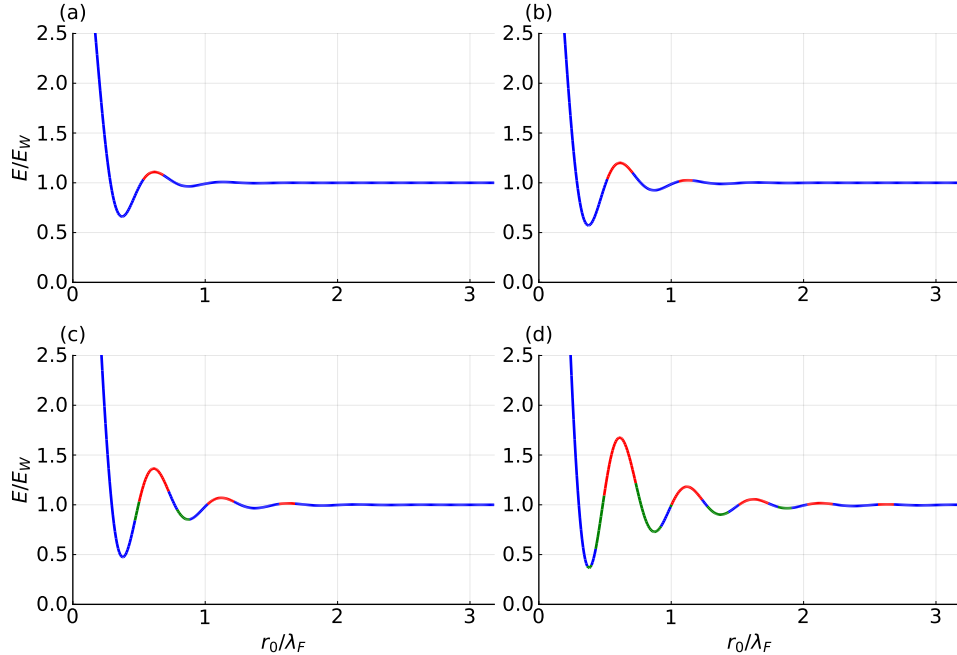
Figure 2.6: The dependence of the wave intensity, E (see equation (2.30)), relative to that of a walker, E_W, on the orbital radius for $\kappa_0 = 1.6$ and $\Gamma = $ (a) 0.7, (b) 0.75, (c) 0.8, and (d) 0.85. The colour scheme is the same as in figure 2.2. The onsets of monotonic and wobbling instabilities are correlated with, respectively, the local maxima and minima of the wave intensity, E.

where $\mathcal{I}_0(0)$ (defined in equation (2.6a)) is the amplitude of the wave field beneath the droplet [31]. Since the wave intensity and droplet gravitational potential energy are proportional to each other for orbital motion, either quantity serves equally well as a diagnostic measure of orbital stability. We may now use the tangential force balance (2.12) to deduce that the orbital wave intensity (2.29) reduces to

$$\hat{E} = \frac{1}{\mu^2}\left(1 - \frac{U^2}{2}\right), \qquad (2.30)$$

where $U = r_0\omega$ is the orbital speed. For fixed wave decay rate, μ, we conclude that the wave intensity is smaller for faster orbiters. Moreover, the transition from stationary bouncing ($U = 0$) to orbiting ($U > 0$) serves to decrease the wave energy, as does the transition from bouncing to rectilinear walking [32]. Finally, combining the bound $\hat{E} > 0$ with (2.30) supplies the upper bound on the orbital speed noted in §2.2.2, namely $U < \sqrt{2}$.

To explore the connection between wave intensity (or, equivalently, droplet gravitational potential energy) and orbital stability, we present the dependence of the wave intensity on the orbital radius in figure 2.6. As the wave decay rate, μ, is decreased, we observe that all monotonic instabilities arise in the vicinity of radii that *maximise* the wave intensity, while wobbling instabilities generally arise close to the orbital radii that *minimise* the wave intensity. (We note that the other wobbling instabilities appear as side bands to the first monotonic instability tongue; see figure 2.2(b).) This correlation is thus indicative of an

49
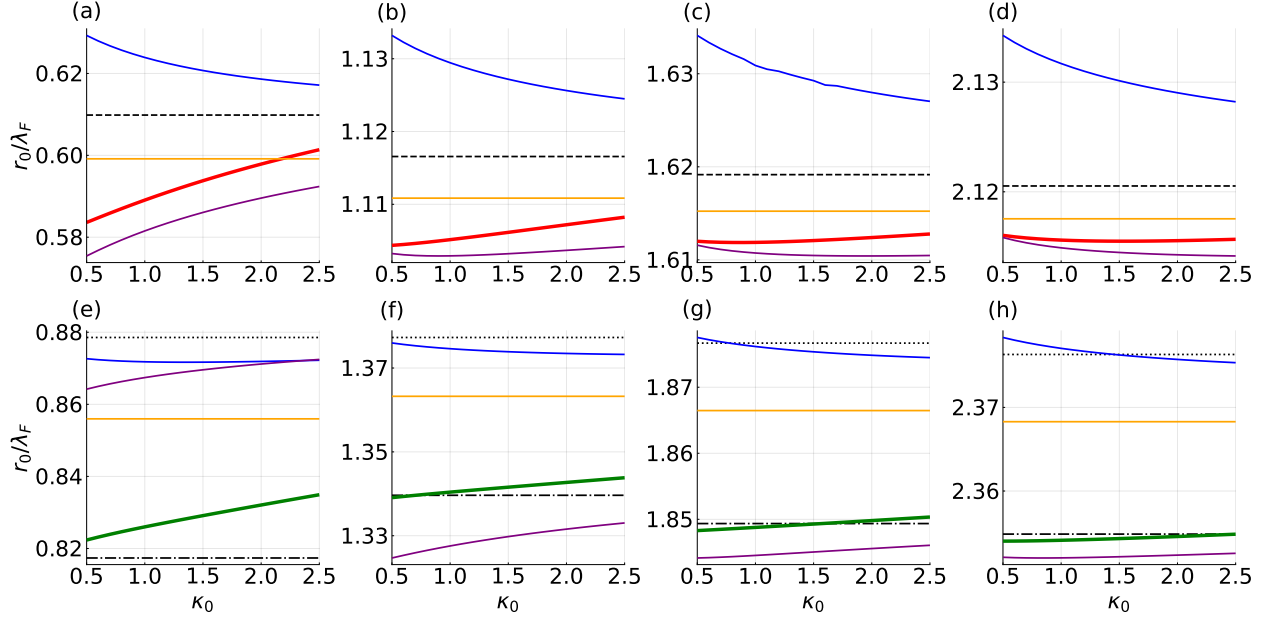
Figure 2.7: The dependence of the critical orbital radius on the inertia-to-drag ratio, $\kappa_0 = m/DT_W$, for (a)-(d) monotonic (red) and (e)-(h) wobbling (green) instabilities. Each panel corresponds to a different instability tongue in figure 2.2(b), with radius increasing from left to right. We compare the critical radii of monotonic and wobbling instabilities to those that maximise and minimise the wave intensity (equation (2.29), blue) and the derivative of the mean wave force (orange, §2.4.2), respectively. We also compare the critical radii with those predicted by the asymptotic formulae for monotonic (equations (2.20) and (2.24)) and wobbling (equations (2.21) and (2.23)) instabilities (purple). The black horizontal lines correspond to zeros of $J_0(k_F r_0)$ (dotted), $J_1(k_F r_0)$ (dashed), and $J_2(k_F r_0)$ (dot-dashed), whose relation to orbital stability was noted by Labousse et al. [64]. With increasing orbital radius, the range of each vertical axis narrows, reflecting the improved predictions of each heuristic.

underlying orbital energy principle, according to which the magnitude of the wave intensity prescribes the stability of the corresponding circular orbit [28]. To test this hypothesis, we present in figure 2.7 the orbital radius arising at the tip of each of the first four wobbling (green curves) and monotonic (red curves) instability tongues, i.e. the radii that locally minimise Γ along the stability boundary (the white curve in figure 2.2(b)). For each critical value of Γ (or $\mu = 1 - \Gamma$), we compare the corresponding critical orbital radius to the extrema of the wave field intensity (blue curves), confirming our observation that maxima and minima of E roughly correspond to the tips of the monotonic and wobbling instability tongues, respectively, with the agreement improving for larger orbital radius.

To further assess the utility of different energy-based heuristics, we also compare the critical radii to the zeros of $J_0(r_0)$, $J_1(r_0)$ and $J_2(r_0)$, as suggested by Labousse et al. [64]. As presented in figure 2.7, the monotonic instabilities appear at radii slightly smaller than the zeros of $J_1(r_0)$, while the wobbling instabilities typically align closely with the zeros of $J_2(r_0)$. We note, however, that the critical radii exhibit a weak dependence on κ_0 that is not

captured by the zeros of Bessel functions. On the other hand, the zeros of $J_1(r_0)$ approach the radii satisfying $\sin(2r_0) = 1$ for larger orbital radius, consistent with our asymptotic analysis of the monotonic instability (§2.3.2). Likewise, the zeros of $J_0(r_0)$ and $J_2(r_0)$ both approach the radii satisfying $\sin(2r_0) = -1$, in agreement with our analysis of wobbling instabilities (§2.3.2). We thus rationalise Labousse's conjecture that the zeros of Bessel functions are likely to identify the loci of the most unstable orbital radii.

Finally, we compare the critical orbital radii of the numerically computed stability boundary with our asymptotic formulae derived in §2.3.2 and §2.3.3. Specifically, we numerically minimise the first-order solutions, corresponding to the combination of equations (2.20) and (2.24) for the monotonic instability tongues (figure 2.7(a)-(d)), and equations (2.21) and (2.23) for the wobbling instability tongues (figure 2.7(e)-(h)). Our asymptotic results appear as purple curves in figure 2.7, and agree favourably with the critical radii of the numerical stability boundary, generally capturing the correct trend with increasing κ_0, and satisfying the anticipated $O(r_0^{-2})$ convergence as the orbital radius is increased. One limitation of this approach, however, is the absence of a local minimum for the first wobbling tongue when using the first-order correction (2.23) (owing to the parasitic influence of the $\cot(2r_0)$ term). Instead, we compare the critical radius in this case to that computed from the leading-order solution given in equation (2.21), which explains the larger discrepancy in figure 2.7(e). Nevertheless, our large-radius asymptotic results work surprisingly well in this case, where the orbital radius is relatively small.

In summary, we find that the simple heuristic criteria for the critical orbital radii are moderately successful, with the agreement improving for larger orbital radius. The zeros of Bessel functions generally give better agreement with the numerical results than the extrema of the wave intensity, or, equivalently, the droplet's gravitational potential energy. Notably, incorporating the droplet's kinetic energy within this latter heuristic does not significantly affect the critical orbital radii, with the resultant curves generally being indistinguishable from the blue curves in figure 2.7. Finally, these heuristic arguments are limited by their inability to predict the critical memory at the onset of instability and to capture the dependence of the critical radii on κ_0. Both quantities may be accurately computed using our asymptotic framework.

2.4.2 The mean wave field

Although the zeros of $J_1(r_0)$ and $J_2(r_0)$ provide satisfactory agreement with the numerical results for the tip of each instability tongue [64], this heuristic does not provide rationale for the *type* of instability. We proceed to develop a new dynamic rationale that is asymptotically equivalent to the heuristic of [64], yet explains the alternation between monotonic and wobbling instabilities with increasing orbital radius evident in figure 2.2(b).

We proceed by developing a dynamical interpretation of orbital instability in terms of the force applied by the mean wave field, specifically that averaged over one orbital period. One may decompose the orbital wave field into a continually evolving, non-axisymmetric component that serves to propel the droplet at a constant horizontal speed [15, 62], and a static axisymmetric component (the mean wave field) that imparts either an inward or outward radial force to the droplet [33, 63]. We note that a similar decomposition of the wave field applies when considering small perturbations from orbital motion, for which the

mean wave field may now be regarded as a quasi-static potential. Notably, Perrard et al. [84] used this potential to determine the radii of quantised circular orbits; in contrast, we use this potential to explain the onset of orbital instability.

The dimensionless axisymmetric mean wave field, $\bar{h}(r)$, accompanying a droplet executing a circular orbit of radius r_0 about the origin is given by [84, 93]

$$\bar{h}(r) = \frac{1}{\mu}\mathrm{J}_0(r_0)\mathrm{J}_0(r).$$

We thus deduce that the dimensionless radial wave force,

$$\mathcal{F}(r_0) = -2\frac{\mathrm{d}\bar{h}}{\mathrm{d}r}\bigg|_{r=r_0},$$

applied by the mean wave field along the droplet's trajectory is

$$\mathcal{F}(r_0) = \frac{2}{\mu}\mathrm{J}_0(r_0)\mathrm{J}_1(r_0) = -\frac{2\cos(2r_0)}{\mu\pi r_0} + O\left(\frac{1}{r_0^2}\right),$$

with derivative

$$\mathcal{F}'(r_0) = \frac{4\sin(2r_0)}{\mu\pi r_0} + O\left(\frac{1}{r_0^2}\right). \tag{2.31}$$

As shown in §2.3.1, wobbling instabilities occur when $\sin(2r_0) < 0$, whereas monotonic instabilities occur when $\sin(2r_0) > 0$. Equation (2.31) suggests that, for sufficiently large r_0, the type of instability exhibited by increasing the memory at constant r_0 is thus related to the derivative of the mean wave force. Specifically, if $\mathcal{F}'(r_0) < 0$, then the corresponding circular orbit destabilises via a wobbling instability. Conversely, if $\mathcal{F}'(r_0) > 0$, then the circular orbit destabilises via a monotonic instability.

This correlation between the sign of $\mathcal{F}'(r_0)$ and the form of instability can be interpreted physically through consideration of figure 2.8. As in our linear stability analysis (§2.2.3), we posit that the instantaneous orbital radius, $r_p(t)$, has the form $r_p(t) = r_0 + \epsilon r_1(t)$, where $0 < \epsilon \ll 1$ is a small parameter and $r_1(t)$ denotes the perturbation to the orbital radius. It follows that the force exerted by the mean wave field may be approximated by $\mathcal{F}(r_p) \approx \mathcal{F}(r_0) + \epsilon r_1\mathcal{F}'(r_0)$; thus, the direction and magnitude of the perturbed wave force is prescribed by $\mathcal{F}'(r_0)$. When $\mathcal{F}'(r_0) > 0$, an outward radial perturbation ($r_1 > 0$) results in an increase in the outward force that drives the droplet away from equilibrium. Similarly, an inward perturbation ($r_1 < 0$) decreases the outward force. When $\mathcal{F}'(r_0) > 0$, we may thus regard the mean wave force as a repulsive spring force that induces monotonic changes in the orbital radius. Conversely, when $\mathcal{F}'(r_0) < 0$, the mean wave force behaves like an attractive spring that opposes any perturbations in the orbital radius from r_0 and so induces oscillations in the orbital radius. This physical picture is consistent with the observation that the type of instability changes when $\mathcal{F}'(r_0)$ changes sign (see figure 2.8). Moreover, the mean wave field's opposition to perturbations from r_0 hinders the onset of the corresponding wobbling instabilities, which is consistent with wobbling instabilities occurring at higher memory than their monotonic counterparts. Finally, the magnitude of the radial wave force increases as μ decreases, thereby increasing the sensitivity to perturbation at higher memory.

52
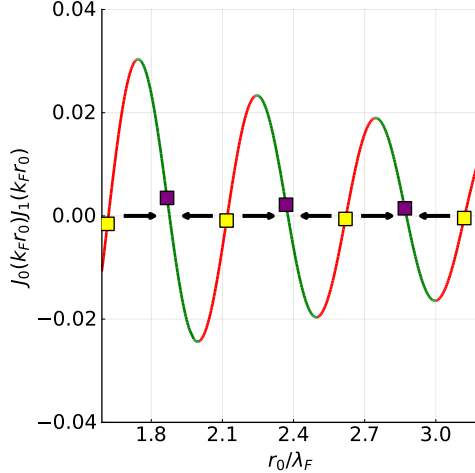
Figure 2.8: Schematic representation of orbital instability in terms of the mean wave force. We present the dependence of $\frac{1}{2}\mu\mathcal{F}(r_0) = J_0(k_F r_0)J_1(k_F r_0)$, which is proportional to the mean wave force, on the orbital radius for $\kappa_0 = 1.6$. The curve is colour-coded according to the type of instability arising along the stability boundary (white curve in figure 2.2(b)). Along green and red portions of the curve, the mean wave field acts like an attractive and repulsive spring, respectively, giving rise to wobbling and monotonic instabilities. The sign of the mean wave force is denoted by arrows, and its slope is maximised and minimised at the yellow and purple squares, respectively.

In an attempt to rationalise the radii of the most unstable circular orbits (corresponding to the tips of the stability tongues in figure 2.2(b)), we follow the above argument and posit that these will correspond to the radii marked by the largest relative change in the perturbation force, as characterised by the coefficient $\mathcal{F}'(r_0)$. The coefficient $\mathcal{F}'(r_0)$ is maximised in magnitude at critical radii, r_c, satisfying $\mathcal{F}''(r_c) = 0$. Specifically, maxima in $\mathcal{F}'(r_0)$ correspond to monotonic instabilities, and minima in $\mathcal{F}'(r_0)$ to wobbling instabilities. In figure 2.7, we observe that the most unstable radii predicted by this heuristic ($\mathcal{F}''(r_c) = 0$) exhibit excellent quantitative agreement with the numerical solution for monotonic instabilities, and a favourable agreement for wobbling instabilities. The limitation of this heuristic for wobbling instabilities is presumably rooted in small deviations of the mean wave field from a quasi-static potential for oscillatory droplet motion.

In summary, we have developed a new rationale for the onset of wobbling and monotonic instabilities in terms of the force exerted on the droplet by the mean wave field. Specifically, our investigation indicates that the critical radii, r_c, at the onset of instability approximately satisfy $\mathcal{F}''(r_c) = 0$. In contrast to the heuristic arguments presented in §2.4.1, our rationale explains the alternation of wobbling and monotonic instabilities with increasing orbital radius. Moreover, our study suggests that the oscillatory and quasi-periodic nature of the stability boundary (see figure 2.2(b)) is correlated with the quasi-monochromatic mean wave field. As a caveat, our rationale is only valid for circular orbits near the stability boundary, and so cannot be used to differentiate between stable and unstable orbits. Like the heuristic arguments presented in §2.4.1, our rationale neither predicts the critical memory of instability nor accounts for the dependence on the parameter κ_0. Nevertheless, it performs

remarkably well over the range of values of the inertia-to-drag parameter, κ_0, accessible in the laboratory.

2.5   Discussion

We have examined the stability of circular inertial orbits executed by droplets walking in a rotating frame. We have developed an asymptotic framework for studying orbital stability, specifically for characterising the critical memory at the onset of the wobbling and monotonic instabilities. Our asymptotic model rationalises the repeating structure of the stability diagram in figure 2.2, which we demonstrate to be rooted in the periodic nature of the mean wave field. Our theory not only rationalises the preponderance of 2-wobble instabilities, but also predicts that the destabilisation frequency is exactly twice the angular frequency at the most unstable orbital radii, corresponding to the tips of the stability tongues. In rationalising the most unstable wobbling frequencies reported in the experiments of [52] and simulations of [80], our study has demonstrated the importance of resonant instability in orbital pilot-wave dynamics.

Our asymptotic results show that orbital instability is enhanced through resonance. Resonant instabilities have been reported in other pilot-wave systems, including the in-line speed oscillations of the free walker [4, 35], 4ω orbital instabilities in a linear central force [60], and 2ω, 3ω and 4ω instabilities for pairs of orbiting droplets [28, 81]. This naturally raises the question of the prevalence of resonant instabilities in other pilot-wave systems. In subsequent work, we will consider the more complex orbits arising for a droplet in a linear central force, where richer resonances are expected to arise. We expect the asymptotic framework developed here to be well-suited to addressing this class of problems.

It is worth enumerating the limitations of our study. In our study, we have assumed resonant bouncing at constant bouncing phase, and neglected the far-field exponential decay of the wave field [70, 91, 98]. Both of these approximations are known to break down for multi-droplet systems [2, 17, 46, 81], and so might become significant at sufficiently high orbital memory. In addition, we have restricted our attention to the linear stability of circular orbits, and so not considered nonlinear effects such as the jump up/down instabilities reported by Harris and Bush [52] and Oza et al. [80]. Finally, we have not considered instability in the large-radius limit inaccessible in the laboratory, which one expects to be related to the instability of the free, rectilinear walking state [4, 35, 56], which is the subject of chapter 7.

We have also compared the success of various heuristics for predicting the onset of orbital instability in our system. Our study has lead us to introduce two new heuristics, specifically the wave intensity and the mean wave force. We show that the orbital radii corresponding to the onset of monotonic and wobbling instabilities generally arise near the radii that maximise and minimise the wave intensity, respectively. We have also demonstrated the equivalence of the wave intensity and wave height beneath the drop as proxies for the droplet energy; specifically, the wave energy is proportional to the gravitational potential energy of the drop. This result provides new insight into the observations made by Couchman and Bush [16] and Thomson et al. [96] that a ring of droplets rearranges itself so as to minimise the mean gravitational potential of the droplets, suggesting that they are doing so in order to

minimise the global wave energy.

[64] proposed that wobbling and monotonic instabilities arise from orbits that receive little wave energy from the J_1 and J_2 modes, and postulated that the most unstable orbital radii occur at zeros of these Bessel functions. We have demonstrated that this heuristic leads to impressive agreement with our numerical calculations over a wide range of parameter values, and outperforms our wave intensity extremisation principle, defined in §2.4.1. However, Labousse's heuristic does not provide a physical mechanism that distinguishes between the wobbling and monotonic instabilities. Our new heuristic based on the form of the mean wave field (§2.4.2) indicates the correlation between the type of instability and the derivative of the mean wave force, and so sheds light on the alternation between wobbling and monotonic instabilities with increasing orbital radius. The general utility of mean-pilot-wave-based heuristics will be considered in more detail in chapter 5.

Having considered orbital stability in hydrodynamic pilot-wave system in a rotating frame, we now apply our mathematical framework to the linear central force.

Chapter 3

Orbital instabilities in constrained pilot-wave hydrodynamics

3.1 Introduction

Quantised orbital motion may be induced when the droplet is confined by a central force. This configuration was first explored experimentally by Perrard et al. [83, 84], who applied a vertical magnetic field with a radial gradient to a droplet filled with ferrofluid, thereby imparting a linear spring force to the droplet motion. The authors discovered that the droplet has a propensity for orbits that are quantised in both mean radial position and mean angular momentum, which include circles, lemniscates and trefoils. While the radii of the circular orbits were found to be quantised in a fashion similar to those arising in a rotating frame [64], the frequency of the wobbling instabilities that set in as the memory is increased were non-resonant, specifically incommensurate with the orbital frequency, ω, marking a departure from the behaviour in a rotating frame [62, 94]. In addition, Labousse and Perrard [62] noted the presence of $\sqrt{2}\omega$-frequency oscillations both in their experiments and in investigations of their Rayleigh oscillator model. At higher memory, the periodic orbital states destabilize, leading to an intermittent switching between unstable periodic orbits [62].

A similar progression was reported by Cristea-Platon et al. [22] in their study of walkers in small corrals. Specifically, as the memory was increased progressively, periodic orbital states, such as circles, lemniscates and trefoils, gave way to chaotic motion marked by intermittent switching between these orbits, a progression also captured in the simulations of Durey et al. [34]. Circular orbits have also been observed for walkers confined by an oscillatory potential [93], and an inverted conical topography [97]. Other confining potentials, including a two-dimensional Coulomb potential [94], have been explored numerically. Thus, while the linear central force will be the main point of comparison in our study, we will also consider a more general confining force.

We here present a theoretical study of the onset of orbital instability for walker motion confined by a radial or Coriolis force, paying particular attention to the systems considered experimentally. We compare the walker system with classical orbital mechanics in §3.2, and examine the influence of the constancy of the orbital speed on orbital stability in the pilot-

wave system. We then introduce the pilot-wave system in §3.3, and discuss the differences between orbital stability in the Coriolis and linear central force systems. In §3.4, we rationalise the stability of circular orbits at low memory and demonstrate the prevalence of near-critical non-resonant perturbations for a droplet confined by a central force. In §3.5, we detail our framework for characterising orbital stability at higher memory, and prove a connection between monotonically growing perturbations and the steady radial force balance for orbital motion. In §3.6, we use asymptotic analysis to deduce the stability boundaries for both resonant and non-resonant instabilities, and explain the influence of the form of the confining potential on orbital stability. Finally, in §3.7, we discuss the similarities and differences between the Coriolis and central force systems, which we rationalise in terms of the preponderance of non-resonant instabilities in an axisymmetric potential.

3.2 Physical picture

We consider the behaviour of walkers executing circular orbits in 2D in the presence of an axisymmetric potential. Celestial mechanics, where satellites may execute circular orbits under the influence of the axisymmetric gravitational force, provides a natural and valuable point of comparison for our study. More generally, in classical orbital dynamics, the form of the applied external potential affects the stability of circular orbits. Specifically, it is well established that stable circular orbits can only be supported for confining potentials of the form $V(r) \propto r^q$ provided $q > -2$ (Goldstein et al. [49]). We begin by re-deriving this result in §3.2.1, and then compare it to the analogous stability condition relevant to the hydrodynamic pilot-wave system in §3.2.2.

3.2.1 Classical orbital mechanics

We consider the dynamics of a particle of mass m moving in response to an axisymmetric potential, $V(r)$, in two dimensions. By denoting the particle position in polar coordinates as $\boldsymbol{x}_p(t) = r(t)(\cos\theta(t), \sin\theta(t))$, one may express the radial force balance as

$$m(\ddot{r} - r\dot{\theta}^2) = -V'(r). \tag{3.1}$$

Conservation of angular momentum implies that $l = mr^2\dot{\theta}$ is constant for all time. By substituting $\dot{\theta} = \frac{l}{mr^2}$ into (3.1), we thus deduce that the radial motion of the particle satisfies

$$m\ddot{r} - \frac{l^2}{mr^3} = -V'(r). \tag{3.2}$$

For steady orbital motion with radius r_0, the radial force balance implies that $l^2 = mr_0^3 V'(r_0)$, which can only be satisfied when $V'(r_0) > 0$. In this case, if $r(t) = r_0 + \epsilon r_1(t)$, the radial perturbation will necessarily evolve according the linearised equation $\ddot{r}_1 + \omega_c^2 r_1 = 0$, where

$$\omega_c^2 = \omega^2 \left(3 + \frac{r_0 V''(r_0)}{V'(r_0)} \right). \tag{3.3}$$

For a power-law potential of the form $V(r) \propto r^q$, we deduce from (3.3) the relationship $\omega_c^2 = (q + 2)\omega^2$, which may be used to assess the linear stability of circular orbits. If

58

$q < -2$, perturbations grow exponentially in time, with circular orbits thus being unstable. Conversely, circular orbits are stable for $q > -2$, with radial perturbations undergoing bounded oscillations (which follows from the reversibility of (3.2)). Notably, the perturbation frequency, ω_c, is generally incommensurate with the orbital frequency, ω, except when $q+2$ is a perfect square. Special cases of resonant oscillations include the case of a three-dimensional Coulomb force field, for which $q = -1$ and $\omega_c = \omega$, and the case of a linear spring force, for which $q = 2$, and $\omega_c = 2\omega$.

3.2.2 Orbital mechanics at a constant speed

A feature of walker motion in a rotating frame is that the droplet speed varies negligibly [52]. Conversely, in the presence of a linear central force, variations in droplet speeds are appreciable [84]. Nevertheless, for nearly circular orbits, one expects the droplet speed to remain nearly constant for both systems. To gain insight into the influence of a fixed speed on the stability of circular orbits, we consider the motion of a particle of mass m moving in response to a potential, V, with the particle speed fixed at u_0 for all time. The radial motion of the particle is thus governed by (3.1), whereas the constancy of the particle speed gives rise to the condition $u_0^2 = \dot{r}^2 + r^2\dot{\theta}^2$. By eliminating $\dot{\theta}^2$ from (3.1), we deduce that the radial motion of the constant-speed particle is governed by

$$m\left(\ddot{r} - \frac{u_0^2 - \dot{r}^2}{r}\right) = -V'(r), \tag{3.4}$$

which plays the analogous role to (3.2). In a manner similar to §3.2.1, we deduce that the steady orbital radius satisfies $mu_0^2 = r_0 V'(r_0)$ for $V'(r_0) > 0$. Furthermore, perturbations of the form $r(t) = r_0 + \epsilon r_1(t)$ evolve according to the linearised equation $\ddot{r}_1 + \omega_r^2 r_1 = 0$, where

$$\omega_r^2 = \omega^2 + \frac{V''(r_0)}{m}, \quad \text{or} \quad \omega_r^2 = \omega^2\left(1 + \frac{r_0 V''(r_0)}{V'(r_0)}\right), \tag{3.5}$$

which has a similar form to that of ω_c for classical orbital mechanics (see (3.3)). Notably, the circular orbit is unstable when $V'(r_0) + r_0 V''(r_0) \leq 0$, with perturbations growing monotonically in time, and stable otherwise.

We proceed by evaluating the perturbation frequency, ω_r, for different forms of the confining potential relevant to pilot-wave hydrodynamics. For the power-law potential $V(r) \propto r^q$, it follows directly from (3.5) that $\omega_r = \omega\sqrt{q}$. Consequently, the perturbation frequency is scaled by a factor $\sqrt{q}$ relative to the orbital frequency when $q > 0$, with perturbations instead growing in time when $q \leq 0$. For the special case of a linear central force, for which $V(r) \propto r^2$, equation (3.5) indicates that $\omega_r = \sqrt{2}\omega$, which is precisely equal to the instability frequency reported by Labousse and Perrard [62] for a droplet executing circular orbits in a harmonic potential. For the logarithmic potential $V(r) \propto \log(r)$, corresponding to a two-dimensional Coulomb force, equation (3.5) yields $\omega_r = 0$, indicating monotonic growth of radial perturbations, a feature prevalent in the simulations of Tambasco et al. [94]. Finally, we note that the perturbation frequency is incommensurate with the orbital frequency when $\sqrt{q}$ is irrational, and so is referred to as 'non-resonant' henceforth.

A very different physical picture emerges for a constant-speed particle moving in response to a Coriolis force, $\boldsymbol{F} = -2m\boldsymbol{\Omega} \times \dot{\boldsymbol{x}}_p$, where $\boldsymbol{\Omega} = \Omega\hat{\boldsymbol{z}}$ is the rotation vector orthogonal to

the plane of the particle motion. In this case, radial perturbations evolve according to the linearised equation $\ddot{r}_1 + \omega^2 r_1 = 0$, where $\omega = -2\Omega$ is the orbital frequency. Notably, the perturbation frequency is precisely equal to the orbital frequency, reflecting the translational invariance of the particle motion. Indeed, if a particle were perturbed from its circular motion then it would immediately commence another circular orbit, but with a slight shift in the orbital centre. In contrast to the case of a central force, for which the orbital centre is fixed in space, there are no non-resonant oscillations for particle motion in a Coriolis force.

We now explain why the instability condition on q depends on whether angular momentum or speed is conserved. For angular momentum conservation, we rewrite the radial force balance as

$$m\ddot{r} = \frac{l^2}{mr^3} - kr^{q-1}, \tag{3.6}$$

where k is a generalised spring constant, and we consider a power-law central force. If we consider this equation as a force balance in one dimension, $\frac{l^2}{mr^3}$ corresponds to an effective potential set up because of the centrifugal force. We observe that if $q < -2$, then the effective potential decays slower than the confining potential. This indicates that the total potential energy of the system, $\frac{l^2}{2mr^2} + \frac{k}{q}r^q$, decreases to 0 as $r \to \infty$, indicating that it is energetically favourable for outwards perturbations to continue to infinity. In the constant-speed system, the corresponding centrifugal force takes the form $\frac{mU^2}{r}$, and the total potential energy becomes $-mU^2 \log\left(\frac{r}{r_s}\right) + \frac{k}{q}r^q$, for some length scale r_s. If $q < 0$, then, for large r, the potential energy diverges to $-\infty$ as $r \to \infty$, again showing that it is energetically favourable for outwards perturbations to approach infinity, and that circular orbits are unstable. These arguments indicate that monotonic instabilities arise when the confining force decays too quickly, which will form the basis for Theorem 1 and Corollary 1.1, to be introduced in §3.5.

Our simplified physical picture of walkers as particles moving at a constant speed highlights several features that are present throughout our study. First, the radial perturbation frequency, $\omega_r = \sqrt{q+2}\omega$, for orbital pilot-wave dynamics differs from that of celestial mechanics, $\omega_c = \sqrt{q}\omega$, giving rise to instability in power-law potentials for $q < 0$ instead of the classical result of $q < -2$ [49]. Furthermore, the oscillation frequency ω_r is exclusive to particle motion confined by a central force; in a Coriolis force, the analogous oscillations correspond to translations. Finally, the perturbation frequency $\omega_r = \sqrt{q}\omega$ is non-resonant when $\sqrt{q}$ is irrational, but can resonate with the orbital frequency, ω, when the potential is chosen so that q is a perfect square. Notably, this simplified physical picture does not account for the influence of memory on orbital pilot-wave dynamics, specifically the geometric constraint imposed by the quasi-monochromatic pilot-wave field. We thus seek to explain the influence of the self-generated wave field and memory on orbital stability for the hydrodynamic pilot-wave system, paying particular attention to the emergence of resonant and non-resonant instabilities.

3.3   Pilot-wave hydrodynamics

We consider the dynamics of a millimetric droplet of mass m, self-propelling across the surface of a fluid bath vibrating vertically with frequency f and acceleration $\gamma \sin(2\pi f t)$. When the
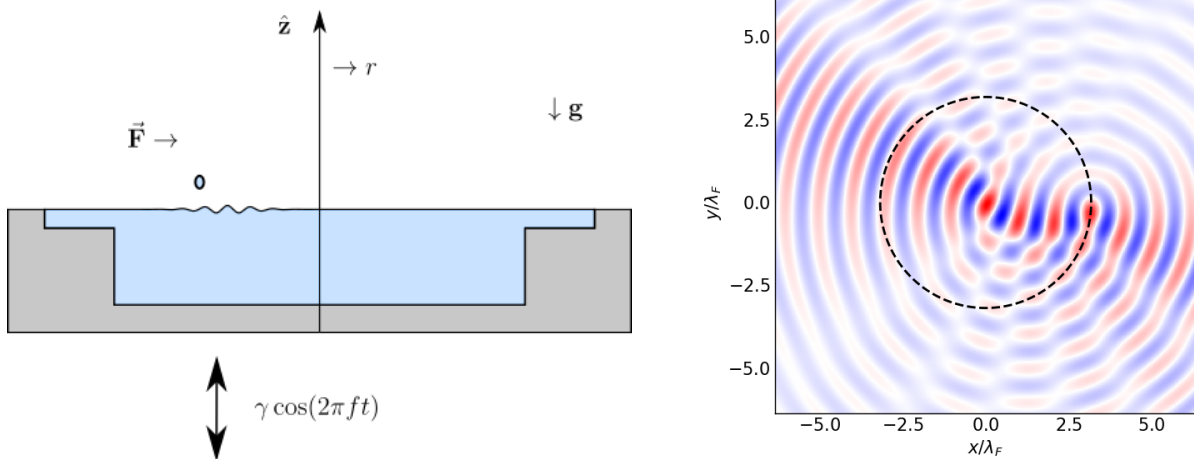
Figure 3.1: (a) Schematic of the physical system, in which a droplet walks along a fluid bath driven vertically with acceleration $\gamma \cos(2\pi f t)$. Two distinct systems are described with the same mathematical framework. In the first, the system rotates at an angular velocity $\boldsymbol{\Omega} = \Omega \boldsymbol{e}_z$, so the droplet is subjected to a Coriolis force, and is prone to anticyclonic circular orbits. In the second, the droplet is constrained by a central force $\vec{\boldsymbol{F}} = -\nabla V(r)$. The vertical axis represents either the centre of force for a central force, or the rotation axis, $\hat{\boldsymbol{z}}$, in the rotating system. (b) Simulated wave field generated by a droplet walking in a circular orbit (black dashed lines) at high memory, where the influence of the mean wave field, centred at the orbital centre, is comparable to that of the wave field generated by the most recent impacts. Red and blue designate wave field displacements of opposite signs, white indicates no surface displacement.

vibrational acceleration exceeds the Faraday threshold, $\gamma > \gamma_F$, the fluid surface is unstable to standing, subharmonic Faraday waves with period $T_F = 2/f$ and wavelength $\lambda_F = 2\pi/k_F$, where k_F is prescribed by the water-wave dispersion relation [6]. The parameter range of interest is $\gamma < \gamma_F$, corresponding to an undisturbed bath in the absence of the droplet. We focus on the hydrodynamic parameter regime considered by Harris and Bush [52], who used a fluid of density 949 kg m^{-3}, kinematic viscosity 20 cSt, surface tension 0.0206 N m^{-1}, and depth 4 mm, with a vibrational frequency $f = 80$ Hz and a droplet of radius 0.4 mm whose free walking speed was approximately $u_0 = 11$ mm s^{-1}. Further parameters are given in table 3.1.

3.3.1 Integro-differential trajectory equation

The droplet's horizontal motion is modelled using the stroboscopic trajectory equation developed by Oza et al. [78, 79], as is deduced by time-averaging the dynamics over a bouncing period, T_F [70]. The droplet's horizontal position, $\boldsymbol{x}_p(t)$, thus evolves according to

$$m\ddot{\boldsymbol{x}}_p + D\dot{\boldsymbol{x}}_p = -mg\nabla h(\boldsymbol{x}_p(t), t) + \boldsymbol{F}, \tag{3.7a}$$

where dots denote differentiation with respect to time, t. The drop is propelled by the wave force, $-mg\nabla h(\boldsymbol{x}_p(t), t)$, and resisted by the linear drag force, $-D\dot{\boldsymbol{x}}_p$. We consider two

Dimensional parameters	Definition
$\boldsymbol{x}_p$, m	Droplet position and mass
$\boldsymbol{\Omega}$, k	Rotation vector, central force constant
T_M, T_d	Wave decay time with and without forcing
λ_F, $k_F = 2\pi/\lambda_F$	Faraday wavelength and wavenumber
f, $T_F = 2/f$	Forcing frequency and Faraday period
A	Pilot wave amplitude
D	Drag coefficient
g	Gravitational acceleration
$F = mgAk_F$	Wave force coefficient
γ	Vibrational acceleration
γ_F, $\gamma_W/\gamma_F = 1 - \sqrt{Fk_FT_d^2/2DT_F}$	Faraday threshold, walking threshold
$c = \sqrt{F/DT_Fk_F}$	Maximum walking speed
$u_0 = \frac{c}{2}\sqrt{4 - (1-\Gamma)^2 - (1-\Gamma)\sqrt{(1-\Gamma)^2 + 8}}$	Free-walking speed
r_0, ω	Orbital radius and angular frequency
$T_O = 2\pi/\omega$	Orbital period
$U = r_0\omega$	Orbital speed
$T = 1/ck_F$	Free-walking time scale
s	Asymptotic complex growth rate of perturbations
$S = |\text{Im}(s)|$	Perturbation frequency

Dimensionless parameters	Definition
$M = m/DT$	Inertia-to-drag ratio
$\Gamma = (\gamma - \gamma_W)/(\gamma_F - \gamma_W)$	Memory parameter
$\hat{r}_0 = r_0k_F$	Dimensionless orbital radius
$\hat{\omega} = \omega T$	Dimensionless orbital frequency
$\hat{U} = \hat{r}_0\hat{\omega}$	Dimensionless orbital speed
$M_e^O = T_M/T_O$	Orbital memory
$\beta = 1/\omega T_M = 1/2\pi M_e^O$	Reciprocal orbital memory parameter
$\hat{s} = sT$	Dimensionless perturbation growth rate
$\xi = S/\omega$	Perturbation frequency relative to orbital frequency

Table 3.1: The parameters appearing in the pilot-wave system (3.8) and subsequent analysis. A and D are defined in terms of physical parameters in appendix A.1.

different forms of the external force, $\boldsymbol{F}$ (see figure 3.1). For a droplet in a rotating frame, the droplet is subjected to a Coriolis force, $\boldsymbol{F} = -2m\boldsymbol{\Omega} \times \dot{\boldsymbol{x}}_p$, where $\boldsymbol{\Omega} = \Omega\hat{\boldsymbol{z}}$ is the vertical rotation vector. When the droplet is confined by an axisymmetric potential, $V(|\boldsymbol{x}|)$, the applied force is $\boldsymbol{F} = -\nabla V(|\boldsymbol{x}_p|)$.

The stroboscopic pilot wave,

$$h(\boldsymbol{x}, t) = \frac{A}{T_F} \int_{-\infty}^{t} \mathrm{J}_0(k_F|\boldsymbol{x} - \boldsymbol{x}_p(s)|)\mathrm{e}^{-(t-s)/T_M}\,\mathrm{d}s, \qquad (3.7b)$$

is modelled as a continuous superposition of axisymmetric waves of amplitude A centred along the droplet's path, decaying exponentially in time over the memory time scale, $T_M = T_d/(1 - \gamma/\gamma_F)$ [78]. The memory parameter $M_e = \frac{T_M}{T_F}$ describes the number of prior impacts that are relevant for the drop dynamics; for large M_e, the dynamics are strongly affected by the droplet's past, and thus M_e is a measure of the droplet's path memory. Projecting the pilot wave onto the droplet's path makes clear the influence of path memory on the droplet motion, as is encapsulated within the integro-differential trajectory equation [78, 79]

$$m\ddot{\boldsymbol{x}}_p + D\dot{\boldsymbol{x}}_p = \frac{F}{T_F} \int_{-\infty}^{t} \frac{\mathrm{J}_1(k_F|\boldsymbol{x}_p(t) - \boldsymbol{x}_p(s)|)}{|\boldsymbol{x}_p(t) - \boldsymbol{x}_p(s)|}(\boldsymbol{x}_p(t) - \boldsymbol{x}_p(s))\mathrm{e}^{-(t-s)/T_M}\,\mathrm{d}s + \boldsymbol{F}, \qquad (3.8)$$

where $F = mgAk_F$ denotes the magnitude of the wave force. The quasi-monochromatic form of the pilot wave field imposes a geometric constraint on the droplet's motion whose effects are most pronounced at high memory, where the Faraday waves are most persistent.

3.3.2 Memory and orbital memory

In the absence of an applied force, the droplet self-propels at a constant speed, u_0, when the vibrational acceleration, γ, exceeds the walking threshold, γ_W. As the vibrational forcing remains below the Faraday threshold in experiments, $\gamma < \gamma_F$, it is convenient to characterise the pilot-wave dynamics in terms of the dimensionless memory parameter $\Gamma = (\gamma - \gamma_W)/(\gamma_F - \gamma_W)$ [13, 35, 82]. Notably, $\Gamma = 0$ corresponds to the walking threshold in the absence of an applied force ($\gamma = \gamma_W$), while $\Gamma = 1$ corresponds to the Faraday threshold ($\gamma = \gamma_F$), and thus infinite path memory [13].

For orbital pilot-wave dynamics, a key concept is that of 'orbital memory' [79], which determines the extent to which an orbiting droplet interacts with the waves generated on its prior orbit. For a droplet moving in a circular orbit at angular frequency ω, the waves generated along the droplet path decay by a factor e^{-T_O/T_M} over the orbital period, $T_O = 2\pi/\omega$. We thus define $M_e^O = T_M/T_O$ as the orbital memory. Notably, $M_e^O \approx T_M u_0/(2\pi r_0)$ increases with vibrational forcing and decreases for larger orbits owing to the relative constancy of the orbital speed, with $\omega \approx u_0/r_0$. For $M_e^O \ll 1$, the wave decays quickly relative to the orbital period, so the droplet is largely unperturbed by its wake. Conversely, if $M_e^O \gg 1$, the droplet is strongly influenced by its past history, with the quasi-monochromatic form of the Faraday wave field imposing a geometric constraint on the droplet motion. The onset of orbital instability arises at an intermediate regime, $M_e^O \approx 1$ [79]. The precise dependence of this critical orbital memory on the orbital radius will be established in §3.6.

3.3.3 Orbital stability diagram

We begin by comparing the dynamical behaviour of circular orbits for the cases of an applied Coriolis force and a droplet confined by a linear spring force, $\boldsymbol{F} = -k\boldsymbol{x}_p$. Specifically, we follow Oza et al. [79, 82] and Liu et al. [66] in summarising the dependence of the stability of circular orbits on their radius, r_0, and the memory parameter, Γ. By substituting $\boldsymbol{x}_p(t) = r_0(\cos\omega t, \sin\omega t)$ into (3.8), we deduce the radial and tangential force balances

$$-mr_0\omega^2 = \frac{F}{T_F} \int_0^\infty \mathrm{J}_1\left(2k_F r_0 \sin\left(\frac{\omega s}{2}\right)\right) \sin\left(\frac{\omega s}{2}\right) \mathrm{e}^{-s/T_M} \, \mathrm{d}s + \boldsymbol{F} \cdot \boldsymbol{n}, \tag{3.9a}$$

$$Dr_0\omega = \frac{F}{T_F} \int_0^\infty \mathrm{J}_1\left(2k_F r_0 \sin\left(\frac{\omega s}{2}\right)\right) \cos\left(\frac{\omega s}{2}\right) \mathrm{e}^{-s/T_M} \, \mathrm{d}s + \boldsymbol{F} \cdot \boldsymbol{t}. \tag{3.9b}$$

Notably, the applied tangential force vanishes for droplet motion under the influence of either a Coriolis or a spring force, namely $\boldsymbol{F} \cdot \boldsymbol{t} = 0$. Furthermore, $\boldsymbol{F} \cdot \boldsymbol{n} = 2m\Omega r_0\omega$ for a Coriolis force, and $\boldsymbol{F} \cdot \boldsymbol{n} = -kr_0$ for the linear spring force. We consider counter-clockwise orbital motion with $\omega > 0$, so that $U = r_0\omega$ is the orbital speed. Owing to the droplet's tendency to move along circular orbits at speeds close to the free-walking speed, u_0 [15], the orbital speed satisfies $U \approx u_0$ and is bounded above by the maximum steady walking speed, $U < c$ [66].

We begin by considering the radial force balance in the limit of zero memory, i.e. $M_e, T_M \to 0$, where the exponential terms in (3.9a) vanish. This balance provides suitable time scales for orbital motion in the rotating frame and central force systems respectively. When $T_M \to 0$, the radial force balance reduces to, in a rotating frame,

$$\omega = -2\Omega, \tag{3.10a}$$

and, in the presence of a central force,

$$\omega = \sqrt{\frac{k}{m}}. \tag{3.10b}$$

The orbital time scale t_o is then given by $t_o = \frac{1}{\omega}$. A second time scale is the rectilinear time scale $t_s = \frac{\lambda_F}{u_0}$, over which a droplet walking in a straight line at the free-walking speed u_0 travels a single Faraday wavelength, λ_F. The ratio of these two time scales leads to dimensionless groups for the rotation rate Ω and spring constant k.

The stability of circular orbits of radius r_0 at memory Γ in these two systems is indicated by the colour of the corresponding data point in figure 3.2(c,d) (Details of the orbital stability framework used to generate figure 3.2 are provided in §3.5). Stable circular orbits are indicated in blue. As the memory parameter, Γ, is increased progressively, circular orbits destabilise via either a monotonic (red) or oscillatory (green or orange) instability. The form of instability may be further characterised by the wobble number, ξ, defined as the ratio of the instability frequency, S, to the orbital frequency, ω (see figure 3.2(e,f). In both systems, $\xi = 0$ (red) indicates monotonic instability, for which perturbations grow monotonically in time (see figure 3.3(a)). Furthermore, $\xi \approx 2$ (green) indicates resonant instabilities with wobbling frequencies near 2ω, the so-called 2-wobbles (see figure 3.3(b)) [52, 79, 80]. For the linear spring force, a new class of instability (orange) arises with a wobbling frequency of

$\xi \approx \sqrt{2}$, which is incommensurate with the orbital frequency (see figure 3.3(c)). Notably, this frequency is precisely that deduced from our analysis of particles moving at constant speed in a linear spring force (§3.2.2), and coincides with the findings of Labousse and Perrard [62].

For the Coriolis force, orbital quantisation arises due to the emergence of monotonic instability tongues (red), for which the corresponding orbital radii are inaccessible in the laboratory [79]. This result is intimately connected to the form of the stability curve (see figure 3.2(a)) when parameterised by the orbital radius, r_0, for a fixed value of the memory parameter, Γ. Specifically, by denoting $\Omega = \Omega_0(r_0)$ as the solution to the radial force balance (3.9a), Oza et al. [79] proved that circular orbits have an unstable real eigenvalue when $\mathrm{d}|\Omega_0|/\mathrm{d}r_0 > 0$, corresponding to the upward-sloping branches in figure 3.2(a). Although a similar result holds for a central force with the spring coefficient $k = k_0(r_0)$ satisfying (3.9a) for given r_0 (see Theorem 1), namely that there exists an unstable real eigenvalue when $\mathrm{d}k_0/\mathrm{d}r_0 > 0$, it is evident from the orange instability tongues in figure 3.2(d) that this result is insufficient to explain the onset of instability for a linear spring force. Instead, a series of non-resonant instability tongues arise at a lower memory than the monotonic instabilities, serving as a new dominant mechanism for orbital instability for pilot-wave dynamics in a central force. Consequently, all perturbations at the onset of instability in a linear central force are oscillatory, with the perturbation frequency either close to $\sqrt{2}\omega$ or 2ω.

It is evident from figure 3.2 that the non-resonant instability (at frequency $\sqrt{2}\omega$) represents the principal difference between the linear spring and Coriolis force systems. The remainder of this paper thus focuses on the manifestation of this frequency and its interplay with resonant instabilities. We first show in §3.4 that the non-resonant frequency emerges as a near-critical stable eigenvalue even at low orbital memory, before investigating the onset of resonant and non-resonant instabilities in §3.6. To more deeply understand the emergence of non-resonant instabilities, we generalise our analysis to power-law potentials, $V(r) \propto r^q$, for which the perturbation frequency $\omega_r = \sqrt{q}\omega$ was postulated in §3.2.2. We pay particular attention to the case when q is a perfect square, for which ω_r resonates with the orbital frequency and a more complex stability diagram emerges.

3.4   Low orbital memory

The regime of low orbital memory, $M_e^O \ll 1$, in which the droplet's horizontal velocity evolves slowly relative to the memory time, T_M, emerges for relatively large orbits or weak vibrational forcing. In this weak-acceleration limit, one may substitute the approximation $\boldsymbol{x}_p(t) - \boldsymbol{x}_p(s) \approx (t-s)\dot{\boldsymbol{x}}_p(t) + \frac{1}{2}(t-s)^2\ddot{\boldsymbol{x}}_p(t)$ into the wave force integral term in (3.8), and evaluate the resulting integrals [15].

The droplet's trajectory equation may be approximated by the local form

$$\frac{\mathrm{d}\boldsymbol{p}}{\mathrm{d}t} + D_w(|\dot{\boldsymbol{x}}_p|)\dot{\boldsymbol{x}}_p = \boldsymbol{F}, \tag{3.11a}$$

where $\boldsymbol{p} = m\gamma_B(|\dot{\boldsymbol{x}}_p|)\dot{\boldsymbol{x}}_p$ is the droplet's effective momentum, expressed in terms of the wave-induced added mass, or 'hydrodynamic boost factor',

$$\gamma_B(|\dot{\boldsymbol{x}}_p|) = 1 + \frac{gAk_F^2T_M^3}{2T_F\big(1 + (k_FT_M|\dot{\boldsymbol{x}}_p|)^2\big)^{3/2}}. \tag{3.11b}$$
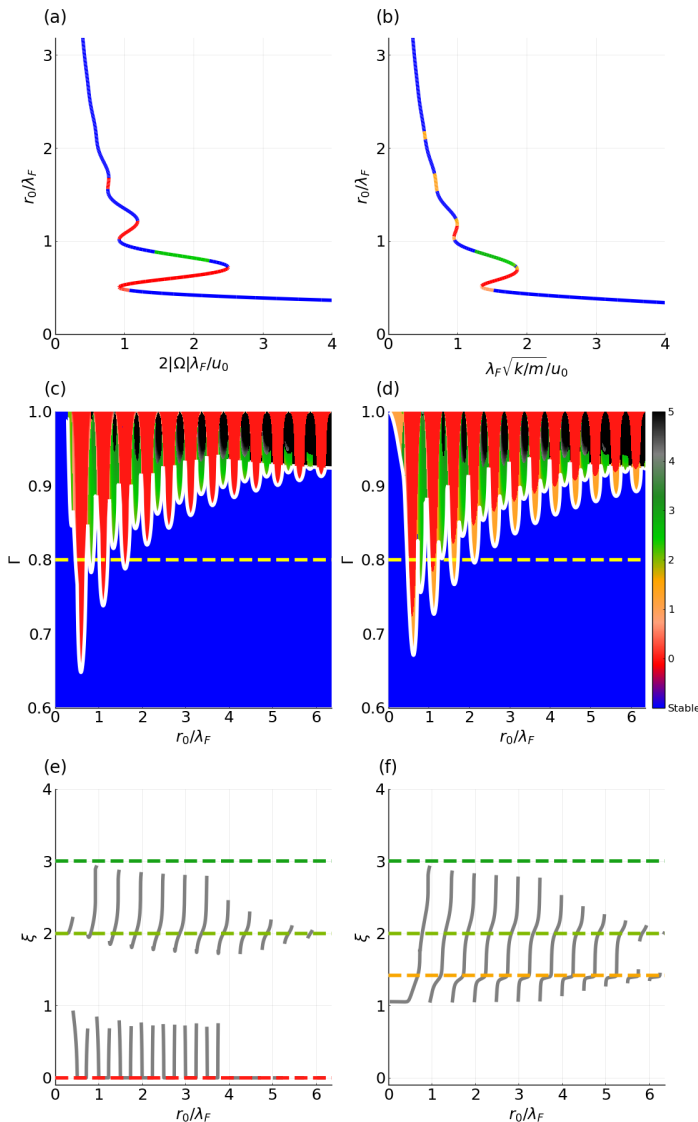
Figure 3.2: Stability curves for circular orbits in the presence of (a) a Coriolis force [79] and (b) a linear central force for $\Gamma = 0.8$, for the experimental parameters are given right before §3.3.1. Orbital radii, in units of wavelengths, are plotted against the non-dimensionalised time, $\frac{t_o}{t_w}$, where t_o and t_w are the orbital and free-walking time scales described in the discussion in (3.10). Blue represents stable circular orbits, all other colours represent unstable circular orbits colour-coded by the scaled destabilisation frequency. Red, in particular, represents circular orbits destabilising via a monotonic instability. $\frac{\mathrm{d}\Omega}{\mathrm{d}r_0} > 0$ in (a) is always accompanied by a monotonic instability, whereas $\frac{\mathrm{d}k}{\mathrm{d}r_0} > 0$ in (b) may lead to oscillatory instabilities. The plots in (a,b) correspond to the horizontal yellow slices in memory in (c,d), which are stability diagrams for a Coriolis force [79] and a linear central force. The white curves represent stability boundaries tracked numerically; above the white curves, all circular orbits are unstable. We note the additional orange instabilities in (d), corresponding to $\sqrt{2}\omega$ instabilities. (e, f) Scaled destabilisation frequency, ξ, along the stability boundaries for a Coriolis force [66], and a linear central force. The four dotted lines correspond to $\xi = 0, \xi = \sqrt{2}, \xi = 2$ and $\xi = 3$, using the same colour scheme as in (a) and (b). We emphasise that monotonic instabilities are replaced by the $\sqrt{2}\omega$ instabilities in (f).
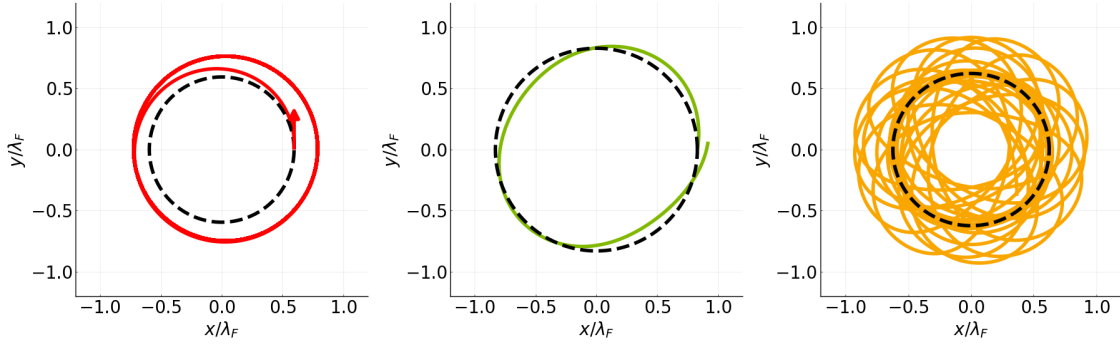
Figure 3.3: Unstable circular orbits, corresponding to (a) a monotonic instability, (b) a 2ω instability, and (c) a $\sqrt{2}\omega$ instability. The same colour scheme as in figure 3.2 is used to represent the type of instability. We observe that, in trajectories undergoing a 2ω instability, the oscillation period is approximately half the orbital period, whereas in trajectories undergoing a $\sqrt{2}\omega$ instability, the oscillations are incommensurate with the orbital frequency, ω. Monotonic instabilities may involve jumps to stable circular orbits of larger or smaller orbital radius, as in (a).

The wave field also results in a speed-dependent drag coefficient,

$$
D_w(|\dot{\boldsymbol{x}}_p|) = D \left[1 - \frac{c^2}{|\dot{\boldsymbol{x}}_p|^2} \left(1 - \frac{1}{\sqrt{1 + (k_F T_M |\dot{\boldsymbol{x}}_p|)^2}} \right) \right], \tag{3.11c}
$$

that drives the droplet towards the steady walking speed, u_0 [15], which is bounded above by $c = \sqrt{mgA/DT_F}$ [66, 78]. Specifically, the walking speed satisfies $D_w(u_0) = 0$, with $D_w > 0$ if $|\dot{\boldsymbol{x}}_p| > u_0$ and $D_w < 0$ otherwise. Owing to the relative simplicity of this so-called boost model (3.11), we examine the key mechanics of orbital motion in an applied force, before presenting our orbital stability framework in all of its complexity. This boost formulation will reveal the first effects of the wave field on the orbital stability.

3.4.1 Orbital solutions

Following Bush et al. [15], we consider steady orbital motion of the form $\boldsymbol{x}_p(t) = r_0(\cos \omega t, \sin \omega t)$, where $r_0 > 0$ is the orbital radius and ω is the angular frequency. Without loss of generality, we consider the case $\omega > 0$ so that $U = r_0 \omega$ is the orbital speed. We then project the droplet motion (3.11) onto the unit outward-pointing normal and tangent vectors, denoted $\boldsymbol{n} = (\cos \omega t, \sin \omega t)$ and $\boldsymbol{t} = (-\sin \omega t, \cos \omega t)$, yielding

$$
-m\gamma_B r_0 \omega^2 = \boldsymbol{F} \cdot \boldsymbol{n} \quad \text{and} \quad D_w(U)U = \boldsymbol{F} \cdot \boldsymbol{t}.
$$

For droplets executing circular orbits in a Coriolis force, $\boldsymbol{F} = -2m\boldsymbol{\Omega} \times \dot{\boldsymbol{x}}_p$, or an axisymmetric potential, $\boldsymbol{F} = -\nabla V(|\boldsymbol{x}_p|)$, the external force has a vanishing tangential component, namely $\boldsymbol{F} \cdot \boldsymbol{t} = 0$. We thus deduce that $D_w(U) = 0$, corresponding to the orbital speed, $U = r_0 \omega$, being precisely equal to the steady walking speed, u_0, arising in the absence of any external

forces. The normal force balance then prescribes the orbital radius, with

$$r_0 = \gamma_B \frac{u_0}{2|\Omega|} \tag{3.12}$$

for anticyclonic orbits in a Coriolis force [15]. For a droplet confined to an axisymmetric potential, the orbital radius r_0 satisfies

$$r_0 V'(r_0) = m\gamma_B(u_0)u_0^2, \tag{3.13}$$

provided that the radial force is inward, namely $V'(r_0) > 0$.

3.4.2 Orbital stability

We proceed to assess the response of the droplet motion to small perturbations away from a circular orbit, as predicted by the boost model (3.11), thereby gaining insight into orbital stability in the weak-acceleration limit. Specifically, we express

$$\boldsymbol{x}_p(t) = r(t)(\cos\theta(t), \sin\theta(t)) \quad \text{and} \quad \boldsymbol{u}(t) = u(t)(\cos\phi(t), \sin\phi(t)),$$

where $\boldsymbol{u} = \dot{\boldsymbol{x}}_p$ denotes the droplet velocity and $u(t) > 0$ its speed, and write

$$r(t) = r_0 + \epsilon r_1(t) \quad \text{and} \quad u(t) = u_0 + \epsilon u_1(t),$$

where r_0 satisfies the normal force balance (3.12)–(3.13) and $0 < \epsilon \ll 1$ is a small parameter governing the size of the perturbation. We similarly perturb the polar angles, writing $\theta(t) = \omega t + \epsilon\theta_1(t)$ and $\phi(t) = \omega t + \frac{1}{2}\pi + \epsilon\phi_1(t)$. As detailed in appendix B.1, we substitute this perturbation ansatz into the boost model (3.11) and expand nonlinear expressions in terms of the small parameter, ϵ, deriving linearised equations governing the evolution of the perturbation variables. We then eliminate the perturbed polar angles, deriving a coupled set of equations governing the evolution of the perturbed radius, $r_1(t)$, and the perturbed speed, $u_1(t)$, whose forms we analyse in the cases of a Coriolis force and an axisymmetric potential, as follows.

Walking in a rotating frame

When the droplet motion is subjected to a Coriolis force, the radial and speed perturbations evolve according to (see appendix B.1.2)

$$\ddot{r}_1 + \omega^2 r_1 = \omega\left(\frac{u_0 p'(u_0)}{p(u_0)}\right)u_1 \quad \text{and} \quad p'(u_0)\dot{u}_1 + u_0 D'_w(u_0)u_1 = 0, \tag{3.14}$$

where $p(u) = m\gamma_B(u)u$ is the magnitude of the boosted droplet momentum. Although the eigenvalues $s_\pm = \pm i\omega$ and $s_0 = -u_0 D'_w(u_0)/p'(u_0)$ may be readily computed (see appendix B.1.3), it is more illuminating to understand the interplay between radial and speed perturbations governed by (3.14). Specifically, radial perturbations evolve as would those of a forced oscillator with natural frequency, ω, corresponding to that of the circular orbit. The forcing is governed by perturbations in the droplet speed, which decay exponentially in

time when $p'(u_0) > 0$, where we recall that $D'_w(u_0) > 0$. Notably, the evolution of speed perturbations away from the base state of uniform speed along a circular orbit is identical to that of a droplet walking in a straight line [97]. Over the orbital time scale, $\tau = \omega t$, we observe that the evolution of the speed perturbation,

$$p'(u_0)\frac{\mathrm{d}u_1}{\mathrm{d}\tau} + r_0 D'_w(u_0)u_1(\tau) = 0,$$

determines that speed perturbations are damped rapidly relative to the orbital time when the orbital radius, r_0, is large. Finally, we note that perturbations in the droplet radius do not induce speed modulations, which reflects the translational invariance of orbital motion when subjected to a Coriolis force.

Walking in a central force

For a droplet confined to an axisymmetric potential, the response to perturbations is markedly different from that arising in the presence of a Coriolis force. Although the radial and speed perturbations are ostensibly similar (see appendix B.1.2), with

$$\ddot{r}_1 + \omega_r^2 r_1 = \omega\left(1 + \frac{u_0 p'(u_0)}{p(u_0)}\right)u_1 \quad \text{and} \quad p'(u_0)\dot{u}_1 + u_0 D'_w(u_0)u_1 = -\frac{p(u_0)}{r_0}\dot{r}_1, \qquad (3.15)$$

where

$$\omega_r = \omega\sqrt{1 + \frac{r_0 V''(r_0)}{V'(r_0)}}, \qquad (3.16)$$

two important differences emerge. First, the shape of the confining potential induces a shift in the natural frequency of radial perturbations, with ω_r being identical to the radial oscillation frequency derived in §3.2.2 for particles propelling at a constant speed. Second, radial perturbations excite speed perturbations, corresponding to the exchange of potential and kinetic energy as the droplet navigates its potential. As discussed in §3.2.2, radial perturbations evolve according to a forced oscillator only when $V'(r_0) + r_0 V''(r_0) > 0$; otherwise, radial perturbations grow monotonically in time, prompting the onset of instability. For power-law potentials of the form $V(r) \propto r^q$, orbits may be stable only when $q > 0$, with $\omega_r = \sqrt{q}\omega$ being the corresponding oscillation frequency of radial perturbations.

The coupling between radial and speed perturbations decreases for large orbital radii (when $p(u_0)\dot{r}_1/r_0$ becomes small), hinting that the frequency ω_r may become significant in the large-radius limit. We show in appendix B.1.3 that the eigenvalues of the linear system (3.15) are

$$s_0 = -\frac{u_0 D'_w(u_0)}{p'(u_0)} + O(r_0^{-2}) \quad \text{and} \quad s_\pm = \pm i\omega_r + O(r_0^{-2}), \qquad (3.17)$$

where s_0 is related to the decay of speed perturbations (as in the case of a Coriolis force), and $s_\pm$ reflect the natural frequency of radial oscillations. The eigenvalues $s_\pm$ are thus near-critical in the limit of large orbital radius. Although our analysis is restricted to the weak-acceleration limit, for which $s_\pm$ are both stable in the parameter regime relevant to experiments (see appendix B.1.3 for higher-order corrections to $s_\pm$), it seems conceivable that these near-critical eigenvalues might destabilise as the vibrational forcing is increased,

69

giving rise to instabilities associated with the natural frequency ω_r. We assess the validity of this hypothesis in §3.6.1.

3.4.3 Summary

By analysing the stability of large circular orbits in the weak-acceleration limit, we have characterised the emergence of a pair of near-critical stable eigenvalues close to $\pm i\omega_r$, where ω_r is the frequency of radial perturbations established in §3.2.2 for particles executing orbital motion at a constant speed in an axisymmetric potential. Our analysis here supersedes the physical picture developed in §3.2.2, demonstrating that radial perturbations in fact decay exponentially in time (owing to the dissipative action of viscosity), rather than executing sustained radial oscillations. Moreover, our analysis highlights the coupling of radial and speed oscillations for motion in a central force, corresponding to the exchange of kinetic and potential energy as the droplet explores the confining potential. In contrast, circular orbits are neutrally stable for orbital motion in a rotating frame, consistent with our assertions in §3.2.2. We stress that our analysis of the weak-acceleration limit cannot account for the emergence of wobbling and monotonic instabilities evident in the stability diagram (figure 3.2) as the vibrational forcing is increased, nor the instability associated with in-line speed oscillations arising for very large circular orbits at high memory. Nevertheless, our analysis provides insight into the mechanisms at play for non-resonant radial oscillations induced by a confining potential, with the onset of instability at higher memory to be explored in §3.6.

Finally, we emphasise that the wave-induced added mass, $\gamma_B > 1$, does not influence the qualitative behaviour predicted by the boost model (3.11) and serves only to augment the orbital radius for a fixed confining force. Specifically, the natural frequency of radial oscillations, corresponding to ω for a Coriolis force and ω_r for an axisymmetric potential, is independent of γ_B for a given orbital radius. Indeed, the emergence of oscillations at a frequency close to $\sqrt{2}\omega$ for a harmonic potential ($V(r) \propto r^2$) was predicted by Labousse and Perrard [62] on the basis of the Rayleigh oscillator model, which corresponds to the special case of $p(u) = mu$ and $D_w(u) = D_0(u^2/u_0^2 - 1)$. We thus conclude that the emergence of $\sqrt{2}\omega$-wobbles is a generic property of self-propelled particles moving along circular orbits in a linear central force at a preferred speed, which does not depend explicitly on the form of the wave forcing. We note, however, that the instabilities arising at larger orbital memory depend critically on the form of the wave field, as will be demonstrated in §3.6.

3.5 Orbital stability framework

We proceed by outlining a general framework for orbital stability, an extension of that developed by Oza et al. [79]. We then use this framework to deduce general insights into the stability problem that will enhance our intuition for orbital stability. Finally, we derive a theorem that generalises the stability condition of circular orbits in classical orbital mechanics in §3.2 to the pilot-wave system.

To investigate the stability of circular orbits in the hydrodynamic pilot-wave system, we

recast the trajectory equation (3.8) into polar coordinates, namely

$$\boldsymbol{x}_p(t) = r(t)(\cos\theta(t), \sin\theta(t)), \tag{3.18}$$

and infinitesimally perturb the droplet motion from a circular orbit at time $t = 0$ [79]. The radial and tangential force balances thus take the form

$$m(\ddot{r} - r\dot{\theta}^2) + D\dot{r} = \frac{F}{T_F}\int_{-\infty}^{t}\frac{\mathrm{J}_1(\mathfrak{D}(t,s))}{\mathfrak{D}(t,s)}[r(t) - r(s)\cos(\theta(t) - \theta(s))]\mathrm{e}^{-(t-s)/T_M}\,\mathrm{d}s$$
$$+\boldsymbol{F}\cdot\boldsymbol{n} + \epsilon c_r\delta(t), \tag{3.19a}$$

$$m(2\dot{r}\dot{\theta} + r\ddot{\theta}) + Dr\dot{\theta} = \frac{F}{T_F}\int_{-\infty}^{t}\frac{\mathrm{J}_1(\mathfrak{D}(t,s))}{\mathfrak{D}(t,s)}r(s)\sin(\theta(t) - \theta(s))\mathrm{e}^{-(t-s)/T_M}\,\mathrm{d}s$$
$$+\boldsymbol{F}\cdot\boldsymbol{t} + \epsilon r(t)c_\theta\delta(t), \tag{3.19b}$$

where $\mathfrak{D}(t,s) = |\boldsymbol{x}_p(t) - \boldsymbol{x}_p(s)|$ denotes the distance between the particle's position at times t and $s < t$, namely

$$\mathfrak{D}(t,s) = \sqrt{r^2(t) + r^2(s) - 2r(t)r(s)\cos\big(\theta(t) - \theta(s)\big)}.$$

The magnitude of the perturbation is governed by the small parameter $0 < \epsilon \ll 1$, with c_r and c_θ appearing in (3.19) being arbitrary constants that prescribe the sizes of the radial and tangential perturbations. Finally, we consider the case where the external force, $\boldsymbol{F}$, is parameterised in the form $\boldsymbol{F} = \zeta\boldsymbol{f}(r,\dot{r},\ddot{r},\dot{\theta},\ddot{\theta})$, and that $\boldsymbol{F}\cdot\boldsymbol{t} = 0$ for steady orbital motion, as is the case for both Coriolis and central forces. For a Coriolis force, ζ is the frame rotation rate, Ω, and $\boldsymbol{F} = -2m\boldsymbol{\Omega}\times\dot{\boldsymbol{x}}_p$. For a power-law central force, ζ is the generalised spring constant, k, and $\boldsymbol{F} = -k|\boldsymbol{x}_p|^{n-1}\boldsymbol{x}_p$. This parameterisation allows us to jointly consider both forces.

For ease of analysis and interpretability, we recast (3.19) into the following general form,

$$f_r(r,\dot{r},\ddot{r},\dot{\theta},\ddot{\theta}) + \zeta f_{\mathrm{ext},r}(r,\dot{r},\ddot{r},\dot{\theta},\ddot{\theta}) + \int_{-\infty}^{t} w_r(r(t), r(s), \theta(t) - \theta(s), t - s)\,\mathrm{d}s = \epsilon c_r\delta(t),$$
$$\tag{3.20a}$$

$$f_\theta(r,\dot{r},\ddot{r},\dot{\theta},\ddot{\theta}) + \zeta f_{\mathrm{ext},t}(r,\dot{r},\ddot{r},\dot{\theta},\ddot{\theta}) + \int_{-\infty}^{t} w_\theta(r(t), r(s), \theta(t) - \theta(s), t - s)\,\mathrm{d}s = \epsilon r_0 c_\theta\delta(t),$$
$$\tag{3.20b}$$

where ζ is the force coefficient, and f_{ext} is the external force. Notably, f_r and f_θ describe the radial and tangential forces, whereas $w_r = w_r(x_1, x_2, x_3, t)$ and $w_t = w_t(x_1, x_2, x_3, t)$ are the projections of the wave force kernel. For an attractive linear spring force, $\zeta f_{\mathrm{ext},r}(r,\dot{r},\ddot{r},\dot{\theta},\ddot{\theta}) = \zeta r, \zeta > 0$. The first argument of w_r and w_t, x_1, refers to the radial position of the droplet, while the second argument, x_2, refers to the radial position of the past trajectory over which the integration is taken. The rotational invariance of the pilot-wave system requires that the governing equations depend on θ only through its time derivatives and temporal differences in the memory kernels.

71

While our investigation is rooted in the stroboscopic model (3.8), we emphasise that (3.20) does not depend on the precise effect of memory on the dynamics, nor on the external forcing. As outlined below, this relative generality more clearly highlights the underlying structure in the orbital stability problem, thereby allowing us to draw important connections between orbital stability and the force balance equations for steady orbital motion (§3.5.1).

3.5.1 Linear stability analysis

To analyse the linear stability of circular orbits, we assume that the droplet executes a circular orbit of radius r_0 and angular frequency ω for all $t < 0$. Following Oza [77] and Liu et al. [66], we parameterise steady circular orbits in terms of their orbital radius. We express the corresponding angular frequency as $\omega(r_0)$, and the force coefficient required to sustain the circular orbit as $\zeta_0(r_0)$. It follows that $\omega(r_0)$ and $\zeta_0(r_0)$ satisfy the force balance equations $F_r(r_0, \omega, \zeta_0) = 0$ and $F_\theta(r_0, \omega) = 0$, where

$$F_r(r_0, \omega, \zeta) = f_r(r_0, 0, 0, \omega, 0) + \zeta f_{\text{ext},r}(r_0, 0, 0, \omega, 0) + \int_0^\infty w_r(r_0, r_0, \omega s, s) \, \mathrm{d}s, \qquad (3.21a)$$

$$F_\theta(r_0, \omega) = f_\theta(r_0, 0, 0, \omega, 0) + \int_0^\infty w_\theta(r_0, r_0, \omega s, s) \, \mathrm{d}s. \qquad (3.21b)$$

We note that the independence of F_θ on the force parameter, ζ, is a direct consequence of the assumption that $\boldsymbol{F} \cdot \boldsymbol{t} = 0$ for steady orbital motion, which implies that the tangential force balance does not involve the external force. In addition, the first two arguments of w_r and w_θ are r_0 to reflect the fact that the past trajectory is a circle, and the droplet is currently moving along that circle.

In order to account for the influence of the infinitesimal forcing at $t = 0$ on the droplet motion for $t > 0$, we substitute the ansatz

$$r(t) = r_0 + \epsilon H(t) r_1(t) \quad \text{and} \quad \theta(t) = \omega t + \epsilon H(t) \theta_1(t) \qquad (3.22)$$

into (3.20), where r_1 and θ_1 are the perturbed radius and polar angle, and $H(t)$ denotes the Heaviside function. As the droplet position is continuous for all time, we conclude that $r_1(0) = \theta_1(0) = 0$; however, the acceleration impulse gives rise to a jump in droplet velocity, yielding $\frac{\partial f_r}{\partial \dot{r}} \dot{r}_1(0^+) = c_r$ and $\frac{\partial f_\theta}{\partial \dot{\theta}} \dot{\theta}_1(0^+) = r_0 c_\theta$ [66, 79].

We substitute (3.22) into (3.20), retain terms of size $O(\epsilon)$, and take Laplace transforms of the resulting linearised equations. By denoting the Laplace transforms of $r_1(t)$ and $\theta_1(t)$ as $R(s) = \mathscr{L}[r_1](s)$ and $\Theta(s) = \mathscr{L}[\theta_1](s)$, respectively, we obtain the system of equations

$$\begin{pmatrix} \mathscr{A}(s) & -\mathscr{B}(s) \\ \mathscr{C}(s) & \mathscr{D}(s) \end{pmatrix} \begin{pmatrix} R(s) \\ r_0 \Theta(s) \end{pmatrix} = \begin{pmatrix} c_r \\ r_0 c_\theta \end{pmatrix}, \qquad (3.23)$$

where the matrix elements are defined in terms of the complex Laplace parameter, s in appendix B.2.1. Finally, the asymptotic growth rates of perturbations, s, are the poles of (3.23) and thus satisfy $\mathscr{F}(s) = 0$, where

$$\mathscr{F}(s) = \mathscr{A}(s)\mathscr{D}(s) + \mathscr{B}(s)\mathscr{C}(s). \qquad (3.24)$$

We use properties of the stability coefficients outlined in appendix B.2.2 to prove Theorem 1, which lends mathematical support to the numerical verification performed by Oza et al. [79].

Theorem 1 *Consider the stroboscopic pilot-wave model* (3.19) *with an attractive external force that acts radially on circular orbits, i.e.* $\boldsymbol{F} \cdot \boldsymbol{t} = 0$ *in* (3.9). *Let the external force be parameterised by* $\boldsymbol{F} \cdot n = -\zeta f(r_0, \omega)$, *where* $f(r_0, \omega) = -2mr_0\omega$ *for a Coriolis force, and* $f(r_0, \omega) = f_c(r)$ *for a central force, where* $f(r_0, \omega) > 0$ *for an attractive force, and let* ζ_0 *be the force coefficient that satisfies the force balance equations* (3.9) *at a given orbital radius* r_0. *At constant* T_M, *if* $\mathrm{d}\zeta_0/\mathrm{d}r_0 > 0$, *then there exists a real and positive eigenvalue.*

We recast Theorem 1 in an alternative form to aid physical intuition, and to avoid derivatives of force coefficients. From the radial force balance (3.9a) and (3.21), we rewrite F_r as

$$F_r = -mr_0\omega^2 - \frac{F}{T_F} \int_0^\infty \mathrm{J}_1\left(2k_F r_0 \sin\left(\frac{\omega s}{2}\right)\right) \sin\left(\frac{\omega s}{2}\right) \mathrm{e}^{-s/T_M} \, \mathrm{d}s + \zeta f_{\mathrm{ext}}(r_0, \omega), \quad (3.25)$$

which is the negative of the net radial force, and f_{ext} is the external force. At equilibrium, $F_r = 0$. The sign of $\frac{\mathrm{d}F_r}{\mathrm{d}r_0}$ is opposite to the direction of the net radial force on an outward radial perturbation of a circular orbit of radius r_0. Intuitively, if the net radial force increases with outward radial perturbations, then these perturbations should continue to grow, and the circular orbit should be unstable. This is formalised by Corollary 1.1.

Corollary 1.1 *If* $f_{\mathrm{ext}}(r_0, \omega) > 0$, *as in the case of an attractive radial force, and, holding* ζ *constant,* $\frac{\mathrm{d}F_r}{\mathrm{d}r_0} < 0$, *then there exists a real and positive eigenvalue.*

We note that Oza et al. [79] prove a version of Theorem 1 for the special case of the stroboscopic model in the presence of a Coriolis force; our proof demonstrates that this theorem is actually a fundamental property of dynamical systems with memory and rotational invariance. In particular, the theorem holds independent of the type of wave kernel and external potential, as long as the potential has radial symmetry. This theorem and its corollary allow us to understand many features of the pilot-wave system. It guarantees instability of circular orbits when the restoring force decays too quickly to support circular orbits at higher orbital radii. In figure 3.2(a,b), we observe that whenever $\frac{\mathrm{d}\Omega}{\mathrm{d}r_0} > 0$ or $\frac{\mathrm{d}k}{\mathrm{d}r_0} > 0$, circular orbits are unstable. We rationalise the periodicity of the monotonic instability tongues in figure 3.2(c,d) by noting that the radial wave force is oscillatory in the orbital radius, and the monotonic instability tongues arise when the wave force increases with the orbital radius. In addition, Corollary 1 will be useful for explaining the observation in §3.6.3 that monotonic instabilities are more prevalent in the presence of concave potentials, and why small radius circular orbits are always unstable in these potentials.

We stress, however, that Theorem 1 does not assert that $\frac{\mathrm{d}\zeta_0}{\mathrm{d}r_0} > 0$ leads to monotonic instabilities, as the positive eigenvalue identified may not have the largest real part; a complex eigenvalue with larger real part may also exist, in which case the instability would be oscillatory in nature. This possibility appears in figure 3.2(b), where there are oscillatory

instabilities in the regions where $\frac{\mathrm{d}k}{\mathrm{d}r_0} > 0$. Thus, this theorem only provides a sufficient condition for the onset of monotonic instabilities. While it is valuable in describing the onset of monotonic instabilities, it is unable to describe oscillatory instabilities.

We now explain the relationship between Theorem 1, classical orbital mechanics, and the pilot-wave system. In §3.2, when considering potentials of the form $V(r) \propto r^q$, we demonstrated that if $q < -2$, circular orbits undergo monotonic instabilities. Theorem 1 is a sufficient condition for instability for a class of dynamical systems that encompasses the classical orbital mechanics system, which is obtained by setting $w_r = w_\theta = 0$ in (3.20). As we show in appendix B.2.4, applying Theorem 1 to classical orbital mechanics also shows that if $q < -2$, circular orbits are unstable, indicating that Theorem 1 is a more fundamental statement of circular orbit instabilities in memory-driven dynamical systems, like the pilot-wave hydrodynamic system. While Theorem 1 provides physical insight into understanding the onset of monotonic instabilities, it does not explain the onset of oscillatory instabilities, which, in some central force systems, are much more prevalent. We thus focus on the stroboscopic model to study the onset of the non-resonant instability.

3.6 Onset of instability

We turn our attention now to the stroboscopic model specifically, and substitute for f_r, w_r, f_θ and w_θ, which can be found by comparing (3.20) with (3.19). To eliminate the applied force as a parameter in the stability problem, we use the radial force balance (3.9a) to replace the applied force in the stability functions in (B.8) with the inertial and wave forces, as was outlined by Liu et al. [66]. Following this procedure, the stability coefficients are given as

$$\mathscr{A}(s) = m\big(s^2 + (n-1)\omega^2\big) + D\left(s + \frac{1}{T_M}\right) + Fk_F\left[\mathcal{C}_0(s) + \mathcal{I}_1(s) - \frac{n+1}{k_F^2 r_0}\frac{\partial \mathcal{I}_0(0)}{\partial r_0} - 2\mathcal{I}_0(0)\right],$$
(3.26a)

$$\mathscr{B}(s) = (2-\Delta)m\omega s + Fk_F\left[\left(s\Delta - \frac{1}{T_M}\right)\frac{1}{k_F^2 r_0 \omega}\frac{\partial \mathcal{I}_0(0)}{\partial r_0} - \mathcal{S}_0(s)\right],$$
(3.26b)

$$\mathscr{C}(s) = (2-\Delta)m\omega s + 2D\omega + Fk_F\left[\left(s\Delta + \frac{1}{T_M}\right)\frac{1}{k_F^2 r_0 \omega}\frac{\partial \mathcal{I}_0(0)}{\partial r_0} - \mathcal{S}_0(s)\right],$$
(3.26c)

$$\mathscr{D}(s) = ms^2 + D\left(s - \frac{1}{T_M}\right) + Fk_F\left[\mathcal{C}_0(s) - \mathcal{I}_1(s)\right],$$
(3.26d)

where the asymptotic growth rates s satisfy $\mathscr{F}(s) = 0$. $\Delta = 0$ corresponds to the case of a nonlinear spring force ($\boldsymbol{F} = -k|\boldsymbol{x}_p|^{n-1}\boldsymbol{x}_p$) and $\Delta = 1$ denotes the case of a Coriolis force ($\boldsymbol{F} = -2m\boldsymbol{\Omega} \times \dot{\boldsymbol{x}}_p$). Notably, in the case of a Coriolis force, the above expressions use $n = 1$. The stability functions are defined in terms of the following integrals (for all integers $m \geq 0$

and $\mathrm{Re}(s) + T_M^{-1} > 0$)

$$\mathcal{I}_m(s) = \frac{1}{2T_F} \int_0^\infty \mathrm{J}_{2m}\left(2k_F r_0 \sin\left(\frac{\omega t}{2}\right)\right) \mathrm{e}^{-\left(\frac{1}{T_M}+s\right)t}\, \mathrm{d}t, \tag{3.27a}$$

$$\mathcal{C}_m(s) = \frac{1}{2T_F} \int_0^\infty \mathrm{J}_{2m}\left(2k_F r_0 \sin\left(\frac{\omega t}{2}\right)\right) \cos(\omega t)\mathrm{e}^{-\left(\frac{1}{T_M}+s\right)t}\, \mathrm{d}t, \tag{3.27b}$$

$$\text{and} \quad \mathcal{S}_m(s) = \frac{1}{2T_F} \int_0^\infty \mathrm{J}_{2m}\left(2k_F r_0 \sin\left(\frac{\omega t}{2}\right)\right) \sin(\omega t)\mathrm{e}^{-\left(\frac{1}{T_M}+s\right)t}\, \mathrm{d}t, \tag{3.27c}$$

which encode the effects of path memory on the response of the walking droplet to perturbations from a circular orbit. Finally, we use integration by parts to recast the tangential force balance (3.9b) (with $\boldsymbol{F} \cdot \boldsymbol{t} = 0$) in terms of the stability integral $\mathcal{I}_0$, giving [66]

$$\frac{2T_F}{T_M}\mathcal{I}_0(0) = 1 - \frac{r_0^2 \omega^2}{c^2}, \tag{3.28}$$

where $c = \sqrt{mgA/DT_F}$ is the maximum steady orbital speed [66].

In summary, equations (3.24) and (3.28), which are defined in terms of the stability coefficients (3.26) and integrals (3.27), comprise the orbital stability problem, which we parameterise in terms of the orbital radius, r_0 [77, 79]. We emphasise, as explained in §B.2.1, that the stability coefficients depend explicitly on the form of the applied force, as indicated by $\Delta \in \{0, 1\}$ in (3.26). The stability integrals (3.27) present the main challenge with analysing the response of an orbiting droplet to small perturbations. Conveniently, all the stability integrals may be evaluated analytically [66, Appendix B], either in terms of Bessel functions of complex order,

$$\mathcal{I}_m(s) = \frac{\pi}{2\omega T_F}\mathrm{J}_{m+\mathrm{i}\eta}(k_F r_0)\mathrm{J}_{m-\mathrm{i}\eta}(k_F r_0)\operatorname{csch}(\pi\eta), \tag{3.29a}$$

or in terms of infinite sums,

$$\mathcal{I}_m(s) = \frac{\eta}{2\omega T_F} \sum_{n=-\infty}^{\infty} \frac{(-1)^n \mathrm{J}_{m+n}(k_F r_0)\mathrm{J}_{m-n}(k_F r_0)}{\eta^2 + n^2}, \tag{3.29b}$$

with

$$\mathcal{C}_m(s) = \frac{1}{2}\Big(\mathcal{I}_m(s + \mathrm{i}\omega) + \mathcal{I}_m(s - \mathrm{i}\omega)\Big), \quad \mathcal{S}_m(s) = \frac{1}{2\mathrm{i}}\Big(\mathcal{I}_m(s - \mathrm{i}\omega) - \mathcal{I}_m(s + \mathrm{i}\omega)\Big) \tag{3.29c}$$

and $\eta = \left(s + T_M^{-1}\right)/\omega$. Although the integral evaluations in (3.29) are fairly complicated, we leverage various asymptotic expansions of Bessel functions of complex order to deduce analytical expressions for the onset of instability for large orbital radius, as detailed in §3.6.1. Finally, we note that the various combinations of stability integrals appearing in (3.26) may be reduced to a more concise form, as detailed by Liu et al. [66, Appendix B].

The orbital solution is unstable if there are any roots, s, of $\mathscr{F}$ satisfying $\mathrm{Re}(s) > 0$. By denoting s_* as the unstable root with largest real part, the instability is monotonic if $\mathrm{Im}(s_*) = 0$ and oscillatory otherwise. The stability function, $\mathscr{F}$, has a trivial eigenvalue at

0, corresponding to rotational invariance of the orbital motion. In the case of the Coriolis force, $\mathscr{F}$ has an additional trivial eigenvalues at $\pm i\omega$ due to translational invariance [79]. It follows, therefore, that the nontrivial roots of the stability problem satisfy $\mathscr{G}(s) = 0$, where

$$\mathscr{G}_{\text{Cor.}}(s) = \frac{\mathscr{A}(s)\mathscr{D}(s) + \mathscr{B}(s)\mathscr{C}(s)}{s(s^2 + \omega^2)}, \tag{3.30a}$$

$$\mathscr{G}_{\text{spr.}}(s) = \frac{\mathscr{A}(s)\mathscr{D}(s) + \mathscr{B}(s)\mathscr{C}(s)}{s}. \tag{3.30b}$$

We apply the method of Delves and Lyness [27] to find the roots of $\mathscr{G}$ in the domain over which $\mathscr{G}$ is analytic, i.e. $\text{Re}(s) > -\frac{1}{T_M}$. To ascertain whether a particular orbital state is stable or unstable, we typically utilise a rectangular integration contour spanning the domain $\text{Re}(s) \in [0, 20]$ and $\text{Im}(s) \in [0, 5]$, which we find to be sufficient for identifying all roots with a positive real part across the parameter regime outlined in §3.3, and $0 \leq \Gamma \leq 0.999$.

3.6.1 Asymptotic framework

Liu et al. [66] determined an asymptotic expression for the critical memory of instability, valid for $r_0 k_F \gg 1$, by determining suitable scaling relationships for the destabilisation frequency, S, and the inverse orbital memory parameter, $\beta = \frac{1}{2\pi M_e^O}$, in terms of the orbital radius, r_0. We thus begin by reviewing the procedure in which we scaled these two quantities, and then derive the analogous asymptotic expressions for the linear central force.

To simplify analysis, we define the non-dimensional radius $\hat{r}_0$ and speed $\hat{U}$ by $\hat{r}_0 = r_0 k_F$, and $\hat{U} = \frac{r_0 \omega}{c}$. From Liu et al. [66], in the Coriolis force system, $e^{\pi\beta} = O(\hat{r}_0^2)$ for both the monotonic and wobbling tongues. In contrast, as figure 3.4 demonstrates, there are two scalings involved in the central force system: $e^{\pi\beta}$ scales as $O(\hat{r}_0^2)$ and $O(\hat{r}_0^3)$ for different types of instabilities. In each case, however, we observe that $\beta = O(\ln(\hat{r}_0)) = o(\sqrt{\hat{r}_0})$, and thus we may consider both scalings simultaneously by employing the same asymptotic framework as Liu et al. [66]. Using the large-argument expansions of the Bessel functions [1], we can recast the tangential force balance (3.28) as

$$1 - \hat{U}^2 = \frac{1}{\beta \hat{r}_0} + O\left(\frac{1}{\hat{r}_0^3}\right), \tag{3.31}$$

which we use to eliminate the orbital speed in the analysis.

As our aim is to determine the imaginary roots of $\mathscr{G}(s)$, we write $s = iS$, and expand the orbital speed $\hat{U}$, inverse orbital memory $\beta = \omega T_M$ and scaled destabilisation frequency $\xi = \frac{S}{\omega}$ as

$$\hat{U} = U_0 + \frac{U_1}{\hat{r}_0} + O\left(\frac{1}{\hat{r}_0}\right), \qquad \xi = \xi_0 + \frac{\xi_1}{\hat{r}_0} + O\left(\frac{1}{\hat{r}_0^2}\right), \qquad \beta = \beta_0 + \frac{\beta_1}{\hat{r}_0} + O\left(\frac{1}{\hat{r}_0^2}\right). \tag{3.32}$$

We proceed to use the asymptotic formalism outlined in appendix B.3 to determine the asymptotic expressions for the critical memory of instability, and the destabilisation frequencies.
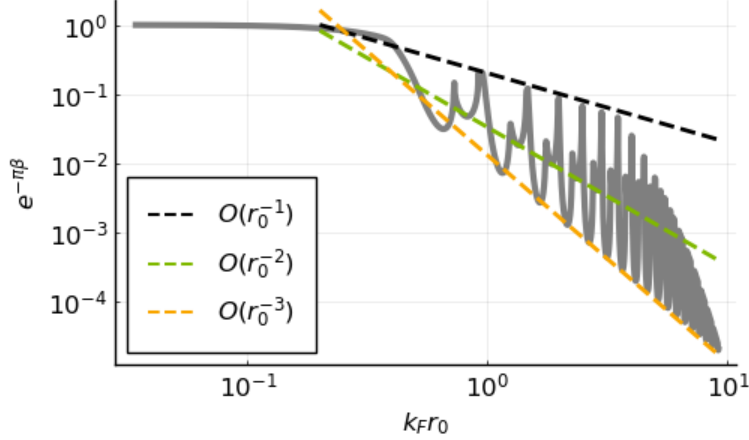
Figure 3.4: The dependence of the wave damping factor over half an orbital period, denoted $e^{-\pi\beta} = e^{-\frac{T_O}{2T_M}}$, at the onset of instability on the orbital radius, r_0, for a linear central force, $\boldsymbol{F} = -k\boldsymbol{x}_p$ ($n = 1$). The grey curve is a rescaling of the stability boundary (white curve) presented in figure 3.2(b). Notably, the envelopes of the instability tongues satisfy the scaling $e^{-\pi\beta} = O(r_0^{-l})$, for $l = 2$ and $l = 3$. These scalings motivate the algebraic scalings for $e^{-\pi\beta}$ presented in §3.6.1.

3.6.2 Walking in a rotating frame

In Liu et al. [66], we demonstrated that the only oscillatory instabilities possible are resonant instabilities with $S = n\omega$, and that the dominant instability, occurring at lowest memory, occurs for $n = 2$. The stability boundaries are then characterised in terms of the reciprocal orbital memory parameter β.

$$\beta_0 = \frac{1}{\pi} \ln \left(\frac{8k_F^2 r_0^2 \sin(2k_F r_0)}{1 + 2M} \right) + O \left(\frac{\ln(k_F r_0)}{k_F r_0} \right), \tag{3.33a}$$

$$\beta_{2\omega} = \frac{1}{\pi} \ln \left(-\frac{8k_F^2 r_0^2 \sin(2k_F r_0)}{3(1 + 2M)} \right) + O \left(\frac{\ln(k_F r_0)}{k_F r_0} \right), \tag{3.33b}$$

$$\xi = 2 - \frac{4\beta_{\text{wob}}}{\pi k_F r_0} \cot(2k_F r_0) + O \left(\frac{1}{k_F^2 r_0^2} \right). \tag{3.33c}$$

where the dimensionless mass parameter $M = mck_F/D$ represents the ratio of inertia to drag. Notably, β is related to the normalised vibrational forcing, Γ, via $\Gamma = 1 - \sqrt{2}\omega\beta/ck_F \approx 1 - \sqrt{2}\beta/r_0 k_F$. Increasing the value of M increases the critical value of Γ for each instability, corresponding to shortening of the instability tongues in the stability diagram. Furthermore, the monotonic and 2-wobbles instabilities are interlaced, alternating over half the Faraday wavelength as the orbital radius is increased.

Importantly, both of the monotonic and 2ω stability boundaries satisfy the scaling relationship $e^{\pi\beta} = O(\hat{r}_0^2)$. In the next section, we show that the onset of the non-resonant instability, in the central force system, occurs at lower memory, and thus dominates both the monotonic and 2ω instabilities.

n	Monotonic instability	2ω instability	ω_r instability
$-1 < n < 0$	$+$	$-$	$-$
$0 < n < 3$	$+$	$-$	$+$
$3 < n \leq 4$	$+$	$+$	$-$

Table 3.2: The correspondence between the sign of $\sin(2k_F r_0)$ and the existence of monotonic, 2ω and $\omega_r = \sqrt{n+1}$ instabilities for a droplet walking in a nonlinear spring force, $\boldsymbol{F} = -k|\boldsymbol{x}_p|^{n-1}\boldsymbol{x}_p$. We restrict our attention to the case $-1 < n \leq 4$ and $4M > 1$, both of which are amply satisfied in experiments.

3.6.3 Walking in a power-law central force

The results in a general power-law central force are quite different. We follow the same procedure to derive resonant and non-resonant stability boundaries in appendix B.3:

$$\beta_{\text{res}} = \frac{1}{\pi} \ln\left(-\frac{8k_F^2 r_0^2 \sin(2k_F r_0)}{(4N^2 - n - 1)(1 + 2M)}\right) + O\left(\frac{\ln(k_F r_0)}{k_F r_0}\right), \tag{3.34a}$$

$$\xi_{\text{res}} = 2N + \frac{N}{\pi k_F r_0}\left(\frac{4M - 1}{4N^2 - n - 1} - 4\beta_{\text{res}}\cot(2k_F r_0)\right) + O\left(\frac{1}{k_F^2 r_0^2}\right), \tag{3.34b}$$

$$\beta_{\text{nr}} = \frac{1}{\pi} \log\left(-\frac{16 k_F^3 r_0^3 \sin(2k_F r_0)\sin(\pi\xi_{\text{nr}})}{\xi_{\text{nr}}(4M - 1)(2M + 1)}\right), \quad \frac{\sin(2k_F r_0)\sin(\pi\xi_{\text{nr}})}{4M - 1} < 0 \tag{3.34c}$$

$$\xi_{\text{nr}} = \sqrt{n+1} + o(1), \tag{3.34d}$$

where N is an integer that depends on n; for $n \leq 4$, as considered in this paper, $N = 0, 1$. We remark that monotonic instabilities are simply a type of resonant instability. β_{nr} and ξ_{nr} describe the memory of instability and the destabilisation frequency of the non-resonant instability, first discussed in §3.4.

Linear central force

We begin by discussing some differences between the linear central force and Coriolis systems. First, we observe that monotonic and 2ω instability envelopes, obtained by setting $|\sin(2k_F r_0)| = 1$ and $N = 0, 1$, coincide in the case of a linear central force, $n = 1$, but not for a Coriolis force. This behaviour is seen in figure 3.2, and also in the investigations of Tambasco et al. [94], but not in Labousse et al. [64]. Second, the wobble number at the onset of instability is no longer exactly 2 at the memory minima; the most unstable orbital radius no longer corresponds to a perfectly resonant instability. To leading order, (3.33) and (3.34) suggest that the memory minima occur when $|\sin(2\hat{r}_0)| = 1$, i.e. $\cos(2\hat{r}_0) = 0$, which sets $\xi = 2$ in the Coriolis force system, and $\xi = 2 + \frac{4M-1}{\pi\hat{r}_0(3-n)}$ in the central force system. Thirdly, the critical memory of instability for the new non-resonant instability scales as $e^{\pi\beta} = O(\hat{r}_0^3)$, which occurs at lower memory than the monotonic instability, indicating that this instability asymptotically dominates all of the resonant instabilities with $e^{\pi\beta} = O(r_0^2)$. For the linear central force, this indicates that the monotonic instability is dominated by the non-resonant instability.

In §3.4.2, we demonstrated that radial perturbations, in a power-law force field $F(r) = V'(r) \propto r^n$, have a tendency to oscillate at a frequency $\omega\sqrt{n+1}$, which, in the context of the linear central force, reflects the preponderance of $\sqrt{2}$ instabilities as shown in §3.6.3. To further investigate the extent to which the boost results explain the forms of the additional instabilities, we plot horizontal lines in figure 3.5 in the right hand column corresponding to $\xi = 2$ and $\xi = \sqrt{n+1}$. We observe that there is always an instability branch near $\xi = \sqrt{n+1}$, and the destabilisation frequency at the memory minima, highlighted in green and black dots, approach $\xi = 2$ and $\xi = \sqrt{n+1}$, validating the analysis in §3.4.2, and emphasising the origins of the additional non-resonant instability in the curvature of the confining potential.

Our analysis of the non-resonant instability is predicated on the assumption $4M - 1 > 0$, which is satisfied in the hydrodynamic regime. Under this assumption, our analysis predicts that, in a linear central force, the non-resonant instability occurs for $\sin(2k_F r_0) > 0$, as $\sin(\pi\sqrt{n+1}) < 0$. For smaller M, outside the hydrodynamic regime, the asymptotic result for the non-resonant boundary may no longer. The behaviour of the non-resonant stability boundary becomes more complex, and we defer this discussion to chapter 4.

Thus far, we have observed two main qualitative differences between the Coriolis and central force systems: the introduction of potential curvature instabilities, and the domination of monotonic instabilities by this non-resonant instability. We now seek to understand how these differences vary for different types of central force systems.

Convex potentials

Convex potentials are associated with attractive radial forces that increase in magnitude with radial position. This indicates that the attractive force on outwards perturbations increases, which pulls the perturbed trajectory inwards, and leads to oscillatory motion. This suggests that oscillatory instabilities may be more prevalent in the presence of convex potentials. We see, in figure 3.5 and in table 3.2, that the monotonic instability is always subdominant to an oscillatory instability for $n > 0$, and so only oscillatory instabilities appear at the onset of instability.

For $n < 3$, along a single branch of the stability boundary, the non-resonant instability occurs at lower $\hat{r}_0$ than the 2ω instability. The opposite is true for $n > 3$. This can be explained by noting that the scaled destabilisation frequency ξ, increases monotonically with $\hat{r}_0$ along stability boundaries up until a change of branch. Using this observation, for $n < 3$, $\sqrt{n+1} < 2$, so the non-resonant instability occurs at smaller $\hat{r}_0$ than the resonant instability, but for $n > 3$, $\sqrt{n+1} > 2$, so the converse is true. This phenomenon highlights the limitations of the heuristic introduced in Liu et al. [66], which suggested one could determine the type of instabilities that would arise for a given orbital radius by looking at the mean wave force. However, we revisit mean wave force heuristics in chapter 5, where we rigorously justify the applicability of mean wave force heuristics at very high memory.

Conical potential

To further highlight the relationship between the nature of orbital instabilities and the curvature of the confining potential, we examine the special case $n = 0$, corresponding to a
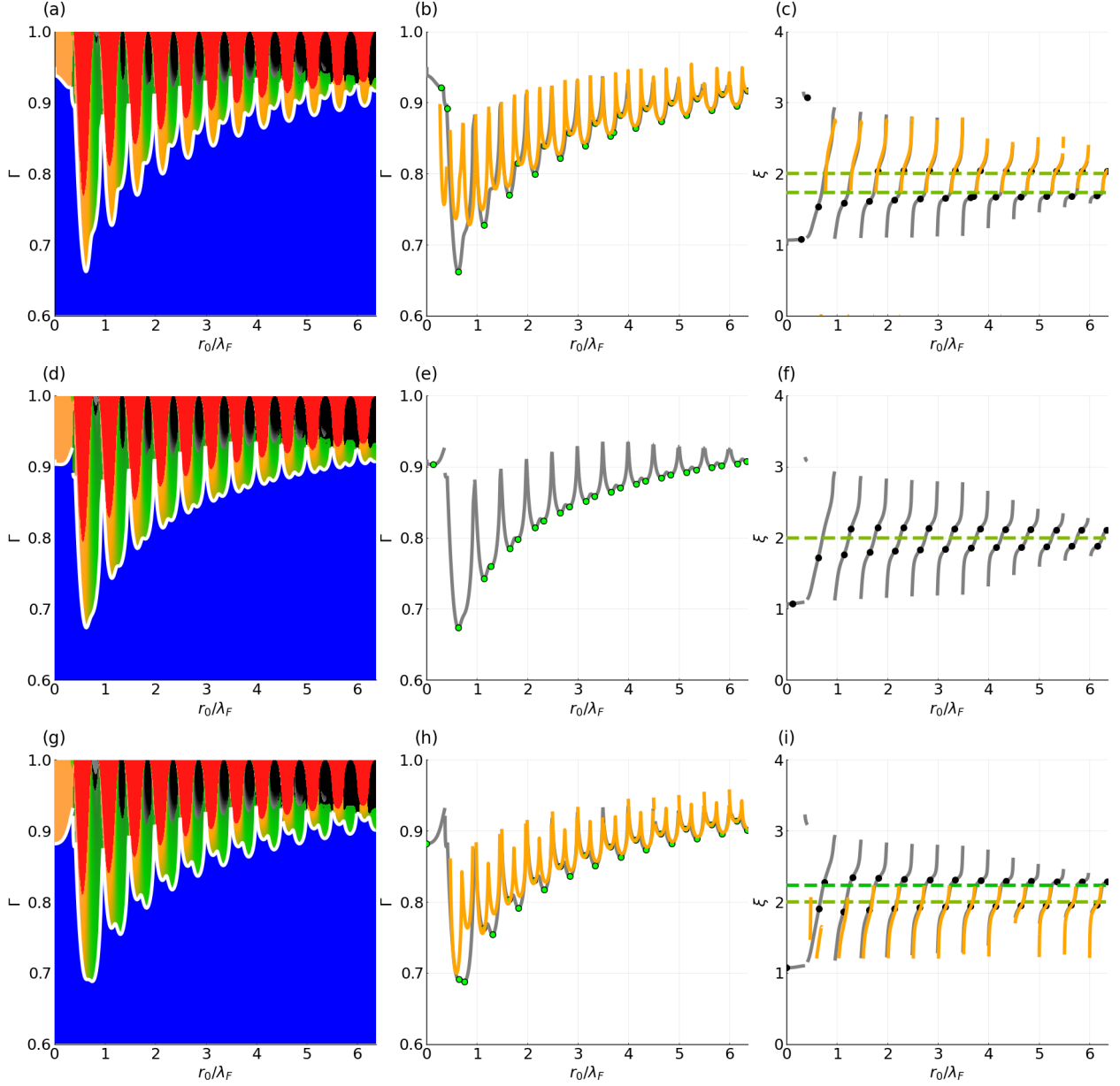
Figure 3.5: Stability diagrams and scaled destabilisation frequencies for a central force with $F(r) = -kr^n$, and $n = 2, 3$ and 4, at the same experimental parameters as in §3.3. Top row: $n = 2$. Middle row: $n = 3$. Bottom row: $n = 4$. The left column contains stability diagrams, where the stability of circular orbits is given by the same color scheme as in 3.2. The middle column contains plots of the critical memory of instability, with numerical boundaries (grey) and asymptotic boundaries (orange dashed). Green dots represent the most unstable radii, where instabilities arise at lowest memory. The right column plots the destabilisation frequencies, with numerical results (grey) and asymptotic results (orange). The horizontal dashed lines represent the 2ω and $\sqrt{n+1}\omega$ instabilities, and the black dots correspond to the scaled destabilisation frequencies of the green dots in the middle column. We emphasise how close the black dots in the right column are to the 2ω and $\sqrt{n+1}\omega$ horizontal lines, and how the destabilisation frequencies generally monotonically increase with r_0.
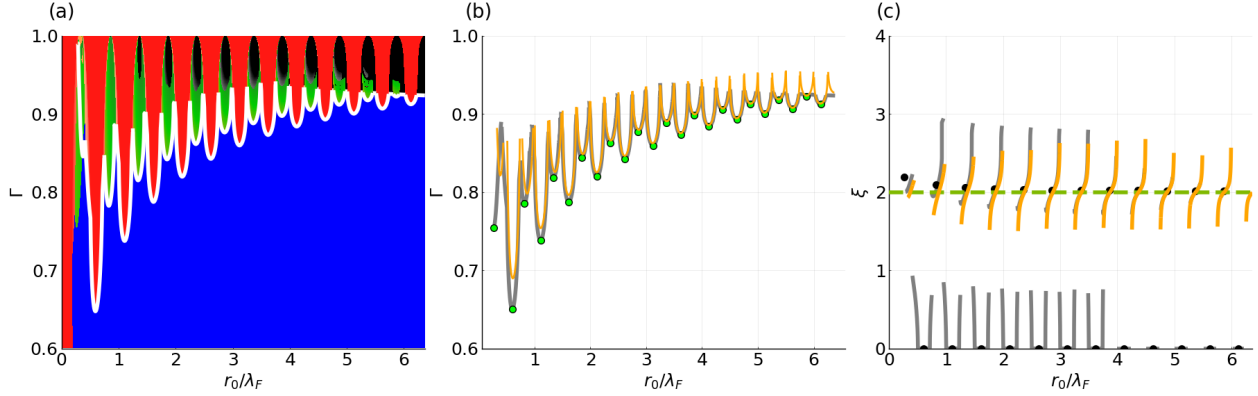
Figure 3.6: Stability diagram (a, b) and scaled destabilisation frequencies (c) for a constant central force $(n = 0)$, for the parameter regime defined before the beginning of 3.3.1. The color scheme is as in figure 3.2. In (a), the white curve represents the stability boundaries tracked for the Coriolis system. The asymptotic solutions plotted in (b) are the Coriolis force solutions, not the constant force solutions. We note the strong agreement between the numerical results for the constant force and the asymptotic results for the Coriolis force, due to the lack of curvature in the confining potential.

conical potential, where there is a constant attractive radial force. As the magnitude of the Coriolis force only varies with the orbital speed, and as the orbital speed varies slowly with the orbital radius, as we see in (B.21a), we note that the large-radius behaviour of the Coriolis force and conical potential are similar. We demonstrate this similarity by remarking that (3.33) and (3.34) are very similar when $n = 0$. In figure 3.6, we plot the numerical stability boundary for the $n = 0$ central force, and overlay the Coriolis force asymptotic results for the critical memory of instability, and the destabilisation frequency. We emphasise the remarkable agreement between the asymptotic results for the $n = 0$ central force and the rotating frame, and also the agreement between the numerical boundaries. This agreement is explained by the absence of the non-resonant instability, prompted by the vanishing of the curvature of the potential in this system. The most significant difference between the two systems arises at small $\hat{r}_0$, since circular orbits are stable for sufficiently small orbital radii at any memory in a Coriolis force system [77], but are unstable for sufficiently small $\hat{r}_0$ in a central force for all $n < 1$, a result we prove in appendix B.5.

Concave potentials

We now consider the case of a concave potential, for which the attractive radial force decreases in magnitude with radial position. To aid visualisation of the stability in this case, we plot stability diagrams in figure 3.7 when the power in the power-law force is negative. When $n = -1$, corresponding to a 2D Coulomb force, as considered by Tambasco et al. [94], the boost model analysis in §3.4.2 predicts that monotonic radial perturbations become more common, and we observe that circular orbits destabilise via monotonic instabilities for memory near the walking threshold, $\Gamma = 0$, a phenomenon not observed with other central force systems. We rationalise the proliferation of monotonic instabilities by remarking
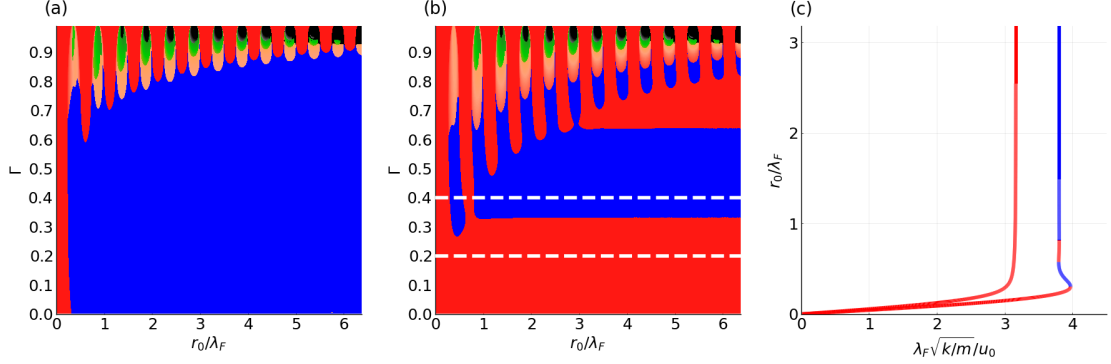
Figure 3.7: Stability diagrams for a central force with (a) $n = -0.5$, and (b) -1 at the same parameters as in §3.3. Note that in (a), the non-resonant instability (light red) covers the 2ω instability tongues (green), because the confining potential is concave. We observe the proliferation of monotonic instabilities in (b), as the non-resonant instability occurs at a frequency $\omega_o = \sqrt{n+1}\,\omega = 0$. Orbital stability curves in (c) plotting the orbital radius against the central force constant non-dimensionalised by the free walking speed, u_0, corresponding to the dashed lines in (b). We observe that stable circular orbits in (c) occur when $\frac{\mathrm{d}k}{\mathrm{d}r_0} < 0$, and unstable circular orbits occur when $\frac{\mathrm{d}k}{\mathrm{d}r_0} > 0$, in agreement with Theorem 1.

that when $n < 0$, and an outwards radial perturbation occurs, the restoring force weakens, prompting exponential growth of the perturbations and thus monotonic instabilities. This argument is similar to the argument behind Corollary 1.1, which states that monotonic instabilities arise when the net radial force increases with radial position. Indeed, when $n < 0$, the restoring force weakens the fastest for small orbital radii, explaining why monotonic instabilities occur for small orbital radii at all memory. Notably, monotonic instabilities are also prevalent when $n = -0.5$; the non-resonant instability dominates the 2ω and not the monotonic instability. These observations indicate that the non-resonant instability filters out the 2ω instability, which is the resonant instability less compatible with the concavity of the external potential.

The 2D Coulomb potential, $n = -1$, is especially interesting because its orbital stability diagram is qualitatively different from all the other cases. As seen in figure 3.7, we see multiple flat plateaus, where $\Gamma = O(1)$, and thus $\beta = O(r_0)$, as $r_0 \to \infty$, which is in sharp contrast to the scaling in (3.34), where $\beta = O(\log(r_0))$. In addition, we observe that the critical memory of instability is no longer a single-valued function of r_0, which suggests that if given r_0, the critical memory of instability can not be solved explicitly. These peculiarities are related to the fact that $n + 1 = 0$, and so the expression for β_{nr} in §3.6.3 is not valid. In addition, the assumption that $\beta^2 \ll r_0$, made in appendix B.3 that underpins the asymptotic theory, also breaks down, necessitating the need for another theory.

3.7 Discussion

Orbital pilot-wave dynamics has provided one of the central paradigms for the emergence of quantisation and quantum-like statistics from classical pilot-wave dynamics Bush and Oza [14]. The particle is able to access only a discrete number of orbitals owing to the dynamic constraint imposed on it by its quasi-monochromatic pilot-wave field. At high memory, the droplet switches intermittently between unstable periodic orbits. This physical picture suggests that the superposition of dynamical states in quantum systems may be rooted in an underlying, but currently unresolved, chaotic pilot-wave dynamics.

For droplets executing circular orbits under the influence of an axisymmetric potential, we have demonstrated that a natural frequency of oscillation is given by (3.5). The difference between (3.5) and its analog in classical orbital mechanics (3.3) arises because the system acts to conserve orbital speed rather than angular momentum, and because the system does not exhibit translational invariance; the natural frequency of oscillation of the Coriolis force system, which also conserves speed, is given by $\pm\omega$, as seen in §3.2.2. Equation (3.5) indicates that in radial potentials $V(r) \propto r^q$, stable circular orbits can arise in our system only if $q > 0$. In this case, the near-critical oscillatory modes of frequency ω_r are resonant if and only if q is a perfect square.

We emphasise that the intuition gained from the boost model and Theorem 1 has a few limitations. While the boost model analysis justifies (3.5) for a dynamical system which has a preferred orbital speed, it does not provide accurate information about the memory of instability, and thus does not explain the root causes of instability. Theorem 1 and its corollary provide a sufficient but not necessary condition for the onset of monotonic instabilities. As it is unable to determine the onset of oscillatory instabilities, it only partially explains the onset of instabilities in the pilot-wave system.

We proceed by commenting on the generality of Theorem 1, as first derived by Oza et al. [79] in their consideration of walkers in a rotating frame, and how it holds for a general class of memory-driven dynamical systems. Theorem 1 is a generalisation of the instability condition $q < 0$ for circular orbits in a radial potential $V(r) \propto r^q$. Specifically, it generalises the notion that if the confining potential decays too rapidly to rein in outwards perturbations, the perturbations grow, and circular orbits destabilise. This intuition can then be used to rationalise why, at the onset of instability, monotonic instabilities occur more for attractive external forces decreasing in magnitude with radial position. In addition, it explains why, in the presence of a decaying external force, small circular orbits are always unstable; if we consider a radial force of the form $f(r) = r^n$, for $n < 0$, we see that the radial force decreases the most rapidly for small r.

It is also worth applying our results for the case of circular orbits in an oscillatory potential of the form $V(|\boldsymbol{x}|) \propto J_0(k_F|\boldsymbol{x}|)$, as was explored experimentally and numerically by Tambasco and Bush [93]. By using Bessel's equation to evaluate $V''(r_0)$, we compute $\omega_r = \omega\sqrt{r_0 k_F J_0(k_F r_0)/J_1(k_F r_0)}$. When the orbital radius is such that $J_0(k_F r_0)$ and $J_1(k_F r_0)$ are of the same sign, radial perturbations oscillate in time, with the oscillation frequency increasing with proximity to the zeros of $J_1(k_F r_0)$. However, when the signs of $J_0(k_F r_0)$ and $J_1(k_F r_0)$ differ, radial perturbations grow exponentially in time, giving rise to instability. Our model thus predicts that circular orbits are stable only within narrow radial intervals

separated approximately by half the Faraday wavelength, in accordance with the experimental observations of Tambasco and Bush [93]. Such a case is particularly interesting given that the mean pilot wave of a droplet executing a circular orbit takes a comparable form in the high-memory limit, so one can then consider the stability of an orbiting droplet in its self-potential. This approach is used in chapter 5 in describing a novel form of quantisation.

Our analysis has considered a single point in parameter space in the generalised pilot-wave framework [13], corresponding to the experimental parameters used by Harris and Bush [52]. Our theoretical formalism allows for a broader exploration of orbital pilot-wave dynamics at a much wider range of parameter values. For instance, we observe that, for smaller dimensionless mass M, entirely new types of instabilities arise, corresponding to different types of orbital quantisation. These new orbital states will be characterised in chapters 4 and 5.

There are a few limitations to our mathematical formulation. Firstly, our analysis is based on the stroboscopic approximation, so it assumes resonance between the droplet's bouncing motion and the vibration of the bath. Moreover, we also neglect the far-field decay of the wave field. The shortcomings of these approximations are being explored elsewhere. It also focuses on the linear regime, and so cannot treat nonlinear effects, such as the jump up/down instabilities reported by Harris and Bush [51] and Oza et al. [80]. Secondly, our analysis does not include an assessment of the instability in the large-radius limit, where we expect circular orbits to destabilise in a manner similar to free walkers [35, 77], which would be characterised by $S = O(1)$ and $\xi = O(r_0)$, a sharp contrast from our analysis for which $\xi = O(1)$. This is a matter to be considered in chapter 7. Finally, in §3.6.3, we have assumed that the dimensionless mass number $M > \frac{1}{4}$. While this assumption is valid in the experimental regime, numerical investigations have shown that when $M < \frac{1}{4}$, richer dynamics emerge, motivating their study with a more comprehensive mathematical framework. We turn our attention now to this mathematical framework.

Chapter 4

Quantised islands in a classical pilot-wave system

4.1 Introduction

When a droplet is filled with a ferrofluid and placed in a non-uniform magnetic field, Perrard *et al.*[83, 84] showed that a linear magnetic force could be imparted on the droplet, and observed that the resulting periodic orbits tended to be quantised in both radial position and angular momentum. Using the stroboscopic model, Labousse et al. [65] found that circular orbits were quantised in a similar fashion to that arising in the rotating frame. However, by reducing the walker system to a Rayleigh-friction system, Labousse and Perrard [62] observed that circular orbits underwent $\sqrt{2}\omega$ oscillatory instabilities, but did not provide a mechanism for these non-resonant instabilities. Through adapting the stroboscopic model by inclusion of spatial damping in the wave kernel, Kurianski et al. [60] demonstrated the existence of 4ω instabilities. The existence of 4ω instabilities is specific to the central force system, as in chapter 2, we demonstrated that 4ω instabilities are always subdominant to 2ω instabilities in a rotating frame. In this chapter, we demonstrate that 4ω instabilities may also arise at the onset of instability for certain central force systems. These studies clearly distinguish the central force system from the rotating frame system, motivating further study into the origins of orbital stability and quantisation.

We studied the origins of the non-resonant $\sqrt{2}\omega$ instabilities in chapter 3, where we studied the stroboscopic model with a linear central force in the experimental parameter regime considered by Harris & Bush[52]. We demonstrated that in a confining power-law potential of the form $V(r) \propto r^q$, the non-resonant instability has frequency $\sqrt{q}\omega$, and argued that it arises from a combination of the form of the confining potential and a preference of the walker to propel at a preferred orbital speed. In addition, we showed that the non-resonant instability dominates monotonic instabilities when the confining potential is convex ($q > 1$), dominates resonant wobbling instabilities when the confining potential is concave ($q < 1$), and is subdominant to both resonant wobbling and monotonic instabilities when the curvature of the confining central potential vanishes ($q = 1$). Finally, we identified that perturbations with frequency close to $\sqrt{q}\omega$ decay very slowly for large stable circular orbits, and so may be regarded as being more susceptible to instability as the system parameters

are varied.

In this chapter, we demonstrate that, for circular orbits in central force systems, the non-resonant instability in the GPWF behaves very differently to that in the experimental regime studied in chapter 3. In the experimental regime, the non-resonant instability dominates either the wobbling or monotonic instability, depending on the type of central force. The non-resonant stability boundaries were shown to be similar shapes to the resonant stability boundaries, and the separations between non-resonant stability tongues was demonstrated to be the same as that between resonant stability tongues. In the GPWF, however, all of the statements above can change. For increasing orbital radius, the memory at the onset of the non-resonant instability may no longer increase with the orbital radius, and the instability tongues may merge to form an instability plateau. Large circular orbits may then destabilise in a manner very differently to that of free particles [33]; the instability frequency of the former decreases with orbital radius. Furthermore, the non-resonant instability plateau gives rise to a new form of orbital quantisation consisting of 'islands' of stable orbits in the orbital stability diagram, for which stable circular orbits may destabilise at both lower and higher memory, as we will see in figure 4.1. These quantised islands lead to the existence of many more quantised orbital states than in the experimental regime, and may be regarded as a new paradigm for orbital quantisation induced by particle's tendency to propel at a constant speed. Even in the absence of instability plateaus, the separation between the non-resonant stability tongues may differ significantly from that between resonant stability tongues. This behaviour can cause the non-resonant instability to dominate different types of resonant instabilities for different values of the orbital radius. When the non-resonant instability dominates the 2ω instability instead of the 4ω instability, this allows for the appearance of the latter type of instability at the onset of instability.

This chapter is structured as follows. We describe the governing equations of the generalised pilot-wave system in §4.2, and define the stability problem [66, 79]. In §4.2.2, we show how different orbital stability is outside the experimental parameter regime, and highlight why a new mathematical formulation is necessary to capture the new features. In §4.3, we show that, for low inertia and large circular orbits, the memory of instability may vary very slowly with the orbital radius, resulting in a plateau instability, for which circular orbits are unstable for memory higher than the plateau memory, for any orbital radius beyond a critical value. At constant memory, large orbital radius, and thus low orbital memory, as the particle does not feel the influence of its wake, the main driver of instability is the confining potential, which, as discussed in §3.2.2, in conjunction with the approximate conservation of speed, leads to the instability frequency $S = \sqrt{n+1}\omega$. We thus show that the primary effects of the wave force are to select a preferred walking speed, and to influence the critical memory of instability. We then provide rigorous asymptotic analyses of this phenomenon, and show that the plateau instability is an extension of the non-resonant instability first studied in chapter 3. Furthermore, we demonstrate that it is possible for circular orbits to re-stabilise as memory is further increased beyond the critical memory of instability. In §4.4, we analyse the non-resonant instabilities leading to the plateau instability, and demonstrate that the plateau is always accompanied by stable quantised islands, whereby circular orbits may destabilise for higher or lower memory, in stark contrast to the rotating frame system, where circular orbits are observed to become less stable with increasing memory [43, 52, 66, 79, 80]. The resulting quantised islands are special, because many more quantised orbits can be ob-

served at a fixed value of memory, and represent a new quantisation paradigm, whereby both the memory and orbital radii of stable circular orbits are restricted. We provide an extension of the asymptotic formalism introduced in chapter 2 to explain all of these phenomena, and use our formalism to describe when the frequency of the non-resonant instability becomes an integer multiple of the orbital frequency, and may thus be regarded as resonant. Finally, in §4.4.7, we show that the most unstable orbital radii in each stability branch is determined by a balance between the geometric confinement induced by the pilot-wave, and the spatial variation of the central force.

4.2 Pilot-wave dynamics

We consider an idealised dynamical system in two dimensions first introduced by Bush [13] and further studied by Durey et $al.$[31, 35], consisting of a vibrating particle with position $\boldsymbol{x}_p$ and mass m being propelled by the local slope of its guiding quasi-monochromatic pilot wave, itself generated by the particle vibration. The particle motion is resisted by a linear drag and confined by a central force, $\boldsymbol{F} = -k|\boldsymbol{x}_p|^{n-1}\boldsymbol{x}_p$, associated with a power-law ($n \neq -1$) or logarithmic ($n = -1$) potential. Averaging over the particle's vibration period, T, leads to a trajectory equation of the form

$$m\ddot{\boldsymbol{x}}_p + D\dot{\boldsymbol{x}}_p = -F\nabla h(\boldsymbol{x}_p, t) - k|\boldsymbol{x}_p|^{n-1}\boldsymbol{x}_p, \tag{4.1}$$

where D is the drag coefficient, F is the time-averaged force exerted due to the interactions between the particle and the wave field, and dots denote time derivatives. The wave field h is described as a continuous superposition of the axisymmetric standing waves generated by the particle along its trajectory, and the standing waves decay exponentially in time over a time scale τ, which prescribes the extent to which the particle's past trajectory influences its motion, also referred to as its memory. Thus, the pilot-wave field h is defined by

$$h(\boldsymbol{x}, t) = \frac{A}{T} \int_{-\infty}^{t} \mathrm{J}_0(k_F|\boldsymbol{x} - \boldsymbol{x}_p(s)|)\mathrm{e}^{-(t-s)/\tau}\,\mathrm{d}s, \quad k_F = \frac{2\pi}{\lambda}, \tag{4.2}$$

where $k_F = 2\pi/\lambda$ is the wavenumber of the quasi-monochromatic wave field and A is the amplitude of the wave form generated at each moment in time. Upon projecting the wave field, h, onto the particle path, we non-dimensionalise the resulting integro-differential trajectory equation to obtain [35, 66, 78, 79, 82]

$$M\ddot{\hat{\boldsymbol{x}}}_p + \dot{\hat{\boldsymbol{x}}}_p = \int_{-\infty}^{\hat{t}} \frac{\mathrm{J}_1(|\hat{\boldsymbol{x}}_p(\hat{t}) - \hat{\boldsymbol{x}}_p(s)|)}{|\hat{\boldsymbol{x}}_p(\hat{t}) - \hat{\boldsymbol{x}}_p(s)|}(\hat{\boldsymbol{x}}_p(\hat{t}) - \hat{\boldsymbol{x}}_p(s))\mathrm{e}^{-\sigma(\hat{t}-s)}\,\mathrm{d}s - \hat{k}|\hat{\boldsymbol{x}}_p|^{n-1}\hat{\boldsymbol{x}}_p, \tag{4.3}$$

where $\hat{\boldsymbol{x}}_p = k_F\boldsymbol{x}_p$ and $\hat{t} = t/t_s$ denote the dimensionless particle position and time variable, respectively. The unit of time is $t_s = 1/(k_Fc)$, where $c = \sqrt{AF/DT}$ is the maximum steady walking speed. The dimensionless parameters $\sigma = T/\tau$ and $M = m/Dt_s$ describe the wave decay rate and the relative importance of drag and inertia, respectively, while $\hat{k} = \frac{kt_s}{Dk_F^{n-1}}$ determines the magnitude of the nonlinear spring force. The advantage of the non-dimensionalisation utilised in this study over that of Durey et al. [35], Liu et al. [66] and

Dimensionless parameters	Definition
M	Inertia-to-drag ratio
k	Central force constant
σ	Wave decay rate
r_0	Orbital radius, normalised by the inverse pilot-wavenumber
$R_0 = r_0/(2\pi)$	Orbital radius, normalised by the pilot-wavelength
ω	Orbital angular frequency
$\omega_{\mathrm{orb}} = \omega/\sigma$	Orbital memory parameter
$\beta = \sigma/\omega = \omega_{\mathrm{orb}}^{-1}$	Inverse orbital memory parameter
$U = r_0\omega$	Orbital speed
s	Asymptotic complex growth rate of perturbations
$S = \mathrm{Im}(s)$	Destabilisation frequency
$\xi = S/\omega$	Destabilisation frequency relative to orbital frequency
$\sigma = S/U$	Destabilisation frequency relative to orbital speed

Table 4.1: The dimensionless parameters appearing in the pilot-wave system (4.3) and subsequent analysis.

in chapter 2 is that the maximum non-dimensional speed becomes 1, which simplifies many equations. Moreover, we choose a more intuitive time scale, t_s, representing the ratio of the wavelength to the maximum steady walking speed. Notably, t_s is related to the memory time at the onset of walking, denoted T_W, via $t_s = T_W/\sqrt{2}$, where T_W was chosen as the typical time scale in previous investigations [30, 66, 78]. σ and M are related to their counterparts in chapter 2, ν and κ_0, by $\sigma = \frac{\nu}{\sqrt{2}}$ and $M = \sqrt{2}\kappa_0$, a change that proves to be notationally convenient.

We characterise the pilot-wave dynamics in terms of the dimensionless vibration parameter $\Gamma = 1 - \sqrt{2}\sigma$, which increases with increasing path memory [13, 30, 66, 82]. Notably, $\Gamma = 0$ is the onset of stable steady self-propelling states for a free particle, and $\Gamma = 1$ is the limit of infinite memory, where the waves do not decay. Owing to our choice of the reciprocal pilot-wavenumber as the unit of length, we often characterise the pilot-wave dynamics in terms of the orbital radius normalised by the wavelength of the pilot wave, denoted $R_0 = r_0/2\pi$. We list all of the parameters relevant to this chapter and future chapters in table 4.1.

4.2.1 Orbital dynamics

We characterise circular orbits by their orbital radius, r_0, and orbital frequency, ω. By omitting hats and substituting $\boldsymbol{x}_p(t) = r_0(\cos(\omega t), \sin(\omega t))$ into the integro-differential trajectory equation (4.3), the radial and tangential force balance equations are given by [66, 79]

$$-Mr_0\omega^2 = \int_0^\infty \mathrm{J}_1\left(2r_0\sin\left(\frac{\omega t}{2}\right)\right)\sin\left(\frac{\omega t}{2}\right)\mathrm{e}^{-\sigma t}\,\mathrm{d}t - kr_0^n, \tag{4.4a}$$

$$r_0\omega = \int_0^\infty \mathrm{J}_1\left(2r_0\sin\left(\frac{\omega t}{2}\right)\right)\cos\left(\frac{\omega t}{2}\right)\mathrm{e}^{-\sigma t}\,\mathrm{d}t. \tag{4.4b}$$

For given values of the confining force coefficient, k, wave decay rate, σ, and mass, M, these equations may be solved numerically to find solutions for r_0 and ω. Notably, the central force does not appear in the tangential force balance, which provides an equation for the orbital speed, $U = r_0\omega$, for given orbital radius.

4.2.2 Orbital stability diagrams

We begin by presenting the dynamical behaviour of circular orbits in the presence of various confining potentials to visually represent the plateaus and the quantised islands. The stability framework, and its modifications from §2.2.3 and §3.5, are introduced in §4.2.3.

As indicated by Oza et al. [79] and Liu et al. [66], if one fixes the particle mass M, then a circular orbit may be parameterised by its radius, r_0, and memory parameter, Γ. We thus represent the stability of circular orbits corresponding to each point in the (r_0, Γ) plane by colour, where stable orbits are indicated in blue, and unstable circular orbits are colour-coded by their wobble number $\xi = \frac{S}{\omega}$. In general, circular orbits tend to destabilise for increasing Γ. As studied in chapter 2, there are three common types of instabilities present for a confining force of the form $\boldsymbol{F} = -k|\boldsymbol{x}_p|^{n-1}\boldsymbol{x}_p$: monotonic instabilities, coloured in red, 2ω resonant instabilities, coloured in light green, and $\sqrt{n+1}\omega$ non-resonant instabilities (orange or dark green). We now point out the features of figure 4.1 that cannot be explained by the mathematical formulation of chapters 2 and 3.

1. Instability plateaus arise for sufficiently small values of the dimensionless mass, M, indicating that there are bands of memory for which no stable circular orbits exist for sufficiently large orbital radius (see 4.1(a,b)). The critical memory along the corresponding stability boundary varies very slowly with the orbital radius, approaching a constant value in the large-radius limit. As the orbital speed varies slowly with orbital radius, we see that the reciprocal orbital memory, defined $\beta = \sigma/\omega = \sigma r_0/U$, and thus depends linearly on r_0 for large orbits. We deduce that the orbital memory shrinks to zero in the large-radius limit, with the wake having a decreasingly small influence on the particle motion. In stark contrast, the reciprocal orbital memory parameter satisfies the scaling $\beta = O(\log(r_0))$ along the wobbling and monotonic instability boundaries present in the parameter regime representative of experiments [66], as seen in chapters 2 and 3. In addition, the mathematical formulation of those chapters explicitly require $\beta^2 \ll r_0$, which is violated by the plateaus. We study the origins of these instability plateaus in §4.3.

2. When the instability plateaus exist, multiple stability boundaries come into existence, leading to an alternation of stability with increasing memory. As we can see in figure 4.1 (a,b), if we hold the orbital radius constant and gradually increase memory, circular orbits are stable at low memory, then destabilise and restabilise, before finally destabilising again at sufficiently high memory. The quantised islands then occur in the intermediate stable regime, where they destabilise for sufficiently low or high memory. We rationalise the existence of the multiple stability boundaries in §4.4.5.

3. A key requirement in (3.34) is that the instability frequency $\sqrt{n+1}\omega$ is incommensurate with the orbital frequency, ω. Otherwise, $\sin(\pi\xi) = 0$, and the argument of
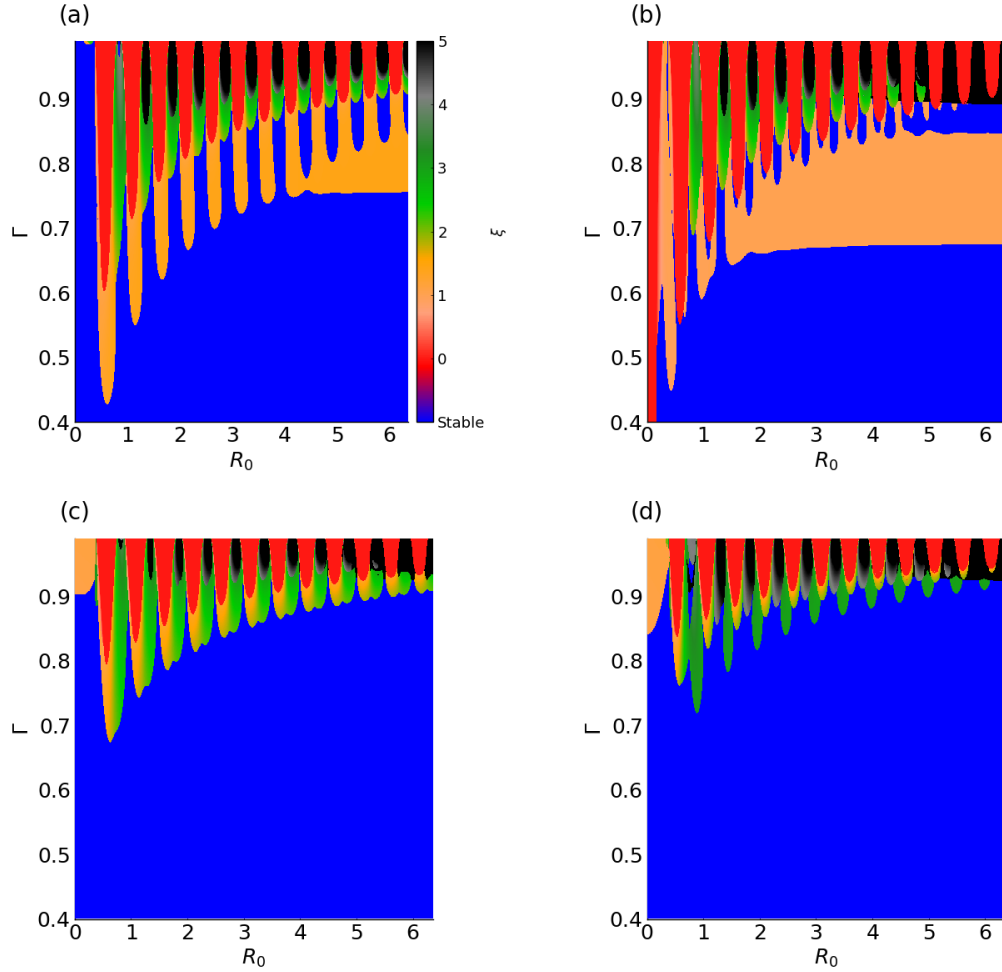
Figure 4.1: Orbital stability diagrams for different values of the spring power, n, and dimensionless mass, M. We consider (n, M) equal to (a) $(1, 0.14)$, (b) $(0, 0.28)$, (c) $(3, 2.2)$, and (d) $(8, 2.2)$. Stable orbits are highlighted in blue, with unstable orbits colour-coded by the wobble number $\xi = \frac{S}{\omega}$ predicted using linear stability analysis. (a,b) Non-resonant instability plateaus emerge, where the memory parameter $\Gamma = 1 - \sqrt{2}\sigma$ varies slowly with the orbital radius expressed in terms of pilot-wave wavelengths, $R_0 = \frac{r_0}{2\pi}$, along the stability boundary. Above these plateaus are small stability islands, which give rise to an especially unusual form of orbital quantisation. (b) Multiple plateaus are visible; circular orbits are stable for memory higher than the second plateau. (c) The non-resonant instability tongues (light green) and the 2ω resonant instability tongues (yellow/orange) studied by Liu *et al.*[66] and chapter 3 merge, with the non-resonant and resonant instability frequencies both equal to 2ω for $n = 3$. (d) The non-resonant instability frequency is 3ω for $n = 8$, with non-resonant instability tongues (dark green) forming between the resonant stability tongues (red/orange) for lower orbital radii. For larger orbital radii, the non-resonant instability tongues start to overlap the red/orange resonant instability tongues, with 4ω instability tongues (grey) emerging.

the logarithm vanishes. However, this assumption is violated for certain potentials for which $\sqrt{n+1}$ is an integer. For instance, when $n = 3, \xi = \sqrt{n+1}\omega = 2\omega$, the same instability frequency as the 2ω instability. The coincidence of the non-resonant and 2ω instability frequencies is reflected by the merging of the orange and green instability tongues in figure 4.1(c). We show that our new asymptotic framework handles these cases in §4.4.6.

4. For sufficiently small values of the dimensionless mass M (see figure 4.1(a)), corresponding to weak inertia, or for sufficiently high values of the force power n (see figure 4.1(d)), corresponding to highly nonlinear spring forces, the stability boundaries are not a function of the orbital radius, which was the case for the wobbling and monotonic instability tongues evident in the hydrodynamic regime. Instead the instability regions adopt a tear-drop shape (see figure 4.1(d)), indicating that the critical memory of instability cannot be solved for explicitly for a given value of the orbital radius. In addition, the spacing of the instability tongues changes, to the extent that the monotonic, 2ω and non-resonant instability tongues can all overlap for sufficiently large radius. We outline an implicit equation for the critical memory in equation (4.33), which supersedes the explicit expressions derived for the resonant and non-resonant instability tongues derived for the hydrodynamic regime.

4.2.3 Orbital stability

Orbital stability is characterised by analysing the linear growth rates of perturbations from circular orbits. We begin by following the framework introduced by Oza *et al.*[79], and later developed by Liu *et al.*[66] and §3.6. Specifically, we write

$$\boldsymbol{x}_p(t) = r(t)(\cos\theta(t), \sin\theta(t)), \tag{4.5}$$

where $r(t)$ and $\theta(t)$ are the time-varying radial and angular polar coordinates of the particle position, respectively. We assume perturbations arise due to an impulse at time $t = 0$, which thus take the form

$$r(t) = r_0 + \epsilon r_1(t)H(t), \quad \theta(t) = \omega t + \epsilon \theta_1(t)H(t), \tag{4.6}$$

where r_0 and ω satisfy the orbital equations (4.4), $\epsilon \ll 1$ is a small parameter controlling the sizes of perturbations, and $H(t)$ is the Heaviside step function. Substituting (4.6) into (4.3), and taking Laplace transforms, we recover the matrix system

$$\begin{pmatrix} \mathscr{A}(s) & -\mathscr{B}(s) \\ \mathscr{C}(s) & \mathscr{D}(s) \end{pmatrix} \begin{pmatrix} R(s) \\ r_0\Theta(s) \end{pmatrix} = \begin{pmatrix} c_r \\ r_0 c_\theta \end{pmatrix}, \tag{4.7}$$

where $R(s)$ and $\Theta(s)$ are the Laplace transforms of $r_1(t)$ and $\theta_1(t)$ respectively, and c_r and c_θ are the sizes of the initial radial and tangential perturbations respectively. The asymptotic growth rates of perturbations, s, correspond to the singularities of $R(s)$ and $\Theta(s)$, which thus satisfy $\mathscr{F}(s) = 0$, where $\mathscr{F}(s) = \mathscr{A}(s)\mathscr{D}(s) + \mathscr{B}(s)\mathscr{C}(s)$.

By using the radial force balance (4.4a) to eliminate the spring force constant, k, from the linearised equations, the stability coefficients $\mathscr{A}, \mathscr{B}, \mathscr{C}$ and $\mathscr{D}$ and the tangential force balance take the form, as in 3,

$$\mathscr{A}(s) = M\left(s^2 + (n-1)\omega^2\right) + s + \sigma - \frac{n+1}{r_0}\frac{\partial \mathcal{I}_0(0)}{\partial r_0} - \mathcal{I}_0(0) + \mathcal{C}_0(s) + \mathcal{I}_1(s), \quad (4.8\text{a})$$

$$\mathscr{B}(s) = 2M\omega s - \left(\frac{\sigma}{r_0\omega}\frac{\partial \mathcal{I}_0(0)}{\partial r_0} + \mathcal{S}_0(s)\right), \quad (4.8\text{b})$$

$$\mathscr{C}(s) = 2M\omega s + 2\omega + \frac{\sigma}{r_0\omega}\frac{\partial \mathcal{I}_0(0)}{\partial r_0} + \mathcal{S}_0(s), \quad (4.8\text{c})$$

$$\mathscr{D}(s) = Ms^2 + s - \sigma + \mathcal{C}_0(s) - \mathcal{I}_1(s), \quad (4.8\text{d})$$

$$1 - r_0^2\omega^2 = \sigma \mathcal{I}_0(0), \quad (4.8\text{e})$$

where the integrals $\mathcal{I}_m, \mathcal{C}_m$ and $\mathcal{S}_m$ are defined, for $\text{Re}(s + \sigma) > 0$,

$$\mathcal{I}_m(s) = \frac{1}{2}\int_0^\infty \mathrm{J}_{2m}\left(2r_0\sin\left(\frac{\omega t}{2}\right)\right)\mathrm{e}^{-(\sigma+s)t}\,\mathrm{d}t, \quad (4.9\text{a})$$

$$\mathcal{C}_m(s) = \frac{1}{2}\int_0^\infty \mathrm{J}_{2m}\left(2r_0\sin\left(\frac{\omega t}{2}\right)\right)\cos(\omega t)\mathrm{e}^{-(\sigma+s)t}\,\mathrm{d}t, \quad (4.9\text{b})$$

$$\text{and} \quad \mathcal{S}_m(s) = \frac{1}{2}\int_0^\infty \mathrm{J}_{2m}\left(2r_0\sin\left(\frac{\omega t}{2}\right)\right)\sin(\omega t)\mathrm{e}^{-(\sigma+s)t}\,\mathrm{d}t, \quad (4.9\text{c})$$

As demonstrated in §2.2.3, all of the integrals may be evaluated in terms of Bessel functions of complex order. Using the complex Bessel function integral evaluations in $\mathscr{A}(s), \mathscr{B}(s), \mathscr{C}(s)$ and $\mathscr{D}(s)$, and eliminating $1 - r_0^2\omega^2$ in $\mathscr{A}(s)$ and $\mathscr{D}(s)$ using (4.8e), we reduce the stability coefficients to

$$\mathscr{A}(s) = M(s^2 + \omega^2(n-1)) + \frac{(n+1)}{r_0\omega}\left(\frac{\mathrm{i}}{r_0} - f_{01}(\beta, r_0)\right) + \frac{1}{\omega}\left[f_{11}(\eta, r_0) - f_{00}(\beta, r_0)\left(1 + \frac{\beta\eta}{r_0^2}\right)\right],$$
$$(4.10\text{a})$$

$$\mathscr{B}(s) = 2M\omega s - \frac{\mathrm{i}s}{r_0^2\omega^2} + \frac{1}{r_0\omega}\left[-\beta f_{01}(\beta, r_0) + \eta f_{01}(\eta, r_0)\right], \quad (4.10\text{b})$$

$$\mathscr{C}(s) = 2M\omega s + 2\omega - \frac{\mathrm{i}s}{r_0^2\omega^2} + \frac{1}{r_0\omega}\left[\beta f_{01}(\beta, r_0) + \eta f_{01}(\eta, r_0)\right], \quad (4.10\text{c})$$

$$\mathscr{D}(s) = Ms^2 + 2s + \frac{\eta}{r_0^2\omega}\left[\beta f_{00}(\beta, r_0) - \eta f_{00}(\eta, r_0)\right], \quad (4.10\text{d})$$

where we define the parameters $\beta = \sigma/\omega$ and $\eta = (\sigma + s)/\omega$, and the auxiliary functions

$$f_{ab}(\eta, r_0) = \pi\,\mathrm{csch}(\pi\eta)\frac{\mathrm{d}^a}{\mathrm{d}r_0{}^a}(\mathrm{J}_{-\mathrm{i}\eta}(r_0))\frac{\mathrm{d}^b}{\mathrm{d}r_0{}^b}(\mathrm{J}_{\mathrm{i}\eta}(r_0)) \quad \text{for } a, b \in \{0, 1\}. \quad (4.11)$$

In addition, the orbital speed is prescribed by the tangential force balance (4.4b)

$$1 - r_0^2\omega^2 = \beta f_{00}(\beta, r_0). \quad (4.12)$$

The orbital solution is unstable if there are any roots, s, of $\mathscr{F}$ satisfying $\mathrm{Re}(s) > 0$. Denoting s_* as the unstable root with largest real part, the instability is monotonic if $\mathrm{Im}(s_*) = 0$ and oscillatory otherwise. Notably, $\mathscr{F}$ has a trivial eigenvalue at 0, corresponding to rotational invariance of the orbital motion. We denote the stability problem by $\mathscr{G}(s) = 0$, where

$$\mathscr{G}(s) = \frac{\mathscr{A}(s)\mathscr{D}(s) + \mathscr{B}(s)\mathscr{C}(s)}{s}. \tag{4.13}$$

As demonstrated in §2.2.3, the stability problem can be expressed solely in terms of the tangential force balance (4.12), and the stability condition (4.13), eliminating the central force from consideration. To ascertain whether a particular orbital state is stable or unstable, we typically utilise a rectangular integration contour spanning the domain $\mathrm{Re}(s) \in [0, 20]$ and $\mathrm{Im}(s) \in [0, 5]$, which we find to be sufficient to identify all roots with positive real part; extending the integration to regions of higher $\mathrm{Re}(s)$ does not lead to additional roots. The stability boundary is defined by $\mathscr{G}$ having roots lying on the imaginary axis, namely $\mathscr{G}(\mathrm{i}S) = 0$ for real S.

Having introduced the stability problem, we proceed to derive our new asymptotic framework to account for the anomalous behaviours found in different central force systems. We begin by establishing the instability thresholds corresponding to the flat plateaus, occurring when the critical memory of instability varies slowly relative to the orbital radius as $r_0 \to \infty$.

4.3 Plateau instability thresholds

The purpose of this section is to derive asymptotic formulae that may be solved to estimate the critical memory and instability frequency of the instability plateaus evident in figure 4.1(a, b). In doing so, we determine the combinations of the dimensionless mass, M, and spring power, n, for which zero, one or two instability plateaus form. Our analysis confirms that the instability frequency remains very close to $\sqrt{n+1}\omega$, highlighting how the non-resonant instability, studied in chapter 3, is responsible for these anomalous instability regions.

We begin by determining the scaling relationships for the asymptotic analysis of the flat plateaus (§4.3.1). We then outline an asymptotic framework for characterising the instability boundaries for large orbital radius and constant memory, which we solve to find the instability frequency (§4.3.2) and the critical memory of instability (§4.3.3). We conclude by comparing our asymptotic results to their numerical counterparts, and argue that there is always an eigenvalue near $\mathrm{i}\sqrt{n+1}\omega$ for sufficiently large orbital radius, corresponding to near-critical perturbations.

As demonstrated in §3.2.2 and 3.4.2, if $n < -1$, all circular orbits destabilise via a monotonic instability, as the nonlinear spring then decays too quickly to rein in perturbations. Here, we assume that $n > -1$, so that the non-resonant instability is not the monotonic instability. The case $n = -1$, corresponding to a logarithmic or two-dimensional Coulomb potential, was explored numerically by Tambasco et al. [94] and in §3.6.3.

4.3.1 Scalings and parameter expansions

From figure 4.1, we observe that, for low M, circular orbits are unstable above a critical memory, that varies very slowly with r_0. Following the discussion in §3.4, and from numerical simulations, we expect this instability to satisfy $\xi = S/\omega = O(1)$. As $\beta = \sigma r_0/U = O(r_0)$, the orders and arguments of the complex-order Bessel functions in (4.10) are of similar order, and the asymptotic expansions are complicated and unwieldy [76]. Thus, we take another approach, where we modify the expansion used by Oza[77] to expand the stability integrals, presented in appendix C.2.

We proceed to analyse each order of the stability condition $\mathscr{G} = 0$, where $\mathscr{G}$ is defined as in (4.13), using the integral expansions outlined in appendix C.2. The details of the calculation are left to appendix C.2, and the results are summarised in (C.15), where we introduce the notation

$$L_{m,n}(x) = \int_0^\infty t^n \mathrm{J}_m(t)\mathrm{e}^{-xt}\,\mathrm{d}t \quad \text{and} \quad M_{m,n}(x) = \int_0^\infty t^n \mathrm{J}'_m(t)\mathrm{e}^{-xt}\,\mathrm{d}t. \tag{4.14}$$

Using the results of (C.15), we expand the stability coefficients along the stability boundary as

$$\mathscr{A}(\mathrm{i}\xi\omega) = \frac{\mathscr{A}_2}{r_0^2} + \frac{\mathscr{A}_3}{r_0^3} + O\left(\frac{1}{r_0^4}\right), \quad \mathscr{B}(\mathrm{i}\xi\omega) = \frac{\mathscr{B}_2}{r_0^2} + \frac{\mathscr{B}_3}{r_0^3} + O\left(\frac{1}{r_0^4}\right), \tag{4.15a}$$

$$\mathscr{C}(\mathrm{i}\xi\omega) = \frac{\mathscr{C}_1}{r_0} + \frac{\mathscr{C}_2}{r_0^2} + O\left(\frac{1}{r_0^3}\right), \quad \mathscr{D}(\mathrm{i}\xi\omega) = \frac{\mathscr{D}_1}{r_0} + \frac{\mathscr{D}_2}{r_0^2} + O\left(\frac{1}{r_0^3}\right), \tag{4.15b}$$

and proceed to study the stability condition $\mathscr{G}(\mathrm{i}\xi\omega) = 0$ at each order, beginning with $O\left(r_0^{-3}\right)$. In the following analysis, we denote $p = \sigma/U$, where $U = r_0\omega$ is the orbital speed.

4.3.2 $O\left(r_0^{-3}\right)$ stability condition

The $O\left(r_0^{-3}\right)$ stability condition takes the form $\mathscr{G}_3 = 0$, where

$$\mathscr{G}_3 = \frac{1}{\xi}\left(\mathscr{A}_2\mathscr{D}_1 + \mathscr{B}_2\mathscr{C}_1\right). \tag{4.16}$$

From (C.15), we observe that

$$\mathscr{C}_1 = \frac{1}{U}L_{2,1}(p) \quad \text{and} \quad \mathscr{D}_1 = \frac{\mathrm{i}\xi}{U}L_{2,1}(p), \tag{4.17}$$

from which we conclude $\mathscr{D}_1 = \mathrm{i}\xi\mathscr{C}_1$. As $\mathscr{D}_1 \neq 0$ for $\xi \neq 0$, we reduce the stability condition $\mathscr{G}_3 = 0$ to

$$\frac{1}{\xi}\left(\mathscr{A}_2 + \frac{\mathscr{B}_2}{\mathrm{i}\xi}\right) = 0. \tag{4.18}$$

From (C.15), we find

$$\mathscr{A}_2 = MU^2(n - 1 - \xi^2) + \frac{(n + 1 - \xi^2)}{2U}L_{1,1}(p) - \frac{1}{2U}L_{0,2}(p), \tag{4.19a}$$

$$\mathscr{B}_2 = \mathrm{i}\xi U\left(2MU + \frac{1}{2U^2}L_{0,2}(p)\right), \tag{4.19b}$$

and substitution into (4.18) leads to

$$\frac{(n + 1 - \xi^2)}{\xi} \left[MU^2 + \frac{1}{2U} L_{1,1}(p) \right] = 0. \tag{4.20}$$

As $L_{1,1}(p)$ is strictly non-negative, this implies $\xi^2 = n + 1$, thereby establishing that the origin of the flat plateaus is in the non-resonant instability, as discussed in §3.4. However, to solve for the critical memory of instability, we must consider the $O\left(r_0^{-4}\right)$ stability condition.

4.3.3 $O\left(r_0^{-4}\right)$ stability condition

The $O\left(r_0^{-4}\right)$ stability condition takes the form $\mathscr{G}_4 = 0$, where

$$\mathscr{G}_4 = \frac{1}{\xi} \left(\mathscr{A}_3 \mathscr{D}_1 + \mathscr{A}_2 \mathscr{D}_2 + \mathscr{B}_3 \mathscr{C}_1 + \mathscr{B}_2 \mathscr{C}_2 \right). \tag{4.21}$$

From (C.15), the required stability coefficients are given by

$$\mathscr{A}_3 = \frac{i\xi}{12U} \left(3L_{0,3}(p) + 2nL_{1,2}(p) \right), \quad \mathscr{B}_3 = \frac{n+1}{4U} L_{0,3}(p), \tag{4.22a}$$

$$\mathscr{C}_2 = \mathscr{B}_2, \quad \text{and} \quad \mathscr{D}_2 = -MU^2(n+1) + \frac{1}{U} \left(-L_{0,2}(p) + L_{1,1}(p) \right). \tag{4.22b}$$

Using all of the known stability coefficients leads to a highly nonlinear equation to solve for σ, which we do numerically. We plot the solutions of the critical memory, σ, against the dimensionless mass, M, in figure 4.2, colour-coding the curves by different values of the spring power, n.

From figure 4.2(a), we see that all of the curves arise from a common point as $\sigma \to 0$. Specifically, by setting $\sigma = 0$ and evaluating all of the $L_{m,n}$ integrals, we show, in appendix C.2.2 that $\sigma = 0$ occurs at $M = \frac{1}{4}$, independent of n. If we then follow the solution curves emanating from $\sigma = 0$ for different n, we see that either M decreases monotonically, corresponding to a single plateau associated with the non-resonant instability frequency $\xi = \sqrt{n+1}$, or it initially increases, and then decreases monotonically for larger values of σ, corresponding to two plateaus. In other words, the onset of the plateau instability occurs at lower memory for lower inertia. For lower values of n, i.e. for central forces that decay faster with radial position than $r^{\frac{9}{16}}$, plateaus may also occur for higher inertia, in which case pairs of plateaus may appear. To solve for the critical value of n above which there is only one plateau, we look for when $\sigma = 0$ is a multiple root of $\mathscr{G}_4$ at $M = \frac{1}{4}$. In appendix C.2.2, we demonstrate that this critical value threshold is $n = \frac{9}{16}$. The dependence of the number of plateaus associated with a non-resonant instability on M is summarised in table 4.2. We display an example of multiple plateaus in 4.2(b), where $n = 0$ is below the critical threshold of $\frac{9}{16}$, with both plateaus highlighted by dashed lines.

In figure 4.2(b), we plot the maximum dimensionless mass, M_m, for which plateau instabilities can be observed. While we observe that M_m approaches approximately 0.45 as $n \to -1$, in §3.6.3, we observe that a plateau instability exists even for $\kappa_0 = 1.6$, or $M = 2.2$, indicating that the 2D Coulomb force system must be analysed differently.
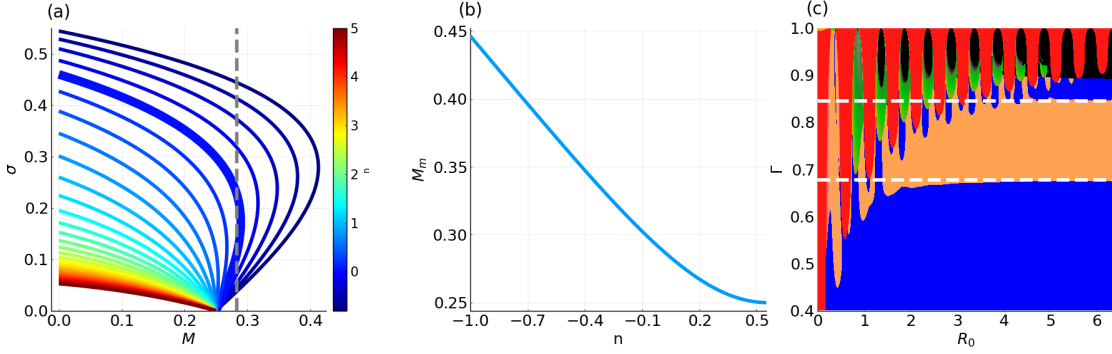
Figure 4.2: Existence of stability plateaus associated with a non-resonant instability of circular orbits with frequency $\sqrt{n+1}\omega$ in a central force $\boldsymbol{F} = -k|\boldsymbol{x}_p|^{n-1}\boldsymbol{x}_p$. (a) The dependence of the wave decay rate, σ, at which plateau instabilities occur on the dimensionless mass, M, colour-coded by the force power, n. Each curve emanates from the point $(\sigma, M) = (0, \frac{1}{4})$. The bold blue curve corresponds to $n = 0$. For $-1 < n < \frac{9}{16}$, two plateaus may form for certain ranges of M. (b) The dependence of the maximum value of M for which plateaus emerge, denoted M_m, on the force power, n. For $-1 < n < \frac{9}{16}$, up to two plateaus are possible provided that $\frac{1}{4} < M < M_m$. (c) Stability diagram for $n = 0$ and $M = 0.28$. There are two plateaus (highlighted by the white dashed lines for large r_0), with the critical memory parameter, $\Gamma = 1 - \sqrt{2}\sigma$, deduced from the two intersections of the grey dashed line and blue bold curve in panel (a).

n	$\frac{1}{4} < M < M_m$	$0 \leq M < \frac{1}{4}$
$-1 < n < \frac{9}{16}$	Two plateaus	One plateau
$n > \frac{9}{16}$	No plateaus	One plateau

Table 4.2: Number of instability plateaus associated with the non-resonant instability frequency $\sqrt{n+1}\omega$ for different values of the dimensionless mass, M, and force power, n. Notably, M_m denotes the maximum value of M for which plateaus are observed, whose dependence on n is presented in figure 4.2(b).

The plateau for $n = 0$ in figure 4.2(c) is particularly interesting, as the frequency $\sqrt{n+1}\omega$ corresponds to a 1-wobble (see §4.3.2), where the instability frequency is equal to the orbital frequency, for which one might expect a slight drift of the circular orbit for small perturbations, before nonlinear effects significantly alter the perturbed trajectory, similar to the drifting instabilities found by Oza et al. [80]. However, we previously argued in §3.6.3 that in the experimental regime, when $n = 0$, the non-resonant instability does not appear, and that the $n = 0$ system behaves qualitatively similar to the Coriolis force system. These statements are evidently both incorrect at lower inertia, in the presence of the plateau instability. Thus, the onset of the plateau instabilities cause our physical picture in §3.6.3 to break down, and lead to the appearance of 1ω instabilities.

We now argue, based on the sizes of the stability coefficients, that, even away from the memory of instability, there is always a near-critical eigenvalue near $s = i\xi\sqrt{n+1}$. We first observe from (4.15) that $\mathscr{A}(i\xi\omega)$ and $\mathscr{B}(i\xi\omega)$ are both of size $O\left(r_0^{-2}\right)$, while $\mathscr{C}(i\xi\omega)$ and

$\mathscr{D}(\mathrm{i}\xi\omega)$ are both of size $O\left(r_0^{-1}\right)$. Upon defining

$$\mathscr{G}'(\xi) = \mathrm{i}\omega\mathscr{G}(\mathrm{i}\xi\omega) = \frac{\mathscr{A}(\mathrm{i}\xi\omega)\mathscr{D}(\mathrm{i}\xi\omega) + \mathscr{B}(\mathrm{i}\xi\omega)\mathscr{C}(\mathrm{i}\xi\omega)}{\xi},$$

we note that $\mathscr{G}' = O\left(r_0^{-3}\right)$, independent of ξ or σ. When $\xi = \sqrt{n+1}$, we see from §4.3.2 that

$$\mathscr{G}'\left(\sqrt{n+1}\right) = O\left(r_0^{-4}\right) \quad \text{and} \quad \frac{\partial\mathscr{G}'}{\partial\xi}\left(\sqrt{n+1}\right) = O\left(r_0^{-3}\right). \tag{4.23}$$

If we now introduce a complex small perturbation, δ, in the wobble number, ξ, from $\sqrt{n+1}$, namely $\xi = \sqrt{n+1} + \delta$, then we may use Taylor expansions to show that

$$\mathscr{G}'(\sqrt{n+1}+\delta) = \mathscr{G}'\left(\sqrt{n+1}\right) + \delta\frac{\partial\mathscr{G}'}{\partial\xi}\left(\sqrt{n+1}\right) + O(\delta^2). \tag{4.24}$$

We proceed to solve for δ satisfying $\mathscr{G}'(\sqrt{n+1}+\delta) = 0$ using this linear approximation, from which we may estimate the size of perturbation of the eigenvalue from $\mathrm{i}\xi\sqrt{n+1}$. Provided that $\frac{\partial\mathscr{G}'}{\partial\xi}(\sqrt{n+1}) \neq 0$, we find that $\delta = \xi - \sqrt{n+1}$ approximately satisfies

$$\delta = -\frac{\mathscr{G}'(\sqrt{n+1})}{\frac{\partial\mathscr{G}'}{\partial\xi}(\sqrt{n+1})} = O\left(\frac{1}{r_0}\right), \tag{4.25}$$

independent of σ. The evaluation of $\delta = O(r_0^{-1})$ follows from the size of the terms outlined in equation (4.23). In other words, $s = \mathrm{i}\sqrt{n+1}\omega$ is always an $O\left(r_0^{-2}\right)$ perturbation away from a zero of $\mathscr{G}$ for arbitrary σ, indicating that for any stable circular orbit, there is always an oscillation mode that is near-critical, where the decay rate scales as $O\left(r_0^{-2}\right)$. This near-criticality of perturbations to large circular orbits mirrors the near-criticality of $\sqrt{n+1}\omega$-frequency oscillations in the boost system (see §B.1.3).

4.4 Moderate orbital memory

Now that we have rationalised the origins of the non-resonant instability at low orbital memory, we proceed to analyse the situation of intermediate orbital memory, a problem considered in §3.6 in the hydrodynamic regime. We begin by summarising the asymptotic formulae derived in §3.6 for the wobbling, monotonic and non-resonant instability boundaries (§4.4.1), and discuss their inability to describe the tear-drop-shaped instability regions and stability pockets evident in figure 4.1c. We then develop a new asymptotic formulation capable of describing these anomalous stability features in §4.4.2 and §4.4.3. We show that prior results for wobbling, monotonic and non-resonant instabilities may be obtained by considering a particular dominant balance in the asymptotic stability function (§4.4.4), before developing various minimal stability functions for describing the non-resonant instabilities in §4.4.5. We consider the case for which the instability frequency $\sqrt{n+1}\omega$ becomes commensurate with the orbital frequency in §4.4.6, from which we derive a stability framework capable of explaining the merging of the instability tongues in figure 4.1(c). Finally, in §4.4.7 we postulate and test a minimal correction to the stability formulation for adequately capturing the movement of the instability tongues for large values of the spring power, n.

n	Monotonic instability	2ω instability	4ω instability	ω_r instability
$-1 < n < 0$	$+$	$-$	$-$	$-$
$0 < n < 3$	$+$	$-$	$-$	$+$
$3 < n < 15$	$+$	$+$	$-$	$-$

Table 4.3: The correspondence between the sign of $\sin(2r_0)$ and the existence of monotonic, 2ω, ω and $\omega_r = \omega\sqrt{n+1}$ instabilities for a droplet walking in a nonlinear spring force, $\boldsymbol{F} = -k|\boldsymbol{x}_p|^{n-1}\boldsymbol{x}_p$. We restrict our attention, in this table, to the case $4M > 1$.

4.4.1 Existing results

The values of the reciprocal orbital memory parameter, $\beta = \frac{\sigma}{\omega}$, and wobble number, $\xi = \frac{S}{\omega}$, as defined in table 4.1, along resonant stability boundaries, for which the instability frequency is close to $2N\omega$ for $N \geq 0$ an integer, take the form (see (3.34))

$$\beta_{\text{res}} = \frac{1}{\pi} \ln\left(-\frac{8r_0^2 \sin(2r_0)}{(4N^2 - n - 1)(1 + 2M)}\right) + O\left(\frac{\ln(r_0)}{r_0}\right), \tag{4.26a}$$

$$\xi_{\text{res}} = 2N + \frac{N}{\pi r_0}\left(\frac{4M - 1}{4N^2 - n - 1} - 4\beta_{\text{res}}\cot(2r_0)\right) + O\left(\frac{1}{r_0^2}\right), \tag{4.26b}$$

while the corresponding non-resonant instability boundaries are given by

$$\beta_{\text{nr}} = \frac{1}{\pi} \log\left(-\frac{16r_0^3 \sin(2r_0)\sin(\pi\xi_{\text{nr}})}{\xi_{\text{nr}}(4M - 1)(2M + 1)}\right) \quad \text{for} \quad \frac{\sin(2r_0)\sin(\pi\xi_{\text{nr}})}{4M - 1} < 0, \tag{4.26c}$$

$$\text{and} \quad \xi_{\text{nr}} = \sqrt{n+1} + o(1). \tag{4.26d}$$

In chapter 3, we restricted our attention to the hydrodynamic regime (namely $M = 2.2$), and for when $n \leq 4$, for which we only observed $N = 1$, corresponding to 2-wobble instabilities. For different n, however, the types of instabilities observed may change. As table 4.3 indicates, if $n > 3$, the 2ω instability no longer dominates the 4ω instability; instead, it dominates the monotonic instability, while the non-resonant instability now dominates the 4ω instability. As we observed in figure 4.1, the separation between consecutive non-resonant stability tongues is no longer the same as the separation between resonant stability tongues, indicating that (4.26c) cannot correctly model the non-resonant instability boundaries, and that the non-resonant instability does not always dominate the 4ω instability. From figure 4.1, we see that 4ω instabilities may thus be observed in an external potential of sufficiently high power, n.

We note that if $M < \frac{1}{4}$, the region of validity of the expression for ξ_{res} switches from $\sin(2r_0) < 0$ to $\sin(2r_0) > 0$, a sudden switch that is not observed numerically. As we shall see in §4.4.5, this apparent sudden switch is an indication that the behaviour of the non-resonant instability becomes significantly more complex for smaller M. These observations motivate our alternative asymptotic formulation.

4.4.2 Asymptotic formulation

The principal shortcoming of the asymptotic procedure developed by Liu *et al.*[66] and §3.6.1 is the manner in which the Bessel functions $J_{i(\beta + i\xi)}(r_0)$ (appearing in the analytical evaluation

of the stability integrals (4.9)) are expanded. The Hankel expansions used by Liu et al. [66] require that $\left|-(\beta + i\xi)^2 + \frac{1}{4}\right| \ll r_0$, an assumption that does not always hold, leading to an ill-ordered expansion where higher order terms do not progressively decay in size. Instead, we relax the assumption to $\beta/r_0 = o(1)$, which we find to be sufficient to explain most of the anomalous features of the stability diagram in figure 4.1. As $\beta/r_0 = \sigma/U$, and the orbital speed, U, is always $O(1)$, the assumption $\beta/r_0 = o(1)$ is identical to the condition $\sigma = o(1)$, corresponding to relatively high memory. Formally, the expansion we employ is in powers of β/r_0. For any instability for which the critical memory of instability increases with orbital radius, we may thus employ the Bessel function modulus and phase asymptotics of Heitman et al.[54], the details of which are outlined in appendix C.3. The stability function is then given by (4.27) to describe the resonant instabilities, and by (4.32) when describing the non-resonant instabilities. We now proceed to use this more general asymptotic formulation to re-derive the results of (3.34), which will inform us on their regime of applicability.

4.4.3   Asymptotic stability function

Following the analysis outlined in appendix C.3, the stability function for $s = i\xi\omega$ may be expressed asymptotically (for large r_0) as

$$\frac{U^2}{i\xi}(\mathscr{A}\mathscr{D}+\mathscr{B}\mathscr{C}) = F_1+F_2+F_3+F_4+F_5+F_6+O\left(\frac{1}{r_0^7}\right)+O\left(\frac{e^{-\pi\beta}}{r_0^3}\right)+O\left(\frac{e^{-2\pi\beta}}{r_0^2}\right), \quad (4.27a)$$

where the coefficients F_l (roughly corresponding to powers of r_0^{-l}) are defined

$$F_1 = -\frac{8e^{-\pi\beta}\left(\sin\left(r_b\right) + e^{-i\pi\xi}\sin\left(r_e\right)\right)}{r_0}, \quad (4.27b)$$

$$F_2 = \frac{e^{-\pi\beta}}{\xi r_0^2}\Bigg[\left(8i\beta - 2\xi(3+4n)\right)\cos(r_b) + 4\xi\left(\beta + i\xi(1-2M)\right)\left(\sin(r_b) + \sin(r_e)e^{-i\pi\xi}\right)$$
$$+ 2(-4+i\beta)\cos(r_e)e^{-i\pi\xi}\Bigg], \quad (4.27c)$$

$$F_3 = -\frac{2(1+2M)(\xi^2 - n - 1)}{r_0^3}, \quad (4.27d)$$

$$F_4 = \frac{i}{2r_0^4}\Bigg[2i\beta(1+8M)(1+n-\xi^2) + \xi(-3-2n+2\xi^2 + 4M^2(3+n-\xi^2) + 2M(\xi^2-n)\Bigg], \quad (4.27e)$$

$$F_5 = -\frac{1}{4r_0^5}\Bigg[9 + 3n - 11\xi^2 + 2\xi^4 - 2\beta^2(5M-8)(n+1-\xi^2)$$
$$+ 2i\beta\xi(7+2n-6\xi^2+8M^2(3+n-\xi^2) + M(\xi^2-n)\Bigg], \quad (4.27f)$$

$$F_6 = \frac{\beta}{8r_0^6}\Big[(4 + 2n - 26\xi^2 - 8n\xi^2 + 13\xi^4 + 2\beta^2(4 + 13M)(1 + n - \xi^2)$$

$$+ 2M(4 + 2n - 19\xi^2 - 8n\xi^2 + 6\xi^4)\Big]$$

$$+ \frac{\mathrm{i}\xi}{4r_0^6}\Big[11 + 4n - 20\xi^2 - 4n\xi^2 + 6\xi^4 - M(2 + n + 19\xi^2 + 8n\xi^2 - 6\xi^4)$$

$$+ \beta^2(M(48 + 37n - 37\xi^2) + 4(14 + 7n - 9\xi^2) + 16M^2(3 + n - \xi^2)\Big], \qquad (4.27\mathrm{g})$$

with

$$r_b = 2r_0 - \frac{\beta^2}{r_0} \quad \text{and} \quad r_e = 2r_0 - \frac{\eta^2}{r_0} \qquad (4.27\mathrm{h})$$

defined in terms of the reciprocal orbital memory parameter, $\beta = \sigma/\omega$, and $\eta = (\mathrm{i}\xi\omega + \sigma)/\omega$.

Similarly, the tangential force balance (4.12) is expanded as

$$U = 1 - \frac{\beta}{2r_0} - \frac{\beta^2}{8r_0^2} + \frac{\beta + 3\beta^3}{128r_0^4} + \frac{\beta^2(4 + 11\beta^2)}{128r_0^4} - \frac{\beta^3(114 + 31\beta^2)}{256r_0^5} - \frac{69\beta^6}{1024r_0^6} + O\left(\frac{1}{r_0^7}\right),$$
$$(4.28)$$

We consider the resonant and non-resonant instabilities separately, which correspond to dominant balances between different terms in (4.27). As we will show, the resonant instabilities are governed by balancing the real parts of (4.27), while the non-resonant instabilities are governed by balancing the imaginary parts of (4.27).

We observe that F_1 and F_2, the terms containing $\mathrm{e}^{-\pi\beta}$, also contain terms oscillatory in r_0, whereas F_3 to F_6 do not. Thus, the oscillatory nature of the stability boundaries arises from balancing F_1 and F_2 with F_3 to F_6. A recurring theme of the solution of the stability problem, therefore, is determining which terms from F_3 to F_6 are to balance $F_1 + F_2$. In §4.4.4 and 4.4.5, we derive approximations neglecting F_2, as $F_1 \gg F_2 0$. In §4.4.6, we show that F_2 is needed to describe the asymptotic approximation for the stability boundary, and in §4.4.7, we consider the benefits of including F_2.

4.4.4 Resonant instabilities

In a manner similar to §B.3, we notice that two dominant balances between $\mathrm{e}^{-\pi\beta}$ and powers of r_0 are possible. If $\xi^2 \neq n + 1$, then the dominant balance occurs between F_1 and F_3, and takes the form

$$-\frac{8\mathrm{e}^{-\pi\beta}\left(\sin(r_b) + \mathrm{e}^{-\mathrm{i}\pi\xi}\sin(r_e)\right)}{r_0} = \frac{2(1 + 2M)(\xi^2 - n - 1)}{r_0^3} + O\left(\frac{1}{r_0^4}\right). \qquad (4.29)$$

By approximating $r_e = 2r_0 - \frac{\beta^2 - \xi^2}{r_0} + o(1)$, we write

$$-4r_0^2\mathrm{e}^{-\pi\beta}\sin\left(2r_0 - \frac{\beta^2 - \xi^2}{r_0}\right)\left(1 + \mathrm{e}^{-\mathrm{i}\pi\xi}\right) = (1 + 2M)(\xi^2 - n - 1) + O\left(\frac{1}{r_0}\right). \qquad (4.30)$$

Upon comparing the magnitudes of the real and imaginary parts of both sides of (4.30), we see that ξ must be an integer. This integer cannot be odd, or else the left-hand-side of

(4.30) vanishes, so we conclude that ξ must be an even integer. In addition, $r_0^2 e^{-\pi\beta} = O(1)$, from which we conclude that $\frac{\beta^2 - \xi^2}{r_0} \ll 1$, and thus $\sin(r_b) \approx \sin(2r_0)$. These asymptotic simplifications lead us to the resonant instability equations detailed in (4.26).

Notably, the solution process detailed here arrive at the same asymptotic stability boundaries as those deduced by (2.21) and (3.34), for which the scaling $e^{\pi\beta} = O(r_0^2)$ was assumed from the outset. In the present work, however, the scaling $e^{\pi\beta} = O(r_0^2)$ follows directly from the initial assumption $\beta \ll r_0$, which is a much weaker requirement. In addition, we have shown that the memory of instability was determined by considering the real part of the dominant balance. We now turn to the case of the non-resonant instability, where a scaling of the form $\beta = O(\log(r_0))$ does not hold in general, and where the memory of instability is now determined from considering the imaginary part of the dominant balance.

4.4.5 Non-resonant instabilities

Asymptotic balance

A second possible dominant balance in (4.27) occurs by balancing F_1 with F_4, which can happen only if $F_3 = 0$. In addition, if $F_3 = 0$, then $\xi^2 = n + 1$, and F_4 is purely imaginary. In practice, ξ^2 is not exactly $n + 1$, F_3 does not vanish identically, and F_4 has a small imaginary component. To capture this behaviour, we write

$$\xi = \xi_0 + \frac{\xi_1}{r_0}, \quad \xi_0 = \sqrt{n+1}, \tag{4.31}$$

where ξ_1 is a frequency detuning that will be identified (when necessary) as part of the solution process. We then divide (4.27) by ξ, write $r_b = r_{b,1} - \frac{\xi^2}{r_0}$, substitute (4.31) into the resulting stability function and expand, leading to asymptotic forms of the real and imaginary parts of the stability function. As deduced in appendix C.3.2, the real part of the stability function for $s = i\xi\omega$ may be expressed

$$\mathrm{Re}\left[\frac{U^2 \mathscr{F}}{i\xi^2}\right] = F_{r,1} + F_{r,2} + F_{r,4} + F_{r,5} + F_{r,6} = O\left(\frac{e^{-\pi\beta}}{r_0^3}\right) + O\left(\frac{e^{-2\pi\beta}}{r_0}\right) + O\left(\frac{1}{r_0^7}\right), \tag{4.32a}$$

where the corresponding coefficients of r_0^{-l} may be expressed as

$$F_{r,1} = -\frac{8e^{-\pi\beta}(1 + \cos(\pi\xi_0))\sin(r_{b,1})}{r_0\xi_0}, \tag{4.32b}$$

$$F_{r,2} = \frac{e^{-\pi\beta}}{r_0^2\xi_0^2}\Big[4\xi_0\sin(r_{b,1})\big(\beta(1 + \cos(\pi\xi_0)) + \xi_0(1 - M)\sin(\pi\xi_0)\big)$$
$$+ 2\cos(r_{b,1})\big(\xi_0(1 + \cos(\pi\xi_0) + 4\beta(-1 + 2\xi_0^2)\sin(\pi\xi_0))\big)\Big], \tag{4.32c}$$

$$F_{r,4} = -\frac{4\xi_1(1 + 2M)}{r_0^4}, \tag{4.32d}$$

$$F_{r,5} = \frac{-3 + 4\xi_0^2 - \xi_0^4 + 4\beta(1 + 8M)\xi_0\xi_1 + 4(1 + 2M)\xi_1^2}{2r_0^5\xi_0}, \tag{4.32e}$$

$$F_{r,6} = -\frac{1}{4r_0^6\xi_0^2}\Big[4\beta^2(-8 + 5M)\xi_0^2\xi_1 + 2\xi_1(-3 - 7\xi_0^2 + 3\xi_0^4 + 4(1 + 2M)\xi_1^2)$$
$$+ \beta\xi_0(-2 + 16\xi_0^2 - 5\xi_0^4 + 4\xi_1^2 + 2M(-2 + 9\xi_0^2 + 2\xi_0^4 + 16\xi_1^2))\Big]. \tag{4.32f}$$

Furthermore, the imaginary part of the stability function is

$$\text{Im}\left[\frac{U^2\mathscr{F}}{i\xi^2}\right] = F_{i,1} + F_{i,2} + F_{i,4} + F_{i,5} + F_{i,6} = O\left(\frac{e^{-\pi\beta}}{r_0^3}\right) + O\left(\frac{e^{-2\pi\beta}}{r_0}\right) + O\left(\frac{1}{r_0^7}\right), \quad (4.32g)$$

which is defined in terms of

$$F_{i,1} = \frac{8e^{-\pi\beta}\sin(\pi\xi_0)\sin(r_{b,1})}{r_0\xi_0}, \quad (4.32h)$$

$$F_{i,2} = \frac{e^{-\pi\beta}}{\xi_0^2 r_0^2}\left[\cos(r_{b,1})(8\beta(1-\cos(\pi\xi_0)) + 16\beta\xi_0^2\cos(\pi\xi_0) - 2\xi_0\sin(\pi\xi_0))\right.$$
$$\left.-4\sin(r_{b,1})\left((-1+2M)\xi_0^2(1+\cos(\pi\xi_0)) - 2\pi\xi_0\xi_1\cos(\pi\xi_0) + (\beta\xi_0 + 2\xi_1)\sin(\pi\xi_0)\right)\right], \quad (4.32i)$$

$$F_{i,4} = \frac{(2M+1)(4M-1)}{2r_0^4}, \quad (4.32j)$$

$$F_{i,5} = \frac{-\beta(5 + M + 16M^2 - 4\xi_0^2) + 4(1+2M)(1-M)\xi_0\xi_1}{2r_0^5}, \quad (4.32k)$$

$$F_{i,6} = \frac{1}{8r_0^6}\left[7 - 12\xi_0^2 + 2\xi_0^4 + \beta^2(28 + 11M + 32M^2 - 8\xi_0^2)\right.$$
$$\left.-8\beta(-6 + M - 8M^2)\xi_0\xi_1 + 8\xi_1^2(1-2M^2) - M(1 + 12\xi_0^2 + 2\xi_0^4 - 8\xi_1^2)\right]. \quad (4.32l)$$

Finally, we define

$$r_{b,1} = 2r_0 - \frac{\beta^2 - \xi^2}{r_0}. \quad (4.32m)$$

Here, and for the remainder of this paper, we choose not to expand the contribution of ξ in $r_{b,1}$. It was found that leaving $r_{b,1}$ in this form leads to the best agreement with the numerical stability boundaries.

In §C.3.2, when $\xi_0 = \sqrt{n+1}$ is not an integer, we demonstrate why we can safely neglect ξ_1 when solving for the memory of instability. Neglecting ξ_1 and $F_{i,2}$, and only retaining the $O\left(\beta^2 r_0^{-6}\right)$ term in $F_{i,6}$, the imaginary part of the stability function then reduces to

$$\text{Im}\left[\frac{U^2\mathscr{F}}{i\xi^2}\right] = T_1 + T_4 + T_5 + T_6 = O\left(\frac{1}{r_0^6}\right) + O\left(\frac{e^{-\pi\beta}}{r_0^2}\right) + O\left(\frac{e^{-2\pi\beta}}{r_0}\right), \quad (4.33)$$

where

$$T_1 = \frac{8e^{-\pi\beta}\sin(\pi\xi_0)\sin\left(2r_0 - \frac{\beta^2 - \xi_0^2}{r_0}\right)}{\xi_0 r_0}, \quad T_4 = \frac{(2M+1)(4M-1)}{2r_0^4}, \quad (4.34)$$

$$T_5 = -\frac{\beta(5 + M + 16M^2 - 4\xi_0^2)}{2r_0^5}, \quad \text{and} \quad T_6 = \frac{\beta^2(28 + 11M + 32M^2 - 8\xi_0^2))}{8r_0^6}. \quad (4.35)$$

In the hydrodynamic regime, the dominant balance takes the form $T_1 \sim -T_4$, which indicates that $\beta = O(\log(r_0))$, and so $\frac{\beta^2}{r_0} \ll 1$. Solving for β, and approximating $\sin\left(2r_0 - \frac{\beta^2 - \xi_0^2}{r_0}\right) \approx \sin(2r_0)$, leads to (4.26c), as shown in (3.34). As argued in §4.4.4, the agreement between

the two methods arises from the scaling $\mathrm{e}^{\pi\beta} = O(r_0^3)$, which was derived in this expansion and assumed in §B.3. We now consider the situation where the additional terms are needed. For ease of reference, we define the T_n solution as the solution to (4.33) including all terms up to T_n, so the hydrodynamic solution is the T_4 solution, and turn our attention to when the T_5 solution is required.

Parameter regimes that necessitate the inclusion of T_5

We consider the behaviour of solutions to (4.33) for β at fixed r_0 but varying M. We observe that the T_4 solution is used in the hydrodynamic regime, when $4M - 1 > 0$, and is valid only if T_1 and T_4 have opposite signs. As we can solve $T_1 + T_4 = 0$ when $4M - 1 > 0$ (for which $T_4 > 0$), we conclude that $T_1 < 0$. When $4M - 1 < 0$, T_1 and T_4 are both negative, and thus the balance $T_1 \sim -T_4$ is no longer possible. From (4.33), we see that if $4M - 1 < 0$, then $T_4 < 0$, but for sufficiently large ξ and sufficiently small M, it is possible for $T_5 > 0$. These inequalities imply that the balance $T_1 + T_4 \sim -T_5$ can be solved in some cases.

To show the effect of including T_5 in (4.33), we plot the stability boundaries when including terms up to T_4 (cyan curve) and T_5 (white curve) in figure 4.3 for various values of M and n. For larger M, we observe that there is little difference between both solutions. However, for smaller M, we see that the T_4 solution is out of phase with the numerically computed stability boundary. This discrepancy occurs because the sign of T_4 changes, and so T_1 is balanced with a term with the wrong sign. This inconsistency is rectified by the inclusion of the term T_5 in the asymptotic solution.

The necessity of the implicit nature of (4.33) can be seen in figure 4.3(d). Specifically, both the true stability boundaries and the white asymptotic boundaries fail the vertical line test, and so the critical memory of instability cannot be uniquely determined from r_0. However, in the first row of figure 4.3, all the stability boundaries pass the vertical line test. The ability of our formulation to explain the underlying reasons behind the differences in the nature of the stability boundaries emphasises the need for the formulation in equation (4.33).

For n and M sufficiently small for the flat plateau instability considered in §4.3 to be present, as in figure 4.3(d), two types of solutions to (4.33) arise:

1. Solutions where $\sigma = o(1)$, which are also obtained by solving (4.26c), as here, the dominant balance is solely between T_1 and T_4.

2. Solutions where $\sigma = O(1)$, or $\beta = O(r_0)$, and the dominant balance involves T_1, T_4, T_5 and possibly T_6. These solutions correspond to the flat plateau instability considered in §4.3, and arise because T_1 and T_4 have the same sign, and thus cannot cancel.

The first set of solutions, as seen in figure 4.3(d), represents a special kind of stability boundary, where circular orbits are stabilised for higher memory than the critical memory of instability. The second set of solutions violate the assumptions under which (4.33) was derived. Nevertheless, understanding the behaviour of this set of solutions is key to understanding why the T_6 term is necessary in (4.33). We now turn our attention to studying the significance of T_6.
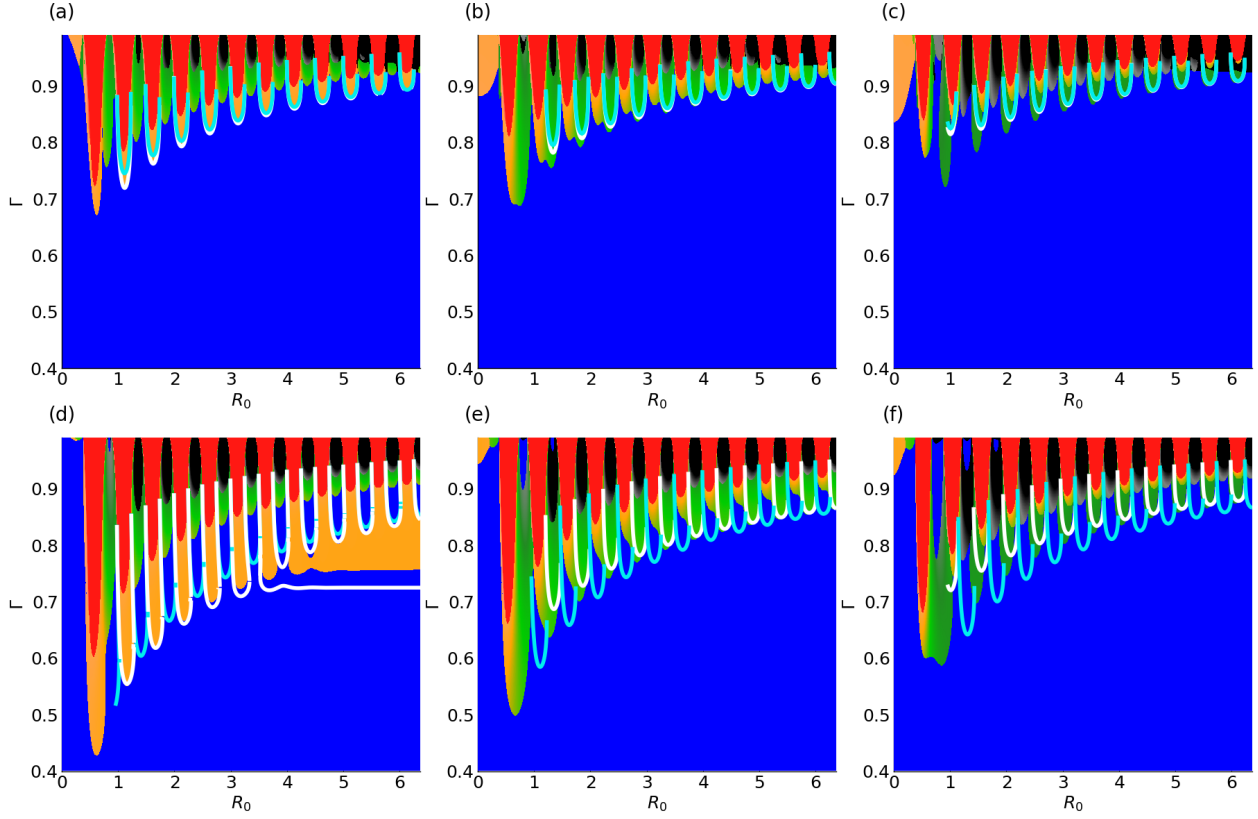
Figure 4.3: The dependence of orbital stability on the particle mass M and force power n. The force power, n, and dimensionless mass, M, are varied across different panels, with $n = 1$ (first column), $n = 4$ (second column), and $n = 9$ (third column), whereas $M = 2.2$ (first row) and $M = 0.14$ (second row). We compare the orbital stability diagrams and the asymptotic stability boundaries computed using all terms in (4.33) up to T_4 (cyan curve) and T_5 (white curve). Both asymptotic stability boundaries work well when $M \approx 2$. However, the phase of the T_4 solution differs completely from the numerically computed stability boundary when $M = 0.14$, yet this behaviour is captured correctly by the T_5 solution. Notably, the T_4 solution (cyan curve) correctly describes the internal non-resonant stability boundaries in (d), despite not capturing the non-resonant instability tongues at smaller radii. The visual convergence of the white curve to the numerically computed stability boundary slows down from the left to right panels, and also from the first row to the second row. This behaviour suggests that the asymptotic results, and thus the accuracy of the predicted locations of the stability tongues, perform worse for higher n and lower Γ, a shortcoming we address and remedy in §4.4.7.

Parameter regimes that necessitate the inclusion of T_6

We consider the extent to which the critical memory of instability predicted by the T_5 and T_6 problems, outside their regime of validity, agrees with the memory of instability derived rigorously in §4.3, and demonstrate that the T_5 solution is qualitatively wrong in the limit as $r_0 \to \infty$. Specifically, we consider the plateau regime, where $\beta = \beta_1 r_0$ and $\beta_1 = O(1)$, and so $e^{-\pi\beta} = e^{-\pi\beta_1 r_0}$ is exponentially small. As $\sigma = \frac{\beta_1}{U}$ and $U = 1 + O\left(\frac{\beta}{r_0}\right)$ from (4.28), $\sigma = \beta_1 + o(1)$. We substitute $\beta_1 = \frac{\beta}{r_0}$ into (4.33), neglect all $o(1)$ terms, and show that β_1 satisfies

$$\frac{(2M+1)(4M-1)}{2} - \frac{\beta_1(5+M+16M^2-4\xi^2)}{2} = 0, \tag{4.36a}$$

$$\frac{(2M+1)(4M-1)}{2} - \frac{\beta_1(5+M+16M^2-4\xi^2)}{2} - \frac{\beta_1^2(-28-11M-32M^2+8\xi^2)}{8} = 0, \tag{4.36b}$$

for the T_5 and T_6 problems respectively.

(4.36) indicates that, for the T_5 problem, β_1, and thus σ, would be uniquely determined from M, which figure 4.2(a) shows is qualitatively incorrect. In addition, the two solutions should only be expected to agree when β_1 is small. We compare the approximate limiting memory obtained from solving (4.36) and the analytical plateau memory obtained from solving (4.21) in figure 4.4. For larger n, the plateaus occur at increasingly high memory, and we observe a decrease in the error between the T_5, T_6 solutions and the asymptotic plateau memory. We rationalise this error by recognising that (4.33) was derived from a series expansion in powers of $\frac{\beta}{r_0} = \frac{\sigma}{U} \sim \sigma$, and the error when truncating this series expansion decreases when σ decreases.

In figure 4.4(c), we see that there are two key differences between the T_5 and T_6 solutions, for $n = -0.5$, namely:

1. The instability tongues predicted by the T_5 solution occur at the wrong orbital radii. This discrepancy occurs because $T_1, T_4, T_5 < 0$ at the true stability boundary for sufficiently small ξ and M. Thus, the balance $T_1 + T_4 \sim -T_5$ is not satisfied by the true stability boundary, which guarantees that the T_5 solution will be incorrect.

2. The T_5 solution plateaus at the wrong value of memory. This observation is supported by figure 4.4(b), where the T_5 approximation for the flat plateau memory of instability is qualitatively incorrect for lower values of n and higher σ.

Figure 4.4(b,c) demonstrates that, although the plateau regime studied in §4.3 is outside the regime of validity of (4.33), it is still important to retain enough terms in (4.33) to ensure that its solution in the limit $\beta = O(r_0)$ still agrees qualitatively with the solution of (4.21). The close relationship between both asymptotic regimes further highlights how the plateau instability forms from the joining of the instability tongues.

We observe that T_1 is responsible for the non-resonant stability tongues. This term vanishes when ξ_0 is an integer, and the non-resonant instability becomes resonant. In this case, we must consider the balance of $F_{i,2}$ against $F_{i,4}, F_{i,5}$ and $F_{i,6}$, and the solution procedure changes.
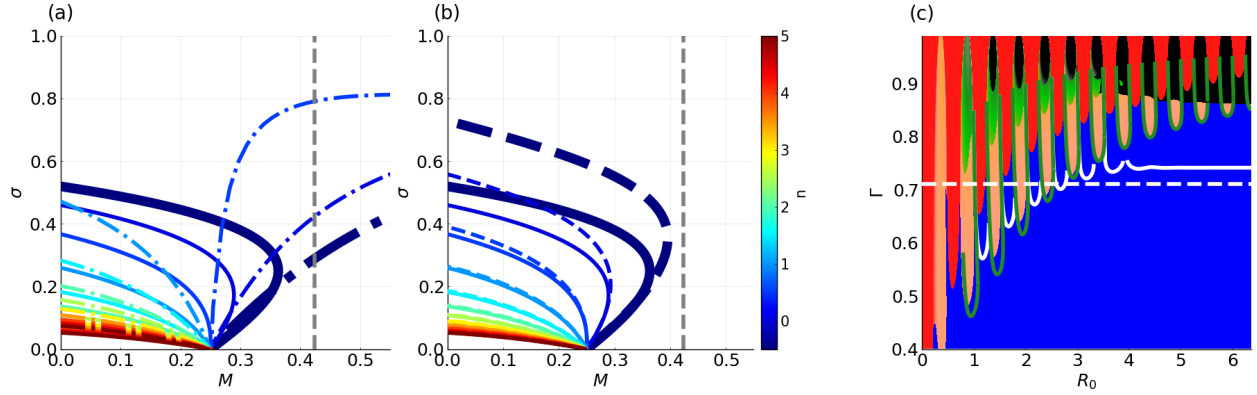
Figure 4.4: (a, b) Comparison between the approximate critical memory of instability (σ, dashed, dot-dashed, (4.36)), and the analytical memory of instability (σ, solid, (4.21)), plotted against the dimensionless mass M, colour-coded by the force index, where $F(r) = -kr^n$. (c) Stability diagram for $M = 0.42$ and $n = -0.5$, and plot the T_5 (white) and T_6 (green) solutions. In (a), we solve (4.36) for β_1, corresponding to the T_5 approximation to the flat plateau instability memory, and remark that the qualitative behaviour of the asymptotic memory of instability is very different from the analytical memory of instability. In (b), we include T_6, and note that agreement improves for larger values of n and lower memory, because, for smaller memory, $\frac{\beta}{r_0}$ is smaller, and the error in the series expansions decreases. We emphasise the analytical and asymptotic memory of instability for $n = -0.5$ in bold in (a, b), and the vertical grey lines in (a, b) intersect the bold curves at the predicted flat plateau memory. Note that at these parameter values, the plateau instability does not actually exist; in (b), the grey line intersects neither bold curve, but intersects the bold curve in (a). This means the T_5 solution has misinferred the existence of a flat plateau, and so the memory of instability has incorrectly plateaued (dashed white, (c)). The white instability tongues in (c) are also predicted to occur at the wrong orbital radii, further motivating the need for T_6, as we develop in the discussion around (4.36).

4.4.6 'Resonant' non-resonant instabilities

We now demonstrate the solution process, in two cases, for when the non-resonant instability frequency, $\omega\sqrt{n+1}$, is an integer multiple of ω, and may thus be regarded as resonant. The two cases considered are $n = 3$ and $n = 8$, whereby the corresponding oscillation frequencies are 2ω and 3ω, respectively. For simplicity, we consider the experimental parameter regime studied by Harris et al. [53] and Liu et al. [66].

Spring power $n = 3$

When $n = 3$ and $\xi_0 = \sqrt{n+1} = 2$, we remark that the oscillation frequencies of the resonant and non-resonant instabilities coincide. From the discussions in §4.4.3, we established that the analysis of the resonant instability proceeds by considering the real part of (4.27), while the analysis of the non-resonant instability proceeds by considering the imaginary part of (4.27). As both types of instabilities merge for $n = 3$, we expect the dominant balance to involve both the real and imaginary parts of (4.32). Substituting $\xi_0 = 2$ into (4.32), we see that

$$F_{r,1} = -\frac{8\mathrm{e}^{-\pi\beta}\sin(r_{b,1})}{r_0}, \quad F_{r,2} = -\frac{2\mathrm{e}^{-\pi\beta}(\cos(r_{b,1}) + 2\beta\sin(r_{b,1}))}{r_0^2}, \quad F_{r,4} = -\frac{4(1+2M)\xi_1}{r_0^4},$$
$$\text{(4.37a)}$$

$$F_{i,1} = 0, \quad F_{i,2} = \frac{\mathrm{e}^{-\pi\beta}(16\beta\cos(r_{b,1}) + 4(2(1-M)+\pi\xi_1)\sin(r_{b,1})}{r_0^2}, \quad F_{i,4} = \frac{(2M+1)(4M-1)}{2r_0^4}.$$
$$\text{(4.37b)}$$

Dropping $F_{r,2}$, as it is asymptotically smaller than $F_{r,1}$, the real and imaginary parts of the stability condition simplify to, respectively,

$$\frac{2\mathrm{e}^{-\pi\beta}\sin(r_b)}{r_0} + \frac{\xi_1(1+2M)}{r_0^4} = o\left(\frac{1}{r_0^4}\right), \tag{4.38}$$

$$\frac{8\mathrm{e}^{-\pi\beta}\left[\sin(r_b)(2-2M+\pi\xi_1) + 4\beta\cos(r_b)\right]}{r_0^2} + \frac{(2M+1)(4M-1)}{r_0^4} = o\left(\frac{1}{r_0^4}\right), \tag{4.39}$$

which we solve simultaneously to plot the asymptotic boundaries in figure 4.5(e). We show that solving for the deviation in ξ from 2 and including $F_{i,2}$ leads to vastly improved accuracy, compared to the leading order asymptotics for $n = 2$ and $n = 4$ presented in figure 3.5, and reproduced in figure 4.5. In addition, our asymptotic approach shows how to merge the 2ω resonant stability boundary and the 2ω 'non-resonant' stability boundary.

We now consider another instance where the non-resonant instability frequency is an integer multiple of the orbital frequency, for which the non-resonant stability boundary does not overlap with a resonant stability boundary.

Spring power $n = 8$

For $n = 8$, the non-resonant instability is a 3ω instability. As the resonant instabilities in the $n = 8$ system are 2ω and 4ω instabilities, the 3ω stability boundary does not overlap
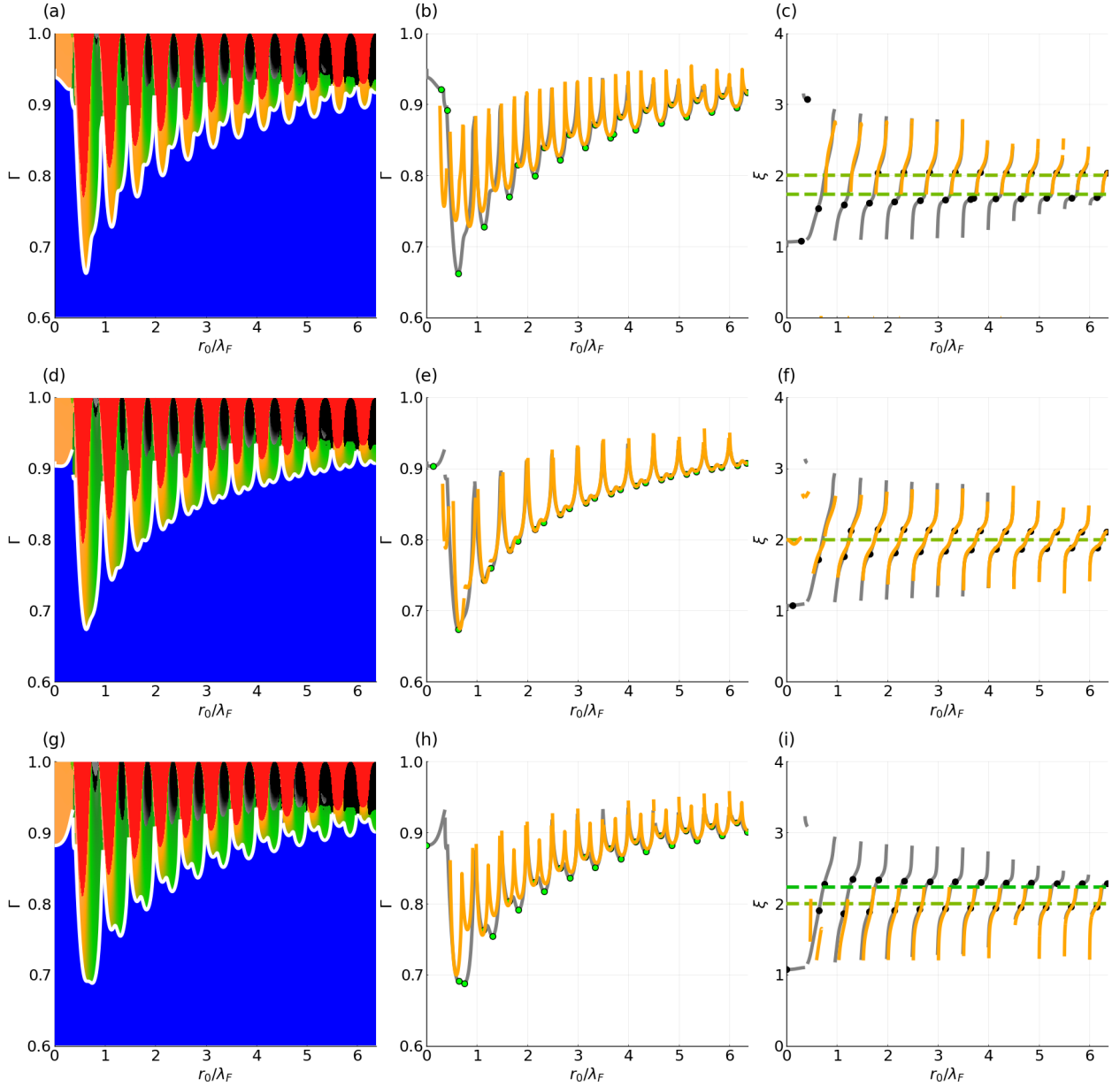
Figure 4.5: Stability diagrams and scaled destabilisation frequencies for $n = 2, 3$ and 4, and $M = 2.2$. Top row: $n = 2$. Middle row: $n = 3$. Bottom row: $n = 4$. The left column contains stability diagrams with numerically tracked boundaries (white), and the color scheme is the same as in figure 4.1. The middle column contains plots the memory of instability, with numerical boundaries (grey) and asymptotic boundaries (orange dashed). Green dots represent the most unstable radii, where instabilities arise at lowest memory. The right column plots the destabilisation frequencies, with numerical results (grey) and asymptotic results (orange). The horizontal dashed lines represent the 2ω and $\sqrt{n+1}\omega$ instabilities, and the black dots correspond to the scaled destabilisation frequencies of the green dots in the middle column. This plot is a reproduction of figure 3.5, with the asymptotic memory of instability and instability frequency for $n = 3$ filled in. We comment on how the asymptotic stability boundaries in the second and third columns agree much better with the numerical boundaries for $n = 3$, than for $n = 2$ and $n = 4$, which arises because the $n = 3$ asymptotic equation required a higher order expansion than that solved for $n = 2$ and $n = 4$.
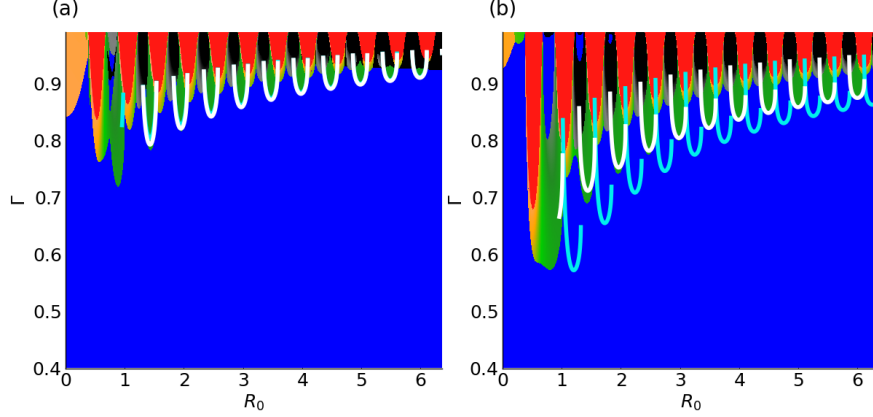
Figure 4.6: Stability diagram for (a) $n = 8$ and (b) $M = 2.2$ and 0.14. Stability of circular orbits are given by the same color scheme as in figure 4.1. T_4 (white) and T_5 solutions of (4.40b) for the critical memory of instability are both shown. Like in the discussion in §4.4.5 and figure 4.3, the T_4 solution performs well for larger M, and produces out-of-phase solutions for smaller M, and the T_5 solution is needed. The T_6 solution is not necessary, because n is sufficiently large, and T_5 is of the opposite sign to T_4 in (4.40b), and so T_5 can balance $T_1 + T_4$.

with any of them. We recall that in §4.4.4, if ξ is an odd integer, then F_1 cannot balance F_3. Similarly, if ξ is an odd integer, $F_{r,1} = 0$. In §4.4.6, we saw that we balanced $F_{r,1}$ with $F_{r,4}$; now that $F_{r,1} = 0$, the stability condition will be quite different. Thus, it is the parity of $\xi_0 = \sqrt{n+1}$ that sets the $n = 8$ case apart from $n = 3$. We first consider the real part of the stability function to determine if we can neglect ξ_1.

We substitute $\xi_0 = 3$ into (4.32), and note that as we are in the experimental regime, we only need to retain terms up to $F_{r,4}$, leading to

$$F_{r,1} = F_{r,2} = 0, F_{r,4} = -\frac{4(1 + 2M)\xi_1}{r_0^4}. \tag{4.40a}$$

This indicates that $F_{r,4}$ must be balancing the neglected $O\left(\frac{e^{-\pi\beta}}{r_0^3}\right)$ terms. As $F_{r,4} = O\left(\frac{\xi_1}{r_0^4}\right)$, the vanishing of $F_{r,1}$ and $F_{r,2}$ indicate $\xi_1 = O(r_0 e^{-\pi\beta}) = o(1)$, and that when considering the imaginary part of the stability problem, we may neglect ξ_1 entirely. As $\sin(\pi\xi_0) = 0, F_{i,1} = 0$, and so we must consider $F_{i,2}$ in the stability problem. Requiring ξ_0 to be an odd integer, and substituting $\xi_1 = 0$ into $F_{i,2}, F_{i,4}$ and $F_{i,5}$, we find

$$-\frac{16\beta(\xi_0^2 - 1)e^{-\pi\beta}\cos(r_{b,1})}{\xi_0^2 r_0^2} + \frac{(4M-1)(1+2M)}{2r_0^4} - \frac{\beta(5 + M + 16M^2 - 4\xi_0^2)}{2r_0^5} = o\left(\frac{1}{r_0^5}\right), \tag{4.40b}$$

which we solve for the instability memory in figure 4.6. We comment that the implicit nature of this equation once again explains why the spacings between the non-resonant stability tongues differs from that of the resonant stability tongues.

A natural question to ask is whether the 1ω instability shown in figure 4.2(c) can be studied using a similar formalism, as if $n = 0, \xi_0 = 1$, and ξ_0 is also odd here. Unfortunately,

109

we find that in this case, the $O\left(\frac{\mathrm{e}^{-\pi\beta}}{r_0^2}\right)$ term in (4.40b) vanishes identically, indicating that the dominant balance is actually between $F_{i,3}$ and $F_{i,4}$, showing that our formalism is unable to describe this specific case. We must thus content ourselves with identifying the two plateaus in figure 4.2(c).

Figure 4.5 and 4.6 show that our prediction for the location of the first few stability tongues for $n = 3$ and $n = 8$ appear to be much better than when $n = 2$ and $n = 4$. The main difference between our approaches for $n = 2, 3, 4$ and 8 is that for $n = 3$ and $n = 8$, we were forced to consider $F_{i,2}$ in the imaginary stability condition, because $F_{i,1} = 0$. We now consider how to use $F_{i,2}$ in the stability condition, without needing to solve for ξ_1.

4.4.7 Improving the prediction for the location of the stability tongues

We remark that when ξ is not an integer, the dominant balance in the imaginary part is primarily between $F_{i,1}$ and $F_{i,4}$; $F_{i,2}$ is a higher-order term that we have neglected until now. We now argue how to augment (4.33) with a simple $O\left(\frac{\mathrm{e}^{-\pi\beta}}{r_0^2}\right)$ term, while avoiding having to solve for ξ_1.

From §4.4.6 and 4.4.6, we saw that the $O\left(\frac{\mathrm{e}^{-\pi\beta}}{r_0^2}\right)$ terms became relevant when $\sin(\pi\xi_0) = 0$. We also observe that the predicted locations of the stability tongues in figure 4.3 are worst for larger n and smaller Γ, corresponding to larger ξ_0 and β. These observations imply that we should include a $\frac{\beta\mathrm{e}^{-\pi\beta}\cos(\pi\xi_0)}{r_0^2}$ term, which would become more important when $\sin(\pi\xi_0)$ is small. From (4.32), we see that, for larger ξ_0, the largest term in $F_{i,2}$ proportional to $\cos(\pi\xi_0)$ is $\frac{16\mathrm{e}^{-\pi\beta}}{r_0^2}\cos(r_{b,1})\cos(\pi\xi_0) = \frac{2\beta\xi_0\cot(\pi\xi_0)\cot(r_{b,1})}{r_0}F_{i,1}$, which becomes more relevant for larger ξ_0 and β. Appending this term to the right hand side of (4.33) gives the following modified stability condition

$$T_1 + \frac{16\mathrm{e}^{-\pi\beta}}{r_0^2}\cos(\pi\xi_0)\cos(r_{b,1}) + T_4 + T_5 = 0, \tag{4.41}$$

where T_1, T_4 and T_5 are as in (4.33), and we include T_5 for superior numerical agreement. We plot the solution of (4.41) in figure 4.7 for various n in the experimental parameter regime.

This concludes our study of both the resonant and non-resonant instabilities. We now combine all of our asymptotic results to create composite boundaries for the various parameter regimes considered in this paper, and plot the results in figure 4.8. Numerically, we find that the modified T_5 solution, as in (4.41), produces the best overall results, except when the T_6 solution is needed for small n. At each value of r_0, we solve for all of the possible instabilities, and then choose the instability occurring at lower memory. An exception is in the plateau regime in 4.8(d), where there exist two non-resonant boundaries and one resonant boundary for large r_0.

4.5 Discussion

We have examined the stability of circular orbits in the generalised pilot-wave system with a power-law central force, and extended the asymptotic framework of chapters 2 and 3 to give
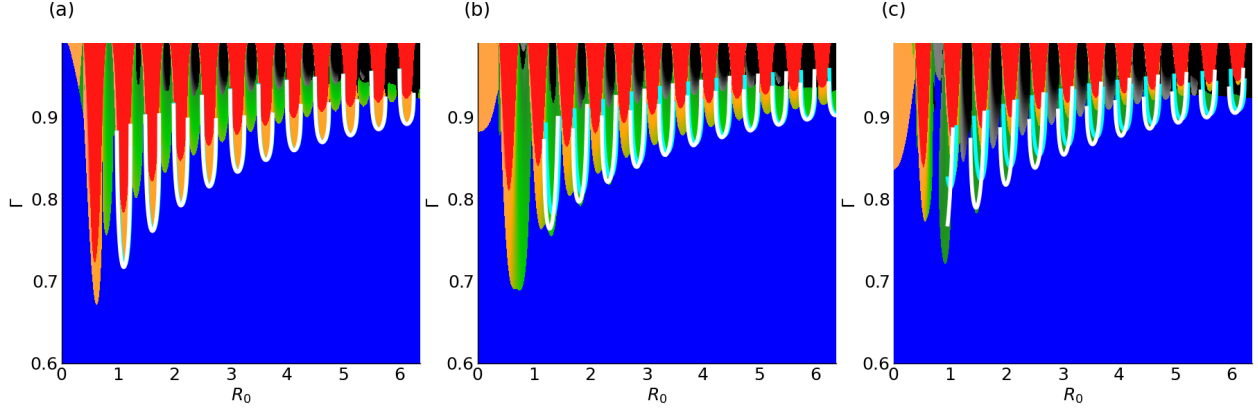
Figure 4.7: Orbital stability diagrams for (a) $n = 1$, (b) $n = 4$, and (c) $n = 9$, with $M = 2.2$ in all panels, comparing the T_5 solution (cyan curve) computed by retaining all terms from T_1 to T_5 in (4.33), and the modified T_5 solution (white curve) computed from equation (4.41) for different values of force power n. Notably, the inclusion of the additional $O\left(\mathrm{e}^{-\pi\beta}r_0^{-2}\right)$ term (white curve) has little impact when $n = 1$ and $n = 4$, but greatly improves the numerical agreement relative to the cyan curve for smaller radii when $n = 9$. In this case, the asymptotic stability tongues are now more closely aligned with the numerically computed stability tongues, justifying the inclusion of the $O\left(\mathrm{e}^{-\pi\beta}r_0^{-2}\right)$ term.

a more complete description of the non-resonant instability. Our numerical investigations have revealed a plethora of new dynamical behaviour in the generalised pilot-wave system, including plateau instabilities, for which large circular orbits are uniformly unstable for an interval of the memory parameter, quantised stability islands, for which circular orbits destabilise when the memory is either increased or decreased, and the subtle interplay between resonant and non-resonant instabilities for certain potentials. All of these phenomena are explained using our novel asymptotic framework, which encompasses all prior results established in the experimental regime as special cases. In demonstrating the importance of the non-resonant instability in all of these new features, we show that non-resonant instabilities can play a larger role than resonant instabilities in orbital quantisation when particle inertia is relatively weak.

Our study has demonstrated that the behaviour of stability boundaries in the generalised pilot-wave system becomes vastly more complex for lower particle inertia. In the experimental parameter regime considered in chapter 3, the non-resonant instability dominates different resonant instabilities for depending on the curvature of the confining potential, with the non-resonant stability boundaries being structurally similar to resonant instabilities. Specifically, the shape and the radial separation between the stability tongues was similar for both resonant and non-resonant instabilities, with all instability tongues being functions of the orbital radius. However, we demonstrate that the shapes of the non-resonant instability tongues change drastically for smaller particle inertia. Specifically, the instability tongues widen for smaller values of the memory, ultimately merging to form an instability plateau for sufficiently large orbital radius. Consequently, the central force causes large circular orbits to destabilise in a manner very distinct to that of free walkers; the instability frequency of large circular orbits is inversely proportional to the orbital radius. In addition, the flatness
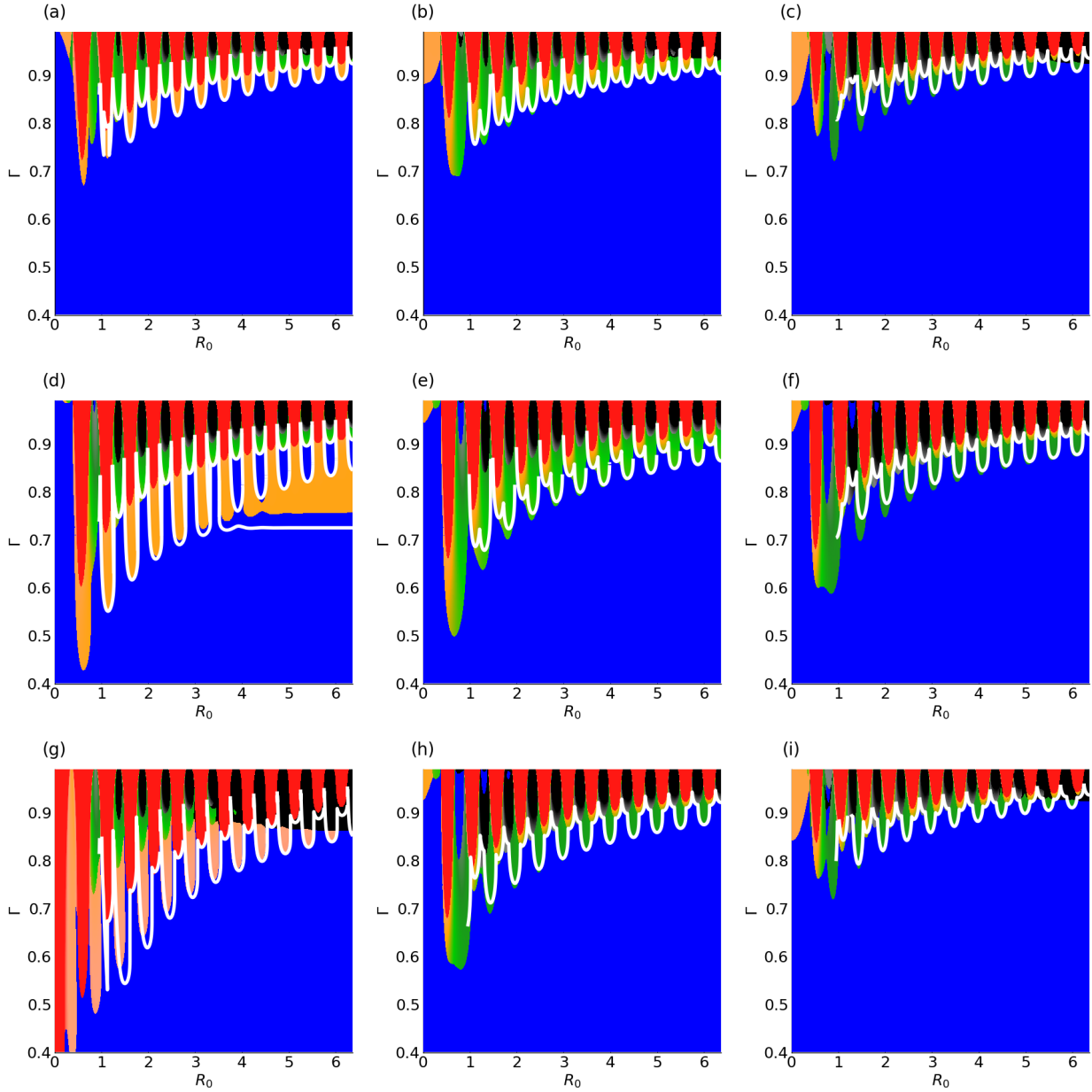
Figure 4.8: Stability diagrams with asymptotic stability boundaries in white, for (a) $(n, M) = (1, 2.2)$, (b) $(4, 2.2)$, (c) $(9, 2.2)$, (d) $(1, 0.14)$, (e) $(4, 0.14)$, (f) $(9, 0.14)$, (g) $(-0.5, 0.42)$, (h) $(8, 0.14)$, (i) $(8.2.2)$. For each plot, we solve (4.41) for the non-resonant instability boundary, and (4.26) for the resonant instability boundary, except in (g), where we include T_6 in (4.41). For any r_0, we plot the lowest memory at which instability occurs. An exception is (d), where we plot all of the stability boundaries for larger r_0. We observe the presence of additional instability islands in $(e), (f), (h)$ and (i) for small orbital radius and high memory, where $\Gamma \approx 0.8 - 0.9$, and $r_0/2\pi \approx 1 - 2$.

of the instability plateau destroys orbital quantisation for a range of memory. Even more strikingly, we show that multiple stability plateaus may exist; circular orbits are then only unstable between the two plateaus, and are stable again at higher memory.

We also show that the non-resonant instability plateau gives rise to a new type of orbital quantisation. Specifically, the instability plateau is one of two types of non-resonant instabilities occurring at low particle inertia and large orbital radius; the second type is an extension of the non-resonant instabilities studied in chapter 3. For this type of stability boundary, since circular orbits are stable for memory higher than the non-resonant critical memory of instability, we demonstrate that increasing memory can restabilise circular orbits. We then observe that many quantised orbits exist inside these stability islands, representing a new paradigm for orbital quantisation, driven by a single instability mechanism.

Our new mathematical formulation is critical to understanding all of these phenomena. Specifically, we can understand the onset of the plateau regime, the quantised islands, and the parameter regimes at which these occur, all from careful analysis of equations (4.32) and (4.33). We demonstrated that different dominant balances are responsible for the plateau and the quantised islands, and showed that the plateau regime is a limiting case of (4.33). To compare our present mathematical formulation with that of Liu *et al.*[66], the Hankel expansion of the complex-order Bessel functions presented there is an expansion in $\beta^2/r_0 \sim \sigma^2 r_0$, which we clearly see in figure 4.8(d) grows in the plateau regime, and cannot explain the onset of plateaus. In contrast, equation (4.33) arises formally from an expansion in σ, and thus we expect it to be valid to describe the non-resonant instabilities outside the plateau regime, and to produce numerically satisfactory results for the onset of plateaus at higher memory, a statement which is supported by figure 4.4(b). From figure 4.4, we showed that understanding the plateau regime is critical to understanding the non-resonant instability boundaries, highlighting that the present formulation is essential for understanding these new instabilities in this generalised pilot-wave system.

In §4.4.7, we showed that adding a single term of size $O\left(r_0^{-2}\mathrm{e}^{-\pi\beta}\right)$ to equation (4.33) vastly improves the prediction of the locations of the stability tongues for higher values of the spring power, n, as is evident in figure 4.7. As this extra term is $O\left(\frac{2\beta\xi_0}{r_0}F_{i,1}\right)$, we see that the shifting of the stability tongues is accentuated for lower memory, corresponding to larger β, and more steeply varying external forces, corresponding to larger $\xi_0 = \sqrt{n+1}\omega$. Hence, the location of the non-resonant stability tongues is a balance between the geometric constraint imposed by the pilot-wave, and the spatial variation of the external wave field. The lack of movement of the resonant stability tongues further suggests that the resonant instabilities are due to the quasi-monochromaticity of the wave field, and the non-resonant instabilities are driven by the external force and the relative constancy of the particle speed. When the non-resonant stability tongues change radius, they may no longer dominate higher-order resonant instabilities, allowing 4ω instabilities to appear at the onset of instability. Such instabilities were observed by Kurianski et al. [60] for a linear central force in a wave kernel with spatial damping. We may thus hypothesise the existence of higher order resonant instabilities for higher n, or for a more rapidly varying external force.

In figure 4.8, we see that at lower values of M, and for larger values of n, a new type of stability island appears for much higher memory and lower orbital radius, potentially giving rise to yet another type of orbital quantisation. This phenomenon, which represents another

paradigm for orbital quantisation, will be addressed in the next chapter. We emphasise, however, how the quantised non-resonant islands appeared for lower particle inertia, further suggesting that quantum-like behaviour appears to be most common in the high-memory, low-inertia limit.

Chapter 5

Sharp quantisation in a classical pilot-wave system

5.1 Introduction

Orbital quantisation [43, 52] is said to arise in pilot-wave hydrodynamics because finite bands of orbital radii are unstable at a given memory. The spacing between the stable orbits is approximately half the Faraday wavelength for sufficiently large radius (see chapters 2 and 3). This form of orbital quantisation is limited in that typically only two or three stable quantised orbital states are accessible for the same value of the system parameters, and vanishes for larger orbital radius (see chapter 7). Furthermore, the intervals of accessible stable radii increases for larger orbits, essentially 'smoothing' the picture of orbital quantisation. For the analogy to quantum mechanics to be more direct, there would ideally be an infinite set of stable quantised orbits contained within narrow intervals of the orbital radius, all accessible with the same system parameters.

In this chapter, we demonstrate that such a scenario is possible in the low-inertia, infinite-memory limit for particle motion confined by a linear spring force, which we explore using the generalised pilot-wave framework [13]. In this setting, we prove that the infinite set of stable orbital radii are confined within infinitesimally narrow intervals at large orbital radius, with the stability tongues in the orbital stability diagram being self-similar in form. In particular, we demonstrate that the stability of the orbits hinges on the subtle interplay of two resonance mechanisms, namely resonance of the perturbation frequency with the orbital frequency, and the resonance of the perturbation wavelength with the wavelength of the pilot wave, as characterised by in-line speed oscillations along the particle path [35]. We refer to this new paradigm of a more quantum-like orbital quantisation in classical pilot-wave dynamics as 'sharp quantisation'.

This chapter is organised as follows. In §5.2, we characterise pilot-wave dynamics in the high-memory limit, for which the instantaneous pilot wave is well approximated by its mean [33]. In particular, we establish several heuristic arguments for explaining the onset of a sharp quantisation in this limit. We make these arguments more robust in §5.3, developing a systematic asymptotic framework for orbital stability in the high-memory, low-inertia limit. Finally, in §5.4, we discuss our results in the wider context of orbital quantisation.

We consider the generalised pilot-wave framework introduced in §4.2, where we restrict our attention to a linear central force, with $n = 1$. The non-dimensional parameters of interest are summarised in table 4.1. Notably, unlike the hydrodynamic system, we may vary the system parameters, M, σ and k arbitrarily. In this chapter, the parametric generalisation leads to new dynamics inaccessible in experiments. Before delving into the complexities of the full orbital stability problem, we consider the effect of high memory on pilot-wave dynamics, which will motivate the necessary asymptotic limits. We begin by considering the behaviour of the force balance in (4.4a) at high memory, where we expect quantum-like behaviour to be possible.

5.2 Physical picture: pilot-wave dynamics at high memory

We develop a physical picture for orbital pilot-wave dynamics in the high-memory limit, in which the instantaneous wave field is well approximated by its mean. We first investigate the radial force balance in this limit (§5.2.1), paying particular attention to the permissible orbital radii. We then consider the tangential force balance in §5.2.2, which we use to establish the resonance between the instability frequency and the orbital frequency. We develop a rigorous asymptotic theory for this physical picture in §5.3.

5.2.1 Radial force balance

At sufficiently high memory, the pilot-wave decays very little over an orbital period. Thus, we can approximate the instantaneous orbital wave field by its average over one orbital period [33, 93]. By denoting the spatial coordinate as $\boldsymbol{x} = R(\cos(\Theta), \sin(\Theta))$ in plane polar coordinates, the mean wave field, $\bar{h}$, generated by a circular orbit of radius r_0, may be expressed [33, 93]

$$\bar{h}(R, \Theta, r_0) = \frac{\mathrm{J}_0(r_0)\mathrm{J}_0(R)}{\sigma}. \tag{5.1}$$

By substituting $\bar{h}$ in place of h in the non-dimensionalised form of the particle trajectory equation(4.3), we find that the radial force balance takes the form

$$-Mr_0\omega^2 = -\frac{\partial \bar{h}}{\partial R}(r_0, \Theta, r_0) - kr_0, \tag{5.2a}$$

which we express as

$$-Mr_0\omega^2 = f_r, \quad \text{where} \quad f_r = \frac{\mathrm{J}_0(r_0)\mathrm{J}_1(r_0)}{\sigma} - kr_0 \tag{5.2b}$$

is the radial force applied by the mean wave field and the linear spring. An equivalent form can also be obtained by applying the large memory expansions of Oza et $al.$ [79] directly to equation (4.4a). We note that the mean wave force diverges in the high-memory limit,

corresponding to $\sigma \to 0$. To derive a similar high-memory equation for the tangential force balance, we apply Oza's large memory expansions to yield

$$1 - r_0^2 \omega^2 = \mathrm{J}_0^2(r_0) + O(\sigma^2), \tag{5.3}$$

which does not depend strongly on the memory. Thus, we begin by studying the mean radial force balance (5.2).

Permissible orbital radii

The mean wave force acts effectively as a self-potential, an axisymmetric self-generated potential interacting with the particle. The local wave field depends on (i) the radius, r_0, of the orbit generating the wave field and (ii) the radial position, R, at which the wave field is evaluated. As we are primarily interested in small perturbations to circular orbits, we consider the direction of the radial force on a radial perturbation of the circular orbit. Specifically, we write $R = r_0 + \Delta R$, while holding the orbital radius constant. We find that the corresponding change in the radial wave force, denoted Δf_r, takes the form

$$\Delta f_r = \Delta R \left(-k + \frac{\mathrm{J}_0(r_0)\mathrm{J}_1'(r_0)}{\sigma} \right) + O(\Delta R^2). \tag{5.4}$$

By using (5.2) to eliminate the spring constant, k, and then applying Bessel function identities [100], we obtain (to leading order in ΔR)

$$\frac{\Delta f_r}{\Delta R} = -\frac{\mathrm{J}_0(r_0)\mathrm{J}_2(r_0)}{\sigma} - M\omega^2. \tag{5.5}$$

For stable circular orbits to be possible, the wave force should pull inwards on outwards radial perturbations, whilst pushing outwards on inwards radial perturbations. Thus, our physical picture predicts that

$$-\frac{\mathrm{J}_0(r_0)\mathrm{J}_2(r_0)}{\sigma} - M\omega^2 < 0$$

is a necessary condition for orbital stability in the high-memory limit. For large orbital radius, we may use Hankel expansions for large argument [100] to show that

$$\mathrm{J}_0(r_0)\mathrm{J}_2(r_0) = -\frac{2\sin^2\left(\frac{\pi}{4} + r_0\right)}{\pi r_0} + O\left(\frac{1}{r_0^2}\right). \tag{5.6}$$

We conclude that $\frac{\Delta f_r}{\Delta R} < 0$ is impossible for sufficiently large dimensionless mass, $M > 0$. Indeed, this argument suggests that we must consider the limit of vanishing inertia, $M = 0$, for arbitrary large circular orbits to be stable in the high-memory limit. In this limit, the orbital radius of stable circular orbits must then satisfy the condition

$$\mathrm{J}_0(r_0)\mathrm{J}_2(r_0) > 0. \tag{5.7}$$

The set of allowed orbital radii is a union of countably many infinitely-thinning disjoint intervals (see figure 5.1), hinting at the possibility of infinitely many sharply quantised orbital
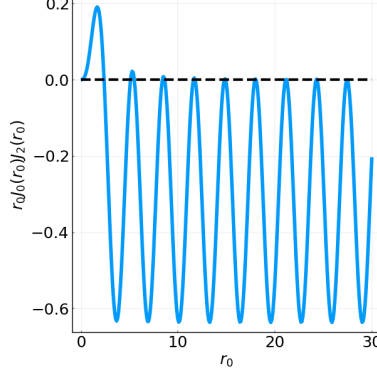
Figure 5.1: Heuristic for establishing the existence of stable circular orbits in the high-memory limit. We present the dependence of $r_0 J_0(r_0) J_2(r_0)$ on the orbital radius r_0. The intervals in which $J_0(r_0)J_2(r_0) > 0$, for which our heuristic predicts that stable circular orbits emerge (see (5.7)), become increasingly narrow for larger circular orbits.

radii for large r_0. Curiously, the inequality (5.7) hints that circular orbits may be stabilised by the mean wave field, even in the limit of infinite memory, which begs the following question: why would instability arise at lower memory? To answer this question, we consider how corrections to the mean wave field affect changes in the radial force, $\Delta f_r / \Delta R$, as defined in equation (5.5).

Onset of instability at lower memory

We first write $x_p(t) = r(t)(\cos(\theta(t)), \sin(\theta(t)))$ and project the integro-differential equation (4.3) into its radial and tangential components, giving [79]

$$M(\ddot{r} - r\dot{\theta}^2) + \dot{r} = \int_{-\infty}^{t} \frac{J_1(\mathfrak{D}(t,s))}{\mathfrak{D}(t,s)}[r(t) - r(s)\cos(\theta(t) - \theta(s))]e^{-\sigma(t-s)}\,ds - kr, \qquad (5.8a)$$

$$M(2\dot{r}\dot{\theta} + r\ddot{\theta}) + r\dot{\theta} = \int_{-\infty}^{t} \frac{J_1(\mathfrak{D}(t,s))}{\mathfrak{D}(t,s)}r(s)\sin(\theta(t) - \theta(s))e^{-\sigma(t-s)}\,ds, \qquad (5.8b)$$

where $\mathfrak{D}(t,s) = |\boldsymbol{x}_p(t) - \boldsymbol{x}_p(s)|$ denotes the distance between the particle's position at times t and $s < t$, namely

$$\mathfrak{D}(t,s) = \sqrt{r^2(t) + r^2(s) - 2r(t)r(s)\cos\big(\theta(t) - \theta(s)\big)}.$$

We proceed by recasting (5.8a) in the form

$$M(\ddot{r} - r\dot{\theta}^2) + \dot{r} = \int_{-\infty}^{t} w_r(r(t), r(s), \theta(t) - \theta(s), t - s)\,ds - kr, \qquad (5.9)$$

where w_r may be understood as the contribution to the radial wave force when integrating over the particle's history. The steady-state circular orbit force balance then can be rewritten as

$$-Mr_0\omega^2 = \int_0^{\infty} w_r(r_0, r_0, \omega t, t)\,dt - kr_0. \qquad (5.10)$$

In the function $w_r = w_r(x_1, x_2, x_3, x_4)$, whose integral represents the radial wave force, the first argument represents the dependence of the wave force on the particle's current radial position, while the second argument represents the dependence of the wave force on the particle's past radial position. In a similar manner to §5.2.1, we thus wish to evaluate $\int_0^\infty \frac{\partial w_r}{\partial x_1}(r_0, r_0, \omega t, t)\, dt$, corresponding to the change in the radial wave force due to a perturbation in the particle's position, keeping the particle's history constant. In appendix D.1, we show that, in the limit of vanishing inertia ($M = 0$), the finite-memory correction to $\frac{\Delta f_r}{\Delta R}$ satisfies

$$\frac{\Delta f_r}{\Delta R} = -k + \int_0^\infty \frac{\partial w_r}{\partial x_1}(r_0, r_0, \omega t, t)\, dt = -\frac{\mathrm{J}_0(r_0)\mathrm{J}_2(r_0)}{\sigma} + c_1 r_0 \sigma + O(\sigma^2), \tag{5.11}$$

where c_1 is a positive quantity that oscillates with r_0, and satisfies $0 < c_1 < \frac{9}{2}$. The set of permissible orbital radii in §5.2.1, satisfying $\mathrm{J}_0(r_0)\mathrm{J}_2(r_0) > 0$, can be seen as a leading order approximation to the condition $\frac{\Delta f_r}{\Delta R} < 0$ in (5.11). Furthermore, the $O(\sigma)$ term in (5.11) can be seen as the effects of perturbations of the instantaneous wave field from its mean, occurring due to the decay of the pilot wave. As $c_1 > 0$, we conclude that $\frac{\Delta f_r}{\Delta R} > 0$ for sufficiently large σ, where σ may still be sufficiently small for (5.11) to be valid. This suggests that the quantised circular orbits are expected to decay due to the influence of perturbations to the mean wave field, and that the mean wave field is responsible for the stability of these orbits. In addition, it suggests a scaling for the memory of instability, namely $\sigma^2 \propto \frac{\mathrm{J}_0(r_0)\mathrm{J}_2(r_0)}{r_0}$.

The radial force balance motivated why it might be necessary to consider the zero-inertia limit ($M = 0$) for stable circular orbits to exist at large orbital radius. In addition, it provides a restriction on the allowed orbital radii of these quantised circular orbits in terms of the response of the mean wave field to perturbations. We now consider the tangential force balance, to see what can be learned in the high-memory limit.

5.2.2 Tangential force balance

As the mean wave field exhibits radial symmetry [33, 93], we must take a different approach to establish the contribution of the orbital wave field to the particle propulsion via the tangential force balance. We first express the wave field, h, in the form

$$h(\boldsymbol{x}, t) = \int_{-\infty}^{t} \mathrm{J}_0(|\boldsymbol{x} - \boldsymbol{x}_p(s)|)\mathrm{e}^{-\sigma(t-s)}\, ds, \tag{5.12}$$

and consider a particle at location $\boldsymbol{x} = R(\cos(\Theta), \sin(\Theta))$ on a wave field generated by a past circular trajectory of the form $\boldsymbol{x}_p(s) = r_0(\cos(\omega s), \sin(\omega s))$. Using Graf's addition theorem [1], we can reduce h to [65, 66]

$$h(\boldsymbol{x}, t) = \sum_{n=-\infty}^{\infty} \frac{\mathrm{J}_n(R)\mathrm{J}_n(r_0)\mathrm{e}^{in(\omega t - \Theta)}}{in\omega + \sigma}, \tag{5.13}$$

which represents a weighted sum of wave modes, with the orbital wave field rotating with the moving particle. We note that the mean wave field [33, 93] is obtained from (5.13) by

taking the limit as $\sigma \to 0$, and retaining the dominant term (which arises from the $n = 0$ term in the infinite sum). The wave force is proportional to the gradient of the wave field, which yields

$$\nabla h(\boldsymbol{x}, t) = \hat{\boldsymbol{e}}_{\boldsymbol{r}} \sum_{n=-\infty}^{\infty} \frac{\mathrm{J}_n'(R)\mathrm{J}_n(r_0)\mathrm{e}^{in(\omega t - \Theta)}}{in\omega + \sigma} - \frac{\hat{\boldsymbol{e}}_{\theta}}{R\omega} \sum_{n=-\infty}^{\infty} \frac{in\omega \mathrm{J}_n(R)\mathrm{J}_n(r_0)\mathrm{e}^{in(\omega t - \Theta)}}{in\omega + \sigma}. \quad (5.14)$$

In the high-memory limit (corresponding to $\sigma \to 0$), the tangential wave force acting on the particle, found by setting $R = r_0$ and $\Theta = 0$, is given by

$$-\hat{\boldsymbol{e}}_{\boldsymbol{\theta}} \cdot \nabla h(\boldsymbol{x}, t) = \frac{1}{r_0\omega} \sum_{n=-\infty}^{\infty} \mathrm{J}_n^2(r_0)\mathrm{e}^{in\omega t} + O(\sigma). \quad (5.15)$$

In the infinite-memory limit, we can thus decouple the tangential wave force into infinitely many wave modes, where the Fourier amplitudes are given by $\mathrm{J}_n^2(r_0)/U$, where $U = r_0\omega$ is the orbital speed. This decoupling indicates that, at the onset of instability, the wave mode corresponding to maximum force is the wave mode n_*, where n_* maximises $\mathrm{J}_n^2(r_0)$ over the integers $n \geq 0$ (for fixed r_0). We thus speculate that, when the circular orbits do destabilise, they do so via a resonant instability, with the destabilisation frequency, $n_*\omega$, being an integer multiple of the orbital frequency ω.

5.3 Mathematical modelling

To verify our deductions made from considering the orbital wave field in the high-memory limit, we turn now to the full stability formulation to rigorously characterise orbital stability in the high memory limit. We outline the stability framework in §5.3.1 and visualise the numerical results in §5.3.2, revealing bounded stability regions in the high-memory, low-inertia limit similar to those envisaged in §5.2. We then develop a systematic asymptotic framework in for characterising the stability boundaries in §5.3.3, which we use to establish an equation for the instability frequency (§5.3.4), whose solution we specify by demanding the memory along the instability boundary is maximised (§5.3.5).

5.3.1 Linear stability analysis

Orbital stability is characterised by analysing the linear growth rates of general perturbations from circular orbits, which are not restricted to radial perturbations, as considered in §5.2.1. We follow the framework introduced by Oza et al. [79], and developed in chapters 2 to 4. As demonstrated in §4.2.3, the asymptotic growth rates of perturbations, s, of linear perturbations correspond to the roots of $\mathscr{F}(s) = \mathscr{A}(s)\mathscr{D}(s) + \mathscr{B}(s)\mathscr{C}(s)$.

The stability coefficients $\mathscr{A}, \mathscr{B}, \mathscr{C}$ and $\mathscr{D}$ and the tangential force balance take the sim-

plified form, as in (4.10) with $n = 1$,

$$\mathscr{A}(s) = Ms^2 + \frac{2}{r_0\omega}\left(\frac{\mathrm{i}}{r_0} - f_{01}(\beta, r_0)\right) + \frac{1}{\omega}\left[f_{11}(\eta, r_0) - f_{00}(\beta, r_0)\left(1 + \frac{\beta\eta}{r_0^2}\right)\right], \quad \text{(5.16a)}$$

$$\mathscr{B}(s) = 2M\omega s - \frac{\mathrm{i}s}{r_0^2\omega^2} + \frac{1}{r_0\omega}\left[-\beta f_{01}(\beta, r_0) + \eta f_{01}(\eta, r_0)\right], \quad \text{(5.16b)}$$

$$\mathscr{C}(s) = 2M\omega s + 2\omega - \frac{\mathrm{i}s}{r_0^2\omega^2} + \frac{1}{r_0\omega}\left[\beta f_{01}(\beta, r_0) + \eta f_{01}(\eta, r_0)\right], \quad \text{(5.16c)}$$

$$\mathscr{D}(s) = Ms^2 + 2s + \frac{\eta}{r_0^2\omega}\left[\beta f_{00}(\beta, r_0) - \eta f_{00}(\eta, r_0)\right], \quad \text{(5.16d)}$$

where we define the parameters $\beta = \sigma/\omega$ and $\eta = (\sigma + s)/\omega$, and the auxiliary functions

$$f_{ab}(\eta, r_0) = \pi \operatorname{csch}(\pi\eta)\frac{\mathrm{d}^a}{\mathrm{d}r_0{}^a}(\mathrm{J}_{-\mathrm{i}\eta}(r_0))\frac{\mathrm{d}^b}{\mathrm{d}r_0{}^b}(\mathrm{J}_{\mathrm{i}\eta}(r_0)) \quad \text{for } a, b \in \{0, 1\}. \quad \text{(5.17)}$$

In addition, the orbital speed is prescribed by the tangential force balance

$$1 - r_0^2\omega^2 = \beta f_{00}(\beta, r_0), \quad \text{(5.18)}$$

The orbital solution is unstable if there are any roots, s, of $\mathscr{F}$ satisfying $\operatorname{Re}(s) > 0$. Denoting s_* as the unstable root with largest real part, the instability is monotonic if $\operatorname{Im}(s_*) = 0$ and oscillatory otherwise. $\mathscr{F}$ has a trivial eigenvalue at 0, corresponding to rotational invariance of the orbital motion. We denote the stability problem by $\mathscr{G} = 0$, where

$$\mathscr{G}(s) = \frac{\mathscr{A}(s)\mathscr{D}(s) + \mathscr{B}(s)\mathscr{C}(s)}{s}. \quad \text{(5.19)}$$

As in §4.2.3, the stability problem can be expressed solely in terms of the tangential force balance (5.18), and the stability condition (5.19). We apply the method of Delves and Lyness [27] to find the roots of $\mathscr{G}$ in the domain over which $\mathscr{G}$ is analytic, i.e. $\operatorname{Re}(s) > -\sigma$. In the limit as $\sigma \to 0$, and for $M = 0$, we observe that if $\mathrm{J}_0(r_0)\mathrm{J}_2(r_0) < 0$, there is a positive eigenvalue at $s = -\frac{\mathrm{J}_0(r_0)\mathrm{J}_2(r_0)}{\sigma} + O(1)$, so the limits of the quadrature must be adjusted accordingly to detect this eigenvalue.

Having introduced the stability problem, we proceed to derive our new asymptotic framework to study orbital stability in the high-memory limit. Motivated by our developments in §5.2, we begin with the zero-inertia limit, corresponding to $M = 0$.

5.3.2 Visualisation

To verify our physical picture presented in §5.2, we summarise in figure 5.2 the stability of circular orbits in the low-inertia limit ($M = 0$) for different values of the orbital radius, r_0, and memory parameter $\Gamma = 1 - \sqrt{2}\sigma$. Following the nomenclature of Oza et al. [79], stable circular orbits are coloured in blue, while unstable circular orbits destabilising via monotonic instabilities are coloured in red, and those destabilising via oscillatory instabilities are coloured in green. We observe the presence of blue stable bands that become progressively

narrower and shorter for larger orbital radii, and appear to repeat indefinitely. We numerically verify that, in each stability boundary, the inequality $J_0(r_0)J_2(r_0) > 0$ is satisfied, supporting the heuristic argument outlined in §5.2.1, and that equality occurs when $\Gamma = 1$ (corresponding to the high-memory limit). This suggests that the critical memory of instability depends on the product $J_0(r_0)J_2(r_0)$, as predicted in §5.2.1. In addition, we observe that circular orbits are stabilised by increasing memory, as stable circular orbits occur at memory higher than the critical memory of instability. This initially appears to be counter-intuitive, as other experimental and theoretical studies of orbital stability [43, 52, 66, 79, 80] indicate that increasing memory destabilises circular orbits. However, in §5.2.1, we showed that such behaviour might arise due to the effects of perturbations to the mean wave field at lower memory.

In §5.2.1, our heuristic for the onset of instability at lower memory suggested that the memory of instability scales as $\sigma^2 = \frac{c_1 J_0(r_0)J_2(r_0)}{r_0}$, where $c_1 < \frac{9}{2}$. We do indeed find that the stability boundaries can be collapsed onto a single line using the scaling $\sigma^2 \sim \frac{J_0(r_0)J_2(r_0)}{r_0}$, and display the results of this scaling in figure 5.2(c), suggesting an asymptotic self-similar form for the stability boundary. While our heuristic is unable to accurately determine the constant of proportionality, it nevertheless predicts the correct scaling for the memory of instability, providing strong support for the physical picture behind our heuristic. Importantly, it verifies that the sharply quantised orbits are stabilised by the mean wave field at high memory, and destabilise at lower memory due to the finite-memory corrections to the mean wave field.

To better understand the nature of the oscillatory instability that is responsible for this sharp quantisation, we track the destabilisation frequency along each of the stability boundaries in figure 5.2. Specifically, we consider the point of minimum memory on each branch (black dots), which correspond to the most stable orbital radius in each stability island, and track the destabilisation frequency of this point. In figure 5.3(a), we plot the destabilisation frequency of the most stable radii of each branch, i.e. all of the black dots in 5.2, against the corresponding orbital radius, in blue dots. We plot the heuristic instability frequency, $n_*\omega$, where $n_* = \arg\max_n J_n^2(r_0)$, in orange dots, but augmented by one for a better numerical fit. The proximity of the fit suggests that although our heuristic does not capture the exact instability frequency, due to the need to add one to n_*, it nevertheless significantly aids our understanding of the stability of these sharply quantised states. In figure 5.3(b), we show that the wobble number, $\xi = \frac{S}{\omega}$, approaches an integer for larger orbital radius, lending further support to the notion that the instability is due to a dominant wave mode.

We now use the scaling $\sigma^2 = O\left(\frac{J_0(r_0)J_2(r_0)}{r_0}\right)$ to determine the scaling of σ with r_0. Firstly, we must determine the size of $J_0(r_0)J_2(r_0)$. If $j_{k,n}$ is the nth non-zero root of J_k, then r_0 lies in between $j_{2,n}$ and $j_{0,n+1}$. For large n, we see that [1]

$$j_{0,n+1} = \pi n + \frac{3\pi}{4} + \frac{1}{8\pi n} + O\left(\frac{1}{n^2}\right), \tag{5.20}$$

$$j_{2,n} = \pi n + \frac{3\pi}{4} - \frac{15}{8\pi n} + O\left(\frac{1}{n^2}\right), \tag{5.21}$$

and so $j_{2,n} - r_0$ and $j_{0,n+1} - r_0$ are both of size $O\left(n^{-1}\right) = O\left(r_0^{-1}\right)$ for $j_{2,n} < r_0 < j_{0,n+1}$. Using $J_\nu(r_0) = \sqrt{\frac{2}{\pi r_0}} \cos\left(\frac{1}{4}(1+2n)\pi - r_0\right) + O\left(r_0^{-3/2}\right)$, and as r_0 is in between zeros of J_0
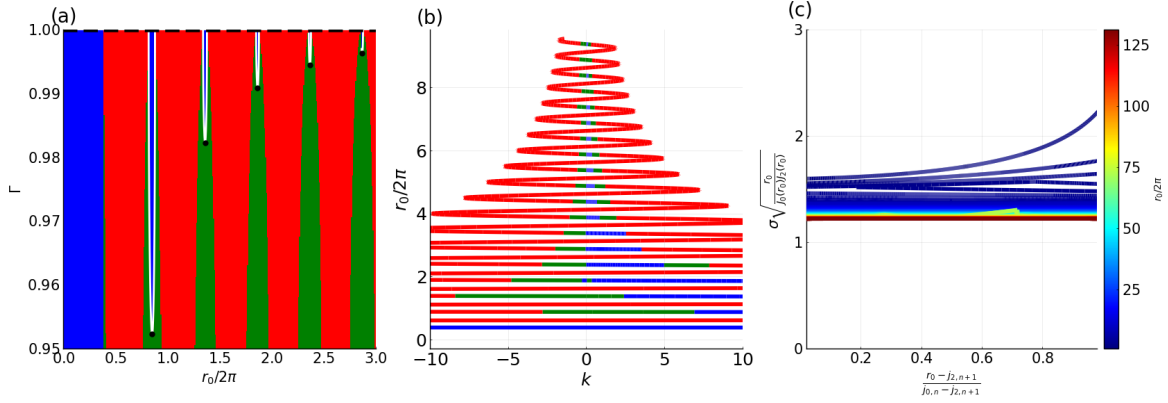
Figure 5.2: The existence and self-similarity of sharp quantisation for circular orbits in a linear spring force for $M = 0$ and low σ. (a) The dependence of the orbital stability on memory, Γ, and orbital radius, $r_0/2\pi$, normalised by the wavelength of the pilot wave. Blue points denote stable circular orbits, whereas red and green points correspond to unstable circular orbits destabilising via monotonic and oscillatory instabilities, respectively. The stability boundaries are shown in white, and the most stable orbital radii are marked in black dots. Consistent with the discussion in §5.2.1, $J_0(r_0)J_2(r_0) > 0$ is satisfied for all of the stability boundaries. Notably, the stable regions are at higher memory than the stability boundaries, as explained in §5.2.1, and the stable regions become increasingly narrow for larger orbital radius. (b) The dependence of the orbital radius on the dimensionless spring force coefficient, k, at high memory, namely $\Gamma = 0.9999$, corresponding to the black dashed line in (a). The stable quantised orbits occur very close to $k = 0$, and may thus be regarded as perturbations of the spin states characterised by Oza et al. [82]. (c) Self-similarity of the stability boundaries. The critical memory of instability, σ, is divided by $\sqrt{J_0(r_0)J_2(r_0)/r_0}$, drawing inspiration from the scaling deduced in §5.2.1. On the horizontal axis, we linearly map the orbital radii in each branch of the stability boundary onto $[0, 1]$, colour-coded by the orbital radius. The relative constancy of the scaled memory for large orbital radius (red curves) lends further support to our heuristic in §5.2.1 that instabilities at lower memory arise due to the deviations of the instantaneous wave field from its mean.
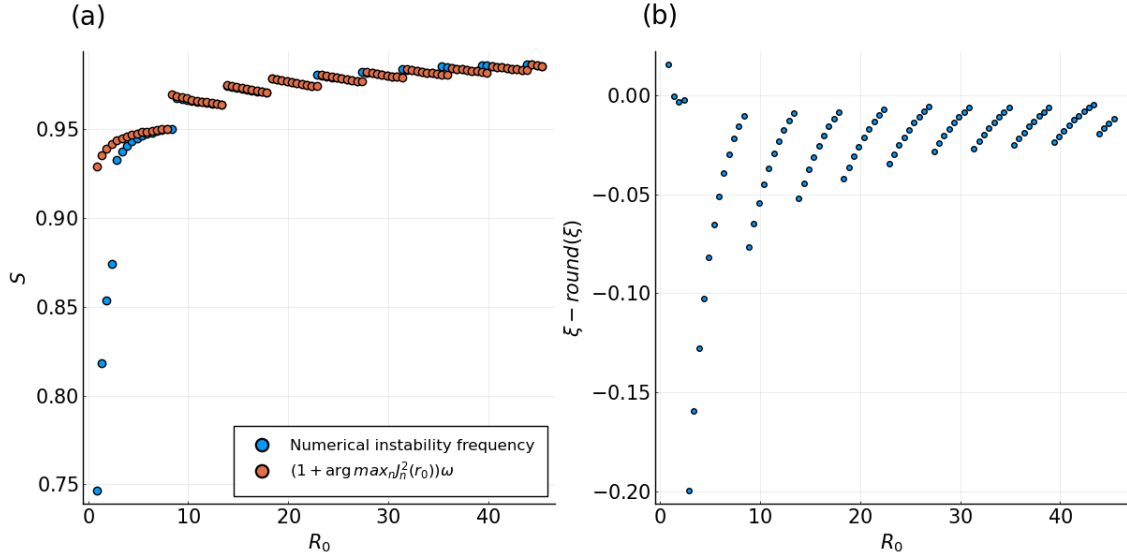
Figure 5.3: Comparison of the instability frequency with that predicted using the heuristic arguments developed in §5.2.2. (a) Dependence of the destabilisation frequency, S, on the orbital radius. The blue dots correspond to the onset of instability, which is defined by the orbital radius that minimises the memory along each stability branch (as denoted by the black dots in figure 5.2(a)). The orange dots represent the predicted instability frequency from a slight amendment to the heuristic presented in §5.2.2 so as to achieve a better numerical fit. The agreement between the numerical instability frequency and the instability frequency predicted by our heuristic provides quantitative support to our physical picture. Notably, S approaches one for large circular orbits. (b) The difference between the scaled destabilisation frequency $\xi = S/\omega$ and the nearest integer. The closeness of ξ to an integer for larger radii further verifies our physical picture connecting the instability mechanism to the dominant Bessel wave mode.

124

and J_2, we observe that $J_0(r_0)J_2(r_0) = O\left(r_0^{-3}\right)$. We thus conclude that $\sigma = O\left(r_0^{-2}\right)$ along the stability boundaries.

Now that we have heuristically characterised the instabilities of the quantised orbits, we utilise the stability framework in §5.3.1 to validate these heuristics, and to solidify the physical understanding gained in §5.2. In §5.3.3, we show, to leading order, that the stability boundaries must occur near roots of $J_0(r_0)$ and $J_2(r_0)$. In §5.3.4, we demonstrate that the instabilities are resonant, in that $\frac{S}{\omega}$ is indeed close to an integer, and in §5.3.5, we verify that the instability mechanism maximises the memory of instability, and provide the constant of proportionality for $\sigma^2 \propto \frac{J_0(r_0)J_2(r_0)}{r_0}$, thereby affirming the physical picture put forth in §5.2.

5.3.3 Leading order solution

We begin by considering the infinite-memory limit $\sigma \to 0$ for fixed r_0, focusing on a single branch of the stability boundary. Beginning with the tangential force balance, we recast (5.18) as

$$1 - r_0^2\omega^2 = J_0^2(r_0) + o(1), \tag{5.22}$$

indicating that $U = r_0\omega = O(1)$. Then, using the approximation $\operatorname{csch}(\pi\beta) = \frac{1}{\pi\beta} + O(\beta)$, $\eta = \mathrm{i}\xi + o(1)$, and taking $M = 0$, the stability coefficients take the form

$$\mathscr{A}(s) = \frac{2}{r_0\omega}\left(\frac{\mathrm{i}}{r_0} - \frac{J_0(r_0)J_0'(r_0)}{\beta}\right) + \frac{1}{\omega}\left[f_{11}(\mathrm{i}\xi, r_0) - \frac{J_0^2(r_0)}{\beta}\left(1 + \frac{\beta\eta}{r_0^2}\right)\right], \tag{5.23a}$$

$$\mathscr{B}(s) = -\frac{\mathrm{i}s}{r_0^2\omega^2} + \frac{1}{r_0\omega}\left[-J_0(r_0)J_0'(r_0) + \mathrm{i}\xi f_{01}(\mathrm{i}\xi, r_0)\right], \tag{5.23b}$$

$$\mathscr{C}(s) = 2\omega - \frac{\mathrm{i}s}{r_0^2\omega^2} + \frac{1}{r_0\omega}\left[J_0(r_0)J_0'(r_0) + \mathrm{i}\xi f_{01}(\mathrm{i}\xi, r_0)\right], \tag{5.23c}$$

$$\mathscr{D}(s) = 2s + \frac{\mathrm{i}\xi}{r_0^2\omega}\left[J_0^2(r_0) - \mathrm{i}\xi f_{00}(\mathrm{i}\xi, r_0)\right], \tag{5.23d}$$

where we define $\xi = \frac{S}{\omega}$.

We observe that, as $\sigma \to 0$, $\mathscr{A}$ diverges, unless

$$-\frac{2J_0(r_0)J_0'(r_0)}{r_0} - J_0^2(r_0) = O(\sigma) \tag{5.24}$$

which simplifies to

$$J_0(r_0)J_2(r_0) = O(\sigma). \tag{5.25}$$

As observed in figure 5.2, stability boundaries begin and end at $\sigma = 0$, which indicate that they must begin and end at zeros of J_0 and J_2. We then show, in appendix D.2.1, that if $J_0(r_0)J_2(r_0) < 0$, then there exists a large positive eigenvalues $s = -\frac{J_0(r_0)J_2(r_0)}{\sigma} + O(1)$, which shows that stability is only possible if $J_0(r_0)J_2(r_0) > 0$, demonstrating the power of the heuristic deduced in §5.2.1.

We now turn our attention to determining the scaling of σ with r_0 over all of the stability branches, and take $r_0 \to \infty$. From the argument in §5.3.2, we observe that $\sigma = O\left(r_0^{-2}\right)$. We

also assume that $S = O(1)$, and thus $\xi = O(r_0)$. From (5.22), this shows that $U = r_0\omega = 1 + o(1)$. Furthermore, we note that $\beta = \sigma/\omega$ may be recast in terms of the orbital speed, U, as $\beta = \sigma r_0/U$. As we consider $\sigma = O(r_0^{-2})$, we conclude that $\beta = O(r_0^{-1})$ for this analysis. Finally, e recall from the discussion in §5.3.2 that $J_0(r_0)J_2(r_0) = O\left(r_0^{-3}\right)$.

5.3.4 First order solution

We now seek an expansion for each stability coefficient for $r_0 \gg 1$ correct to $O\left(r_0^{-1}\right)$, thereby reducing the number of terms under consideration in the stability problem. Under the aforementioned scaling relationships, the only terms that contribute in the stability coefficients are, after letting $\beta = \frac{\beta_1}{r_0} + O\left(\frac{1}{r_0^2}\right)$ and expanding $f_{01}\left(\frac{\beta_1}{r_0}, r_0\right)$ and $f_{00}\left(\frac{\beta}{r_0}, r_0\right)$, are, as given in appendix D.2,

$$\mathscr{A} = \frac{r_0^2 J_0(r_0)J_2(r_0)}{\beta_1} - \frac{\pi^2\beta_1 Y_0^2(r_0)}{4} + r_0 f_{11}(\eta, r_0) + O\left(\frac{1}{r_0^2}\right), \tag{5.26a}$$

$$\mathscr{B} = \xi\omega + \eta f_{01}(\eta, r_0) + O\left(\frac{1}{r_0^2}\right), \tag{5.26b}$$

$$\mathscr{C} = (\xi + 2)\omega + \eta f_{01}(\eta, r_0) + O\left(\frac{1}{r_0^2}\right) \tag{5.26c}$$

$$\mathscr{D} = 2\mathrm{i}\xi\omega - \frac{\eta^2 f_{00}(\eta, r_0)}{r_0} + O\left(\frac{1}{r_0^2}\right), \tag{5.26d}$$

where Y_0 is the Bessel function of the second kind of order 0. Multiplying out the stability coefficients gives

$$\mathscr{F} = \mathscr{A}\mathscr{D} + \mathscr{B}\mathscr{C} = \frac{2\mathrm{i}\xi y}{r_0} - \frac{\eta^2 f_{00}(\eta, r_0) y}{r_0} + 2\mathrm{i}\xi f_{11}(\eta, r_0) + \frac{\xi(\xi + 2)}{r_0^2} + \frac{2\eta(1 + \mathrm{i}\beta)}{r_0} f_{01}(\eta, r_0), \tag{5.27}$$

where we denote

$$y = \frac{r_0^2 J_0(r_0)J_2(r_0)}{\beta_1} - \frac{\pi^2\beta_1 Y_0^2(r_0)}{4}$$

and have used the Bessel function Wronskian [1] $J_{-\xi}(r_0)J'_\xi(r_0) - J_\xi(r_0)J'_{-\xi}(r_0) = \frac{2\sin(\pi\xi)}{\pi r_0}$ to simplify.

The first order solution is found by considering the limit as $\beta \to 0$, where $J_0(r_0)J_2(r_0) = 0$, and $\beta_1 = 0$. This limit yields the equation

$$\mathscr{F}_1 = 2\mathrm{i}\xi\left(f_{11}(\mathrm{i}\xi, r_0) + \frac{f_{01}(\mathrm{i}\xi, r_0)}{r_0}\right) + \frac{\xi(\xi + 2)}{r_0^2} = 2\pi\xi\csc(\pi\xi)J'_{-\xi}(r_0)\left(J'_\xi(r_0)\right.$$

$$\left. + \frac{J_\xi(r_0)}{r_0}\right) + \frac{\xi}{r_0^2}(\xi + 2) = o(1), \tag{5.28}$$

which, in principle, may be solved for the destabilisation frequency, ξ. From figure 5.3, we see that $S \to 1$ for large orbital radius. Given that $U = 1 + o(1)$, and $\xi = S/\omega = r_0 S/U$, we observe that $\xi \approx r_0$, consistent with our numerical computations. By using the Bessel

function transition region expansions [1], we thus conclude that $J'_{\pm\xi}(r_0) = O\left(r_0^{-2/3}\right)$ and $J_{\pm\xi}(r_0) = O\left(r_0^{-1/3}\right)$. The stability condition (5.3.4) then implies

$$\csc(\pi\xi) = O\left(r_0^{\frac{1}{3}}\right), \tag{5.29}$$

necessitating that ξ be close to an integer.

Despite the progress made in this section, equation (5.3.4) does not admit unique solutions for ξ, nor does it relate the destabilisation frequency to the critical memory of instability. As our current findings do not adequately select the instability mechanism, we proceed to the next-order terms in the asymptotic expansion to derive an expression for β_1. We then seek to determine ξ by minimising β_1, so that the stability boundary is the neutral stability boundary that maximises the critical memory.

5.3.5 Second order solution

We now expand the stability coefficients in (5.26) to next order in r_0. Taking $\beta = \frac{\beta_1}{r_0} + O\left(\frac{1}{r_0^2}\right)$ and linearising, the condition $\mathscr{A}\mathscr{D} + \mathscr{B}\mathscr{C} = 0$ leads to, after a series of algebraic manipulations,

$$r_0^2 J_0(r_0)J_2(r_0) = q\beta_1^2, \tag{5.30a}$$

where

$$
\begin{aligned}
q &= \frac{\pi^2 Y_0^2}{4} - \frac{2}{[2i + \xi f_{00}(i\xi, r_0)]}\frac{\partial}{\partial\xi}\left(f_{11}(i\xi, r_0) + \frac{f_{01}(i\xi, r_0)}{r_0}\right), \\
&= \frac{\pi^2 Y_0^2(r_0)}{4} + \frac{2\pi\sin(\pi\xi)}{(2\sin(\pi\xi) - \pi\xi J_\xi(r_0)J_{-\xi}(r_0))}\frac{\partial}{\partial\xi}\left(\csc(\pi\xi)J'_{-\xi}(r_0)\left(J'_\xi(r_0) + \frac{J_\xi(r_0)}{r_0}\right)\right).
\end{aligned}
\tag{5.30b}
$$

As $J_0(r_0)J_2(r_0) > 0$ when $r_0 \in (j_{2,n}, j_{0,n+1})$ for any integer n, we can minimise β_1^2 for fixed r_0 by maximising q. In appendix D.3, we show that the scaling $\xi = r_0 + o(r_0)$ leads to the simplified coefficient

$$q = \frac{\pi^2 Y_0^2(r_0)}{4} - \frac{1}{r_0^2 J_\xi^2(r_0)} + O\left(\xi^{-\frac{5}{3}}\right). \tag{5.31}$$

From (5.30), the reciprocal orbital memory parameter $\beta = \beta_1/r_0$ is minimised by maximising q, which is achieved in turn by maximising $J_\xi^2(r_0)$. As ξ is close to an integer, it would be desirable to remove equation (5.3.4) from consideration, and to demonstrate that ξ can be approximately determined as the integer n that maximises $J_n^2(r_0)$, where we choose $r_0 = \frac{1}{2}(j_{0,n+1} + j_{2,n})$ to coincide with the point on the stability boundary of highest memory. This would demonstrate an approximate resonance between the orbital frequency and the instability frequency, and also would validate the explanation for the instability frequency in terms of the tangential force balance in §5.2.2. We compare $\arg\max_\xi J_\xi^2(r_0)$ to the numerical value of ξ in figure 5.4. As the absolute error in ξ exhibits bounded oscillations, the relative
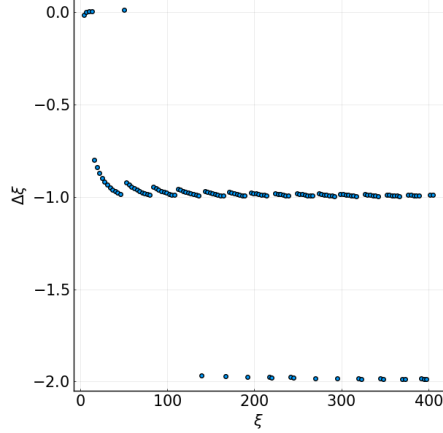
Figure 5.4: Comparing the heuristic for ξ against its numerically computed counterpart, evaluated at the most stable orbital radius in each branch that maximises $J_0(r_0)J_2(r_0)$. The heuristic error is plotted against the true scaled destabilisation frequency, ξ. For larger ξ, the relative heuristic error decreases, and the absolute error oscillates between 1 and 2. As observed in figure 5.3, the heuristic generally predicts ξ incorrectly by 1, which, for large r_0 and ξ, becomes negligible. This validates the $J_n^2(r_0)$ maximisation principle for the instability frequency, $S = n\omega$.

error decays for large r_0 and ξ, indicating that our heuristic performs well for larger r_0 and ξ.

Let us recap the results from each of the three orders of expansion. The leading-order stability condition in equation (5.25) demonstrates that the stability boundaries begin on zeros of J_2 and end on zeros of J_0. The first-order stability condition in equation (5.3.4) prescribes the allowed values of ξ, and demonstrates that $\sin(\pi\xi) = O\left(\xi^{-\frac{1}{3}}\right)$, i.e. ξ is near an integer. The second-order stability condition in equations (5.30) and (5.31), coupled with the memory-maximisation principle, show that ξ is approximately the integer that maximises the Bessel function $J_\xi(r_0)$, where r_0 is the average of the zeros of J_2 and J_0.

We now turn our attention to the memory of instability. As shown in appendix D.4, we may write

$$\beta = \sqrt{\frac{J_0(r_0)J_2(r_0)}{q}}, \tag{5.32}$$

$$\text{or } \sigma = \frac{\beta}{r_0} = \sqrt{\frac{J_0(r_0)J_2(r_0)}{qr_0^2}}, \quad \text{with} \quad q = \frac{\pi}{2r_0}\left(1 - \frac{2^{\frac{1}{3}}}{\pi A_{\max}^2 r_0^{\frac{1}{3}}}\right)\left[1 + O\left(\frac{1}{r_0^{\frac{2}{3}}}\right)\right], \tag{5.33}$$

where $A_{\max}$ is the global maximum of the Airy function $\text{Ai}(x)$, for real x. The $J_0(r_0)J_2(r_0)$ factor explains the symmetrical and self-similar shape of the stability boundaries, and is consistent with the appearance of the stability boundaries at the zeros of J_0 and J_2. In figure 5.5(a), we collapse all of the stability boundaries using the leading-order scaling $\sigma \sim \sqrt{\frac{2J_0(r_0)J_2(r_0)}{\pi r_0}}$, much like in 5.2(c), except now we show that the missing proportionality constant is $\sqrt{\frac{2}{\pi}}$. In figure 5.5(b), we demonstrate that the error in our asymptotic memory

128
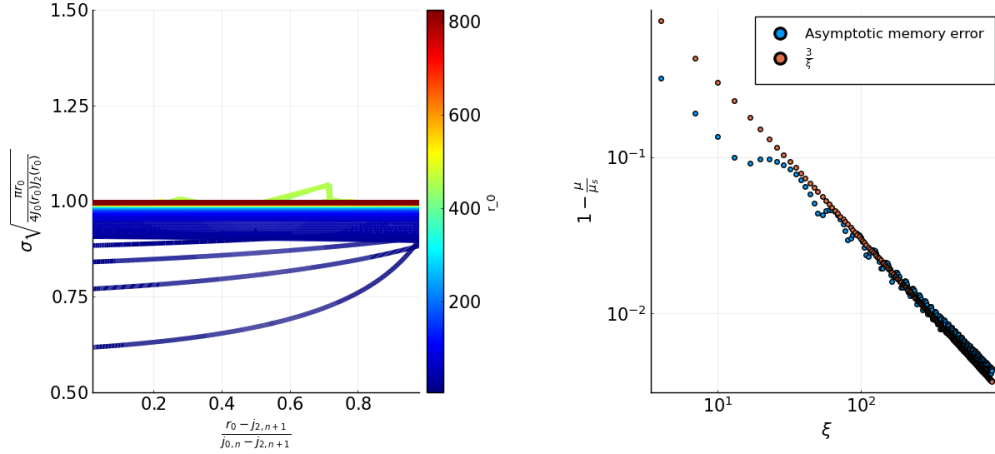
Figure 5.5: (a) Scaled memory plotted against r_0, where we use the fact that $r_0 \in [j_{2,n}, j_{0,n+1}]$ to linearly map all of the orbital radii to $[0, 1]$ for ease of visualisation, and $\sigma_s = \sqrt{\frac{2J_0(r_0)J_2(r_0)}{q_1 r_0}}$. The color bar refers to the value of r_0; for larger r_0, the scaled stability boundaries are flat, where the scaled memory asymptotes to 1. (b) The scaled memory, evaluated at $\frac{r_0 - j_{2,n}}{j_{0,n+1} - j_{2,n}} = \frac{1}{2}$, for increasing n and thus ξ. While our analysis predicts an $O\left(\xi^{-\frac{2}{3}}\right)$ error for the memory of instability for large r_0 and ξ, we instead find numerically an $O\left(\xi^{-1}\right)$ error scaling.

of instability scales exactly as we claimed in (5.32). Our ability to predict the convergence of the asymptotic memory to the numerical memory validates our asymptotic approach for describing the memory of instability, and re-affirms that the instability mechanism is selected to maximise $J_n^2(r_0)$.

5.4   Discussion

We have demonstrated that stable circular orbits may exist in the presence of a linear central force in the high-memory, zero-inertia limit, with the permissible orbital radii r_0 satisfying $J_0(r_0)J_2(r_0) > 0$. As demonstrated by figures 5.1 and 5.2, the regions of permissible orbital radii become infinitely thin when the orbital radius is large. The orbits are then said to be sharply quantised, in contrast to the orbital quantisation described in the experimental parameter regime [43, 66, 79, 80], for which the interval of permitted orbital radii expands, rather than shrinks, for large circular orbits. In this high-memory, low-inertia regime, there exists a large number of quantised states at sufficiently high memory, with this number approaching infinity in the infinite-memory limit.

In §5.2, we presented several heuristic arguments for understanding the three key features of sharp quantisation, which we summarise as follows:

1. The permissible orbital radii for stable circular orbits must satisfy $J_0(r_0)J_2(r_0) > 0$;

2. Circular orbits are stable at higher memory, and destabilise at lower memory;

3. The instability frequency of a circular orbit with radius r_0 and orbital frequency ω is $S = n\omega$, where n maximises $\mathrm{J}_n^2(r_0)$.

We explained the bounds on the permissible orbital radii (given by heuristic 1) in §5.2.1. By considering the mean wave field as a potential [33], we showed that the orbital radius inequality arises from requiring the central force and mean wave force to be able to pull in outwards radial perturbations, an argument similar to that in §3.6.3 when describing monotonic instabilities. By verifying this inequality through consideration of asymptotics in §5.3.5, we validate our reduction of the dynamics to that given by the radial force balance at high memory, for which the instantaneous wave field is well approximated by its mean.

We explained the stabilisation of circular orbits with increased memory (heuristic 2) in §5.2.1, where we considered the influence of deviations from the mean wave force in the radial force balance. In this analysis, we showed that these deviations give rise to a radial force scaling proportionally to both the orbital radius r_0 and the wave decay rate σ, which will further repel outwards radial perturbations for sufficiently low memory. Our arguments thus demonstrate why the instability mechanism observed at the onset of instability maximises the critical memory of instability, which we used in §5.3.5 to derive the memory of instability in our asymptotic framework.

There are two ways to explain the third heuristic, which connects the instability frequency to the orbital frequency. First, we argued that the instability frequency is $S = n\omega$, where $n \approx \arg\max_m \mathrm{J}_m^2(r_0)$, by showing that the nth Bessel wave mode provides the largest contribution to the tangential wave force, leading to the dominant mode of instability. Second, we used our asymptotic framework to show that $S = n\omega$ maximised the memory of instability, in line with the second heuristic outlined above.

The ability of our heuristics to explain the instability mechanism, the scaling for the critical memory of instability, and the lack of stability at lower memory, leads us to suggest the tantalising possibility of developing pilot-wave systems with different kernels, as considered by Durey [29] and Valani et al. [99], to increase the sharpness of the quantisation. In particular, for a general wave field given by

$$h(\boldsymbol{x}, t) = \int_{-\infty}^{t} H(|\boldsymbol{x} - \boldsymbol{x}_p(s)|)\mathrm{e}^{-\sigma(t-s)}\,\mathrm{d}s, \tag{5.34}$$

where $H(0) = 1$ and $H'(0) = 0$, we observe that the stability of circular orbits is governed by the inequality

$$\int_0^\infty \frac{1}{r_0}w_r(r_0, r_0, \omega t, t) + \frac{\partial w_r}{\partial x_1}(r_0, r_0, \omega t)\,\mathrm{d}t < 0 \tag{5.35}$$

in the limit $\sigma \to 0$, where

$$w_r(r(t), r(s), \theta(t) - \theta(s), t - s) = -\frac{H'(\mathfrak{D}(t,s))}{\mathfrak{D}(t,s)}(r(t) - r(s)\cos(\theta(t) - \theta(s)))\mathrm{e}^{-\sigma(t-s)} \tag{5.36}$$

and

$$\mathfrak{D}(t,s) = \sqrt{r^2(t) + r^2(s) - 2r(t)r(s)\cos\big(\theta(t) - \theta(s)\big)}.$$

130

We imagine that judicious choices of the wave kernel, H, may lead to even sharper quantisation, or quantisation arising at lower memory. Equally, increasing the spatial decay of the wave kernel may inhibit sharp quantisation, as the confining influence of the pilot wave would be diminished for waves of smaller amplitude.

Our analysis also explained how the deviations of the wave field from the mean wave field could lead to instability, providing a physical basis for the stability of circular orbits at high memory. Our investigations of the GPWF has revealed new physics, absent in the hydrodynamic system [43, 52, 66, 79]. Curiously, in §2.3.1, we deduced that circular orbits in a rotating frame destabilise via 2ω instabilities because these instabilities occur at lowest memory, whereas we deduced that circular orbits destabilise via $n\omega$ instabilities for sharp quantisation in §5.3.5 to maximise the memory of instability, where $n = \arg\max_m \mathrm{J}_m^2(r_0)$. We can see the origin of the differences in (5.1); in chapters 2 to 4, we showed that orbital instability typically arises when $\mathrm{e}^{-\pi\beta} = O(r_0^2)$ or $O(r_0^3)$, which indicates that $\beta = O(\log(r_0))$, and thus $\sigma = \beta\omega \gg \omega$. Similarly, in §5.2.2, our argument regarding the tangential wave force is also only valid if $\sigma \ll \omega$. Thus, at the typical onset of instability, we cannot approximate the wave field with the mean wave field, and different phenomena trigger orbital instability. This observation may explain the difficulty of generalising the heuristics derived in §2.4.2 to central force systems, as noted in §3.6.3.

It is interesting that our discovery of sharply quantised orbits occurs in the low-inertia high-memory limit. Given that the effect of the wave field can be well approximated by a wave-induced added mass at low memory [15, 79], and that inertial, non-quantised circular orbits arise [43, 52, 79], it is expected that quantum-like behaviour might instead occur in the high memory limit. The possibility that quantum-like behaviour may occur in the low inertia limit was demonstrated by Gilet [48], who showed that if inertia is neglected, then the maxima of the histogram of radial positions in a corral occur at the same radii as the quantum-mechanical histograms of radial positions of particle motion in a 2D infinite cylindrical potential well. In addition, stable spin states were demonstrated by Oza et al. [82] to exist only at low inertia, outside the parameter regime accessible in the laboratory. We remark, from figure 5.2, that our quantised circular orbits are actually perturbations of the spin states considered by Oza et al. [82]. Thus, we turn our attention to the stability of these spin states in the presence of applied forces.

Chapter 6

The influence of external stimuli on spin states in a classical pilot-wave system

6.1   Introduction

In this chapter, we investigate the phenomenon of the so-called 'hydrodynamic spin states', characterised by a particle executing self-sustained circular orbits in the absence of any external forces, with the confinement of the particle to orbital motion driven entirely by the accompanying pilot wave.[65, 82] These spin states, whose existence for the stroboscopic model was first established by Oza *et al.*[79, 82], are unstable in the parameter regime representative of experiments, although drifting spin states, trajectories characterised by circular motion about a moving orbital centre, were detected by [7]. In the high-memory limit, an infinite set of these unstable spin states emerges, with orbital radii corresponding to the zeros of the J_0 and J_1 Bessel functions. However, Oza et al. [82] demonstrated that only the spin state with smallest orbital radius (corresponding to the first zero of J_0) is stable in any parameter regime, namely for sufficiently weak particle inertia and relatively high memory. For weakly unstable spin states, more exotic wobbling states emerge [31]. The purpose of this study is to explore the influence of a weak applied force on the stability of these spin states, focusing on the particular case of a particle moving in response to a Coriolis or linear central force.

Before proceeding with our analysis of hydrodynamic spin states, we first note the key features of orbital motion in an external force field. For a Coriolis force, the rotating frame of reference imposes a symmetry breaking on the orbital motion. For classical particles, only anticyclonic orbits are possible, with the particle orbiting in the opposite direction to the rotating frame. These anticyclonic orbits are also abundant in the hydrodynamic pilot-wave system, and are readily observed in experiments [43, 52]. However, when perturbing stable spin states with a weak Coriolis force, stable cyclonic orbits may survive, in which the particle orbits in the same direction as the rotating frame. This splitting into two orbital states for a weak Coriolis force represents a hydrodynamic analogue of Zeeman splitting, experimentally realised by Eddi et al. [39] for pairs of droplets, and theoretically investigated by Oza [79, 82]. Our study characterises the relative change in the stability region of cyclonic and anticyclonic spin states in the presence of a weak Coriolis force. In particular, we highlight a new form

of instability mechanism that arises for anticyclonic orbits in the high-memory limit, which serves to destabilise orbital states that were stable in the absence of an external force.

For particle motion in a linear spring force, there is no preferred direction of orbital motion, with the dynamics of clockwise and anticlockwise orbital states being identical [64]. However, fixing the orbital centre for particle motion in a central force results in a loss of translational invariance in the particle motion relative to spin states in free space or moving in response to a Coriolis force, for which the particle may orbit about any position in the plane. Our study highlights that this loss of translational invariance is responsible for anomalous jumps in the shape of the stability region, even for an arbitrarily small spring force. In particular, we demonstrate that the stability region for spin states in free space essentially bifurcates into two regions for an arbitrarily weak spring force: the largest region, arising at higher memory, corresponds to a weak attractive spring force, while the smaller region, arising at lower memory, corresponds to a weak repulsive spring force. Our study thus highlights the surprising possibility of spin states being stable for a weak repulsive spring force, but unstable for an attractive spring force of the same magnitude.

This chapter is structured as follows. Using the generalised pilot-wave framework[13], we present in §6.2 the dependence of the orbital stability on the frame rotation rate for a Coriolis force and spring stiffness for a central force. We then analyse the variation in the stability boundary for a weak Coriolis force, demonstrating the existence of two instability mechanisms for anticyclonic orbits (§6.3). We consider the case of a weak spring force in §6.4, highlighting how the loss of translational invariance drastically changes the shape of the stability region relative to spin states in free space. Finally, we discuss our findings in the wider context of orbital pilot-wave dynamics in §6.5.

6.2 Pilot-wave dynamics

We consider the generalised pilot-wave framework introduced in §4.2, where we now allow the external force to be either a central force, $\boldsymbol{F} = -k\boldsymbol{x}_p$, or a Coriolis force, $\boldsymbol{F} = -2m\boldsymbol{\Omega} \times \dot{\boldsymbol{x}}_p$. The corresponding dimensionless integro-differential trajectory equation takes the form Oza et al. [79, 82]

$$M\ddot{\hat{\boldsymbol{x}}}_p + \dot{\hat{\boldsymbol{x}}}_p = \int_{-\infty}^{\hat{t}} \frac{\mathrm{J}_1(|\hat{\boldsymbol{x}}_p(\hat{t}) - \hat{\boldsymbol{x}}_p(s)|)}{|\hat{\boldsymbol{x}}_p(\hat{t}) - \hat{\boldsymbol{x}}_p(s)|}(\hat{\boldsymbol{x}}_p(\hat{t}) - \hat{\boldsymbol{x}}_p(s))\mathrm{e}^{-\sigma(\hat{t}-s)}\,\mathrm{d}s + \hat{\boldsymbol{F}}, \qquad (6.1)$$

where the dimensionless Coriolis force is defined $\hat{\boldsymbol{F}} = -\hat{\boldsymbol{\Omega}} \times \dot{\hat{\boldsymbol{x}}}_p$, whereas the dimensionless linear spring force takes the form $\hat{\boldsymbol{F}} = -\hat{k}\hat{\boldsymbol{x}}_p$, with $\hat{\boldsymbol{\Omega}} = 2\boldsymbol{\Omega}/mD$ and $\hat{k} = \frac{kk_F}{Dc}$. Additional dimensionless parameters are summarised in table 4.1.

While the experimental parameters considered by Harris and Bush [52] correspond to $M = 2.2$, we may vary the system parameters M, σ, $\hat{k}$ and the bath rotation rate $\hat{\Omega} = \hat{\boldsymbol{z}} \cdot \hat{\boldsymbol{\Omega}}$ (where $\hat{\boldsymbol{z}}$ is unit vector perpendicular to the plane of the particle motion) arbitrarily. As this model has its origins in the hydrodynamic walking droplet system, we expect some similar types of orbital instabilities in the experimental system and in this generalised stroboscopic system. However, by considering parameter regimes not easily accessed experimentally, we may probe orbital dynamics in greater generality to seek novel orbital instabilities not accessible experimentally.

6.2.1 Orbital dynamics

We characterise circular orbits by their orbital radius, r_0, and orbital frequency, ω. Upon omitting the hats in the integro-differential equation and substituting $\boldsymbol{x}_p(t) = r_0(\cos(\omega t), \sin(\omega t))$ into (6.1), the radial and tangential force balance equations are given by [66, 79]

$$-Mr_0\omega^2 = \int_0^\infty \mathrm{J}_1\left(2r_0\sin\left(\frac{\omega t}{2}\right)\right)\sin\left(\frac{\omega t}{2}\right)\mathrm{e}^{-\sigma t}\,\mathrm{d}t + f, \qquad (6.2a)$$

$$r_0\omega = \int_0^\infty \mathrm{J}_1\left(2r_0\sin\left(\frac{\omega t}{2}\right)\right)\cos\left(\frac{\omega t}{2}\right)\mathrm{e}^{-\sigma t}\,\mathrm{d}t, \qquad (6.2b)$$

where the radial component of the applied force is $f = \Omega\omega r_0$ for a Coriolis force and $f = -kr_0$ for a linear spring force. Given a confining force constant k or rotation rate Ω, and fixed memory σ and inertia M, these equations may be solved for r_0 and ω. Notably, neither the central force nor the Coriolis force appears in the tangential force balance, which is given by (4.8e), a form that we leverage throughout this investigation.

We focus our investigation on the influence of a weak applied force on 'hydrodynamic spin states', which describe the sustained orbital motion of a particle confined by its wave field in the absence of any applied forces [79, 82]. Although these spin states are unstable in the regime accessible in the laboratory, they are stable in the stroboscopic model for sufficiently small dimensionless mass, M, and wave decay rate, σ, corresponding to the low-inertia, high-memory limit (i.e. Γ close to 1); see figure 6.1(a). In this parameter regime, the orbital radius is close to the first zero of the Bessel function of order zero, with $\mathrm{J}_0(r_0) = 0$ achieved in the high-memory. Furthermore, we note that the instability frequency, S, varies along the stability boundary. The corresponding wobble number, $\xi = S/\omega$, characterising the ratio of the instability frequency to the orbital frequency, increases monotonically along the stability boundary with increasing memory. As we will find particularly significant in our investigation of particle motion in response to a weak linear spring force, we see that S/ω passes through unity near the maximum value of M achieved along the stability boundary, corresponding to $\Gamma \approx 0.76$. We proceed to investigate the influence of applied forces on the form of spin state stability region in the (M, Γ)-plane, leveraging the stability framework outlined in §6.2.2.

6.2.2 Orbital stability

Orbital stability is characterised by analysing the linear growth rates of perturbations from circular orbits. We follow the framework introduced by Oza *et al.*[79], and developed in chapters 2 to 4. As demonstrated in §4.2.3, the asymptotic growth rates of perturbations, s, of linear perturbations correspond to the roots of $\mathscr{F}(s) = \mathscr{A}(s)\mathscr{D}(s) + \mathscr{B}(s)\mathscr{C}(s)$.

As our study considers the effect of small applied forces, we do not eliminate the applied force coefficients in our stability formulation, unlike in earlier chapters. The stability
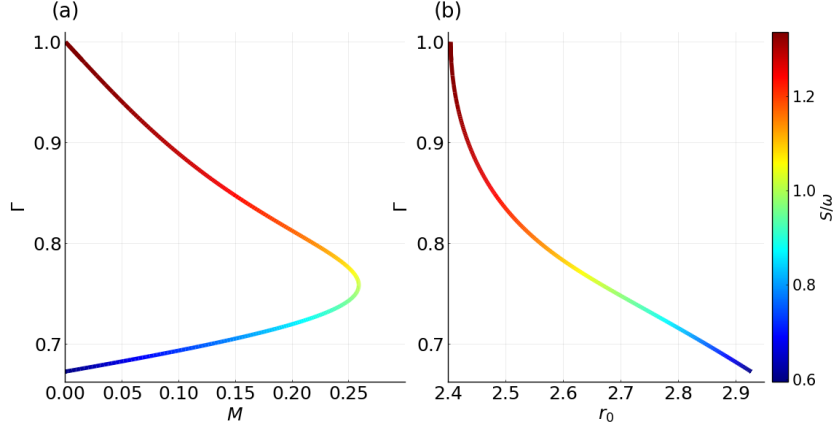
Figure 6.1: Stability boundary for spin states in free space[82], colour-coded by ratio of the destabilisation frequency, S, to the orbital frequency, ω. (a) The dependence of the memory parameter, $\Gamma = 1 - \sqrt{2}\sigma$, on the dimensionless mass M along the stability boundary. Stable spin states are contained within the stability boundary, and so may be found when particle inertia is relatively weak. For comparison, $M \approx 2.2$ in the experimental regime considered by Harris & Bush[52]. Our study focuses on the movement of this stability boundary when the particle motion is subjected to a weak external force. (b) The dependence of the memory parameter, Γ, along the stability boundary on the dimensionless orbital radius, r_0. As $\Gamma \to 1$, in the limit of infinite memory, r_0 approaches the first zero of the Bessel function J_0, approximately 2.40.

coefficients $\mathscr{A}, \mathscr{B}, \mathscr{C}$ and $\mathscr{D}$ and the tangential force balance then take the form [66, 79]

$$\mathscr{A}(s) = M(s^2 - 2\omega^2) + s + \sigma - \frac{2f}{r_0} - 2\mathcal{I}_0(0) + \mathcal{C}_0(s) + \mathcal{I}_1(s), \tag{6.3a}$$

$$\mathscr{B}(s) = 2M\omega s + \frac{\Delta f s}{r_0 \omega} - \sigma\left(M\omega + \frac{f}{r_0\omega}\right) - \mathcal{S}_0(s), \tag{6.3b}$$

$$\mathscr{C}(s) = 2M\omega s + 2\omega + \frac{\Delta f s}{r_0 \omega} + \sigma\left(M\omega + \frac{f}{r_0\omega}\right) - \mathcal{S}_0(s), \tag{6.3c}$$

$$\mathscr{D}(s) = Ms^2 + s - \sigma + \mathcal{C}_0(s) - \mathcal{I}_1(s), \tag{6.3d}$$

$$1 - r_0^2\omega^2 = \sigma\mathcal{I}_0(0), \tag{6.3e}$$

where f is the radial force in (6.2), $\Delta = 0$ denotes the case of a linear central force and $\Delta = 1$ corresponds to a Coriolis force. The integrals $\mathcal{I}_m, \mathcal{C}_m$ and $\mathcal{S}_m$ are defined, for $\mathrm{Re}(s+\sigma) > 0$,

$$\mathcal{I}_m(s) = \frac{1}{2}\int_0^\infty J_{2m}\left(2r_0 \sin\left(\frac{\omega t}{2}\right)\right) \mathrm{e}^{-(\sigma+s)t}\, \mathrm{d}t, \tag{6.4a}$$

$$\mathcal{C}_m(s) = \frac{1}{2}\int_0^\infty J_{2m}\left(2r_0 \sin\left(\frac{\omega t}{2}\right)\right) \cos(\omega t)\mathrm{e}^{-(\sigma+s)t}\, \mathrm{d}t, \tag{6.4b}$$

$$\text{and}\quad \mathcal{S}_m(s) = \frac{1}{2}\int_0^\infty J_{2m}\left(2r_0 \sin\left(\frac{\omega t}{2}\right)\right) \sin(\omega t)\mathrm{e}^{-(\sigma+s)t}\, \mathrm{d}t, \tag{6.4c}$$

136

where $m \geq 0$ is an integer. For this study, it will be convenient to recast the stability integrals as

$$\mathcal{I}_{m,1}(s) = \frac{1}{2} \int_0^\infty \mathrm{J}_{2m}\left(2r_0 \sin\left(\frac{\omega t}{2}\right)\right) \mathrm{e}^{-st}\, \mathrm{d}t, \tag{6.5a}$$

$$\mathcal{C}_{m,1}(s) = \frac{1}{2} \int_0^\infty \mathrm{J}_{2m}\left(2r_0 \sin\left(\frac{\omega t}{2}\right)\right) \cos(\omega t)\mathrm{e}^{-st}\, \mathrm{d}t, \tag{6.5b}$$

$$\text{and} \quad \mathcal{S}_{m,1}(s) = \frac{1}{2} \int_0^\infty \mathrm{J}_{2m}\left(2r_0 \sin\left(\frac{\omega t}{2}\right)\right) \sin(\omega t)\mathrm{e}^{-st}\, \mathrm{d}t, \tag{6.5c}$$

so that $\mathcal{I}_m(s) = \mathcal{I}_{m,1}(\sigma + s)$, and similarly for the other two integrals. Although we showed in §2.2.3 that all of the integrals may be evaluated in terms of complex order Bessel functions, our analysis is most readily performed on the integral form above.

The orbital solution is unstable if there are any roots, s, of $\mathscr{F}$ satisfying $\mathrm{Re}(s) > 0$. By denoting s_* as the unstable root with largest real part, the instability is monotonic if $\mathrm{Im}(s_*) = 0$ and oscillatory otherwise. The stability function, $\mathscr{F}$, has a trivial eigenvalue at 0, corresponding to rotational invariance of the orbital motion. In the case of the Coriolis force, $\mathscr{F}$ has an additional trivial eigenvalues at $\pm i\omega$ owing to translational invariance [79]. It follows, therefore, that the nontrivial roots of the stability problem satisfy $\mathscr{G}(s) = 0$, where

$$\mathscr{G}_{\mathrm{Cor.}}(s) = \frac{\mathscr{A}(s)\mathscr{D}(s) + \mathscr{B}(s)\mathscr{C}(s)}{s(s^2 + \omega^2)}, \tag{6.6a}$$

$$\mathscr{G}_{\mathrm{spr.}}(s) = \frac{\mathscr{A}(s)\mathscr{D}(s) + \mathscr{B}(s)\mathscr{C}(s)}{s}. \tag{6.6b}$$

We apply the method of Delves and Lyness [27] to find the roots of $\mathscr{G}$ in the domain over which $\mathscr{G}$ is analytic, i.e. $\mathrm{Re}(s) > -\sigma$. To ascertain whether a particular orbital state is stable or unstable, we typically utilise a rectangular integration contour spanning the domain $\mathrm{Re}(s) \in [0, 20]$ and $\mathrm{Im}(s) \in [0, 5]$, which we find to be sufficient for identifying all roots with a positive real part across the parameter regime considered in this study, namely $0 \leq \Gamma \leq 0.999$.

6.2.3 Visualisation

Following Oza et al. [79], we present in figures 6.2 and 6.3 the dependence of the orbital radius on the rotation rate and the central force constant, at different values of memory. At low memory (panel (a)), all circular orbits are stable. Notably, there are no orbital solutions at low memory in the absence of an applied force, referred to here as 'spin states'. As the memory is increased, stable circular orbits (blue) gradually destabilise via monotonic (red) or oscillatory (green) instabilities. In addition, as memory is increased, the number of orbital states, at a fixed Ω or k, also increases, with the emergence of spin states in panels (b), (c) and (d). Notably, only the spin states with radii close to the first zero of J_0 are found to be stable. In a rotating frame, anticyclonic orbits are stable for large rotation rate at sufficiently low memory. On the contrary, we observe very narrow regions of stable cyclonic orbits. In a central force, circular orbits likewise appear to be stable for larger central force constants.

The regions of stable circular orbits for repulsive central forces, however, appear to be much narrower. We also note that, for the central force system, there appear to be many quantised orbital states near $k = 0$, unlike in the rotating frame. An exploration of such quantised orbital states was presented in chapter 5.

We now investigate the stability of the lowest orbital radii circular orbits near $\Omega = 0$ and $k = 0$. Particular attention will be paid to the movement of stability boundaries with changing rotation rate or central force constant, and to the introduction of any new instabilities.

6.3 Spin states in the presence of a weak Coriolis force

We proceed to analyse the form of the stability regions presented in figure 6.4 for a particle executing anticyclonic and cyclonic circular orbits in response to a Coriolis force. We use asymptotic analysis to predict the slope of the stability boundary in the low-inertia, high-memory limit, and determine the leading-order instability frequency in each case. Our analysis sheds light on the formation of a corner in the stability boundary for anticyclonic orbits, corresponding to a switch in the instability mechanism. There is no such switch in the instability mechanism for cyclonic orbits, for which the stability region shrinks with increasing M, eventually vanishing when inertial effects are sufficiently strong.

6.3.1 Qualitative effect of small rotation on spin states

In the absence of an external force, circular orbits are invariant to the rotation direction, as prescribed by the sign of the orbital frequency, ω. As pointed out by Oza et al. [79], the bath rotation breaks the degeneracy of positive and negative angular frequencies. Circular orbits with $\Omega\omega > 0$ are cyclonic, while circular orbits with $\Omega\omega < 0$ are anticyclonic. As indicated by figure 6.4, in accordance with physical intuition, anticyclonic states are more stable than cyclonic states. As shown in appendix E.2, stable cyclonic states only exist for $|\Omega| < \Omega_c = 0.0738....$

Notably, the stability boundaries for different values of $|\Omega|$ in the (M, Γ)-plane are mostly nested, suggesting that stronger Coriolis forces uniformly stabilise cyclonic spin states and destabilise anticyclonic spin states. As will be seen in section 6.4, this nesting property arises because the physical system has rotational and translational invariance both with and without the Coriolis force. From figure 6.4, it is apparent that at $M = 0, \Gamma \approx 1$, the movement of the spin state boundary is qualitatively different for cyclonic and anticyclonic states. The stability boundary appears to move progressively downwards from $(M, \Gamma) = (0, 1)$ at a fairly consistent rate as $|\Omega|$ is increased for cyclonic states. For anticyclonic states, though most of the stability boundary expands outwards as $|\Omega|$ is increased, a corner in the stability boundary appears near $\Gamma = 1$. Interestingly, external rotation always destabilises spin states at $\Gamma = 1$; for any $|\Omega| > 0$, there is some Γ_c such that both cyclonic and anticyclonic spin states are unstable for all $\Gamma > \Gamma_c$. To explain this instability near $\Gamma = 1$ and the presence of the corner in the stability boundary, we turn our attention to the analytical study of the spin state stability boundaries for small $|\Omega|$.
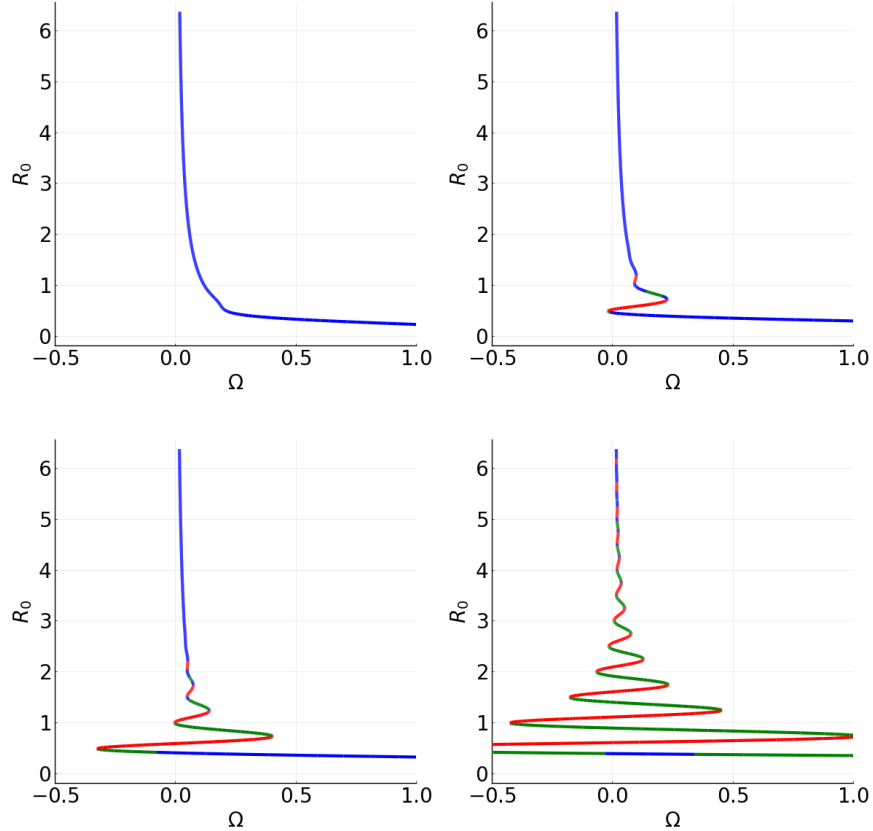
Figure 6.2: Dependence of the orbital radius on the dimensionless bath rotation rate, Ω, for circular orbits moving in response to a Coriolis force for dimensionless mass $M = 0.14$. The orbital radius is normalised by the wavelength of the pilot wave, corresponding to $R_0 = r_0/2\pi$ in dimensionless variables. Different panels correspond to different values of the memory parameter, Γ, with (a) $\Gamma = 0.5$, (b) $\Gamma = 0.7$, (c) $\Gamma = 0.8$ and (d) $\Gamma = 0.9$. The orbital states are orientated clockwise, i.e. $\omega < 0$, so that all anticyclonic states arise for $\Omega > 0$, with cyclonic states for $\Omega < 0$. Stable circular orbits are indicated in blue, with monotonic and oscillatory instabilities highlighted in red and green, respectively. Stable spin states, for which $\Omega = 0$, appear for $\Gamma \geq 0.7$, with all spin states at emerging for larger orbital radius being unstable.
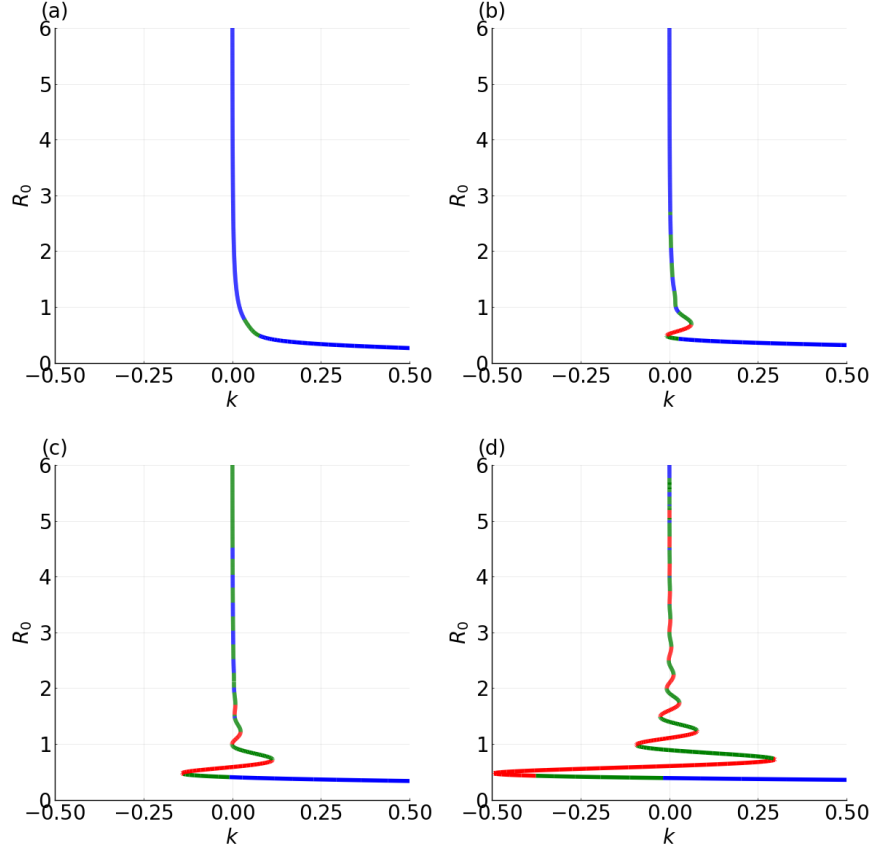
Figure 6.3: Dependence of the orbital radius on the dimensionless spring constant, k, for circular orbits moving in response to a linear spring force for dimensionless mass $M = 0.14$. The orbital radius is normalised by the wavelength of the pilot wave, corresponding to $R_0 = r_0/2\pi$ in dimensionless variables. Different panels correspond to different values of the memory parameter, Γ, with (a) $\Gamma = 0.5$, (b) $\Gamma = 0.7$, (c) $\Gamma = 0.8$ and (d) $\Gamma = 0.9$. In contrast to the Coriolis force case (figure 6.2), the orbital curves are identical for counter-clockwise ($\omega > 0$) and clockwise ($\omega < 0$) orbits. The colour code for stability is the same as in figure 6.2.
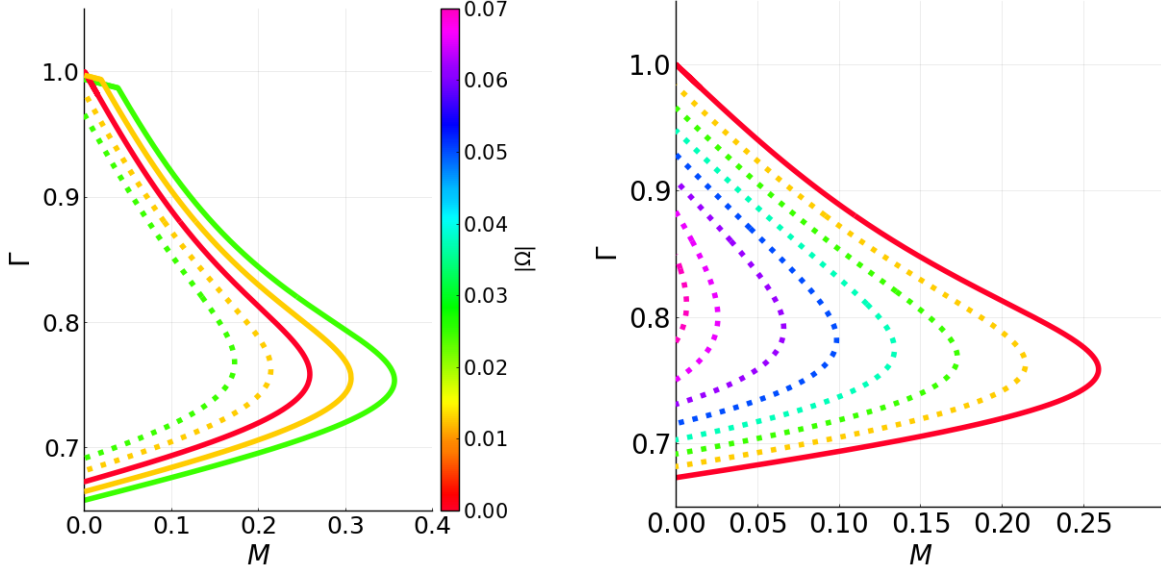
Figure 6.4: The influence of a weak Coriolis force on the form of the stability boundary for spin states. (a) The stability boundary for cyclonic (dotted) and anticyclonic (solid) circular orbits for different values of the frame rotation rate, $|\Omega|$. The stability boundary in the absence of an applied force (corresponding to spin states) is highlighted in red. Circular orbits are stable within the stability boundary. (b) The shrinking of the stability region for cyclonic orbits as $|\Omega|$ is increased.

6.3.2   Quantitative effect of small rotation on spin states

We proceed by developing an asymptotic framework for characterising the form of the stability boundaries in the low-inertia, high-memory limit, $M \ll 1, \sigma \to 0$. Our results may be used to explain the qualitative differences in the stability boundary for a particle executing cyclonic and anticyclonic orbits in response to a Coriolis force.

Leading order solution for $M = 0$

As observed in figure 6.4(a), the corners in the stability boundary arise for small dimensionless mass and high memory. To obtain the leading-order behaviour, we begin by setting $M = 0$ and taking $\sigma \to 0$. From graphical inspection of figure 6.4(c), we observe that $\sigma = O(\Omega)$. By expanding the force balances (6.2) for large memory and applying the procedure outlined in appendix E.1, we reduce the force balance equations to

$$0 = \frac{\mathrm{J}_0(r_0)\mathrm{J}_1(r_0)}{\sigma} + \Omega \omega r_0 + O(\sigma) \tag{6.7a}$$

$$0 = \frac{\mathrm{J}_0^2(r_0)}{\sigma} - \frac{1}{\sigma}\left(1 - r_0^2 \omega^2\right) + O(\Omega). \tag{6.7b}$$

We recognise that the Coriolis force is balancing the mean wave force in (6.7a), similar to the physical picture in §5.2. For fixed σ, the governing equations (6.2) are invariant under the transformation $(\Omega, \omega) \mapsto (-\Omega, -\omega)$: replacing Ω with $-\Omega$ corresponds to reflecting the

141

entire system in the xy plane, and replacing ω with $-\omega$ has the same effect, so applying both transformations to an orbital solution leads to another orbital solution. Consequently, the expansions for r_0 and s in terms of Ω should involve only even powers. Thus,

$$r_0 = R + \Omega^2 r_2 + O(\Omega^4) \quad \text{and} \quad s = s_0 + \Omega^2 s_2 + O(\Omega^4), \tag{6.8}$$

where R is the radius of high-memory spin states, which we identify as follows. As $\sigma = O(\Omega)$, the radial force balance (6.7a) indicates that

$$\mathrm{J}_0(r_0)\mathrm{J}_1(r_0) = O(\Omega^2) = O(\sigma^2), \tag{6.9}$$

which implies that the orbital radius lies close to either a zero of J_0 or J_1. As outlined by Oza et al. [79], circular orbits with orbital radii satisfying $|\mathrm{J}_1(r_0)| \ll 1$ are all unstable in the limit $\sigma \ll 1$. Thus, the orbital radii of interest satisfy $\mathrm{J}_0(R) = 0$, where R appears in (6.8). Finally, we use the tangential force balance (6.7b) and the property $\mathrm{J}_0(R) = 0$ to deduce that $r_0^2\omega^2 = 1 + O(\Omega^2)$, indicating that the orbital speed is close to the maximum walking speed. Consequently, we may eliminate ω from further consideration by using the relationship $\omega = R^{-1} + O(\Omega^2)$.

Now that we have expanded the force balance equations, we proceed to consider the stability problem, for which we write $s = \mathrm{i}S$, where the (real) destabilisation frequency, S, is expanded as $S = S_0 + S_2\Omega^2 + O(\Omega^4)$. Specifically, we seek imaginary roots of $\mathscr{G}_{\mathrm{Cor.}}$, where $\mathscr{G}_{\mathrm{Cor.}}$ is defined in (6.6a). To seek an asymptotic solution, we expand

$$\begin{aligned}
\mathscr{A} &= a_0 + \Omega a_1 + O(\Omega^2), \quad \mathscr{B} = b_0 + \Omega b_1 + O(\Omega^2), \\
\mathscr{C} &= c_0 + \Omega c_1 + O(\Omega^2), \quad \mathscr{D} = d_0 + \Omega d_1 + O(\Omega^2).
\end{aligned} \tag{6.10}$$

For the case $M = 0$, we obtain

$$\begin{aligned}
a_0 &= \mathrm{i}S_0 + \mathcal{C}_{0,1}(\mathrm{i}S_0) + \mathcal{I}_{1,1}(\mathrm{i}S_0), \quad b_0 = -S_0, \\
c_0 &= 2\omega - S_0, \quad d_0 = \mathrm{i}S_0 + \mathcal{C}_{0,1}(\mathrm{i}S_0) - \mathcal{I}_{1,1}(\mathrm{i}S_0).
\end{aligned} \tag{6.11}$$

We may further simplify these expressions by examining the form of the stability integrals defined in (6.5), which are each of the form of the Laplace transform of a periodic function. Following a change over integration variable, we recast the stability integrals (6.5) as

$$\mathcal{I}_{m,1}(s) = \frac{1}{2|\omega| \left(1 - \mathrm{e}^{-\frac{2\pi s}{|\omega|}}\right)} \int_0^{2\pi} \mathrm{J}_{2m}\left(2r_0 \sin\left(\frac{t}{2}\right)\right) \mathrm{e}^{-\frac{st}{|\omega|}} \, \mathrm{d}t, \tag{6.12}$$

$$\mathcal{C}_{m,1}(s) = \frac{1}{2|\omega| \left(1 - \mathrm{e}^{-\frac{2\pi s}{|\omega|}}\right)} \int_0^{2\pi} \mathrm{J}_{2m}\left(2r_0 \sin\left(\frac{t}{2}\right)\right) \cos(t)\mathrm{e}^{-\frac{st}{|\omega|}} \, \mathrm{d}t, \tag{6.13}$$

$$\mathcal{S}_{m,1}(s) = \frac{1}{2\omega \left(1 - \mathrm{e}^{-\frac{2\pi s}{|\omega|}}\right)} \int_0^{2\pi} \mathrm{J}_{2m}\left(2r_0 \sin\left(\frac{t}{2}\right)\right) \sin(t)\mathrm{e}^{-\frac{st}{|\omega|}} \, \mathrm{d}t, \tag{6.14}$$

where we recall that $\omega = \frac{1}{R} + O(\Omega^2)$. By using that S is real, we show in appendix E.1.2 that $\mathcal{I}_{m,1}(\mathrm{i}S)$ and $\mathcal{C}_{m,1}(\mathrm{i}S)$ are both imaginary, yet $\mathcal{S}_{m,1}(\mathrm{i}S)$ is real. Consequently, a_0 and d_0

are both imaginary in the stability function expansion, with b_0 and c_0 both being real. To leading order, the stability condition becomes

$$\mathcal{G}_0(S_0) = 0, \quad \text{where} \quad \mathcal{G} = \frac{a_0 d_0 + b_0 c_0}{S_0}, \tag{6.15}$$

which represents a single real equation to solve for the unknown destabilisation frequency, S_0. The four positive solutions to (6.15) for the destabilisation frequency, S_0, are found to be

$$S_0 \in \{0.556, 0.982, 1.375, 1.686\}. \tag{6.16}$$

This numerical solution to the asymptotic stability problem indicates the presence of different instability mechanisms, each associated with a different destabilisation frequency. Furthermore, the corner in the stability boundary may be a result of different instability mechanisms dominating for different values of M. To quantitatively explain the corner, and the relationship between the movement of the stability boundaries at $M = 0$ and the sign of Ω, we expand the stability coefficients to first order in Ω.

First order solution for $M = 0$

We showed that $r_0 = R + O(\Omega^2)$ and $s = iS_0 + O(\Omega^2)$ using invariance of the system under the transformation $(\Omega, \omega) \mapsto (-\Omega, -\omega)$. As $\sigma = O(\Omega)$, the first-order correction to the stability problem arises from the correction to the memory, where we express $\sigma = \Omega\sigma_1$ with $\sigma_1 = O(1)$. We solve for a_1, b_1, c_1 and d_1, as introduced in (6.3.2). As $s = iS_0 + O(\Omega^2)$, we expand the stability integrals as

$$\mathcal{I}_m(s) = \mathcal{I}_{m,1}(iS_0) + \sigma_1\Omega\mathcal{I}'_{m,1}(iS_0) + O(\Omega^2), \tag{6.17}$$

from which we write, using (E.4) and $J_0(R) = 0$ to simplify $\mathcal{I}_0(0)$,

$$a_1 = \sigma_1 - 2\omega - \frac{\sigma_1}{\pi\omega^2} \int_0^{2\pi} t^2 J_0\left(2r_0 \sin\left(t\right)\right) \mathrm{d}t + \sigma_1(\mathcal{C}'_{0,1}(iS_0) + \mathcal{I}'_{1,1}(is_0)), \tag{6.18a}$$

$$b_1 = c_1 = iS_0 - \sigma_1 \mathcal{S}'_{0,1}(iS_0), \tag{6.18b}$$

$$d_1 = -\sigma_1 + \sigma_1(\mathcal{C}'_{0,1}(iS_0) - \mathcal{I}'_{1,1}(iS_0)), \tag{6.18c}$$

where we recall that $\omega = \frac{1}{R} + O\left(\Omega^2\right)$.

As $i\mathcal{I}_{m,1}(iS_0)$ is a real function of a real argument, S_0, its derivative with respect to S_0 is also real, and so is $\mathcal{I}'_{m,1}(iS_0)$. Similarly, $\mathcal{S}'_{m,1}(iS_0)$ is imaginary. Consequently, a_1 and d_1 are real, while b_1 and c_1 are imaginary. The first-order stability condition thus becomes

$$\mathcal{G}_1(\sigma_1) = 0, \quad \text{where} \quad \mathcal{G}_1 = \frac{a_1 d_0 + a_0 d_1 + b_0 c_1 + b_1 c_0}{S_0} = 0, \tag{6.19}$$

which represents a single equation to solve for the remaining unknown, σ_1. The results for each possible instability mechanism identified by solving (6.15) are given in table 6.1, for which we consider $\omega < 0$ so that $\Omega > 0$ corresponds to anticyclonic orbits.

143

S_0	σ_1
0.556	-1.200
0.982	0.142
1.375	0.228
1.686	0.0385

Table 6.1: Dimensionless wave decay rate at the onset of instability, $\sigma_1 = \sigma/\Omega$ for each instability mechanism identified by solving (6.15). The instability mechanism with the largest positive value of σ_1 corresponds to the dominant instability observed for anticyclonic spin states, while the instability mechanism with negative σ_1 arises for cyclonic spin states.

Of the four identified instability frequencies for $\omega < 0$, three correspond to $\sigma_1 > 0$, where we recall that $\sigma = \sigma_1 \Omega$ along the stability boundary in the high-memory limit, $0 < \sigma \ll 1$. Consequently, these three instability mechanisms are responsible for destabilising anticyclonic orbits (for which $\Omega > 0$) at $M = 0$ and $\sigma = O(\Omega) > 0$. The onset of the instability corresponding to $S_0 = 1.375$ arises at lower memory than the other two instability mechanisms (as σ_1 is maximised), and thus is the dominant instability. For the destabilisation frequency $S_0 = 0.556$, we note that $\sigma_1 < 0$. Hence, $\sigma > 0$ only when $\Omega < 0$, indicating that cyclonic orbits destabilise via this mechanism.

It is curious how, at infinite memory and zero inertia, cyclonic and anticyclonic orbits destabilise via different instability mechanisms. However, figure 6.4 suggests that the stability boundaries of both cyclonic and anticyclonic spin states are continuous deformations of the free spin state boundary at $\Omega = 0$, which indicates that they should destabilise via the same instability mechanism. This is why the corner in the instability boundary is necessary; while at $M = 0$, $S_0 = 0.556$ does not destabilise for $\sigma > 0$, it does destabilise for $\sigma > 0$ if $M > 0$. For small but finite M, $S_0 = 0.556$ eventually destabilises at lower memory than $S_0 = 1.375$, and this interchange of the dominant instability mechanism manifests as the corner. For $\Omega < 0$, however, there are not any corners in the stability boundary, as only one instability mechanism is present.

To solve for the corner, we include inertia in the asymptotic analysis, writing $M = M_1\Omega + O(\Omega^2)$. Although this expansion does not affect the expansions for $\mathscr{G}_0$ (see (6.15)), it does impact the stability problem for $\mathscr{G}_1$ (see (6.19)). When accounting for $M > 0$, the first-order stability coefficients take the form

$$a_1 = M_1(-S_0^2 - 2\omega^2) + \sigma_1 - 2\omega - \frac{\sigma_1}{\pi\omega^2}\int_0^{2\pi} t^2 \mathrm{J}_0\left(2r_0\sin\left(t\right)\right)\,\mathrm{d}t + \sigma_1(\mathcal{C}'_{0,1}(\mathrm{i}S_0) + \mathcal{I}'_{1,1}(is_0)),$$
(6.20a)

$$b_1 = c_1 = 2M_1\omega\mathrm{i}S_0 + \mathrm{i}S_0 - \sigma_1\mathcal{S}'_{0,1}(\mathrm{i}S_0),$$
(6.20b)

$$d_1 = -M_1 S_0^2 - \sigma_1 + \sigma_1(\mathcal{C}'_{0,1}(\mathrm{i}S_0) - \mathcal{I}'_{1,1}(\mathrm{i}S_0)).$$
(6.20c)

We now solve for M_1 by requiring (6.19) be satisfied for $S_0 = 0.556$ and $S_0 = 1.375$, leading to

$$M_1 = 1.368 \quad \text{and} \quad \sigma_1 = 0.472,$$
(6.21)
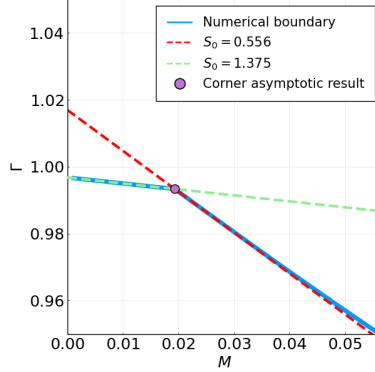
Figure 6.5: The emergence of a corner in the instability boundary in the (M, Γ)-plane for anticyclonic orbits in a rotating frame with angular frequency $\Omega = 0.01$. The curves denote the numerical stability boundary (blue), the asymptotic memory of instability for the instability frequency $S_0 = 0.556$ (red), and the asymptotic memory of instability for the instability frequency $S_0 = 1.375$ (green). The asymptotic result in (6.21) for the memory and inertia at which the corner in the instability boundary occurs overlaid as a purple dot. Notably, the corner arises at the collision of two stability boundaries, with the corner in the stability boundary marking a change in instability mechanism. For sufficiently small M, the memory of instability for $S_0 = 0.556$ exceeds $\Gamma = 1$ (as may be understood from analytical continuation of the stability integrals (6.12)), indicating that this instability mechanism only takes effect at finite M.

from which we can derive the dimensionless $M = M_1\Omega + O(\Omega^2)$ and memory $\sigma = \sigma_1\Omega + O(\Omega^2)$ at which the corner occurs, for small rotation rate Ω. To better understand the relationship between the corners and both instability mechanisms, we plot the asymptotic form of σ for both instability mechanisms over a range of M in figure 6.5, demonstrating how the corners arise at the point where the type of the dominant instability mechanism changes.

We now turn our attention to the broadening of the stability region for anticyclonic spin states. As the instability frequency $S_0 = 0.556$ is responsible for most of the stability boundaries in figure 6.4, we demonstrate that as $\sigma_1 < 0$, the onset of instability via this instability mechanism is suppressed by bath rotation in the opposite direction of the circular orbit, and is enhanced otherwise. This adds to the physical picture presented by Oza et al. [79], where weak bath rotation destroys the degeneracy of orbits with positive and negative angular frequencies, in a manner similar to Zeeman splitting. However, in the presence of a sufficiently large bath rotation rate, the Zeeman splitting is destroyed, as no more stable cyclonic orbits then exist.

We note that for any $\Omega \neq 0$, circular orbits cannot be stabilised at arbitrary memory, even at zero inertia, unlike the case of a free particle [35, 82], where spin states can be stabilised at arbitrarily high memory by lowering the particle inertia. While this observation makes sense for cyclonic orbits, as we have argued that cyclonic orbits are destabilised by rotation, this destabilisation also holds true for anticyclonic orbits, which is less intuitive. Although the anticyclonic stability boundary appears to increase in size for higher Ω and M, this is not the case at very high memory, where the onset of the $S_0 = 1.375$ instability leads to instability at high memory. In contrast, we will show, in 6.4, that the same does not
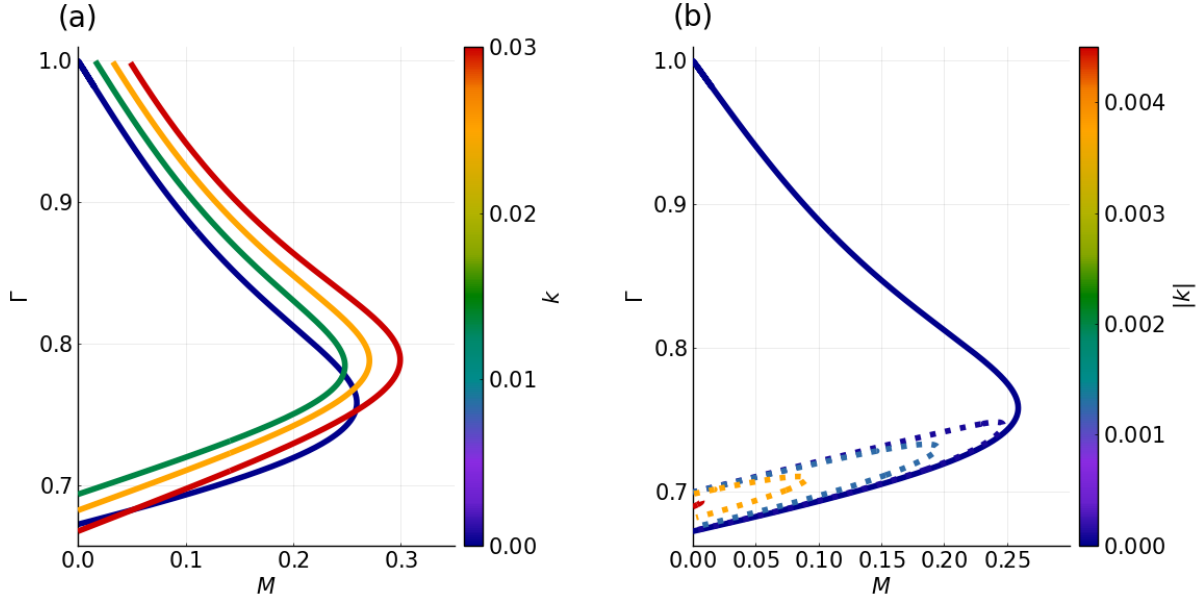
Figure 6.6: The influence of a weak linear spring force on the form of the stability boundary for spin states. (a) The stability boundary for an attractive spring force, $k > 0$. The stability boundary in the absence of an applied force (corresponding to spin states) is highlighted in red. Circular orbits are stable within the stability boundary. (b) The stability boundary for a repelling spring force, $k < 0$. The stability region decreases in size as k becomes increasingly negative (i.e. repellent). For both attracting and repelling spring forces, there is a jump in the stability region even for an infinitesimally weak applied force.

happen in the presence of a spring force, and the stability boundary at high memory does increase in size for an attractive spring force.

Now that we have discussed the behaviour of stability of spin states in the presence of weak rotation, including the onset of corners, and the contrasting behaviour of anticyclonic and cyclonic orbital states, we turn our attention to the effect of a weak linear central force on the stability of spin states.

6.4 Spin states in the presence of a weak central force

In contrast to the Coriolis force, circular orbits in a linear spring force are invariant to the orbital direction, corresponding to the sign of ω. Thus, we no longer distinguish between anticyclonic and cyclonic orbital states. Instead, the sign of the central force constant determines whether the central force is attracting or repelling. For a Coriolis force, we observed that bath rotation stabilised anticyclonic orbits, and destabilised cyclonic orbits. Similarly, it is expected that an attractive central force should enlarge the region of stability of spin states, while a repulsive spring force should shrink the region of stability of a spin state. We assess the accuracy of this intuition in figure 6.6.

We see that for small M and $\Gamma \approx 0.7$, an attractive central force may destabilise circular orbits, whereas the introduction of a repulsive central force discontinuously shrinks the sta-
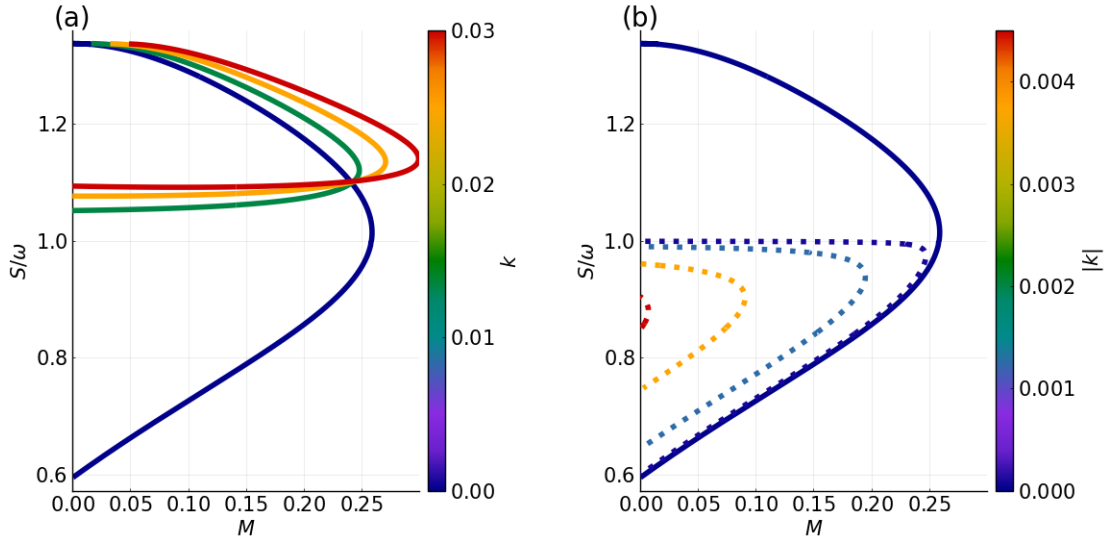
Figure 6.7: The variation of the instability frequency, S, normalised by the orbital frequency, ω, along the stability boundary for a particle executing circular orbits in response to a weak linear spring force. The stability boundary in the absence of an applied force is highlighted in red, and orbits are stable within the stability boundary. We present results for (a) an attractive spring force, $k > 0$ (solid curves), and (b) a repulsive spring force, $k < 0$ (dotted curves). The introduction of a central force discontinuously changes the size of the stability region, even for an arbitrarily small attractive or repulsive spring force. We rationalise this splitting of the stability region in terms of the loss of translational invariance, leading to the destabilisation of the previously trivial iω eigenvalue, as discussed in §6.4, when the particle motion is subjected to a central force, which fixes the orbital centre. Consequently, the attractive and repulsive stability boundaries both trace the line $S/\omega = 1$ for small spring coefficient, $|k| \ll 1$.

bility boundaries. Paradoxically, this implies that near $\Gamma = 0.7$ and $M = 0$, a spin state may destabilise in weak attractive central force, but remain stable in a weak repulsive central force. To better understand the mechanisms behind the counter-intuitive behaviours of the stability boundaries, we plot the destabilisation frequency S scaled by the orbital frequency ω along the stability boundary in figure 6.7.

We remark that introduction of a central force breaks translational symmetry, as there is now a preferred orbital centre. This causes the iω eigenvalue, a previously trivial eigenvalue in the absence of a central force, to no longer be a trivial eigenvalue. Thus, spin states may destabilise by this new iω instability mechanism, leading to qualitatively different dynamics compared to that of a free particle. Figure 6.7 then indicates that the paradoxical destabilisation of circular orbits lying between the green and red boundaries in figure 6.6(a) in the presence of an arbitrarily small attractive central force, orbits which would remain stable in the presence of a sufficiently small repulsive central force, and the discontinuous shrinking of the stability boundaries for a repulsive central force, can be explained by the destabilisation of the previously trivial iω eigenvalue.

S_0	σ_1
0.556	-1.369
0.982	-0.0364
1.375	-0.103
1.686	-0.016

Table 6.2: Dimensionless wave decay rate at the onset of instability, $\sigma_1 = \sigma/k$ for each instability mechanism identified by solving (6.15). As all $\sigma_1 < 0$, we conclude that spin states are stabilised at infinite memory by an attractive spring force, which we observe graphically in figure 6.6.

We now solve the analogous stability problem for the linear central force. We note that the leading order solution corresponds to the stability of spin states, and thus agrees with the leading order stability problem in a rotating frame. Thus, all of the stability coefficients in §6.3.2 agree with those in the central force problem, and the instability frequencies are given by (6.16). For the first order problem, where we expand $\sigma = \sigma_1 k + O(k^2), r_0 = R + O(k^2)$ and similar, we note that $\mathscr{B}$ and $\mathscr{C}$ differ between the Coriolis and central force systems, as seen in (6.3). The corresponding first-order stability coefficients are given by

$$a_1 = \sigma_1 - 2\omega - \frac{\sigma_1}{\pi\omega^2} \int_0^{2\pi} t^2 \mathrm{J}_0 \left(2r_0 \sin\left(t\right)\right) \, \mathrm{d}t + \sigma_1(\mathcal{C}'_{0,1}(\mathrm{i}S_0) + \mathcal{I}'_{1,1}(is_0)), \tag{6.22a}$$

$$b_1 = c_1 = -\sigma_1 \mathcal{S}'_{0,1}(\mathrm{i}S_0), \tag{6.22b}$$

$$d_1 = -\sigma_1 + \sigma_1(\mathcal{C}'_{0,1}(\mathrm{i}S_0) - \mathcal{I}'_{1,1}(\mathrm{i}S_0)). \tag{6.22c}$$

Solving the associated stability problem as in §6.3.2, we solve for σ_1 and store the results in table 6.2.

We thus observe that at high memory, attractive central forces stabilise spin states, but at low memory, attractive central forces do not stabilise spin states, until the central force is sufficiently strong. The converse is true in the rotating frame; at high memory, all circular orbits are destabilised by rotation, while at low memory, anticyclonic circular orbits are stabilised by rotation.

6.5 Discussion

We have characterised the types of instabilities that spin states may undergo when subjected to a weak applied force, focusing on the cases of a Coriolis force and a linear spring force. When one regards spin states as a hydrodynamic analog of the classical model of the electron [82], our analysis highlights the response of the electron to different external forces. While only the lowest orbital radii spin states are stable, the addition of an external attractive spring force stabilises spin states of larger orbital radius. Curiously, however, bath rotation was not found to stabilise spin states of larger radius. The absence of large stable spin states in the rotating frame leads to a series of interesting questions: what causes these higher order spin states to destabilise, and what can stabilise them? Can we stabilise them with any Coriolis-type force, like a magnetic field?

Our study of spin state stability remphasises the importance of symmetry on orbital stability. For orbital motion in a rotating frame, we demonstrated, in chapter 2, that the onset of orbital stability arises due to resonant instabilities, which have their origins in the quasi-monochromaticity of the pilot-wave. However, chapters 3 and 4 show that the loss of translational symmetry imposed by the fixed centre of the central force leads to the non-resonant instability dominating the resonant instabilities, giving rise to many unusual phenomena. In the spin state problem, we showed, in §6.4, that the loss of translational symmetry accompanying the introduction of an arbitrarily weak spring force can cause the previously trivial eigenvalues $\pm i\omega$ to destabilise, leading to discontinuous changes in the spin state stability boundary for attractive and repulsive spring forces. We conclude that the variety of behaviours possible under applied forces of different symmetries adds to the richness of the generalised pilot-wave framework.

We note that the stability region for spin states was universally largest for the limit of vanishing inertia, regardless of the form or magnitude of the external force. This observation supports prior claims [14, 48, 82] that quantum-like behaviour is most likely to occur in this low-inertia limit. We also note that many spin states may be stabilised by a weak spring force for sufficiently weak inertia and high memory, which we investigated in chapter 5. This parameter regime thus appears to be ideal for investigating other existing hydrodynamic quantum analogs, such as diffraction or tunnelling, and may provide a fertile hunting ground for new exotic quantum analogs.

We end our exploration of orbital stability by considering the instability mechanisms of very large radius circular orbits.

Chapter 7

The end of orbital quantisation in classical pilot-wave dynamics

7.1   Introduction

Throughout this thesis, we have considered various types of quantised circular orbits, from the standard types [43, 53, 79, 80] considered in chapters 2 and 3 comprising of the stable orbital radii in between the monotonic and wobbling instability regions, to the non-resonant islands in chapter 4, and the sharply quantised states in chapter 5. Previously, we talked about the various factors contributing to the onset of quantisation. In this chapter, we discuss the instability mechanism that terminates all of the above types of quantisation.

Although several orbital states may be accessed in the laboratory, the orbital quantisation does not continue for arbitrarily large orbital radius. Oza [77] demonstrated that the stability problem for orbits of sufficiently large radius reduces to that of rectilinear walkers, and argued that such orbits are not quantised. Notably, rectilinear walkers destabilise at sufficiently high memory and the instability frequency is such that the length scale over which the droplet speed oscillates is comparable to the Faraday wavelength, λ_F [4, 35, 56]. Specifically, the speed oscillation length, λ_O, is defined in terms of the steady propulsion speed, U, and instability period, $T_O = 2\pi/S$, as $\lambda_O = UT_O$, or $\lambda_O = 2\pi U/S$, where S is the destabilisation frequency [35]. We may equivalently express the ratio of the speed oscillation length to the Faraday wavelength as

$$\frac{\lambda_O}{\lambda_F} = \frac{2\pi U}{S\lambda_F} = \frac{Uk_F}{S}, \tag{7.1}$$

where $k_F = 2\pi/\lambda_F$ is the Faraday wavenumber. Consequently, λ_O/λ_F may be characterised in terms of the relative magnitude of the droplet speed to the instability frequency. Our study focuses on the relationship between the perturbed oscillation length, λ_O, and the Faraday wavelength, λ_F, for circular orbits of large radius, for which speed oscillations dominate wobbling and monotonic instabilities, leading to the termination of all types of orbital quantisation. Particular attention will be paid to parameter regimes for which λ_O/λ_F is close to one, thus representing a resonance between speed oscillations and the wavelength of the guiding quasi-monochromatic wave field. A careful asymptotic treatment will be required for dealing with the near-resonant regime, which may not be adequately captured

by extending the asymptotic framework developed by Oza [77] for large circular orbits.

The generalised pilot-wave framework (GPWF) represents a parametric extension of the stroboscopic model of Oza *et al.* [78], in which the relative magnitudes of particle inertia, drag and wave force may assume any values. It was introduced by Bush [13] as a means to explore classical pilot-wave dynamics in a parameter regime inaccessible to the walker system. In this work, we adapt the GPWF to examine the classical pilot-wave dynamics of a particle in a rotating frame, giving particular attention to the disappearance of orbital quantisation when speed oscillations become the dominant instability mechanism. In §7.2, we outline the governing equations of the dynamical system of interest, formulate the linear stability problem and describe a numerical method for computing stability boundaries. We then proceed to delineate the various large radius asymptotic regimes for the stability problem for the quasi-rectilinear instability: the rectilinear regime (§7.4), for which λ_O is not too close to λ_F, and the transition regime (§7.5), for which the resonance induced by speed oscillations is enhanced (i.e. $\lambda_O \approx \lambda_F$).

7.2 Classical pilot-wave dynamics

The generalised pilot-wave framework (GPWF) captures the key features of the walking-droplet system, specifically the resonance between particle and wave and the monochromatic wave field, while neglecting extraneous details of the hydrodynamic system. Oza et al. [82] used the GPWF to examine the stability of hydrodynamic spin states, as may arise when a particle follows a circular trajectory, confined by its pilot-wave field. Durey et al. [35] demonstrated the instability of the rectilinear walking state to in-line oscillations with wavelengths comparable in size to the wavelength of the pilot wave, a feature not reported by Oza et al. [78] in their examination of the walker system. Durey and Bush [31] present a comprehensive treatment of two-dimensional free-particle motion in the GPWF, and delineated distinct regimes marked by spin states, rectilinear motion with over- and under-damped in-line oscillations and erratic particle motion. In our work, we demonstrate that the appearance of an instability analogous to the rectilinear instability is directly responsible for the disappearance of orbital quantisation. In addition, we highlight the mathematical difficulties introduced by the near-resonance between the wavelength of the pilot-wave, and the wavelength of speed oscillations.

Using the GPWF introduced in §4.2, we consider the motion of a vibrating particle that is propelled by the slope of its self-generated quasi-monochromatic wave field. The guiding, or 'pilot' wave, is the continuous superposition of axisymmetric waves generated by the particle vibration, centred along the particle's path and decaying exponentially in time. When the particle is additionally subjected to a Coriolis force, the dimensionless pilot-wave system may be expressed as [31, 79]

$$M\ddot{\boldsymbol{x}}_p + \dot{\boldsymbol{x}}_p = -\nabla h(\boldsymbol{x}_p, t) - \boldsymbol{\Omega} \times \dot{\boldsymbol{x}}_p, \tag{7.2a}$$

$$h(\boldsymbol{x}, t) = \int_{-\infty}^{t} \mathrm{J}_0(|\boldsymbol{x} - \boldsymbol{x}_p(s)|) \mathrm{e}^{-\sigma(t-s)} \, \mathrm{d}s, \tag{7.2b}$$

where $\boldsymbol{x}_p(t)$ is the particle position at time t, and $h(\boldsymbol{x}, t)$ is the accompanying pilot wave. The pilot-wave system is defined in terms of three dimensionless parameters: $M > 0$ prescribes

the particle inertia-to-drag ratio; $\sigma > 0$ is the wave decay rate, for which the wave longevity, and thus particle path memory, increase as σ decreases; and $\boldsymbol{\Omega} = \Omega\hat{z}$ is the rotation vector, which lies orthogonal to the plane of the particle's motion, thereby inducing orbital motion. It is often convenient, however, to characterise the pilot-wave dynamics in terms of the memory parameter $\Gamma = 1 - \sqrt{2}\sigma$ [13, 35, 82], which increases with increasing path memory; in particular, $\Gamma = 0$ corresponds to the particle propulsion threshold in the absence of a Coriolis force, while $\Gamma = 1$ corresponds to the limit of zero wave decay, and thus infinite path memory. Finally, as the Coriolis force has the same mathematical structure as the magnetic force on a moving charge [43], the pilot-wave system (7.2) is analogous to the motion of a charge in an externally applied magnetic field. The dimensionless parameters are summarised in table 4.1.

This system is the same as in §6.2, where we now only consider a rotating frame. The stability problem is then given in §6.2.2, where we eliminate the Coriolis force by using the radial force balance (6.1), leading to the stability coefficients

$$\mathscr{A}(s) = Ms^2 - \frac{2}{r_0}\frac{\partial \mathcal{I}_0(0)}{\partial r_0} - 2\mathcal{I}_0(0) + \sigma + s + \mathcal{C}_0(s) + \mathcal{I}_1(s), \tag{7.3a}$$

$$\mathscr{B}(s) = M\omega s - \frac{(\sigma - s)}{r_0\omega}\frac{\partial \mathcal{I}_0(0)}{\partial r_0} - \mathcal{S}_0(s), \tag{7.3b}$$

$$\mathscr{C}(s) = M\omega s + 2\omega + \frac{(\sigma + s)}{r_0\omega}\frac{\partial \mathcal{I}_0(0)}{\partial r_0} - \mathcal{S}_0(s), \tag{7.3c}$$

$$\mathscr{D}(s) = Ms^2 + s - \sigma + \mathcal{C}_0(s) - \mathcal{I}_1(s).\mathcal{I}_0(0) = \frac{1}{\sigma}\left(1 - r_0^2\omega^2\right), \tag{7.3d}$$

where $\mathcal{I}, \mathcal{C}$ and $\mathcal{S}$ are defined in (6.4). The stability integrals may be evaluated in terms of complex Bessel functions, as in §4.10, leading to

$$\mathscr{A}(s) = Ms^2 + \frac{1}{r_0\omega}\left(\frac{i}{r_0} - f_{01}(\beta, r_0)\right) + \frac{1}{\omega}\left[f_{11}(\eta, r_0) - f_{00}(\beta, r_0)\left(1 + \frac{\beta\eta}{r_0^2}\right)\right], \tag{7.4a}$$

$$\mathscr{B}(s) = M\omega s - \frac{2is}{r_0^2\omega^2} + \frac{1}{r_0\omega}\left[\left(\frac{s}{\omega} - \beta\right)f_{01}(\beta, r_0) + \eta f_{01}(\eta, r_0)\right], \tag{7.4b}$$

$$\hat{\mathscr{C}}(s) = M\omega s + 2\omega + \frac{1}{r_0\omega}\left[\left(\frac{s}{\omega} + \beta\right)f_{01}(\beta, r_0) + \eta f_{01}(\eta, r_0)\right], \tag{7.4c}$$

$$\mathscr{D}(s) = Ms^2 + 2s + \frac{\eta}{r_0^2\omega}\left[\beta f_{00}(\beta, r_0) - \eta f_{00}(\eta, r_0)\right], \tag{7.4d}$$

and the non-trivial roots of the stability condition satisfy, from (6.6a),

$$\mathscr{G}(s) = \frac{\mathscr{A}(s)\mathscr{D}(s) + \mathscr{B}(s)\mathscr{C}(s)}{s(s^2 + \omega^2)} = 0. \tag{7.5}$$

7.3   Stability regimes

Before characterising the various dynamical regimes arising in the orbital stability problem, we first briefly recapitulate the findings of Oza *et al.* [77, 79, 82] germane to our study. In
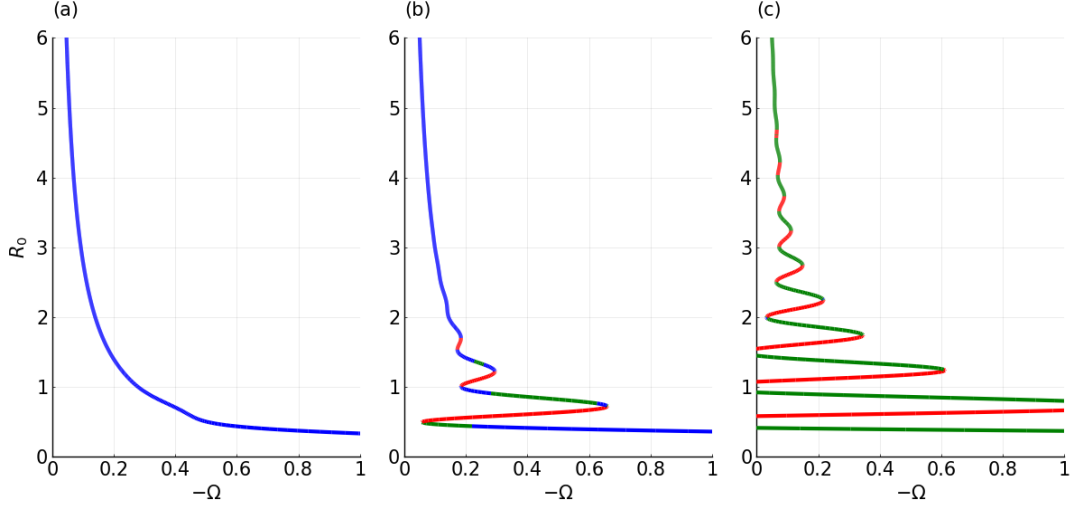
Figure 7.1: Dependence of the orbital radius, $R_0 = \frac{r_0}{2\pi}$, on the bath rotation rate, Ω, for counterclockwise orbits, $\omega > 0$ and $M = 1.4$. The different panels correspond to different values of the path memory, with (a) $\Gamma = 0.55$, (b) 0.8 and (c) 0.9. We denote stable orbital states in blue, with oscillatory and monotonic instabilities highlighted in green and red, respectively. Notably, fewer stable circular orbits exist as the memory (Γ) is increased, thereby restricting the set of quantised orbits (blue plateaus).

particular, we present the dependence of the orbital radius on the frame rotation rate, Ω, in figure 7.1. As the path memory is increased, circular orbits typically destabilise via either a monotonic (red) or oscillatory (green) instability mechanism. Furthermore, stable plateaus (blue), corresponding to orbital quantisation, exist only for sufficiently small orbital radius; at larger orbital radii (for fixed memory), orbital quantisation ceases to exist. For fixed M, we then characterise the dependence of the orbital stability on the orbital radius and path memory in figure 7.2, where each yellow line in figure 7.2(b) corresponds to a stability curve presented in figure 7.1. Orbital quantisation thus appears in the narrow blue strips between the red and green instability 'tongues' in figure 7.2; it follows, therefore, that orbital quantisation is intrinsically linked to the oscillatory form of the stability boundaries, which we present in figure 7.3 for a wider range of orbital radii, and terminates when the stability boundaries are no longer oscillatory functions of the orbital radius.

By constructing orbital stability diagrams over a wide range of M values (similar to figures 7.2 and 7.3), we observe that the critical memory along the stability boundary saturates at a finite value for sufficiently large orbital radius (see the green plateau in the top-right corner of figure 7.2(b), for example), which indicates that quantised orbital radii exist only up to a critical radius. As our study will demonstrate, this plateau arises for all fixed M, provided that r_0 is sufficiently large, and that orbital quantisation never persists for $\sigma \to 0$. We additionally observe the emergence of an instability peninsula near $R_0 = 0.4$ as M increases, a feature that we explore elsewhere.

To better understand the key features of the stability boundaries, we present the dependence of the critical memory and destabilisation angular frequency on the orbital radius in
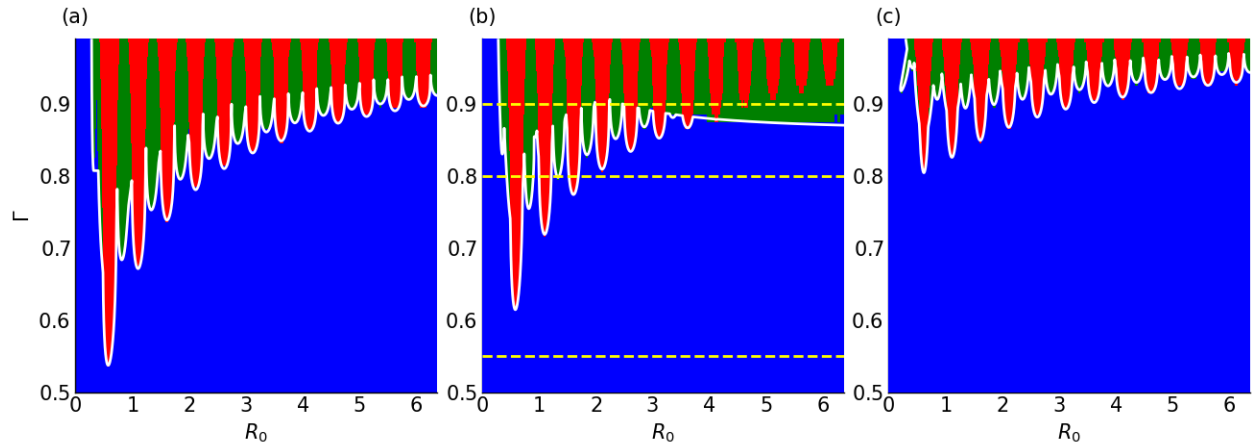
Figure 7.2: Orbital stability diagram in the rotating frame system for different values of the dimensionless mass M, with (a) $M = 0.28$, (b) 1.4, and (c) 5.6. Each point in the stability diagram, at a fixed memory (Γ) and orbital radius ($R_0 = r_0/2\pi$), corresponds to a unique circular orbit, whose stability is indicated by the same colour scheme as in figure 7.1. The horizontal dashed lines in (b) correspond to the three stability curves in figure 7.1. The numerically-evaluated stability boundary is highlighted in white. In the upper right corner of (b), the stability boundaries are no longer oscillatory for larger R_0, in contrast to panels (a) and (c). The instability responsible for this non-oscillatory boundary are speed oscillations along the particle path, considered in §7.4 and 7.5. We see that the onset of the plateau is non-monotonic with M; for both lower and higher values of M, the plateau arises for higher orbital radius. We seek to understand the relationship between the onset of this plateau and M.

figure 7.3. In particular, we normalise the destabilisation angular frequency by two different quantities: (i) the corresponding destabilisation frequency of a rectilinear trajectory [35], denoted S_w; and (ii) the orbital frequency, which we characterise in terms of the quantity $\xi = S/\omega$ (referred to henceforth as the scaled destabilisation frequency or the wobble number). These two quantities help demarcate the main dynamical regimes present for varying orbital radius, which motivates the asymptotic analysis presented in §7.4 and §7.5. Near the stability boundaries, there are three types of instability; the effect of each instability on small perturbations from a circular orbit is presented in figure 7.4, with their respective qualitative behaviour characterised as follows.

1. Monotonic instability: the particle's radius of curvature various monotonically for small perturbations. For weakly unstable circular orbits, this instability typically manifests as a jump to a stable circular orbit of different orbital radius [52, 80].

2. 2-wobble instability: the particle's radius of curvature exhibits growing oscillations, and the corresponding oscillation frequency is comparable to an integer multiple of the orbital frequency. For weakly unstable circular orbits, this instability typically manifests as a wobbling orbit, in which the orbital centre remains roughly constant, but the radius of curvature exhibits bounded oscillations with a frequency approximately twice that of the orbital frequency [52, 80].

3. Quasi-rectilinear instability: the particle's speed exhibits growing in-line oscillations prevalent for the free particle, and the corresponding oscillation frequency, largely independent of r_0, is similar to the destabilisation frequency of free rectilinear propulsion [33, 35]. This instability only arises for circular orbits with small orbital memory and large orbital radius, and is so named due to the similarities with rectilinear trajectories [79]. We see the emergence of two sub-cases depending on the size of $\sigma = S/U$ (corresponding to the ratio λ_F/λ_O when expressed in dimensionless units), which characterises the proximity of the particle's oscillation length to the pilot-wavelength [33]:

    (a) When σ is sufficiently far from unity, the particle oscillation length differs appreciably from the pilot-wavelength, which we refer to as a rectilinear instability.

    (b) When σ is sufficiently close to unity, the perturbed trajectory resonates with the pilot-wavelength, which we refer to as a resonant quasi-rectilinear instability.

    For both instabilities, the particle no longer executes circular motion following a perturbation, and instead traces out erratic orbits [35, 52, 80].

For increasing orbital radius, the dynamical regimes in figure 7.3 are characterised as follows:

1. Wobbling regime: wobbling and monotonic instabilities co-exist, with alternating instability 'tongues' appearing as the orbital radius increases; stable quantised orbits thus arise between consecutive tongues. The tongues are bounded below in memory by the green and red asymptotic curves, respectively, and bounded above by an additional oscillatory instability (purple curve); both the lower and upper bounds increase with orbital radius, and are roughly parallel. The wave field generated over the preceding

156
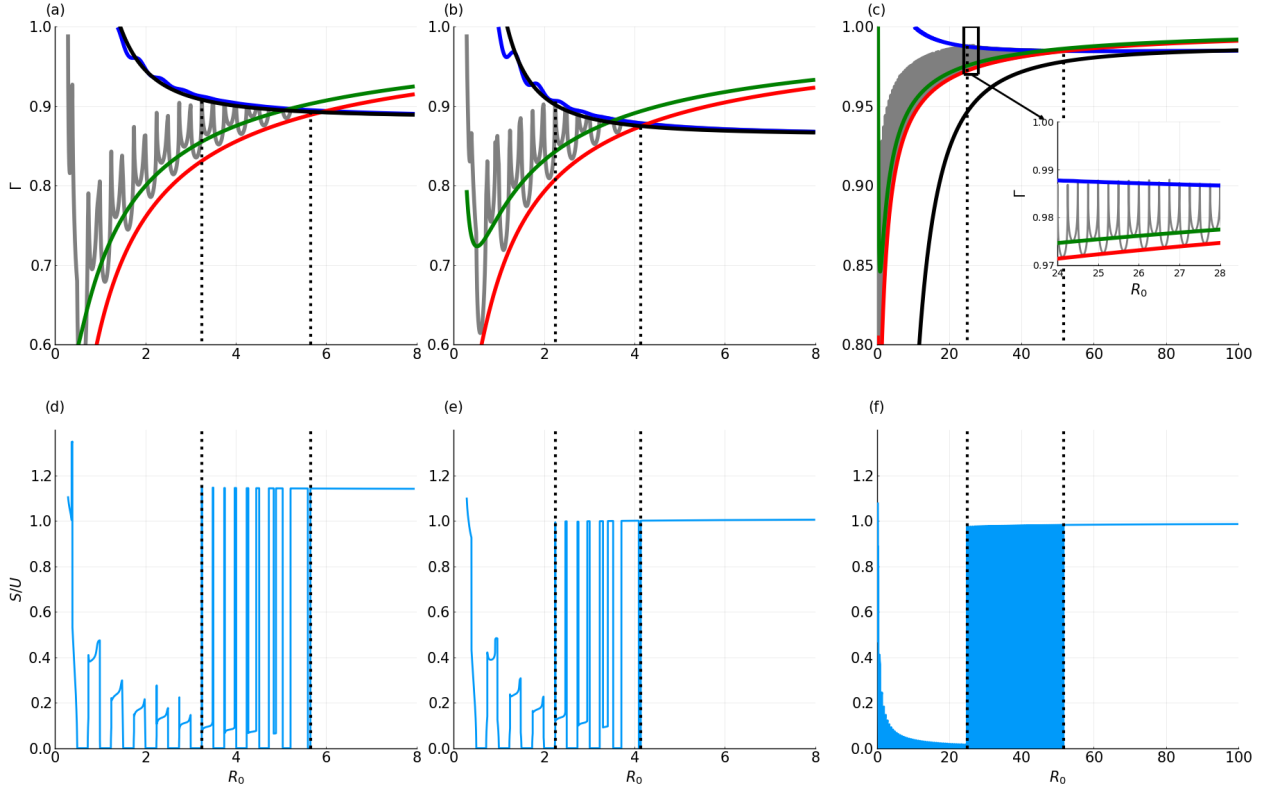
Figure 7.3: Delineation of the qualitative instability regions with increasing orbital radius, for (a) $M = 0.28$, (b) 1.4, (c) 5.6. Top row: the numerical stability boundary (grey) is compared to the following asymptotic envelopes: the minimum memory at which monotonic (red) and wobbling (green) instabilities arise [66]; the rectilinear (black; §7.4) and resonant quasi-rectilinear (blue; §7.5) asymptotic envelopes for the quasi-rectilinear instability. We also present the dependence of the destabilisation frequency scaled by the orbital speed (bottom row) on the orbital radius. We note that the dimensionless destabilisation frequency of the quasi-rectilinear instability is very close to the dimensionless orbital speed. Vertical dashed lines demarcate the boundaries between (from left to right) wobbling, intermediate, and quasi-rectilinear regimes.

157
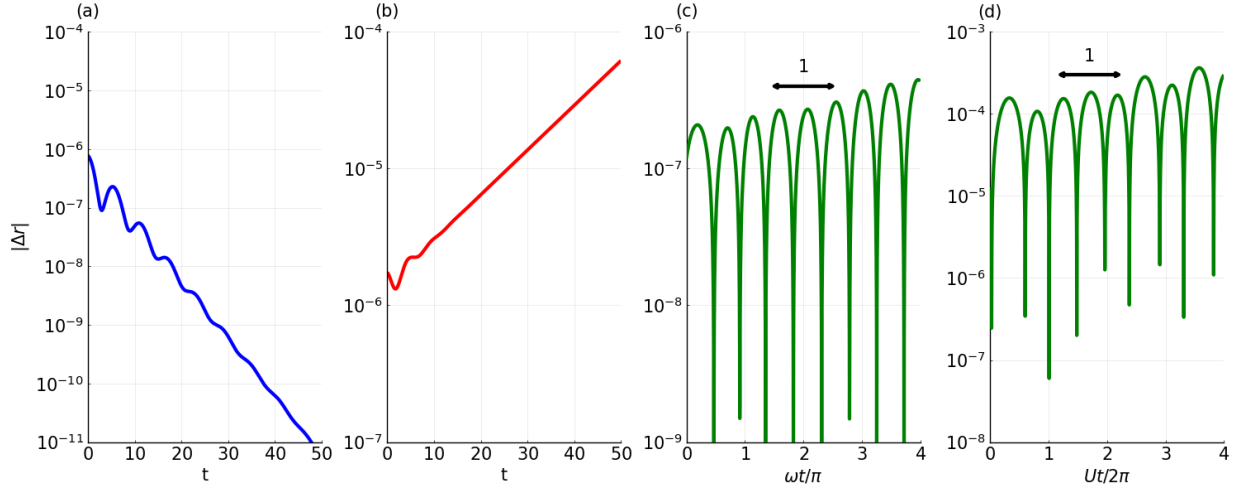
Figure 7.4: Evolution of the perturbed radius of curvature, Δr, for (a) a stable circular orbit, (b) a monotonic instability, (c) a wobbling instability, and (d) an oscillatory (quasi-rectilinear) instability, where $M = 0.7$. (c) The wobbling destabilisation frequency is approximately twice the orbital frequency. (d) The oscillation length for the oscillatory instability is comparable to wavelength of the pilot wave, distinguishing it from the wobbling instability.

orbital period has an appreciable influence on the particle motion, with the geometric constraint imposed by the monochromatic pilot wave resulting in stability tongues that repeat every half wavelength. The asymptotic curves characterising this regime were derived by Liu *et al.* [66].

2. Intermediate regime: the upper bound of each of the wobbling and monotonic instability tongues is reduced by the presence of a quasi-rectilinear instability (black and blue curves), whose critical memory decreases as the orbital radius increases. For sufficiently large orbital radius, the quasi-rectilinear instability eventually intersects the wobbling and monotonic stability tongues, marking the upper quantisation radius. The asymptotic curves characterising the quasi-rectilinear stability are derived in §7.4 and §7.5.

3. Quasi-rectilinear regime: the quasi-rectilinear instability arises at lower memory than the wobbling and monotonic instability tongues for all radii in this regime, thereby precluding orbital quantisation. The circular orbits are dynamically reminiscent of rectilinear trajectories arising in the absence of a Coriolis force, with the critical memory approaching the instability threshold of the rectilinear state [35] as $r_0 \to \infty$, the destabilisation frequency approaching that of the rectilinear state, and the orbital memory decaying to zero. The asymptotic curves characterising this regime are derived in §7.4 and 7.5.

7.3.1 From integral asymptotics to dynamical regimes

Although the stability integrals in (7.3) may be evaluated analytically Liu et al. [66], the purpose of this section is to motivate the different asymptotic scaling relationships arising in various dynamical regimes. In particular, we determine the main contributions to each stability integral arising along a stability boundary ($s = \mathrm{i}S$ with S real) in the large-radius limit ($r_0 \to \infty$), for which each integrand is highly oscillatory. By representing $\cos(\omega t)$ and $\sin(\omega t)$ in terms of complex exponential functions, we first observe that

$$\mathcal{C}_m(s) = \frac{1}{2}\Big(\mathcal{I}_m(s + \mathrm{i}\omega) + \mathcal{I}_m(s - \mathrm{i}\omega)\Big) \quad \text{and} \quad \mathcal{S}_m(s) = \frac{1}{2\mathrm{i}}\Big(\mathcal{I}_m(s - \mathrm{i}\omega) - \mathcal{I}_m(s + \mathrm{i}\omega)\Big),$$
(7.6a)

from which it follows that we may simply focus our attention on the study of $\mathcal{I}_m$. Furthermore, by recognising that $\mathcal{I}_m$ is a Laplace transform of a periodic function, we reduce the integral (6.4a) to

$$\mathcal{I}_m(\mathrm{i}S) = \frac{1}{\omega\left(1 - \mathrm{e}^{-(\beta+\mathrm{i}S)}\right)} L_m(\xi), \quad \text{where} \quad L_m(\xi) = \int_0^{2\pi} \mathrm{J}_{2m}\left(2r_0 \sin\left(\frac{\theta}{2}\right)\right) \mathrm{e}^{-(\beta+\mathrm{i}\xi)\theta}\,\mathrm{d}\theta,$$
(7.7)

$\beta = \sigma/\omega$ is the inverse orbital memory and $\xi = S/\omega$ is the scaled destabilisation frequency (see table 4.1).

Before proceeding with the asymptotic expansions, we first provide a physical interpretation for the integral $L_m(\xi)$. Notably, the argument $2r_0 \sin\left(\frac{\theta}{2}\right) \geq 0$ is the length of the chord spanning between two points lying an angle θ apart on a circle of radius r_0. This distance reflects the influence of the particle's path memory on the evolution of the perturbed trajectory, where the extent of the path memory is controlled by the damping rate $\beta > 0$. Notably, $\mathrm{e}^{-\pi\beta}$ is the damping factor over half an orbital period, accounting for the contribution of waves generated when the particle was last diametrically opposite its current position; likewise, $\mathrm{e}^{-2\pi\beta}$ determines the wave damping factor over a complete orbital period. Finally, the factor $\mathrm{e}^{-\mathrm{i}\xi\theta}$ accounts for oscillations in the perturbed particle trajectory. For large r_0, the integrand of $L_m(\xi)$ is generally highly oscillatory, with dominant contributions arising over non-oscillatory intervals centred about critical points; these critical points are either internal points of stationary phase, denoted $\theta_\pm$ below, or boundary points arising when the argument of J_{2m} vanishes, i.e. at $\theta = 0$ and $\theta = 2\pi$ [8]. We proceed to determine the magnitude of the contribution arising from each critical point.

We first examine the contributions to L_m arising about $\theta = 0$ and $\theta = 2\pi$, which we denote $L_{m,0}$ and $L_{m,2\pi}$, respectively. We derive in appendix A the leading-order contribution $L_{m,0} = O(r_0^{-1})$, which is valid provided that β and ξ are of size at most $O(r_0)$: both of these conditions are satisfied in the cases enumerated below. Using the structure of the integrand, we similarly determine that the leading-order contribution about $\theta = 2\pi$ satisfies $L_{m,2\pi}(\xi) = \mathrm{e}^{-2\pi(\beta+\mathrm{i}\xi)}L_{m,0}(\xi)$; thus, the relative size of $L_{m,0}(\xi)$ and $L_{m,2\pi}(\xi)$ is determined by the orbital damping factor $\mathrm{e}^{-2\pi\beta}$.

We proceed to determine the locations of any internal stationary points, and determine bounds on their existence. If θ is sufficiently far from the integration boundaries so that

159
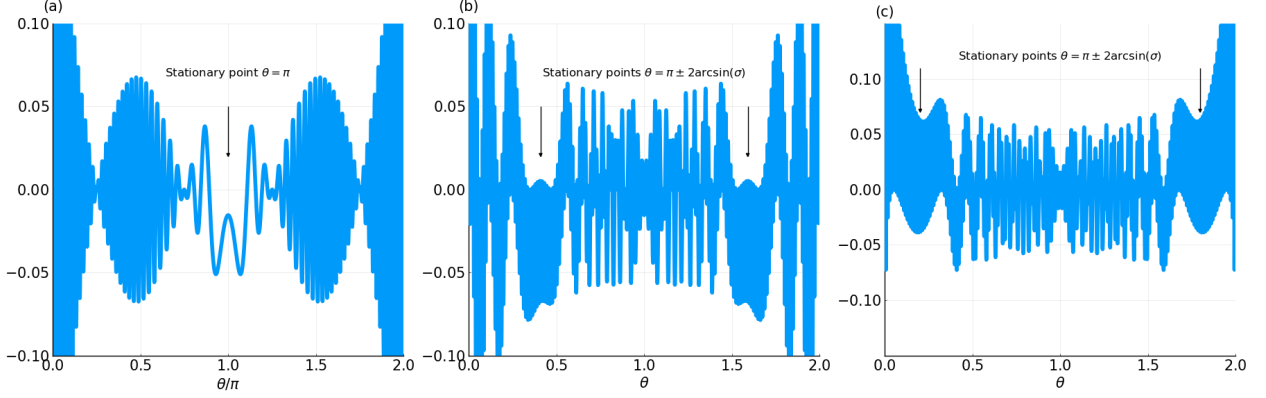
Figure 7.5: The real part of the function $J_0\left(2r_0 \sin\left(\frac{\theta}{2}\right)\right)e^{-i\xi\theta}$ for $r_0 = 100$ and (a) $\xi = 2$, (b) 80, and (c) 95. In each plot, the stationary point(s) are point(s) where the integrand either oscillates more slowly, or does not oscillate about zero. Therefore, these points contribute significantly to the integrals over intervals containing the stationary points. As ξ increases, the stationary point moves from $\theta = \pi$ towards $\theta = 0, \theta = 2\pi$. The merging of the stationary point with the endpoints complicates the mathematical analysis of the stability problem.

$2r_0 \sin\left(\frac{\theta}{2}\right) \gg 1$, we use the large-argument expansion of the Bessel function to approximate [1]

$$J_{2m}\left(2r_0 \sin\left(\frac{\theta}{2}\right)\right)e^{-(\beta+i\xi)\theta} \sim \frac{e^{-\beta\theta}}{2\sqrt{\pi r_0 \sin\left(\frac{\theta}{2}\right)}} \sum_{\pm} e^{-i\phi_\pm(\theta)r_0}e^{\pm i\varphi_m},$$

where $\phi_\pm(\theta) = \sigma\theta \pm 2\sin\frac{\theta}{2}$ is the phase, $\sigma = S/U = \xi/r_0$ is the instability frequency normalised by the orbital speed, and $\varphi_m = \frac{1}{4}\pi(1+4m)$ is a constant phase shift. As $r_0 \to \infty$, the integral is dominated by the non-cancelling contributions arising about the points of stationary phase, corresponding to the points $\theta_\pm = \pi \pm 2\arcsin(\sigma)$ satisfying $\phi'_\pm(\theta_\pm) = 0$. The method of stationary phase (see appendix A) may be used to determine the interior point contributions at $\theta_\pm$ have size

$$L_{m,\theta_\pm} = O\left(\frac{e^{-\beta\theta_\pm}}{r_0}\right).$$

We note that the stationary points, $\theta_\pm$, exist only for $0 < \sigma < 1$; in particular, θ_+ and θ_- coincide in the limit $\sigma \to 0$, whilst $\theta_- \to 0$ and $\theta_+ \to 2\pi$ in the limit $\sigma \uparrow 1$ (corresponding to potential interaction with the boundary points). Moreover, as $\theta_- < \theta_+$ for $0 < \sigma < 1$, we deduce that $e^{-\beta\theta_-} > e^{-\beta\theta_+}$, which implies that the interior contribution at θ_- exceeds that of θ_+.

The relative contributions of the interior and boundary critical points depends on the value of θ_-, which delineate the possible dynamical regimes as follows.

1. The case when $\xi = O(1)$ as $r_0 \to \infty$, corresponding to $\sigma = O(r_0^{-1})$: this regime corresponds to wobbling ($\xi \neq 0$) and monotonic ($\xi = 0$) instabilities. In this limit, the

160

internal points coincide about $\theta = \pi$; as such, there are potential integral contributions about $\theta = 0$, π and 2π, where the relative weight of each of these contributions seemingly decreases consecutively by a factor $\mathrm{e}^{-\beta\pi}$. However, the contribution about $\theta = \pi$ becomes significant when $\mathrm{e}^{\pi\beta}$ scales algebraically with r_0. This contribution corresponds to a strong influence of the waves generated diametrically opposite the particle's current position, as is characteristic of high orbital memory. The dynamics of the wobbling regime was studied by Liu[66], who demonstrated the appearance of the dominant balance $\mathrm{e}^{\pi\beta} = O(r_0^2)$.

2. The case when $\sigma > 1$, with $\sigma = O(1)$ and $\beta = O(r_0)$ as $r_0 \to \infty$: this regime corresponds to the rectilinear instability. As $\sigma > 1$, there are no internal critical points, with the integral expansion dominated by the contribution arising about $\theta = 0$, and the contribution about $\theta = 2\pi$ is exponentially small in comparison. The integrand may thus be approximated, to leading order, by the linear approximation $2r_0 \sin\left(\frac{\theta}{2}\right) \approx r_0\theta$, which locally approximates the circular trajectory by a straight line, as is characteristic of the low-orbital-memory limit, $\omega_{\mathrm{orb}} = O(r_0^{-1})$. We study the dynamics of the rectilinear regime in section 7.4.

3. The case when $\sigma < 1$, with $\sigma = O(1)$ as $r_0 \to \infty$: this regime also corresponds to the quasi-rectilinear instability, but with potential for resonant and non-resonant contributions. As $\sigma < 1$, internal critical points arise at $\theta_\pm = \pi \pm 2\arcsin(\sigma)$, where their relative contribution depends subtly on their proximity to the boundary points $(\theta = 0, 2\pi)$ and the size of β. We consider two subcases:

    (a) When $\mathrm{e}^{-\beta\theta_-}$ is very small, the integral is dominated by the contribution about $\theta = 0$, giving rise to a rectilinear instability. Specifically, we show in §A that $L_{m,\theta_-} = O\left(r_0^{-1}\mathrm{e}^{-2\sqrt{2(1-\sigma)}\beta}\right)$. Thus, the interior contribution can be neglected even in the limit $\sigma \uparrow 1$, for which $\theta_- \sim \sqrt{8(1-\sigma)} \to 0$, provided that $\beta\sqrt{1-\sigma} \to \infty$ as $r_0 \to \infty$.

    (b) When $\mathrm{e}^{-\beta\theta_-}$ fails to be sufficiently small, the internal contributions are significant and must be taken into account. Of particular note is the limit $\sigma \uparrow 1$, for which the near-resonant quasi-rectilinear regime arises when $\beta\sqrt{1-\sigma} = O(1)$ for large r_0 (see section 7.5).

Having motivated the utility of the asymptotic integral expansions in delineating the three asymptotic regimes, we proceed to detail the analysis of the quasi-rectilinear regime in the following sections. We first characterise the rectilinear instability in §7.4 by extending the formalism of Oza *et al.* [79] and §4.3, and demonstrate that when σ is sufficiently close to 1, the rectilinear expansion fails to capture the qualitative behaviour of the quasi-rectilinear instability. In §7.5, we provide the necessary expansions to understand the resonant quasi-rectilinear regime. We then develop a composite asymptotic model for the quasi-rectilinear instability in §7.5.3 that combines ingredients from both the resonant and rectilinear regimes, and provides a uniformly valid model of the quasi-rectilinear instability. This allows us to determine the largest quantised radius for any M.

7.4 Rectilinear expansion

The quasi-rectilinear instability is characterised by a destabilisation frequency similar to the free particle rectilinear instability studied by Durey *et al.* in the GPWF [33, 35], and manifests as in-line speed oscillations. As pointed out by Oza [77], the stability problem for sufficiently large circular orbits reduces to that of a rectilinear state. In other words, for sufficiently large circular orbits, the critical memory of instability is found from the solution of the stability problem of a free rectilinear trajectory. This is significant because, according to equations (3.8) and (3.9) in Liu *et al.* [66], as $r_0 \to \infty$, $\sigma \to 0$ for the wobbling and monotonic instabilities. However, for any fixed M, a free particle in a rectilinear trajectory destabilises at finite σ. Thus, for any M, it is guaranteed that the wobbling and monotonic instabilities will eventually become subdominant to the quasi-rectilinear instability for sufficiently large orbital radius, and thus orbital quantisation will terminate. Our first attempt to analyse the quasi-rectilinear instability will then be via an expansion about the rectilinear instability, which is valid when $\sigma = S/U$ is not close to 1.

We begin by detailing the differences in the scalings in the asymptotic expansion with the wobbling regime [66]. We anticipate that the orbital speed, $U = r_0 \omega$, will approach the rectilinear propulsion speed [35] at large radius, where we recall that $U \leq 1$; as such, we consider $U = O(1)$ in our formulation. Furthermore, as the rectilinear instability boundary occurs at finite σ for all M [33, 35], we deduce that $\sigma = O(1)$ as $r_0 \to \infty$, which implies that the orbital memory $\omega_{\mathrm{orb}} = \omega/\sigma = U/(\sigma r_0) = O(r_0^{-1})$, and thus $\beta = \omega_{\mathrm{orb}}^{-1} = O(r_0)$. Consequentially, we cannot apply the same large-argument asymptotic expansions to the complex-order Bessel functions. Instead, we include higher-order corrections to the procedure presented by Oza [77], which treats the large-radius orbital stability problem as a perturbation of rectilinear motion.

Oza's expansion of the stability problem [77] expanded the integrals by approximating the integrand by its Maclaurin series. More specifically, consider an integral of the form

$$I(r_0) = \int_0^\infty f\left(2r_0 \sin\left(\frac{\omega s}{2}\right)\right) P(\omega s) \mathrm{e}^{-\nu s} \, \mathrm{d}s,$$

where ν is complex with non-negative real part, P is a smooth 2π-periodic function that is either even or odd, and f is a smooth function. Oza's approach was to derive an asymptotic series in powers of r_0^{-2} through direct expansion of the integrand, which can be achieved by recasting the integral as

$$I(r_0) = \frac{1}{U} \int_0^\infty f\left(2r_0 \sin\left(\frac{s}{2r_0}\right)\right) P\left(\frac{s}{r_0}\right) \mathrm{e}^{-\nu s/U} \, \mathrm{d}s. \tag{7.8}$$

To leading order, the stability problem of a large-radius circular orbit reduces to that of a free rectilinear trajectory, which only provides the critical memory of instability in the limit as $r_0 \to \infty$. This formulation does not, however, describe the dependence of the critical memory on r_0, which hides the failure of the rectilinear expansion for larger M. Nor does it accurately describe the rectilinear instability for smaller M when the rectilinear expansion is applicable. The limitations motivate our expansion to $O\left(r_0^{-2}\right)$.

In appendix B, we extend this asymptotic expansion to expand the integrals correct to $O\left(r_0^{-4}\right)$. Specifically, we demonstrate that

$$I_{\text{even}}(r_0) = \frac{1}{U} \int_0^\infty \left(P(0)f(s) + \frac{s^2}{2r_0^2} P''(0)f(s) - \frac{s^3 P(0)}{24r_0^2} f'(s) \right) e^{-\nu s/U} \, \mathrm{d}s + O\left(\frac{1}{r_0^4}\right),$$

$$I_{\text{odd}}(r_0) = \frac{1}{U} \int_0^\infty \left(\frac{s}{r_0} P'(0)f(s) + \frac{s^3}{6r_0^3} P^{(3)}(0)f(s) - \frac{s^4}{24r_0^3} P'(0)f'(s) \right) e^{-\nu s/U} \, \mathrm{d}s + O\left(\frac{1}{r_0^5}\right),$$

where I_{even} and I_{odd} correspond to the cases of P being even and odd, respectively. Observing that the integral expansions form an asymptotic series in powers of r_0^{-2}, we motivate the following expansion of the $O(1)$ quantities U, σ and s in powers of r_0^{-2}:

$$U = U_0 + \frac{U_2}{r_0^2} + O\left(\frac{1}{r_0^4}\right), \quad \sigma = \sigma_0 + \frac{\sigma_2}{r_0^2} + O\left(\frac{1}{r_0^4}\right), \quad s = \mathrm{i}\left(s_0 + \frac{s_2}{r_0^2} \right) + O\left(\frac{1}{r_0^4}\right).$$

The expanded force balance equations are presented in appendix B.2.

The leading order stability problem takes the form $a_0 d_0 = 0$, where the coefficients a_0 and d_0 are all given in appendix B.2. As noted by Oza [77] and in §3.5, a_0 describes the response to the radial force balance of radial perturbations to the circular trajectory, and d_0 describes the response to the tangential force balance of tangential perturbations to the circular trajectory. As we expect circular orbits of large radius to destabilise like a free rectilinear state, and those destabilise via in-line oscillations [33], d_0 is the relevant stability coefficient. This is Oza's result that the stability problem of sufficiently large circular orbits is a perturbation of the stability problem of a free rectilinear state. Numerically, we observe that solutions to the leading order stability problem satisfy $d_0 = 0$ [35, 78], which, in combination with the leading order tangential force balance equations (B.2.12a), prescribe the parameters s_0, U_0 and σ_0.

The first order stability problem takes the form $a_0 d_2 + a_2 d_0 + b_1 c_1 = 0$, which simplifies to

$$a_0 d_2 + b_1 c_1 = 0,$$

upon recalling that $d_0 = 0$. The coefficients b_1, c_1 and d_2 are given in appendix B.2. In figure 7.6, we illustrate the agreement between the critical memory of instability as calculated from numerical solutions to the full stability problem, and from the first-order rectilinear expansion.

For relatively small M, it is seen that the rectilinear expansion does appear to converge to the numerical asymptotic result as $r_0 \to \infty$. However, the rate of convergence appears to slow down as M increases. While for $M = 1.4$, the error in the $O\left(r_0^{-2}\right)$ rectilinear expansion is $O\left(r_0^{-4}\right)$ for $R_0 > 6$, for $M = 4.2$, the corresponding error scales as $O\left(r_0^{-4}\right)$ only for $R_0 > 200$, while for $M = 8.4$, the large radius asymptotic error scales as $O\left(r_0^{-4}\right)$ only for $R_0 > 30000$. This is noteworthy because as figure 7.6(d) demonstrates, beyond about $r_0 = 2\pi R_0 = 1000$, the critical memory of instability no longer oscillates with increasing r_0 for $M = 8.4$, and orbital quantisation has already ceased. The only instability present is the quasi-rectilinear instability, yet the rectilinear expansion visibly overestimates the critical memory of instability. This suggests that another phenomenon is slowing down the convergence for larger M.
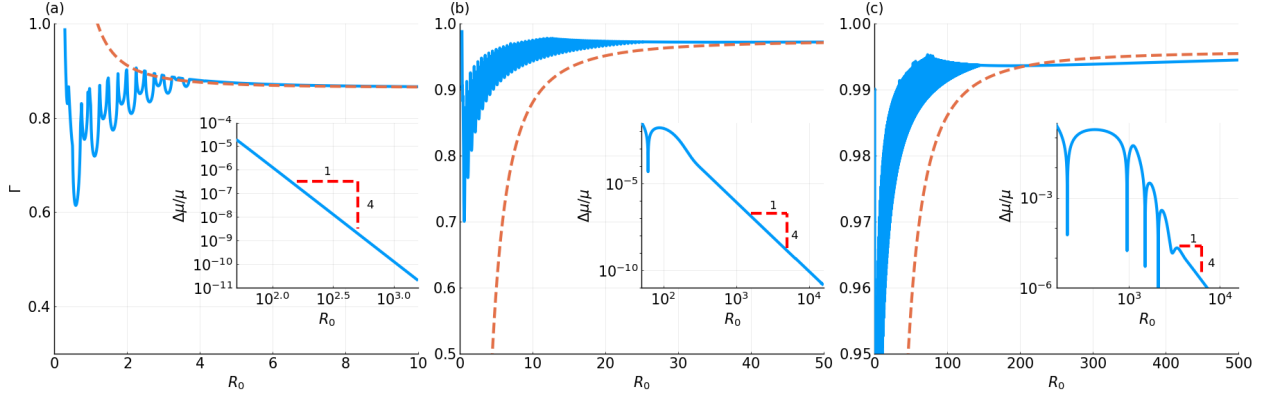
Figure 7.6: Comparison of the numerically computed critical memory of instability (blue) with that predicted by the rectilinear expansion (orange dashed curves) for $M =$ (a) 1.4, (b) 4.2, and (c) 8.6. We remark how, for larger M, the qualitative behaviour of the critical memory of instability predicted by the rectilinear expansion is incorrect unless R_0 is very large. Inset: the relative error in the asymptotic formulation, with the anticipated $O(r_0^{-4})$ scaling.

As demonstrated in section 7.3.1, the rectilinear expansion considers stationary phase contributions from $\theta = 0$ only. Durey et $al.$ [33] showed that the rectilinear state for a free particle satisfies $s_0/U_0 = \sigma_0 \sim \sqrt{1 - M^{-2}}$ for large M. However, the interior stationary phase contribution occurs at $\theta = \theta_- \sim \pi - 2\arcsin(\sigma_0) = O\left(M^{-2}\right)$, which merges with the boundary contribution at $\theta = 0$ for sufficiently large M. This motivates the need for a new asymptotic expansion, which must account for the merging critical points. The critical point merging condition, $s_0/U_0 \approx 1$, corresponds to the length scale of speed oscillations being' comparable to the wavelength of the pilot wave; see (7.1) for this connection expressed in dimensional variables. We thus deduce that the resonance between the wavelength of destabilisation and the pilot wavelength is enhanced for larger values of M, complicating the asymptotic stability analysis.

The rectilinear expansion describes the onset of the quasi-rectilinear instability at sufficiently high orbital radius for all M. However, for larger M, it is unable to rationalise the onset of the quasi-rectilinear instability, which appears at orbital radii outside of the range of validity of the rectilinear expansion. A new model is thus required to describe the disappearance of orbital quantisation. We turn now to the asymptotic model necessary to describe the quasi-rectilinear instability both in the near-resonant regime, whereby the dimensionless destabilisation frequency S is close to the dimensionless orbital speed U; and in the intermediate regime (see section 7.3), where $\beta = o(r_0)$. This is in contrast to the scalings in the rectilinear expansion, where $\sigma = O(1)$ and $\beta = O(r_0)$.

7.5 Near-resonant quasi-rectilinear instability

7.5.1 Full near-resonant expansion for the quasi-rectilinear instability

We seek an asymptotic expansion valid at the onset of the quasi-rectilinear instability, where $\beta = o(r_0)$. In addition, we consider the situation where the dimensionless destabilisation frequency is close to the dimensionless orbital speed, $S/U \approx 1$. The failure of the rectilinear expansion coincides with the presence of merging critical points, as discussed in §7.3.1. The archetypal example of this phenomenon, in the context of stationary phase or steepest descent, is the integral defining the Airy Ai function [1]; this integral exhibits the merging of saddle points, much like the behaviour of the interior critical points $t_{\pm} = \pi \pm 2 \arcsin(\sigma)$ as $\sigma \uparrow 1$. Daalhius & Temme [75] show that the phenomenon of merging critical points can lead to Airy-type asymptotic expansions. Instead of deriving the Airy-type expansions directly in our work, we proceed to use the Airy-type expansions of the Bessel functions to expanding the complex Bessel function representations of the stability integrals in (7.4), as provided by Liu *et al.* [66].

The Bessel functions of complex order in the stability coefficients (7.4) take the form $J_{\pm i(\beta + i\xi)}(r_0)$, where $s = i\omega\xi$ along the stability boundary and ξ is real. The assumption of near-resonance, namely $s \approx iU = ir_0\omega$, implies that $\xi \approx r_0$. Furthermore, we call that we have assumed that the reciprocal orbital memory satisfies $\beta = o(r_0)$, and so is subdominant to the contribution of ξ in the order of the Bessel function. By combining these assumed scaling relationships, we thus seek an asymptotic expansion in which the Bessel function order is close to the argument. Consequently, we utilise the Airy-type Bessel function transition region asymptotic expansions [1, 76], which take the form

$$J_{\nu}\left(\nu + \tau\nu^{1/3}\right) = \left(\frac{2}{\nu}\right)^{\frac{1}{3}} \mathrm{Ai}\left(-2^{\frac{1}{3}}\tau\right)\left[1 - \frac{\tau}{5\nu^{\frac{2}{3}}}\right] + \frac{2^{\frac{2}{3}}}{\nu}\frac{3\tau^2}{10}\mathrm{Ai}'(-2^{\frac{1}{3}}\tau) + O\left(\frac{1}{\nu^{\frac{4}{3}}}\right), \quad (7.10a)$$

where Ai is the Airy Ai function [1], $\tau = O(1)$ and $\nu \to \infty$. By comparing the form of the expansion (7.10) to the complex-order Bessel functions determined in the analytical evaluation of the stability integrals [66], we choose ν and τ so that $\nu + \tau\nu^{\frac{1}{3}} = r_0$ and $\nu = -i\beta + \xi$, which gives

$$\tau = \frac{r_0\left(1 - \sigma\right) + i\beta}{\nu^{\frac{1}{3}}}, \quad \text{where} \quad \sigma = \frac{\xi}{r_0} = \frac{S}{U}. \tag{7.10b}$$

Using that

$$J_{-\nu}(x) = J_{\nu}(x)\cos(\pi\nu) - Y_{\nu}(x)\sin(\pi\nu), \tag{7.11}$$

and the associated expansions for $Y_{\nu}\left(\nu + \tau\nu^{\frac{1}{3}}\right)$ [1, 76], we can expand all of the Bessel functions appearing in (7.4) when evaluated along the stability boundary. We call this expansion the full near-resonant expansion for the quasi-rectilinear instability, and retain terms to $O\left(\nu^{-1}\right)$ to more clearly present when the full near-resonant expansion fails. Analysis of the stability condition using the full near-resonant expansion is complicated by the complex nature of ν, so we proceed to simplify the asymptotic procedure.

7.5.2 Approximate resonant expansion

In the near-resonant regime, we note that $\beta = o(r_0) = o(\xi)$ and $\nu + \tau \nu^{1/3} = r_0$. It follows that we may derive a second approximation by taking $\nu = r_0$ (valid to leading order) and only retaining the $O\left(\nu^{-1/3}\right)$ terms in (7.10), which greatly simplifies analysis. We may thus replace (7.10b) by

$$\nu = r_0 \quad \text{and} \quad \tau = \frac{r_0\,(1 - \sigma) + \mathrm{i}\beta}{\nu^{\frac{1}{3}}}. \tag{7.12}$$

Specifically, we approximate the complex Bessel functions using

$$\mathrm{J}_{-\mathrm{i}\beta+\xi}(r_0) \sim \left(\frac{2}{r_0}\right)^{\frac{1}{3}} \mathrm{Ai}\left(-2^{\frac{1}{3}}\tau\right), \quad \text{where} \quad \tau = \frac{r_0(1 - \sigma) + \mathrm{i}\beta}{r_0^{\frac{1}{3}}}, \tag{7.13}$$

which we call the approximate near-resonant expansion. By using equations (7.13) and (7.11), the Bessel function expansions in equation (C.1.16) can be substituted into the stability coefficient expressions in (7.4). In appendix C, we demonstrate that under the assumptions made in this section, the stability condition can be approximated by $\mathscr{D} = 0$ to leading order, which is consistent with the notion that the speed oscillations arise predominantly along the path of the particle, rather than invoking appreciable radial perturbations. By taking $s = \mathrm{i}S$, the problem solved by the approximate near-resonant expansion is then

$$-MS^2 + \mathrm{i}S + \frac{(\omega\beta + \mathrm{i}S)}{r_0^2\omega^2} - \frac{2(\omega\beta + \mathrm{i}S)^2\pi}{r_0^2\omega^2}\left(\frac{2}{r_0}\right)^{\frac{2}{3}} \mathrm{e}^{-\frac{\pi\mathrm{i}}{3}}\mathrm{Ai}\left(-2^{\frac{1}{3}}\tau\right)\mathrm{Ai}\left(-\mathrm{e}^{\frac{2\pi\mathrm{i}}{3}}2^{\frac{1}{3}}\tau\right) = 0, \tag{7.14}$$

where it remains to find S and β for a given value of the orbital radius, r_0 (where ω is determined from the tangential force balance).

In figure 7.7, we compare the near-resonant expansions (7.10) and (7.14) with the non-resonant expansion developed in §7.4 and the numerically computed stability boundary. As elaborated upon in appendix C, the near-resonant expansions (7.10) and (7.14) are valid if $\tau = O(1)$ as $r_0 \to \infty$. As τ is complex, this restriction comprises of two separate conditions: (i) $r_0^{2/3}\,(1 - \sigma) = O(1)$ and (ii) $\beta r_0^{-1/3} = O(1)$. The first condition provides a measure as to how close σ needs to be to unity at finite radius, corresponding the closeness of the speed oscillation length to the pilot-wavelength, whereas the second condition determines the magnitude of the orbital memory, and is consistent with the assumption $\beta = o(1)$ as $r_0 \to \infty$. We thus anticipate that there is an intermediate range of radii for which the results of this asymptotic framework will be valid, with necessary assumptions for τ being valid in the large-radius limit. This restriction of our asymptotic framework is evident in figure 7.8, for which we see that the full near-resonant expansion is only valid when $r_0^{2/3}\,(1 - \sigma)$ and $\beta r_0^{-1/3}$ are of size $O(1)$, and the non-resonant expansion is preferred when these parameters become large. These restrictions allow us to quantify the phenomenon of 'near-resonance': the quasi-rectilinear instability is near-resonant if $1 - \sigma$, the deviation from resonance between the pilot-wave wavelength and the wavelength of instability, is comparable to the asymptotically small quantity $r_0^{-2/3}$.
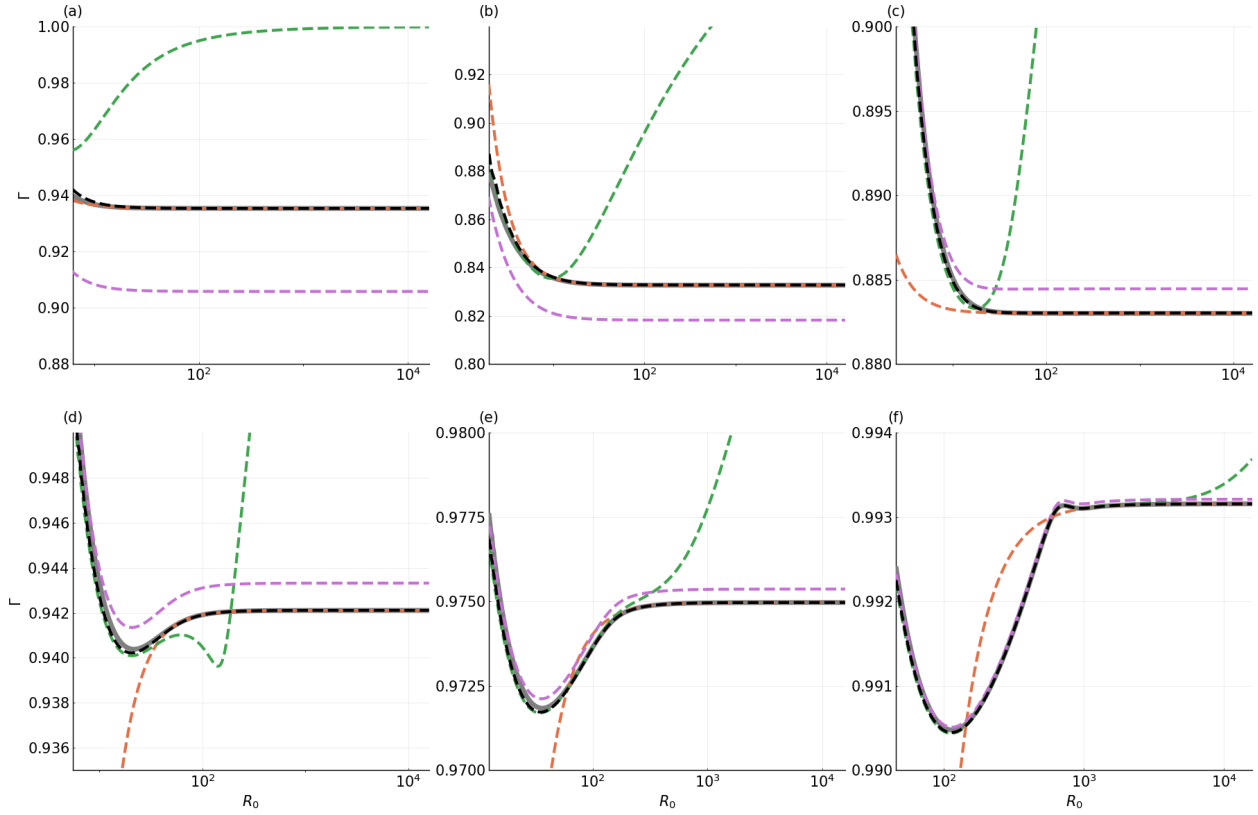
Figure 7.7: Comparison between the numerically computed critical memory (grey) to the various near-resonant asymptotic expansions (section 7.5) and the rectilinear expansion (section 7.4), where $M =$ (a) 0.14 , (b) 0.71, (c) 1.7, (d) 2.8, (e) 4.2 and (f) 7.1. Only the boundaries corresponding to a quasi-rectilinear instability are displayed. The full near-resonant expansion (green, defined in (7.10))) outperforms the rectilinear expansion (orange, considered in §7.4) only for larger M, and for a limited range of R_0; the regime of validity increases significantly with M. The approximate near-resonant expansion (purple, given in (7.13)) qualitatively agrees with the numerical solution for larger R_0, and the agreement improves with increasing M. The ad-hoc near-resonant expansion (black, given in §7.5.3) compares favourably with the numerical solution for all M and for a wide range of R_0.
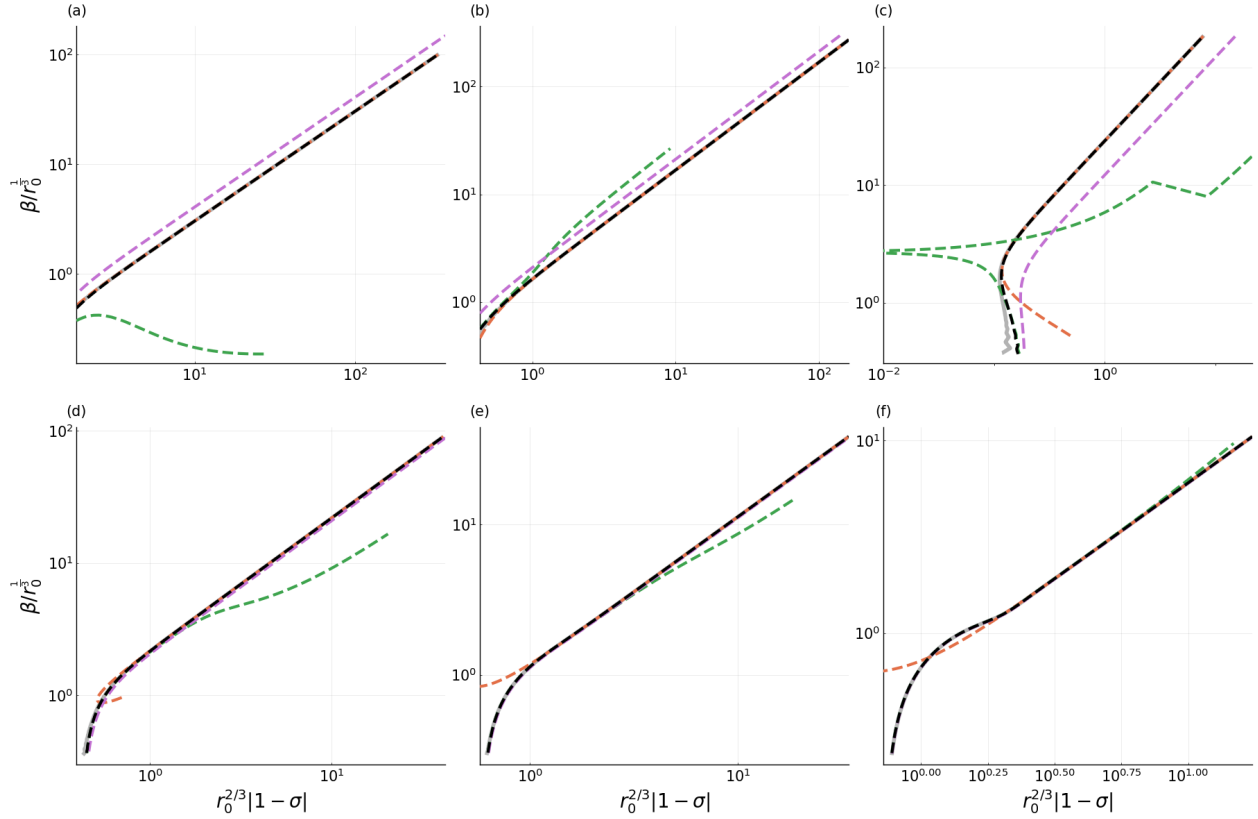
Figure 7.8: Plots of the expansion parameters $\beta r_0^{-\frac{1}{3}}$ and $r_0^{\frac{2}{3}}(1-\sigma)$ for $M = (a)0.14$, (b) 0.71, (c) 1.7, (d) 2.8, (e) 4.2 and (f) 7.1. We show that the near-resonant regime is when these two quantities are $O(1)$, and that the rectilinear expansion may be used when these two quantities are large. Observe how the full non-resonant expansion (green, defined in (7.10)) performs best when the expansion parameters $\beta r_0^{-1/3}$ and $r_0^{2/3}(1-\sigma)$ are around 1, and fails otherwise. Conversely, the approximate (purple, (7.13)) and ad-hoc (black, §7.5.3) near-resonant expansions agree qualitatively and quantitatively respectively with the full numerical solution across all parameter values. The rectilinear expansion (orange) is seen to provide good agreement if at least one of $\beta r_0^{-1/3}$ and $r_0^{2/3}(1-\sigma)$ is large.

7.5.3 Ad-hoc resonant expansion

The principal discrepancy between the full and approximate near-resonant expansions and the numerical stability boundary arises from the choice of expansion parameters ν and τ. In particular, as seen in figure 7.7, the approximate near-resonant expansion performs worse at smaller orbital radius, but its predictions agree qualitatively with the numerical boundary better for larger orbits than the full near-resonant expansion. This observation indicates that retaining more terms in the Airy function expansions in the full near-resonant expansion (as was the case in the expansion (7.10) relative to (7.13)) does not necessarily lead to better agreement with numerical solution of the stability boundary. Specifically, the critical memories of instability as predicted by the approximate near-resonant instability and by the non-resonant expansion appear to differ by a constant for larger values of R_0. Notably, this constant decreases with the dimensionless mass, M.

Based on these developments, a natural goal is to determine the problem that is solved by the approximate near-resonant expansion in the region where $r_0^{2/3}(1-\sigma)$ and $\beta r_0^{-1/3} \to \infty$, i.e. outside the regime of validity of the full near-resonant expansion. In appendix C.3, we demonstrate that the approximate near-resonant and free rectilinear stability conditions take the form

$$-MS^2 + \mathrm{i}S - \sigma + \frac{(\sigma + \mathrm{i}S)}{U^2}\left(1 + \frac{x_{1,2}(\sigma + \mathrm{i}S)}{U}\right) = 0$$

in this regime, where

$$x_1 = \frac{\mathrm{i}}{\sqrt{2\gamma}}, \quad x_2 = -\frac{1}{\sqrt{1 + \left(\frac{\sigma + \mathrm{i}S}{U}\right)^2}}, \quad \gamma = -\left(1 - \sigma + \frac{\mathrm{i}\sigma}{S}\right), \quad \text{and} \quad x_1 - x_2 = O\left(\frac{1}{M}\right).$$

For sufficiently large M, the difference between the two equations vanishes. This raises the tantalising possibility of modifying the stability condition solved by the approximate near-resonant expansion to develop an asymptotic model that agrees with both the full near-resonant and rectilinear expansions in their respective regimes of validity. We call this model the ad-hoc near-resonant expansion, which involves solving (C.3.34) for σ and S.

Despite the ad-hoc form of the ad-hoc near-resonant expansion, it has a favourable numerical agreement across both the near-resonant and non-resonant regimes for all M (see figure 7.7), superseding the formal expansions given by (7.10) and (7.14). From figure 7.7, we see that for smaller M, the first two near-resonant expansions perform poorly, but the ad-hoc near-resonant expansion maintains excellent agreement throughout a wide range of orbital radii. Figure 7.8 shows that the ad-hoc near-resonant expansion solution is visually indistinguishable from the full numerical solution. Impressively, the ad-hoc near-resonant expansion provides numerically satisfactory results even for small M, when the rectilinear expansion is valid, and the quasi-rectilinear instability cannot be considered 'near-resonant'. Our construction has thus unified the near-resonant and rectilinear asymptotic regimes, to leading order, across a wide range of parameter regimes. The problem of developing a higher order uniform expansion is left for future work.

7.6 Discussion

We have studied the mechanism by which arbitrarily large circular orbits destabilise, referred to as the quasi-rectilinear instability, which is rooted in the in-line oscillations of free rectilinear trajectories prevalent in the generalised pilot-wave framework [33, 98]. Intuition suggests that circular orbits of sufficiently large orbital radius should destabilise via a mechanism similar to that of free rectilinear trajectories. We demonstrate that this intuition is correct for sufficiently large orbital radii, and that the orbital stability problem can be considered as a perturbation of the free rectilinear trajectory stability problem. For intermediate values of the orbital radius, we show that the oscillation amplitude is particularly close to the wavelength of the pilot wave. This near-resonance presents complications in the mathematical analysis, which we address with our near-resonant expansions in §7.5. We then show that the degree of 'near-resonance' depends on the detuning of the length scale over which speed perturbations oscillate from the wavelength of the pilot wave, as well as the magnitude of the orbital memory.

The significance of the quasi-rectilinear instability lies in its universality. In both §7.4 and §7.5, the quasi-rectilinear instability is, to leading order, described by the equation $\mathscr{D} = 0$. As pointed out in §3.5, $\mathscr{D}$ contains information about tangential perturbations to the tangential force balance. This aligns with our intuition regarding the relationship with the free rectilinear instability, because the quasi-rectilinear instability manifests as the in-line speed oscillations first studied by Durey *et al.* [33]. However, as §3.5 also points out, $\mathscr{D}$ is only affected by forces whose tangential components depend explicitly on angular displacements, velocities, or accelerations. Some common types of forces acting on single particles, like electromagnetic forces, either act radially, or perpendicular to the particle's velocity. In neither case is the form of $\mathscr{D}$ affected, meaning most of the analysis performed in this work will remain for different confining forces; the only changes would involve the higher-order rectilinear expansion, in which the other three stability coefficients appear. Nevertheless, our analysis of the quasi-rectilinear instability provides a means to destabilise many kinds of stable quantised states. We show an example in figure 7.9, in the presence of an attractive linear spring force, where the white quasi-rectilinear plateau acts as an upper bound for the memory at which non-resonant quantised islands may occur (flat plateau paper). A similar phenomenon occurs in the limit of small inertia, where the sharply quantised orbital states considered in (sharp quantisation paper) also destabilise at memory higher than the quasi-rectilinear memory of instability.

Our discussion of the quasi-rectilinear instability can be compared with the experiments [43, 52] and theoretical developments [79]. Fort et al. [43] demonstrated that circular orbits are quantised at higher memory. Harris and Bush [52] and Oza et al. [79] demonstrated that the quantised circular orbits may destabilise via various wobbling and monotonic instability mechanisms as memory is increased. However, none of the experimental or theoretical studies considered circular orbits of sufficiently large radius to observe the predicted termination of quantisation, nor the quasi-rectilinear instability. As pointed out by Oza et al. [82], the dimensionless droplet mass tends to be in the range $M \in [1.3, 2.2]$, for which orbital quantisation ceases relatively early, and so experimental verification of the end of quantisation could be achieved with a reasonably large bath. As a practical note, we expect the termina-
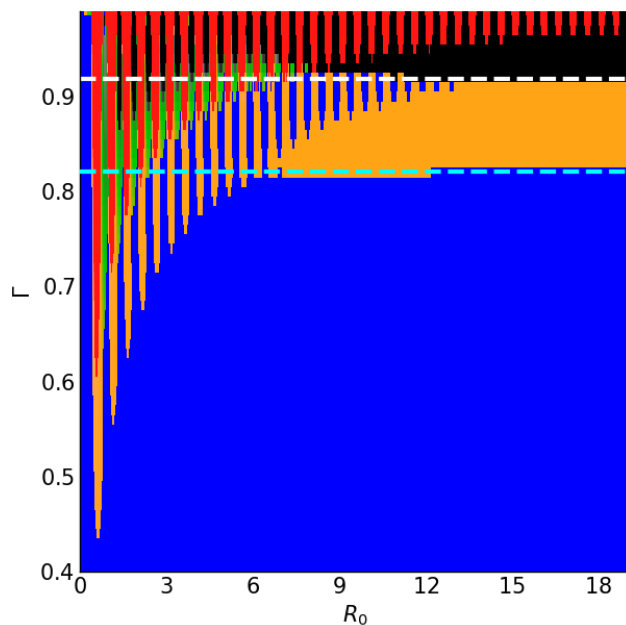
Figure 7.9: Orbital stability diagram for $M = 0.184$ in the presence of a linear spring force, instead of a Coriolis force, where each point in the diagram corresponds to a circular orbit at a given orbital radius $R_0 = \frac{r_0}{2\pi}$, and memory parameter Γ. The stability of each circular orbit uses the same colour scheme as in figure 4.1. Black regions represent circular orbits desetabilising via the quasi-rectilinear instability. We note the presence of two plateaus. The cyan plateau at $\Gamma \approx 0.8$ is the non-resonant plateau considered in §4.3, whereas the white plateau at $\Gamma \approx 0.9$ corresponds to the limiting memory of the quasi-rectilinear instability at infinite radius. We observe that there are several quantised islands of stability in between the two plateaus, studied in §4.4, which are cut off by the quasi-rectilinear instability.

tion of quantisation to only be observable in experimental setups for which the free walking state destabilises [35].

We now consider the behaviour of the quasi-rectilinear instability in a generalised pilot-wave system, for which the wave kernel, J_0, is replaced by another quasi-monochromatic function. As the quasi-rectilinear instability is rooted in the in-line speed oscillations of free rectilinear trajectories [33, 98], we expect a similar type of instability to appear for sufficiently large circular orbits in other pilot-wave systems, provided the free rectilinear trajectory destabilises. Then, the quasi-rectilinear instability may also exhibit near-resonance if the oscillation amplitude is close to the pilot-wave wavelength. Building on our understanding gained from figure 7.9, we then expect the corresponding quasi-rectilinear instability to likewise terminate orbital quantisation in those systems.

From a mathematical perspective, the rectilinear expansion arises when the different critical points, obtained through stationary phase or steepest descent analysis, are distinct, while the near-resonant expansion arises from the collision of these critical points. The ad-hoc resonant expansion was derived from the approximate near-resonant expansion to match the free rectilinear stability condition, outside the regime of validity of the near-resonant expansions. The numerical agreement between the stability boundaries predicted from our one-term *ad-hoc* expansion considered in §7.5.3 and the full numerical boundaries suggest the utility of such matching procedures, where asymptotic expansions in different regimes of validity may be amended and matched to produce uniformly valid expansions. We delay a more rigorous justification of the *ad-hoc* resonant expansion to another work.

In our work, we have restricted our attention to the linear stability of circular orbits. Specifically, we do not consider the stability of the nonlinear states that may arise when the circular orbits are linearly unstable [52, 80]. A study of the stability of such nonlinear wobbling states and the associated wobbling frequencies may provide further insight into orbital pilot-wave dynamics.

Chapter 8

Concluding remarks

In this thesis, we have studied the stability of circular orbits in the generalised pilot-wave framework, with a focus on the effect of different external forces. Our analysis is the first to analytically evaluate the stability integrals in the stability problem, thus allowing conclusions to be drawn on a mathematically rigorous basis. Indeed, many of the phenomena reported in this thesis were predicted through creating various stability diagrams, and observing the different patterns in different parameter regimes for different external forces. Our work has provided valuable insight on the factors that influence orbital stability in pilot-wave hydrodynamics.

In chapter 2, we showed the efficacy of our asymptotic analysis in understanding the self-similarity of the stability boundaries in a rotating frame. We explained the abundance of stable wobbling states with wobbling frequency approximately twice the orbital frequency. We also compared the efficacy of various heuristics in explaining the location of the stability tongues. We established that the wave energy is proportional to the gravitational energy of the droplet, thus unifying heuristics previously thought to be disparate. While Labousse's heuristic regarding the zeros of Bessel functions [64] was shown to provide the closest numerical agreement, it did not provide a mechanism for the type of instability; we demonstrate that the sign of the radial derivative of the mean wave force provides information on the type of instability observed.

In chapter 3, we compared the stability of circular orbits in a rotating frame with those in a central force. We showed that the main difference between the two types of systems involve the non-resonant instability, absent with the Coriolis force, whose frequency depends on the form of the central force. We highlighted how this instability arises from the fact that the orbital speed is always close to the free walking speed, and the lack of translational symmetry. We also developed intuition for understanding the onset of monotonic instabilities, in terms of the direction of the net radial force on an outwards radial perturbation. Using this intuition, we were able to heuristically explain the appearance and disappearance of monotonic instabilities at the onset of instability for different central forces. However, due to the complex relationship between the types of oscillatory instabilities present and the form of the central force, we noted the difficulty of extending our mean wave field heuristic to the central force system.

In chapter 4, we presented a new asymptotic formulation of the stability problem, which is valid in a wider range of circumstances compared to the procedure introduced in chapter 2.

Using this new formulation, we showed that the dynamical behaviour is significantly more complex outside the experimental parameter regime. In particular, we showed that large orbital radius instabilities defy intuition that relate their stability to that of free walkers. While the critical memory of instability for large orbital radii depends weakly on the orbital radius, manifesting as plateaus in the orbital stability diagrams in figure 4.1, the instability mechanism of these large circular orbits is not the in-line speed oscillations studied by Durey et al. [35], but rather the non-resonant instability introduced in chapter 3. We demonstrated that these instability plateaus are accompanied by the existence of circular orbits that are stabilised by increased memory, leading to a new paradigm of orbital quantisation and a vastly increased number of accessible quantised states. Finally, we showed how the location of the stability tongues, i.e. the most unstable orbital radii, is determined by the influence of both the geometric constraint imposed by the quasi-monochromatic wave field, and the spatial variation of the external force.

In chapter 5, we develop a sharper analog of orbital quantisation. Specifically, we show that, for high memory and low inertia in a linear central force, the allowed orbital radii lie strictly in between successive zeros of J_0 and J_2. In addition, we showed that these circular orbits destabilise via a dual resonance with the orbital frequency and the pilot wavelength. Specifically, the instability frequency is approximately an integer multiple of the orbital frequency, like the resonant instabilities in the Coriolis system studied in chapter 2, but the oscillation amplitude is similar to the pilot wavelength, like the quasi-rectilinear instabilities studied in chapter 7. We show that the dominance of the mean wave field, in the limit of high memory, is responsible for the sharpness of the allowed orbital radii, and suggest that it is the deviations from the mean wave field, at lower memory, that cause instabilities of these quantised states. We also demonstrate that the instability mechanism is chosen from the wave mode that maximises the tangential wave force. In doing so, we rigorously demonstrated that mean wave field arguments are expected to work best for circular orbits at very high orbital memory.

In chapter 6, we considered the effects of external stimuli on spin states. We showed that in a rotating frame, cyclonic orbits exist for rotation rates below a critical value. We also observed that, in the presence of a central force, the stability boundaries of spin states change discontinuously, which arises from the loss of translational symmetry, and the subsequent destabilisation of the previously trivial $i\omega$ eigenvalue.

In chapter 7, we showed how the quasi-rectilinear instability terminates orbital quantisation, as the corresponding stability boundaries vary slowly with the orbital radius. At very large orbital radii, the quasi-rectilinear instability was demonstrated to be a perturbation of the instability of free walkers. At intermediate orbital radii, we show that the oscillation amplitude of the quasi-rectilinear instability is close to the wavelength of the pilot-wave. Using the method of stationary phase on the stability integrals, we delineate the different asymptotic regimes in the rotating frame, and quantify when the quasi-rectilinear instability is 'near-resonant'. We also established how this approach is valid independent of the type of external force.

It is worth highlighting the advantages and disadvantages of our approach. We have successfully reduced the stability problem of circular orbits in the generalised pilot-wave framework to a problem of asymptotics of complex-order Bessel functions, which allows us to understand orbital stability in a large variety of external forces. We have also shown

that instability is guaranteed if the net radial force increases with outwards perturbations, for a general class of pilot-wave systems. However, our analysis is restricted to the special case where the droplet maintains resonant bouncing with the bath, in the absence of boundaries. While this model has been fruitful in predicting many features of the pilot-wave system, the resonant bouncing assumption breaks down at high memory, where the droplet may transition to a chaotic bouncing state[69, 70]. In addition, the stroboscopic model does not naturally treat boundaries or submerged topography, and thus is unable to model other quantum phenomena, like diffraction or tunnelling. How to incorporate non-resonant bouncing, boundaries and bottom topography into the stroboscopic model in a manner amenable to analysis are areas of current research.

The work in this thesis has presented a comprehensive study of orbital stability in the GPWF in the presence of a Coriolis force and power-law central forces of the form $\boldsymbol{F} \propto |\boldsymbol{x}_p|^{n-1}\boldsymbol{x}_p$. Our investigations in the GPWF have revealed much richer orbital pilot-wave dynamics than can be observed in the experimental regime, some of which represent closer quantum analogs, and show that the most interesting quantum-like dynamical behaviour occurs in the low-inertia and high-memory limit. We hope that the theoretical developments and results in this thesis will spur modifications to the generalised pilot-wave framework to encompass a wider range of quantum-like behaviours.

Appendix A

Chapter 2 appendices

A.1 Physical parameters

We here define the Faraday wavenumber, k_F, drag factor, D, and wave amplitude parameter, A, in terms of physical quantities [78, 79]. Specifically, the Faraday wavenumber satisfies the gravity-capillary dispersion relation [6]

$$(\pi f)^2 = \left(gk_F + \frac{\sigma k_F^3}{\rho}\right)\tanh(k_F H),$$

where σ is the coefficient of surface tension, ρ is the fluid density, and H is the fluid depth. Furthermore, we define the drag factor,

$$D = 0.17 mg\sqrt{\frac{\rho R_D}{\sigma}} + 6\pi\mu_{\text{air}}R_D\left(1 + \frac{\rho_{\text{air}}gR_D}{12\mu_{\text{air}}f}\right),$$

and wave amplitude,

$$A = \frac{1}{\sqrt{2\pi}}\frac{k_F R_D}{3k_F^2 R_D^2 + Bo}\frac{R_D k_F^2 \nu_{\text{eff}}^{1/2}}{\sigma\sqrt{T_F}}mgT_F\sin\Phi,$$

where R_D is the droplet radius, μ_{air} and ρ_{air} are the dynamic viscosity and density of air, respectively, ν_{eff} is the effective fluid kinematic viscosity [70], $Bo = \rho g R_D^2/\sigma$ is the Bond number and $\sin\Phi = 0.2$ is the droplet impact phase [78, 80].

A.2 Evaluation of stability integrals

We proceed to analytically evaluate the stability integrals defined in (2.6), where we leverage the relationship between the stability integrals (equation (2.8)) to evaluate $\mathcal{S}_m$ and $\mathcal{C}_m$ in terms of $\mathcal{I}_m$ only. The evaluation of each stability integral hinges on the observation that $J_{2m}(2r_0\sin(x))$ is even and π-periodic, and so may be expressed in terms of its bi-infinite cosine series (derived from Gradshteyn and Ryzhik [50, section 6.681]),

$$J_{2m}\left(2r_0\sin(x)\right) = \sum_{n=-\infty}^{\infty}(-1)^n J_{m+n}(r_0)J_{m-n}(r_0)\cos(2nx). \tag{A.1}$$

By performing the change of integration variable $t \mapsto \omega t$ in equation (2.6a) and using the cosine series expansion (A.1), the integral $\mathcal{I}_m(s)$ may be recast as the infinite sum

$$\mathcal{I}_m(s) = \frac{1}{\omega} \sum_{n=-\infty}^{\infty} (-1)^n \mathrm{J}_{m+n}(r_0) \mathrm{J}_{m-n}(r_0) \int_0^{\infty} \cos(nt) e^{-\eta t} \, \mathrm{d}t,$$

where $\eta = (\mu + s)/\omega$ and $\mathrm{Re}(\eta) > 0$. By integrating each of the resultant integrals analytically, we deduce that the stability integral is equivalent to

$$\mathcal{I}_m(s) = \frac{\eta}{\omega} \sum_{n=-\infty}^{\infty} \frac{(-1)^n \mathrm{J}_{m+n}(r_0) \mathrm{J}_{m-n}(r_0)}{\eta^2 + n^2}. \tag{A.2}$$

This formulation is convenient for numerical computation of the stability integrals and is used in the construction of orbital stability diagrams and the tracking of orbital stability boundaries (e.g. figure 2.2). However, further analytical progress can be made by using a partial fraction expansion in equation (A.2) and applying the Lerche-Newberger sum rule [5, 74], giving rise to the closed form expression given in (2.7), which forms the basis of our analytical developments.

Notably, the sum (or difference) appearing in the Bessel function orders in equation (2.7) when $m = 1$ complicates the application of large-argument asymptotic expansions in our study. As such, we derive two Bessel function identities that assist with the elimination of the sum in the order, thereby allowing us to derive a set of convenient equations for further analysis. To proceed, we first recall the Bessel function Wronskian, recurrence relation and derivative expression given by [1]

$$\mathrm{J}_\nu(x) \mathrm{J}_{1-\nu}(x) + \mathrm{J}_{-\nu}(x) \mathrm{J}_{\nu-1}(x) = \frac{2 \sin(\nu \pi)}{\pi x}, \tag{A.3a}$$

$$\mathrm{J}_{\nu-1}(x) + \mathrm{J}_{\nu+1}(x) = \frac{2\nu}{x} \mathrm{J}_\nu(x), \tag{A.3b}$$

$$\text{and} \quad \mathrm{J}_{\nu-1}(x) - \mathrm{J}_{\nu+1}(x) = 2\mathrm{J}'_\nu(x), \tag{A.3c}$$

respectively, which form the basis of our forthcoming algebraic manipulations. To derive the first identity, we apply the recurrence relation (A.3b), add and subtract $(2\nu/x)\mathrm{J}_{-\nu}(x)\mathrm{J}_{\nu-1}(x)$ to the resultant expression, and simplify using the Wronskian (A.3a) and derivative relation (A.3c) to obtain

$$\mathrm{J}_{1-\nu}(x) \mathrm{J}_{-1+\nu}(x) - \mathrm{J}_{1+\nu}(x) \mathrm{J}_{-1-\nu}(x) = \frac{4\nu \sin(\nu \pi)}{\pi x^2} - \frac{4\nu}{x} \mathrm{J}_{-\nu}(x) \mathrm{J}'_\nu(x). \tag{A.4}$$

To derive the second identity, we differentiate the Wronskian identity (A.3a) and apply the recurrence relation (A.3b) to find that

$$\mathrm{J}_{1-\nu}(x) \mathrm{J}'_\nu(x) + \mathrm{J}_{1+\nu}(x) \mathrm{J}'_{-\nu}(x) = -2\mathrm{J}'_{-\nu}(x) \mathrm{J}'_\nu(x) - \frac{2\nu \sin(\pi \nu)}{\pi x^2}. \tag{A.5}$$

We now use the relations (A.4) and (A.5) in conjunction with (2.7) and (2.8) to evaluate the integrals and integral combinations arising in the stability problem (2.5), yielding

$$\mathcal{I}_0(0) = \frac{\pi \operatorname{csch}(\pi\beta)}{\omega} J_{i\beta}(r_0) J_{-i\beta}(r_0), \tag{A.6a}$$

$$\frac{\partial \mathcal{I}_0(0)}{\partial r_0} = \frac{-2\pi \operatorname{csch}(\pi\beta)}{\omega} \left(\frac{i \sinh(\beta\pi)}{\pi r_0} - J_{-i\beta}(r_0) J'_{i\beta}(r_0) \right), \tag{A.6b}$$

$$\mathcal{S}_0(s) = \frac{2\pi\eta \operatorname{csch}(\pi\eta)}{\omega} \left(\frac{i \sinh(\pi\eta)}{\pi r_0^2} - \frac{J_{-i\eta}(r_0) J'_{i\eta}(r_0)}{r_0} \right), \tag{A.6c}$$

$$\mathcal{C}_0(s) - \mathcal{I}_1(s) = -\frac{2i\eta\pi \operatorname{csch}(\pi\eta)}{r_0^2\omega} \left(\frac{i \sinh(\pi\eta)}{\pi} - i\eta J_{i\eta}(r_0) J_{-i\eta}(r_0) \right), \tag{A.6d}$$

$$\mathcal{C}_0(s) + \mathcal{I}_1(s) = \frac{2\pi \operatorname{csch}(\pi\eta)}{\omega} \left(\frac{\eta \sinh(\pi\eta)}{\pi r_0^2} + J'_{i\eta}(r_0) J'_{-i\eta}(r_0) \right), \tag{A.6e}$$

where we recall that $\eta = (\mu + s)/\omega$ and $\beta = \mu/\omega$ is the reciprocal of the orbital memory.

A.3 Stationary phase point contributions to stability integrals

We seek the contributions at each critical point to the integral $\mathcal{L}_m(\xi)$, defined in equation (2.14), for which we consider $r_0 \gg 1$ and $\xi = O(1)$. We first consider the contribution to $\mathcal{L}_m(\xi)$ near the edges of the integration region, namely $\theta = 0$ and $\theta = 2\pi$, which we denote by $\mathcal{L}_{m,0}(\xi)$ and $\mathcal{L}_{m,2\pi}(\xi)$, respectively. To determine $\mathcal{L}_{m,0}(\xi)$, we approximate $\sin\left(\frac{\theta}{2}\right) \approx \frac{\theta}{2}$ in the argument of the Bessel function, and recast the integration region as

$$\mathcal{L}_{m,0}(\xi) = \int_0^\infty J_{2m}(r_0\theta) e^{-(\beta+i\xi)\theta} \, d\theta - \int_{2\pi}^\infty J_{2m}(r_0\theta) e^{-(\beta+i\xi)\theta} \, d\theta. \tag{A.7}$$

The first integral may be evaluated analytically [1], and it remains now to estimate the size of the second integral. We approximate the integrand by utilising the large-argument Bessel function expansion [1] and noting that $\theta \geq 2\pi$ across the integration domain; then, by evaluating the resultant integral analytically, we obtain the approximate bound

$$\int_{2\pi}^\infty J_{2m}(r_0\theta) e^{-(\beta+i\xi)\theta} \, d\theta \sim \sqrt{\frac{1}{\pi^2 r_0}} \int_{2\pi}^\infty \cos\left(r_0\theta - \varphi_m\right) e^{-(\beta+i\xi)\theta} \, d\theta = O\left(\frac{e^{-2\pi\beta}}{r_0\sqrt{r_0}}\right),$$

where $\varphi_m = \frac{1}{4}\pi(1 + 4m)$ is a constant phase shift. Provided β is of size at most $O(r_0)$, the analytical evaluation of the first integral in (A.7) determines that this term is the dominant contribution to $\mathcal{L}_{m,0}$. By neglecting the contribution from the second integral in (A.7), we deduce that $\mathcal{L}_{m,0} = O(r_0^{-1})$. The periodicity of the non-exponential portion of the integrand indicates that the contribution near $\theta = 2\pi$ satisfies $\mathcal{L}_{m,2\pi}(\xi) = \mathcal{L}_{m,0}(\xi) e^{-2\pi(\beta+i\xi)}$. The factor $e^{-2\pi\beta}$ ensures that the contribution $\mathcal{L}_{m,2\pi}(\xi)$ is negligible relative to $\mathcal{L}_{m,0}(\xi)$ and may henceforth be neglected.

We now determine the contributions arising near points of stationary phase. The internal contribution is localised about $\theta = \pi$, and we denote this contribution by $\mathcal{L}_{m,\pi}(\xi)$. To

proceed, we deform the integration region to a small region about $\theta = \pi$, namely $\pi - \delta < \pi < \theta + \delta$ with $0 < \delta \ll 1$, and define

$$\mathcal{L}_{m,\pi}(\xi) = \int_{\pi-\delta}^{\pi+\delta} \mathrm{J}_{2m}\left(2r_0 \sin\left(\frac{\theta}{2}\right)\right) \mathrm{e}^{-(\beta+\mathrm{i}\xi)\theta} \, \mathrm{d}\theta.$$

By applying the large-argument expansion for the Bessel function [1] and utilising the Taylor expansion $\sin\left(\frac{\theta}{2}\right) \approx 1 - \frac{1}{8}(\theta - \pi)^2$, we determine the approximation

$$\mathcal{L}_{m,\pi}(\xi) \sim \frac{\mathrm{e}^{-(\beta+\mathrm{i}\xi)\pi}}{2\sqrt{\pi r_0}} \sum_{\pm} \mathrm{e}^{\pm \mathrm{i}\varphi_m} \int_{\pi-\delta}^{\pi+\delta} \mathrm{e}^{\mp \mathrm{i}2r_0\left(1-\frac{1}{8}(\theta-\pi)^2\right)} \, \mathrm{d}\theta.$$

The leading-order form of the resultant integral may be determined using method of stationary phase for $r_0 \gg 1$, giving rise to the contribution

$$\mathcal{L}_{m,\pi}(\xi) \sim -\frac{2\mathrm{e}^{-\pi(\beta+\mathrm{i}\xi)}}{r_0} \cos\left(2r_0 + \varphi_m\right).$$

A.4   Asymptotic expansions for the wobbling regime

Along stability boundaries (with $s = \mathrm{i}\xi\omega$), the stability integrals (2.6) are all evaluated in terms of Bessel functions of complex order, $\pm \mathrm{i}\zeta$, and real argument, r_0, where $\zeta \in \{\beta, \beta + \mathrm{i}\xi\}$ (see equation (A.6)). For wobbling and monotonic instabilities, corresponding to $\beta = O(\ln(r_0))$ and $\xi = O(1)$, the order of the Bessel function is much smaller than the argument. Thus, we may expand each of the Bessel function products in equation (A.6) by applying the large-argument asymptotic expansion to each Bessel function [1]. Direct evaluation by Mathematica yields

$$\mathrm{J}_{-\mathrm{i}\zeta}(r_0)\mathrm{J}_{\mathrm{i}\zeta}'(r_0) = \frac{\cos(2r_0) + \mathrm{i}\sinh(\zeta\pi)}{\pi r_0} - \frac{\cosh(\zeta\pi)}{2\pi r_0^2} + \frac{(4\zeta^2 - 1)\sin(2r_0)}{4\pi r_0^2}$$
$$+ \frac{3(1 + 4\zeta^2)\cosh(\zeta\pi)}{16\pi r_0^4} + O\left(\frac{1}{r_0^3}\right), \tag{A.8a}$$

$$\mathrm{J}_{\mathrm{i}\zeta}(r_0)\mathrm{J}_{-\mathrm{i}\zeta}(r_0) = \frac{\sin(2r_0) + \cosh(\zeta\pi)}{\pi r_0} - \frac{(1 + 4\zeta^2)}{4\pi r_0^2}\left(\frac{\cosh(\zeta\pi)}{2r_0} + \cos(2r_0)\right) + O\left(\frac{1}{r_0^3}\right), \tag{A.8b}$$

$$\mathrm{J}_{\mathrm{i}\zeta}'(r_0)\mathrm{J}_{-\mathrm{i}\zeta}'(r_0) = \frac{-\sin(2r_0) + \cosh(\zeta\pi)}{\pi r_0} + \frac{(3 + 4\zeta^2)\cosh(\zeta\pi)}{8\pi r_0^3}$$
$$+ \frac{(-3 + 4\zeta^2)\cos(2r_0)}{4\pi r_0^2} + O\left(\frac{1}{r_0^3}\right), \tag{A.8c}$$

where all terms necessary for the dominant balance $\mathrm{e}^{\pi\beta} = O(r_0^2)$ have been retained, and the expansions (A.8) are valid when $|\zeta^2 + \frac{1}{4}| \ll r_0$ [1]. By substituting these expansions into the analytical expressions for each of the stability integrals (see equation (A.6)), we deduce that

the stability coefficients (see equation (2.11)) have the asymptotic form

$$
\mathscr{A} = -\frac{2\sin(2r_0)}{U}\left(\operatorname{csch}(\pi(\beta + \mathrm{i}\xi)) + \operatorname{csch}(\pi\beta)\right) + \frac{(4\beta^2 - 7)\cos(2r_0)\operatorname{csch}(\pi\beta)}{2Ur_0}
$$
$$
+\frac{3 - \xi^2}{Ur_0^2} - \frac{\kappa_0\xi^2 U^2}{r_0^2} + \frac{\cos(2r_0)\operatorname{csch}(\pi(\beta + \mathrm{i}\xi))(-3 + 4\beta^2 + 8\mathrm{i}\beta\xi - 4\xi^2)}{2Ur_0} + O\left(\frac{1}{r_0^4}\right), \quad \text{(A.9a)}
$$

$$
\mathscr{B} = \frac{\mathrm{i}\kappa_0\xi U^2}{r_0^2} - \frac{2\mathrm{i}\xi}{Ur_0^2} + \frac{2\cos(2r_0)}{Ur_0}\left(\operatorname{csch}(\pi\beta)(\mathrm{i}\xi - \beta) + \operatorname{csch}(\pi(\beta + \mathrm{i}\xi))(\beta + \mathrm{i}\xi)\right) + O\left(\frac{1}{r_0^4}\right),
$$
$$
\text{(A.9b)}
$$

$$
\mathscr{C} = \frac{2U}{r_0} - \frac{2(\beta + \mathrm{i}\xi)}{Ur_0^2} + \frac{\mathrm{i}\kappa_0\xi U^2}{r_0^2} + O\left(\frac{1}{r_0^3}\right), \quad \text{(A.9c)}
$$

$$
\mathscr{D} = \frac{2\mathrm{i}\xi U}{r_0} - \frac{2\mathrm{i}\xi(\beta + \mathrm{i}\xi)}{Ur_0^2} - \frac{\kappa_0\xi^2 U^2}{r_0^2} + O\left(\frac{1}{r_0^3}\right), \quad \text{(A.9d)}
$$

where we have again utilised the dominant balance $\mathrm{e}^{\pi\beta} = O(r_0^2)$.

A.5   Wave intensity

A.5.1   Surface energy contribution

We proceed to show that the contribution of surface energy to the wave intensity is proportional to that of gravitational potential energy. For small wave slopes, we define the contribution of surface energy as (in dimensional units)

$$
E_S = \lim_{R \to \infty} \frac{1}{R}\int_{|\boldsymbol{x}| \le R} \frac{\sigma}{2}|\nabla h|^2 \, \mathrm{d}\boldsymbol{x}. \quad \text{(A.10)}
$$

By writing $|\nabla h|^2 = \nabla \cdot (h\nabla h) - h\Delta h$ in equation (A.10), where Δ denotes the Laplacian operator, and applying the divergence theorem to the first term, we obtain

$$
E_S = \lim_{R \to \infty} \frac{1}{R}\left[\frac{\sigma}{2}\int_{|\boldsymbol{x}| = R} h\nabla h \cdot \boldsymbol{n} \, \mathrm{d}s - \int_{|\boldsymbol{x}| \le R} \frac{\sigma}{2}h\Delta h \, \mathrm{d}\boldsymbol{x}\right], \quad \text{(A.11)}
$$

where $\boldsymbol{n}$ is the outward-pointing unit vector to the circle $|\boldsymbol{x}| = R$ and $\mathrm{d}s$ denotes line integration. Owing to the far-field decay of the wave field, we see that the boundary integral in (A.11) vanishes in the limit $R \to \infty$, leaving

$$
E_S = \lim_{R \to \infty} \frac{1}{R}\int_{|\boldsymbol{x}| \le R} -\frac{\sigma}{2}h\Delta h \, \mathrm{d}\boldsymbol{x}. \quad \text{(A.12)}
$$

Finally, we recall that the wave field is composed of monochromatic Bessel functions with wavenumber k_F. It follows that $\Delta h = -k_F^2 h$ for our wave model, which allows us to reduce (A.12) to the simplified form

$$
E_S = \lim_{R \to \infty} \frac{1}{R}\int_{|\boldsymbol{x}| \le R} \frac{\sigma k_F^2}{2}h^2(\boldsymbol{x}, t) \, \mathrm{d}\boldsymbol{x},
$$

which is proportional to the contribution from the gravitational potential energy.

A.5.2 Wave intensity for orbital motion

To compute the wave intensity for a given droplet trajectory, we first introduce the polar coordinate system $\boldsymbol{x} = r(\cos\theta, \sin\theta)$ and decompose the dimensionless wave field (see equation (2.28)) as

$$\hat{h}(\boldsymbol{x}, t) = \sum_{n=-\infty}^{\infty} a_n(t) \mathrm{J}_n(r) \mathrm{e}^{in\theta}. \tag{A.13}$$

By substituting equation (A.13) into (2.28) and applying Graf's addition theorem [1], we find that each coefficient, $a_n(t)$, is defined by the integral [63]

$$a_n(t) = \int_{-\infty}^{t} \mathrm{J}_n(r_p(s)) \mathrm{e}^{-in\theta_p(s)} \mathrm{e}^{-\mu(t-s)} \, \mathrm{d}s, \tag{A.14}$$

where $\boldsymbol{x}_p(t) = r_p(t)(\cos\theta_p(t), \sin\theta_p(t))$ is the droplet position. Finally, by substituting equation (A.13) into (2.27), applying Parseval's theorem in the azimuthal direction, evaluating the integral in the radial direction, and taking the limit $R \to \infty$, we obtain [57, 65]

$$\hat{E}(t) = \sum_{n=-\infty}^{\infty} |a_n(t)|^2. \tag{A.15}$$

We proceed to evaluate the wave intensity for the wave field accompanying a droplet orbiting the origin. By substituting $r_p(t) = r_0$ and $\theta_p(t) = \omega t$ into equation (A.14) and evaluating the resultant integral, we deduce that

$$a_n(t) = \frac{\mathrm{J}_n(r_0) \mathrm{e}^{-in\omega t}}{\mu - in\omega}.$$

Upon substituting $a_n(t)$ into (A.15), we thus deduce

$$\hat{E} = \sum_{n=-\infty}^{\infty} \frac{\mathrm{J}_n^2(r_0)}{\mu^2 + n^2\omega^2},$$

whereupon comparing this equation with (A.2) determines the expression given in (2.29).

Appendix B

Chapter 3 appendices

B.1 Orbital stability of the boost equation

To analyse the response of perturbations away from a circular orbit as predicted by the boost model (3.11), we apply linear stability analysis. To streamline the algebra, we consider simultaneously the cases of Coriolis and central forces, writing

$$\boldsymbol{F} = -2m\boldsymbol{\Omega} \times \dot{\boldsymbol{x}}_p - \frac{V'(|\boldsymbol{x}_p|)}{|\boldsymbol{x}_p|}\boldsymbol{x}_p.$$

Furthermore, we express the droplet position, $\boldsymbol{x}_p = (x_p, y_p)$, in complex form, writing $z_p = x_p + \mathrm{i}y_p$. In complex polar coordinates, we then express $z_p(t) = r(t)\mathrm{e}^{\mathrm{i}\theta(t)}$, where $r(t) > 0$ is the distance to the origin and $\theta(t)$ is the polar angle. We likewise express the droplet velocity in complex form as $u_p = \dot{x}_p + \mathrm{i}\dot{y}_p$, which may be written as $u_p(t) = u(t)\mathrm{e}^{\mathrm{i}\phi(t)}$ in polar form, with $u(t)$ denoting the droplet speed. Upon recasting the boost model (3.11) in this form, we arrive at the coupled complex evolution equations

$$\dot{z}_p = u_p \quad \text{and} \quad \frac{\mathrm{d}}{\mathrm{d}t}\big(m\gamma_B(u)u_p\big) + D_w(u)u_p + 2\mathrm{i}m\Omega u_p + V'(r)z_p = 0,$$

which represent the starting point of our analysis. Finally, by substituting in the polar forms of z_p and u_p, we deduce that

$$\dot{r} + \mathrm{i}r\dot{\theta} = u\mathrm{e}^{\mathrm{i}\alpha}, \tag{B.1a}$$

$$p'(u)\dot{u} + \mathrm{i}p(u)\dot{\phi} + D_w(u)u + 2\mathrm{i}m\Omega u + V'(r)\mathrm{e}^{-\mathrm{i}\alpha} = 0, \tag{B.1b}$$

where $p(u) = m\gamma_B(u)u$ is the magnitude of the boosted droplet momentum and $\alpha(t) = \phi(t) - \theta(t)$ is the difference in the polar angles. We first seek steady orbital solutions (§B.1.1) before analysing the response to small perturbations (§B.1.2).

B.1.1 Steady state solutions

To characterise the dynamics of a droplet executing circular orbits of radius r_0 at constant speed $U = r_0\omega$, we seek solutions to (B.1) of the form $r(t) = r_0$, $u_p(t) = U$, and $\alpha = \text{constant}$.

From (B.1a), we deduce that $i r_0 \dot{\theta} = U e^{i\alpha}$, where $\dot{\theta} = \omega$ is the angular velocity. We thus deduce that $i = e^{i\alpha}$, implying that the difference in the phase angles is $\alpha = \frac{1}{2}\pi$ for steady orbital motion. Furthermore, substituting into (B.1b) and considering real and imaginary parts determines that $D_w(u)u = 0$ and $p(u)\omega + 2m\Omega u - V'(r_0) = 0$. The condition $D_w(u) = 0$ implies that the droplet orbits at the free-walking speed, u_0, with the orbital radius satisfying the condition $V'(r_0) = p(u_0)\omega + 2m\Omega u_0$, or

$$r_0 V'(r_0) = p(u_0)u_0 + 2m r_0 \Omega u_0. \tag{B.2}$$

For a given potential, $V(r)$, and bath rotation rate, Ω, this equation may be solved for r_0, with the corresponding angular frequency being defined $\omega = u_0/r_0$. Notably, this condition reduces to those enumerated in (3.12) and (3.13) for the cases of a droplet walking in a rotating bath or confined by an axisymmetric potential, respectively.

B.1.2 Stability problem

To assess the response of the system to small perturbations, we express the radius and speed as $r(t) = r_0 + \epsilon r_1(t)$ and $u(t) = u_0 + \epsilon u_1(t)$, where $0 < \epsilon \ll 1$ is a small parameter determining the magnitude of the perturbation, with r_0 satisfying the radial force balance... We likewise express the perturbations to the polar angles given as $\theta(t) = \omega t + \epsilon\theta_1(t)$ and $\phi(t) = \omega t + \frac{1}{2}\pi + \epsilon\phi_1(t)$, where the difference in the polar angles is $\alpha = \frac{1}{2}\pi + \epsilon\alpha_1(t)$, with $\alpha_1 = \phi_1 - \theta_1$. We proceed to substitute this perturbation ansatz into (B.1) and use Taylor expansions to derive linear equations for the perturbed variables.

By taking real and imaginary parts of the linearised equations, we deduce from (B.1a) that

$$\dot{r}_1 = -u_0\alpha_1, \tag{B.3a}$$

$$r_0\dot{\theta}_1 + r_1\omega = u_1. \tag{B.3b}$$

Furthermore, we deduce from the real and imaginary parts of the force balance equation (B.1b) that

$$p'(u_0)\dot{u}_1 + u_0 D'_w(u_0)u_1 = \alpha_1 V'(r_0), \tag{B.4a}$$

$$p(u_0)\dot{\phi}_1 + \omega p'(u_0)u_1 + 2m\Omega u_1 - V''(r_0)r_1 = 0. \tag{B.4b}$$

Notably, (B.3)–(B.4) forms a linear system for the four perturbation variables. Although one may characterise the linear stability by computing roots of the characteristic polynomial, we find it more illuminating to first eliminate the perturbed polar angles so as to derive a pair of coupled evolution equations for the perturbed radius and speed. Specifically, we differentiate (B.3a) with respect to time and substitute in $\dot{\alpha}_1 = \dot{\phi}_1 - \dot{\theta}_1$ using equations (B.3b) and (B.4b), giving

$$\ddot{r}_1 + \left(\frac{u_0 V''(r_0)}{p(u_0)} + \omega^2 \right) r_1 = \left[\omega \left(1 + \frac{p'(u_0)u_0}{p(u_0)} \right) + \frac{2m\Omega u_0}{p(u_0)} \right] u_1.$$

Using the orbital condition (B.2) then allows us to determine that radial perturbations evolve according to

$$\ddot{r}_1 + \omega^2 \left(1 + \frac{r_0 V''(r_0)}{V'(r_0) - 2m\Omega u_0} \right) r_1 = \left[\omega \left(1 + \frac{p'(u_0)u_0}{p(u_0)} \right) + \frac{2m\Omega u_0}{p(u_0)} \right] u_1. \tag{B.5a}$$

Finally, we use (B.3a) to eliminate $\alpha_1 = -\dot{r}_1/u_0$ from (B.4a), from which we deduce that speed perturbations evolve according to

$$p'(u_0)\dot{u}_1 + u_0 D'_w(u_0)u_1 = -\frac{V'(r_0)}{u_0}\dot{r}_1. \tag{B.5b}$$

System (B.5) governs the evolution of radial and speed perturbations about a steady circular orbit in the presence of both a Coriolis force and an axisymmetric potential. The perturbation equations for a Coriolis force ($V \equiv 0$) are stated in (3.14), where we have used the force balance (B.2) to eliminate Ω. Likewise, the perturbation equations for a droplet walking in an axisymmetric potential ($\Omega = 0$) are given in (3.15), where we have used the force balance (B.2) to eliminate $V'(r_0)$ on the right-hand side of (B.5b).

B.1.3 Perturbation eigenvalues

To calculate the eigenvalues governing the evolution of the radial and speed perturbations, we recast (B.5) as a three-dimensional first-order linear system, and evaluate the corresponding characteristic polynomial. For a Coriolis force ($V = 0$), we compute

$$\left(s^2 + \omega^2\right)\left(p'(u_0)s + u_0 D'_w(u_0)\right) = 0, \tag{B.6}$$

from which we immediately deduce that the eigenvalues are

$$s_\pm = \pm i\omega \quad \text{and} \quad s_0 = -\frac{u_0 D'_w(u_0)}{p'(u_0)}.$$

Notably, $s_0 < 0$ for the hydrodynamic pilot-wave system. As $\pm i\omega$ are the trivial eigenvalues corresponding to translational invariance, we find that the boost model does not predict instabilities for circular orbits in the presence of a Coriolis system.

We now consider the influence of an axisymmetric potential only, setting $\Omega = 0$ and using $p(u_0)\omega = V'(r_0)$ to eliminate the external potential in (B.5b). It follows that the characteristic polynomial is

$$\left(s^2 + \omega_r^2\right)\left(sp'(u_0) + u_0 D'_w(u_0)\right) + s\left(1 + \frac{u_0 p'(u_0)}{p(u_0)}\right)\frac{u_0 p(u_0)}{r_0^2} = 0, \tag{B.7}$$

which is similar in form to (B.6), but with ω replaced by ω_r and additional terms of size $O(r_0^{-2})$. We are thus motivated to seek a perturbative form for the eigenvalues in powers of r_0^{-2}, from which we deduce that

$$s_0 = -\frac{u_0 D'_w(u_0)}{p'(u_0)} + O\left(r_0^{-2}\right)$$

and

$$s_\pm = \pm i\omega_r - \frac{u_0\left(p(u_0) + u_0 p'(u_0)\right)}{2r_0^2\left(u_0^2 D'_w(u_0)^2 + \omega_r^2 p'(u_0)^2\right)}\left(u_0 D'_w(u_0) \pm i\omega_r p'(u_0)\right) + O\left(r_0^{-4}\right).$$

As $p(u_0)+u_0p'(u_0) > 0$ in the regime that walking droplets may be observed in the laboratory, we conclude that the real part of $s_\pm$ is negative, albeit close to zero. Consequently, we deduce that $s_\pm$ form a pair of near-critical eigenvalues. We remark that this analysis implies that instability requires that $\frac{\mathrm{d}}{\mathrm{d}u}\left(\frac{1}{2}up(u)\right) < 0$, where $up(u)$ can be interpreted as the boosted kinetic energy. In the absence of a boost factor, this derivative is always positive, so the boost factor is critical to the onset of instability. However, we observe that the form of the confining potential does not affect the sign of $s_\pm$, and thus the critical memory of instability, which we observe to be false in figure 3.7, indicating that while the boost analysis explains the instability mechanism, it fails to explain the onset of instability.

B.2 Orbital stability framework details

We provide explicit forms of the stability coefficients here for the dynamical system described by (3.20), and use them to derive general properties, and prove Theorem 1.

B.2.1 Stability coefficients

We consider the time evolution of the perturbations r_1 and θ_1 defined in (3.22), evolving under (3.20), by analysing their Laplace transforms, $R(s) = \mathscr{L}[r_1](s)$ and $\Theta(s) = \mathscr{L}[\theta_1](s)$. The Laplace transforms satisfy (3.23), where the matrix elements are given by

$$\mathscr{A}(s) = \frac{\partial \mathrm{f}_r}{\partial r} + s\frac{\partial \mathrm{f}_r}{\partial \dot{r}} + s^2\frac{\partial \mathrm{f}_r}{\partial \ddot{r}} + \int_0^\infty \frac{\partial w_r}{\partial x_1}(r_0, r_0, \omega t, t)\,\mathrm{d}t + \mathscr{L}\left[\frac{\partial w_r}{\partial x_2}(r_0, r_0, \omega t, t)\right], \quad \text{(B.8a)}$$

$$-r_0\mathscr{B}(s) = s\frac{\partial \mathrm{f}_r}{\partial \dot{\theta}} + s^2\frac{\partial \mathrm{f}_r}{\partial \ddot{\theta}} + \int_0^\infty \frac{\partial w_r}{\partial x_3}(r_0, r_0, \omega t, t)\,\mathrm{d}t - \mathscr{L}\left[\frac{\partial w_r}{\partial x_3}(r_0, r_0, \omega t, t)\right], \quad \text{(B.8b)}$$

$$\mathscr{C}(s) = \frac{\partial \mathrm{f}_\theta}{\partial r} + s\frac{\partial \mathrm{f}_\theta}{\partial \dot{r}} + s^2\frac{\partial \mathrm{f}_\theta}{\partial \ddot{r}} + \int_0^\infty \frac{\partial w_\theta}{\partial x_1}(r_0, r_0, \omega t, t)\,\mathrm{d}t + \mathscr{L}\left[\frac{\partial w_\theta}{\partial x_2}(r_0, r_0, \omega t, t)\right], \quad \text{(B.8c)}$$

$$r_0\mathscr{D}(s) = s\frac{\partial \mathrm{f}_\theta}{\partial \dot{\theta}} + s^2\frac{\partial \mathrm{f}_\theta}{\partial \ddot{\theta}} + \int_0^\infty \frac{\partial w_\theta}{\partial x_3}(r_0, r_0, \omega t, t)\,\mathrm{d}t - \mathscr{L}\left[\frac{\partial w_\theta}{\partial x_3}(r_0, r_0, \omega t, t)\right], \quad \text{(B.8d)}$$

where we define $\mathrm{f}_r(r, \dot{r}, \ddot{r}, \dot{\theta}, \ddot{\theta}, \zeta) = f_r(r, \dot{r}, \ddot{r}, \dot{\theta}, \ddot{\theta}) + \zeta f_{\mathrm{ext},r}(r, \dot{r}, \ddot{r}, \dot{\theta}, \ddot{\theta})$, and similarly for f_θ. In (B.8), $\mathrm{f}_r, \mathrm{f}_\theta, f_r$ and f_θ are understood to be evaluated at the steady circular orbit.

B.2.2 Properties of the stability coefficients

Before proceeding further, it is informative to note some of the limiting properties of the stability function $\mathscr{F}(s)$. In particular, rotational invariance of the pilot-wave system renders $\mathscr{B}(0) = \mathscr{D}(0) = 0$, and hence $\mathscr{F}(0) = 0$. We thus conclude that

$$\mathscr{F}(s) = \mathscr{F}'(0)s + O(s^2) \quad \text{(B.9)}$$

for sufficiently small s, where

$$\mathscr{F}'(0) = \mathscr{A}(0)\mathscr{D}'(0) + \mathscr{B}'(0)\mathscr{C}(0).$$

In fact, the stability coefficients in this case are very closely related to the equilibrium force balance equations in (3.21), with

$$\mathscr{A}(0) = \frac{\partial f_r}{\partial r} + \int_0^\infty \frac{\partial w_r}{\partial x_1}(r_0, r_0, \omega t, t) + \frac{\partial w_r}{\partial x_2}(r_0, r_0, \omega t, t)\, \mathrm{d}t = \frac{\partial F_r}{\partial r_0}, \tag{B.10a}$$

$$-r_0\mathscr{B}'(0) = \frac{\partial f_r}{\partial \dot\theta} + \int_0^\infty t\frac{\partial w_r}{\partial x_3}(r_0, r_0, \omega t, t)\, \mathrm{d}t = \frac{\partial F_r}{\partial \omega}, \tag{B.10b}$$

$$\mathscr{C}(0) = \frac{\partial f_\theta}{\partial r} + \int_0^\infty \frac{\partial w_\theta}{\partial x_1}(r_0, r_0, \omega t, t) + \frac{\partial w_\theta}{\partial x_2}(r_0, r_0, \omega t, t)\, \mathrm{d}t = \frac{\partial F_\theta}{\partial r_0}, \tag{B.10c}$$

$$r_0\mathscr{D}'(0) = \frac{\partial f_\theta}{\partial \dot\theta} + \int_0^\infty t\frac{\partial w_\theta}{\partial x_3}(r_0, r_0, \omega t, t)\, \mathrm{d}t = \frac{\partial F_\theta}{\partial \omega}, \tag{B.10d}$$

and so we may equivalently write

$$r_0\mathscr{F}'(0) = \frac{\partial F_r}{\partial r_0}\frac{\partial F_\theta}{\partial \omega} - \frac{\partial F_r}{\partial \omega}\frac{\partial F_\theta}{\partial r_0}. \tag{B.11}$$

Finally, as all Laplace transforms in (B.8) decay to zero as $s \to \infty$, we conclude that $\mathscr{F}(s) \sim c_\infty s^4 + o(s^4)$ for sufficiently large s, where

$$c_\infty = \frac{1}{r_0}\left[\frac{\partial f_r}{\partial \ddot r}\frac{\partial f_\theta}{\partial \ddot\theta} - \frac{\partial f_r}{\partial \ddot\theta}\frac{\partial f_\theta}{\partial \ddot r}\right]. \tag{B.12}$$

Using the properties of the stability coefficients outlined in appendix B.2.2, we naturally arrive at Proposition 1.1, which provides a sufficient condition for instability.

Proposition 1.1 *If $f_{\mathrm{ext},r}\frac{\mathrm{d}\zeta_0}{\mathrm{d}r_0}\mathscr{D}'(0)$ and c_∞ have the same sign, then the system (3.23) has a real and positive eigenvalue.*

Proof 1.1 *The proof is similar to that outlined by Oza et al. [79] for the case of a Coriolis force, but sidesteps the need to evaluate various integrals defined in terms of Bessel functions. We first note that differentiating the force balance equations (3.21) with respect to r_0 gives*

$$\frac{\partial F_r}{\partial r_0} + \frac{\partial F_r}{\partial \omega}\frac{\mathrm{d}\omega}{\mathrm{d}r_0} + f_{\mathrm{ext},r}\frac{\mathrm{d}\zeta_0}{\mathrm{d}r_0} = 0, \tag{B.13a}$$

$$\frac{\partial F_\theta}{\partial r_0} + \frac{\partial F_\theta}{\partial \omega}\frac{\mathrm{d}\omega}{\mathrm{d}r_0} = 0. \tag{B.13b}$$

By eliminating $\mathrm{d}\omega/\mathrm{d}r_0$, we find that

$$\frac{\partial F_r}{\partial r_0}\frac{\partial F_\theta}{\partial \omega} - \frac{\partial F_r}{\partial \omega}\frac{\partial F_\theta}{\partial r_0} + f_{\mathrm{ext},r}\frac{\mathrm{d}\zeta_0}{\mathrm{d}r_0}\frac{\partial F_\theta}{\partial \omega} = 0,$$

whereupon applying (B.11) to the first two terms immediately yields the relationship

$$r_0\mathscr{F}'(0) + f_{\mathrm{ext},r}\frac{\mathrm{d}\zeta_0}{\mathrm{d}r_0}\frac{\partial F_\theta}{\partial \omega} = 0.$$

We now simplify the triple product by noting that the third term may be replaced by $\mathscr{D}'(0)$ using (B.10d), *giving*

$$\mathscr{F}'(0) = -\frac{1}{r_0} f_{\text{ext},r} \frac{\mathrm{d}\zeta_0}{\mathrm{d}r_0} \mathscr{D}'(0). \tag{B.14}$$

We conclude the proof by exploiting the asymptotic forms of $\mathscr{F}(s) = \mathscr{F}'(0)s + O(s^2)$ for small s and $\mathscr{F}(s) = c_\infty s^4 + o(s^4)$ for large s. Specifically, if $f_{\text{ext},r}\frac{\mathrm{d}\zeta_0}{\mathrm{d}r_0}\mathscr{D}'(0)$ and c_∞ have the same sign, then the sign of $\mathscr{F}(s)$ is different for sufficiently small and large positive s. It follows by the intermediate value theorem that there exists a real and positive root of $\mathscr{F}(s)$.

Notably, the statement in Proposition 1.1 may be simplified when one leverages some of the specific features of the stroboscopic pilot-wave model. First, examining the left-hand side of (3.19) demonstrates that

$$\frac{\partial f_r}{\partial \ddot{\theta}} = \frac{\partial f_\theta}{\partial \ddot{r}} = 0, \quad \frac{\partial f_r}{\partial \ddot{r}} = m \quad \text{and} \quad \frac{\partial f_\theta}{\partial \ddot{\theta}} = m$$

for steady orbital motion, and thus $c_\infty = m^2 > 0$ for circular orbits. In addition, we only consider attractive forces, which correspond to $f_{\text{ext},r} > 0$. Finally, we prove in appendix B.4 that $\mathscr{D}'(0) > 0$ for the stroboscopic model, adding mathematical robustness to the numerical verification performed by Oza [77]. This indicates that if $\frac{\mathrm{d}\zeta_0}{\mathrm{d}r_0} > 0$, then circular orbits are unstable, leading to Theorem 1.

B.2.3   Recasting Theorem 1 into Corollary 1.1

We can recast Theorem 1 by separating the external force from the force balance, as in (3.20). ζf_{ext} is the external force, and $f_{\text{ext}}(r_0) > 0$. As $F_r(r_0, \omega, \zeta) = 0$ for any circular orbit satisfying the force balance (3.21), we use the chain rule to write

$$\frac{\mathrm{d}F_r}{\mathrm{d}r_0} = \frac{\partial F_r}{\partial r_0} + \frac{\partial F_r}{\partial \omega}\frac{\mathrm{d}\omega}{\mathrm{d}r_0} + \frac{\partial F_r}{\partial \zeta}\frac{\mathrm{d}\zeta}{\mathrm{d}r_0} = 0. \tag{B.15}$$

$\frac{\partial F_r}{\partial \zeta} = f_{\text{ext}}(r_0, \omega) > 0$. Therefore, we see that if ζ is held constant, then $\frac{\mathrm{d}F_r}{\mathrm{d}r_0} < 0$. This leads to Corollary 1.1.

B.2.4   Comparison of Theorem 1 with classical orbital mechanics

Theorem 1 is valid for the hydrodynamic system, but it is also valid in the absence of a pilot wave. In this section, we consider the implications of applying Theorem 1 to classical orbital mechanics.

We consider a particle moving in a circular orbit of radius r_0 and orbital frequency ω, and an external potential $\zeta_0 V(|\boldsymbol{x}_p|)$, where $\boldsymbol{x}_p$ is the particle position, and ζ_0 is the required force coefficient to sustain the circular orbit. The radial force balance takes the form

$$mr_0\omega^2 = \zeta_0 V'(r_0). \tag{B.16}$$

By conservation of momentum, $l = mr_0^2 \omega$ is conserved, so

$$\zeta_0 = \frac{l^2}{mr_0^3 V'(r_0)}, \tag{B.17}$$

and by Theorem 1, unstable circular orbits arise if

$$\frac{\mathrm{d}\zeta_0}{\mathrm{d}r_0} = -\frac{\zeta_0}{r_0}\left(3 + \frac{r_0 V''(r_0)}{V'(r_0))}\right) > 0. \tag{B.18}$$

which is the same instability condition derived in §3.2.1. We can also consider what happens in the event of a conserved orbital speed. If $U = r_0 \omega$ is constant, then

$$\zeta_0 = \frac{mU^2}{r_0 V'(r_0)}, \tag{B.19}$$

and by Theorem 1, unstable circular orbits arise if

$$\frac{\mathrm{d}\zeta_0}{\mathrm{d}r_0} = -\frac{\zeta_0}{r_0}\left(1 + \frac{r_0 V''(r_0)}{V'(r_0)}\right) > 0. \tag{B.20}$$

Both of these instability conditions were derived in §3.2, and so Theorem 1 is a generalisation of the instability of circular orbits in classical orbital mechanics to pilot-wave dynamics.

B.3 The onset of orbital instability

To analyse the wobbling tongues, we recast the stability functions by evaluating all integrals analytically [66] and converting to dimensionless variables. Specifically, we take $T = 1/(ck_F)$ to be the unit of time, where $c = \sqrt{F/DT_F k_F}$ is the maximum steady orbital speed. Then, by defining $\hat{\mathscr{A}}(\hat{s}) = \mathscr{A}(s)T/D$ (and likewise $\hat{\mathscr{B}}$, $\hat{\mathscr{C}}$ and $\hat{\mathscr{D}}$) and introducing the dimensionless parameters $M = m/DT$ and $\zeta = T/T_M$, we obtain the tangential force balance

$$1 - \hat{r}_0^2 \hat{\omega}^2 = \beta f_{00}(\beta, \hat{r}_0), \tag{B.21a}$$

where $\hat{r}_0 = k_F r_0$ and $\hat{\omega} = \omega T$ represent the dimensionless radius and orbital frequency, respectively, and

$$f_{ab}(\eta, \hat{r}_0) = \pi \operatorname{csch}(\pi\eta)\frac{\mathrm{d}^a}{\mathrm{d}\hat{r}_0^a}(\mathrm{J}_{-\mathrm{i}\eta}(\hat{r}_0))\frac{\mathrm{d}^b}{\mathrm{d}\hat{r}_0^b}(\mathrm{J}_{\mathrm{i}\eta}(\hat{r}_0)) \quad \text{for } a, b \in \{0, 1\}.$$

Furthermore, the dimensionless stability coefficients are

$$\hat{\mathscr{A}}(\hat{s}) = M(\hat{s}^2 + \hat{\omega}^2(n-1)) + \frac{(n+1)}{\hat{r}_0\hat{\omega}}\left(\frac{i}{\hat{r}_0} - f_{01}(\beta, \hat{r}_0)\right)$$
$$+ \frac{1}{\hat{\omega}}\left[f_{11}(\eta, \hat{r}_0) - f_{00}(\beta, \hat{r}_0)\left(1 + \frac{\beta\eta}{\hat{r}_0^2}\right)\right], \tag{B.21b}$$

$$\hat{\mathscr{B}}(\hat{s}) = (2-\Delta)M\hat{\omega}\hat{s} - \frac{i\hat{s}(\Delta+1)}{\hat{r}_0^2\hat{\omega}^2} + \frac{1}{\hat{r}_0\hat{\omega}}\left[\left(\frac{\hat{s}\Delta}{\hat{\omega}} - \beta\right)f_{01}(\beta, \hat{r}_0) + \eta f_{01}(\eta, \hat{r}_0)\right], \tag{B.21c}$$

$$\hat{\mathscr{C}}(\hat{s}) = (2-\Delta)M\hat{\omega}\hat{s} + 2\hat{\omega} + \frac{i\hat{s}(\Delta-1)}{\hat{r}_0^2\hat{\omega}^2} + \frac{1}{\hat{r}_0\hat{\omega}}\left[\left(\frac{\hat{s}\Delta}{\hat{\omega}} + \beta\right)f_{01}(\beta, \hat{r}_0) + \eta f_{01}(\eta, \hat{r}_0)\right], \tag{B.21d}$$

$$\hat{\mathscr{D}}(\hat{s}) = M\hat{s}^2 + 2\hat{s} + \frac{\eta}{\hat{r}_0^2\hat{\omega}}\left[\beta f_{00}(\beta, \hat{r}_0) - \eta f_{00}(\eta, \hat{r}_0)\right], \tag{B.21e}$$

where $\hat{s} = sT$ represents the dimensionless growth rate with $\eta = \hat{s}/\hat{\omega} + \beta$ and $\beta = \zeta/\hat{\omega}$. ζ has been eliminated by using (B.21a). We aim to determine the critical value of the dimensionless wave decay rate, ζ, at which the growth rate, $\hat{s}$, has vanishing real part, writing $\hat{s} = i\xi\hat{\omega}$ for real $\xi = O(1)$. We recall that the Coriolis force is denoted by $\Delta = 1$ and one should consider the case $n = 1$; for a central force, we define $\Delta = 0$ and treat n as an arbitrary parameter defining the radial power law of the central force.

We proceed to use the large-argument expansions outlined in [66], valid because $\beta = O(\ln(\hat{r}_0))$. However, we now find that $\hat{\mathscr{D}}(i\xi\hat{\omega}) = i\xi\hat{\mathscr{C}}(i\xi\hat{\omega}) + i(\Delta - 1)M\hat{\omega}^2\xi + O(\hat{r}_0^{-3})$, and $\hat{\mathscr{D}}(i\xi\hat{\omega}) = O(\hat{r}_0^{-1})$; only in the case of the Coriolis force, when $\Delta = 1$, can we write $\hat{\mathscr{D}}(i\xi\hat{\omega}) = i\xi\hat{\mathscr{C}}(i\xi\hat{\omega}) + O(\hat{r}_0^{-3})$. In the presence of a central force, we must consider the entire stability function. Using the tangential equation (B.21a) to eliminate $\hat{\omega}$ and approximating $\mathrm{csch}(\pi\beta) = 2\mathrm{e}^{-\pi\beta} + O(\mathrm{e}^{-2\pi\beta})$, we find

$$\frac{(\hat{r}_0\hat{\omega})^2\hat{\mathscr{F}}(i\xi\hat{\omega})}{i\xi} = \frac{\mathrm{e}^{-\pi\beta}}{\hat{r}_0}\left[-16(1+\mathrm{e}^{-i\pi\xi})\sin(2\hat{r}_0) + O\left(\frac{1}{\hat{r}_0}\right)\right] + \frac{-4(1+2M)(-1+\Delta-n+\xi^2)}{\hat{r}_0^3}$$
$$+ \frac{i(-6i\beta(1+4M)(-1+\Delta-n+\xi^2) + \xi(-3+\Delta(2-4M-16M^2)+\Delta^2(1+4M+4M^2)))}{\hat{r}_0^4}$$
$$- \frac{4iM^2(3+n-\xi^2) + 2(M+1)(\xi^2-n)}{\hat{r}_0^4} + O\left(\frac{1}{\hat{r}_0^5}\right), \tag{B.22}$$

which forms the foundation of our analysis of resonant and non-resonant instabilities.

The analysis is now performed by considering the possible dominant balances between $\mathrm{e}^{-\pi\beta}$ and powers of $\hat{r}_0$. There are two possibilities. If $-1+\Delta-n+\xi^2 \neq 0$, then the dominant balance is between the $O\left(\mathrm{e}^{-\pi\beta}\hat{r}_0^{-1}\right)$ and $O(\hat{r}_0^{-3})$ terms. Otherwise, the dominant balance is between the $O\left(\mathrm{e}^{-\pi\beta}\hat{r}_0^{-1}\right)$ and $O(\hat{r}_0^{-4})$ terms. In the presence of a Coriolis force, $\Delta = n = 1$, and the $O(\hat{r}_0^{-3})$ term vanishes only if $\xi^2 = 1$, which is a trivial eigenvalue.

If the $O(\hat{r}_0^{-3})$ term does not vanish, as occurs in the Coriolis system, and for resonant instabilities in the central force system, the dominant balance between the dominant $\mathrm{e}^{-\pi\beta}$

and $\hat{r}_0$ terms takes the form

$$-\frac{16e^{-\pi\beta}(1 + e^{-i\pi\xi})\sin(2\hat{r}_0)}{\hat{r}_0} - \frac{4(1 + 2M)(-1 + \Delta - n + \xi^2)}{\hat{r}_0^3} = O\left(\frac{e^{-\pi\beta}}{\hat{r}_0^2}\right) + O\left(\frac{1}{\hat{r}_0^4}\right),$$
(B.23)

which is the dominant balance leading to the resonant instabilities discussed in Liu et al. [66] and in (3.34). Balancing the imaginary parts requires that ξ be an integer, but balancing the real parts requires that ξ be an even integer. Solving (B.3) for ξ to $O(\hat{r}_0^{-1})$ then leads to the results in (3.33).

In the presence of a central force, where $\Delta = 0$, two dominant balances are possible. If $n = \xi^2 - 1$, as hinted at by the boost calculation in §3.4.2, the dominant balance is between the $O\left(e^{-\pi\beta}\hat{r}_0^{-1}\right)$ and $O(\hat{r}_0^{-2})$ terms, which leads to the balance

$$-\frac{16e^{-\pi\beta}(1 + e^{-i\pi\xi})\sin(2\hat{r}_0)}{\hat{r}_0} + \frac{i\xi(4M - 1)(2M + 1)}{\hat{r}_0^4} = O\left(\frac{e^{-i\pi\beta}}{\hat{r}_0^2}\right) + O\left(\frac{1}{\hat{r}_0^5}\right),$$
(B.24)

which is responsible for the non-resonant instability discussed in (3.34).

For the special case when $n = 3$, and $\xi^2 - 1 = n$ for $\xi = 2$, the resonant and non-resonant boundaries coincide, and a more sophisticated treatment is necessary, given in (cite new paper).

B.4 Proof that $\mathscr{D}'(0) > 0$ for the stroboscopic model

To prove that $\mathscr{D}'(0) > 0$ for the stroboscopic pilot-wave model, with $\mathscr{D}(s)$ defined in (3.26d), we first convert to dimensionless variables. As outlined in appendix B.3, we define $\hat{\mathscr{D}}(\hat{s}) = \mathscr{D}(s)T/D$, where $\hat{s} = sT$ and $T = 1/(ck_F)$ is the unit of time. From (B.21e), it thus remains to prove that $\hat{\mathscr{D}}'(0) > 0$, where

$$\hat{\mathscr{D}}'(0) = 2 - \frac{\pi\beta}{\hat{r}_0^2\hat{\omega}^2}\frac{d}{d\beta}\left(\beta\operatorname{csch}(\pi\beta)J_{-i\beta}(\hat{r}_0)J_{i\beta}(\hat{r}_0)\right).$$
(B.25)

Liu et al. [66] demonstrated that the stability integrals (3.27) can be evaluated in terms of complex-order Bessel functions (as was used in appendix B.3), with equivalent expressions defined using infinite sums. In particular, combining equations (3.29a) and (3.29b) with $m = 0$ gives

$$\pi\beta\operatorname{csch}(\pi\beta)J_{-i\beta}(\hat{r}_0)J_{i\beta}(\hat{r}_0) = \sum_{n=-\infty}^{\infty}\frac{\beta^2 J_n^2(\hat{r}_0)}{n^2 + \beta^2},$$
(B.26)

which we substitute into (B.25) to obtain

$$\frac{\hat{r}_0^2\hat{\omega}^2}{2}\hat{\mathscr{D}}'(0) = \hat{r}_0^2\hat{\omega}^2 - \sum_{n=-\infty}^{\infty}\frac{n^2\beta^2 J_n^2(\hat{r}_0)}{(\beta^2 + n^2)^2}.$$
(B.27)

To proceed, we recognise that the left-hand side of (B.26) is the same as the right-hand side of the tangential force balance (B.21a). We may thus express the tangential force balance

in terms of the infinite sum and then eliminate $\hat{r}_0^2 \hat{\omega}^2$ from the right-hand side of (B.27). A short calculation gives rise to the simplified expression

$$\frac{\hat{r}_0^2 \hat{\omega}^2}{2} \hat{\mathscr{D}}'(0) = 1 - \sum_{n=-\infty}^{\infty} \frac{\mathrm{J}_n^2(\hat{r}_0)\beta^2}{(\beta^2 + n^2)} \left(1 + \frac{n^2}{\beta^2 + n^2} \right), \tag{B.28}$$

where it remains to prove that

$$f(\beta) = \sum_{n=-\infty}^{\infty} \frac{\mathrm{J}_n^2(\hat{r}_0)\beta^2}{(\beta^2 + n^2)} \left(1 + \frac{n^2}{\beta^2 + n^2} \right), \tag{B.29}$$

as appears on the right-hand side of (B.28), is bounded in the interval $0 < f(\beta) < 1$ for all finite $\beta > 0$, treating $\hat{r}_0$ as fixed.

To complete the proof, we first note that

$$\lim_{\beta \to 0} f(\beta) = 0 \quad \text{and} \quad \lim_{\beta \to \infty} f(\beta) = \sum_{n=-\infty}^{\infty} \mathrm{J}_n^2(\hat{r}_0) = 1.$$

Moreover, each term in the series (B.29) is an increasing function of β, with

$$\frac{\partial}{\partial \beta} \left(\frac{\beta^2}{(\beta^2 + n^2)} \left(1 + \frac{n^2}{\beta^2 + n^2} \right) \right) = \frac{4\beta n^4}{(\beta^2 + n^2)^3} > 0. \tag{B.30}$$

Consequently, $f'(\beta) > 0$, so $f(\beta)$ is a monotonically increasing function. We conclude that $0 < f(\beta) < 1$ for all $0 < \beta < \infty$, which proves that $\hat{\mathscr{D}}'(0) > 0$, and thus $\mathscr{D}'(0) > 0$, for the stroboscopic pilot-wave model.

B.5 Instability for low orbital radius

We prove that, for $n < 0$ and sufficiently small r_0, circular orbits are unstable using theorem 1. We remark that theorem 1 does not guarantee that the real and positive eigenvalue found is the dominant growth rate, only that such a growth rate exists. In the stroboscopic model, theorem 1 reduces to requiring $\frac{\partial f_r}{\partial k} \frac{\mathrm{d}k}{\mathrm{d}r_0} \mathscr{D}'(0) > 0$ for instability. For any attractive force, $\frac{\partial f_r}{\partial k} > 0$, and using appendix B.4, we know that $\mathscr{D}'(0) > 0$, so we only need $\frac{\mathrm{d}k}{\mathrm{d}r_0} > 0$.

We proceed to show that $\frac{\mathrm{d}k}{\mathrm{d}r_0} > 0$ for $n < 1$ and sufficiently small r_0. For small r_0, the tangential and radial force balances in (3.9) simplify to

$$D = \frac{Fk}{T_F \left(\frac{1}{T_M^2} + \omega^2 \right)} + O(r_0^2), \tag{B.31a}$$

$$-m r_0 \omega^2 = \frac{F k r_0 \omega^2 T_M}{T_F \left(\frac{1}{T_M^2} + \omega^2 \right)} - k r_0^n + O(r_0^3). \tag{B.31b}$$

Substituting (B.31a) into (B.31b), we can solve for k as

$$k = r_0^{1-n} \omega^2 (m + D T_M). \tag{B.32}$$

At constant memory, T_M is constant, so by (B.31a), ω is constant. Therefore, we find

$$\frac{\mathrm{d}k}{\mathrm{d}r_0} = (1-n)r_0^{-n}\omega^2(m + DT_M), \tag{B.33}$$

which shows that if $n < 1$, then $\frac{\mathrm{d}k}{\mathrm{d}r_0} > 0$ for sufficiently small r_0.

Appendix C

Chapter 4 appendices

C.1 Integral expansions for large radius, constant memory

We wish to find asymptotic expansions for the class of integrals

$$I(r_0) = \int_0^\infty f\left(2r_0 \sin\left(\frac{\omega t}{2}\right)\right) P(\omega t) \mathrm{e}^{-(\sigma + \mathrm{i}S)t} \, \mathrm{d}t,$$

$$= \frac{1}{U} \int_0^\infty f\left(2r_0 \sin\left(\frac{t}{2r_0}\right)\right) P\left(\frac{t}{r_0}\right) \mathrm{e}^{-\left(\frac{\sigma}{U} + \frac{\mathrm{i}\xi}{r_0}\right)t} \, \mathrm{d}t. \tag{C.1}$$

where f and P are infinitely differentiable functions with bounded derivatives as functions of a real argument. From the generalised mean value theorem, applied once to f and once to $\sin\left(\frac{t}{2r_0}\right)$,

$$\left| f\left(2r_0 \sin\left(\frac{t}{2r_0}\right)\right) - f\left(t - \frac{t^3}{24r_0^2}\right) \right| \le ||f'||_\infty \left| 2r_0 \sin\left(\frac{t}{2r_0}\right) - t + \frac{t^3}{24r_0^2} \right|$$

$$\le ||f'||_\infty \frac{t^5}{1920 r_0^4}, \tag{C.2}$$

i.e. as the difference between the arguments is $O\left(\frac{1}{r_0^4}\right)$, so is the difference between the functions.

Therefore, using $|x - y| \le |x - z| + |z - y|$ and another application of the mean value theorem, we see that

$$\left| f\left(2r_0 \sin\left(\frac{t}{2r_0}\right)\right) - f(t) + \frac{t^3}{24r_0^2} f'(t) \right|$$

$$\le \left| f\left(2r_0 \sin\left(\frac{t}{2r_0}\right)\right) - f\left(t - \frac{t^3}{24r_0^2}\right) \right| + \left| f\left(t - \frac{t^3}{24r_0^2}\right) - f(t) + \frac{t^3}{24r_0^2} f'(t) \right|$$

$$\le ||f'||_\infty \frac{t^5}{1920 r_0^4} + \frac{t^6}{1152 r_0^4} = O\left(\frac{1}{r_0^4}\right) \tag{C.3}$$

195

Given a series approximation of P as

$$P\left(\frac{t}{r_0}\right) = P_4(t, r_0) + O\left(\frac{1}{r_0^4}\right),$$

(C.4)

we can apply the triangle inequality again to conclude that

$$\left| f\left(2r_0 \sin\left(\frac{t}{2r_0}\right)\right) P\left(\frac{t}{r_0}\right) - \left(f(t) - \frac{t^3}{24r_0^2} f'(t)\right) P_4(t, r_0) \right| = O\left(\frac{1}{r_0^4}\right).$$

(C.5)

Expanding the exponential finally yields, as a $O\left(\frac{1}{r_0^4}\right)$ approximation to I,

$$I(r_0) = \frac{1}{U} \int_0^\infty \left(f(t) - \frac{t^3}{24r_0^2} f'(t)\right) \left(1 - \frac{\mathrm{i}\xi t}{r_0} - \frac{\xi t^2}{2r_0^2} + \frac{\mathrm{i}\xi^3 t^3}{6r_0^3}\right) P_4(t, r_0) \mathrm{e}^{-\frac{\sigma t}{U}} \, \mathrm{d}t$$
$$+ O\left(\frac{1}{r_0^4}\right).$$

(C.6)

This procedure may be extended to yield expansions of higher order if necessary.

C.2 Low orbital memory integral expansions

We solve for the stability boundaries in the limit $\sigma = O(1), r_0 \to \infty, \xi = O(1)$, and consider a general expansion of the stability coefficients of the form

$$\mathscr{A}(\mathrm{i}\xi\omega) = \mathscr{A}_0 + \frac{\mathscr{A}_1}{r_0} + \frac{\mathscr{A}_2}{r_0^2} + \frac{\mathscr{A}_3}{r_0^3} + O\left(\frac{1}{r_0^4}\right),$$

(C.7)

and similarly for $\mathscr{B}, \mathscr{C}$ and $\mathscr{D}$ evaluated at $s = \mathrm{i}\xi\omega$. Due to the form of the tangential force balance (4.8e) and the integral expansions for $\mathcal{I}_0(0)$ in (C.1), U is expanded in powers of $\frac{1}{r_0^2}$. We now expand the integrals defining the stability coefficients to the orders necessary for

our analysis, giving

$$\mathscr{A}(\mathrm{i}\xi\omega) = \sigma - \frac{1}{2U}(L_{0,0}(p) - L_{2,0}(p)) + \frac{\mathrm{i}U\xi}{r_0}\left(1 - \frac{1}{2U^2}(L_{0,1}(p) + L_{2,1}(p))\right)$$

$$+\frac{1}{r_0^2}\left(MU^2(n - 1 - \xi^2) + \frac{n+1}{2U}L_{1,1}(p) + \frac{1}{24U}M_{0,1}(p) - \frac{1}{48U}(12L_{0,2}(p) + M_{0,3}(p))\right.$$

$$\left.-\frac{1}{48U}M_{2,3}(p) - \frac{\xi^2}{4U}(L_{0,2}(p) + L_{2,2}(p))\right)$$

$$+\frac{1}{r_0^3}\left[\frac{\mathrm{i}\xi}{4U}L_{0,3}(p) + \frac{\mathrm{i}\xi^3}{12U}(L_{0,3}(p) + L_{2,3}(p)) + \frac{\mathrm{i}\xi}{48U}(M_{0,4}(p) + M_{2,4}(p))\right] + O\left(\frac{1}{r_0^4}\right), \quad \text{(C.8a)}$$

$$\mathscr{B}(\mathrm{i}\xi\omega) = \frac{1}{r_0}\left[\frac{p}{2U}L_{1,1}(p) - \frac{1}{2U}L_{0,1}(p)\right] + \frac{1}{r_0^2}\left[2\mathrm{i}\xi MU^2 + \frac{\mathrm{i}\xi}{2U}L_{0,2}(p)\right]$$

$$+\frac{1}{48Ur_0^3}(4(3\xi^2 + 1)L_{0,3}(p) + M_{0,4}(p) - p(L_{1,3}(p) - M_{1,4}(p))) + O\left(\frac{1}{r_0^4}\right) \quad \text{(C.8b)}$$

$$\mathscr{C}(\mathrm{i}\xi\omega) = \frac{1}{r_0}\left(2U - \frac{p}{2U}L_{1,1}(p) - \frac{1}{2U}L_{0,1}(p)\right) + \frac{1}{r_0^2}\left[2\mathrm{i}\xi MU^2 + \frac{\mathrm{i}\xi}{2U}L_{0,2}(p)\right] + O\left(\frac{1}{r_0^3}\right),$$

$$\text{(C.8c)}$$

$$\mathscr{D}(\mathrm{i}\xi\omega) = -\sigma + \frac{1}{U}M_{1,0}(p) + \frac{\mathrm{i}\xi U}{r_0}\left(1 - \frac{1}{2U^2}(L_{0,1}(p) - L_{2,1}(p))\right)$$

$$+\frac{1}{r_0^2}\left[-MU^2\xi^2 + \frac{1}{48U}(-36L_{0,2}(p) + L_{1,3}(p) + 24L_{2,2}(p) + M_{2,3}(p))\right] + O\left(\frac{1}{r_0^3}\right), \quad \text{(C.8d)}$$

where the orbital speed satisfies

$$U^2 = L_{1,0}(p) - \frac{1}{24r_0^2}(3L_{1,2}(p) + M_{1,3}(p)) + O\left(\frac{1}{r_0^4}\right). \quad \text{(C.8e)}$$

In the above equations, we denote $p = \sigma/U$,

$$L_{m,n}(x) = \int_0^\infty t^n \mathrm{J}_m(t)\mathrm{e}^{-xt}\,\mathrm{d}t, \quad \text{(C.9a)}$$

$$\text{and} \quad M_{m,n}(x) = \int_0^\infty t^n \mathrm{J}_m'(t)\mathrm{e}^{-xt}\,\mathrm{d}t. \quad \text{(C.9b)}$$

We begin by simplifying the stability coefficients in equation (C.8) into a more applicable form.

C.2.1 Simplifying the stability coefficients

We begin by using the tangential force balance equation (C.8e) to eliminate several terms in $\mathscr{A}$ and $\mathscr{D}$. Firstly, we note that

$$L_{0,0}(p) - L_{2,0}(p) = 2M_{1,0}(p), \quad \text{(C.10)}$$

using Bessel function identities. Then, integrating by parts, and using (C.8e), we write

$$\sigma - \frac{1}{2U}(L_{0,0}(p) - L_{2,0}(p)) = -\left[-\sigma + \frac{1}{U}M_{1,0}(p)\right]$$

$$= -\frac{p}{24Ur_0^2}(3L_{1,2}(p) + M_{1,3}(p)) + O\left(\frac{1}{r_0^4}\right). \tag{C.11}$$

Secondly, using $J_0(x) + J_2(x) = \frac{2J_1(x)}{x}$ and (C.8e), we note that the $O\left(r_0^{-1}\right)$ term in $\mathscr{A}(i\xi\omega)$ can be simplified to

$$\frac{iU\xi}{r_0}\left(1 - \frac{1}{2U^2}(L_{0,1}(p) + L_{2,1}(p))\right) = \frac{iU\xi}{r_0}\left(1 - \frac{1}{U^2}L_{1,0}(p)\right) = -\frac{i\xi}{24Ur_0^3}(3L_{1,2}(p) + M_{1,3}(p)) + O\left(\frac{1}{r_0^5}\right). \tag{C.12}$$

Finally, many resulting expressions containing multiplicative factors of σ and p can be simplified via integration by parts. For instance, in $\mathscr{B}(i\xi\omega)$,

$$pL_{1,1}(p) - L_{0,1}(p) = -\int_0^\infty tJ_1(t)\frac{\mathrm{d}}{\mathrm{d}t}(e^{-pt})\,\mathrm{d}t - \int_0^\infty tJ_0(t)e^{-pt} = \left[-tJ_0(t)e^{-pt}\right]_0^\infty = 0. \tag{C.13}$$

Similarly, in $\mathscr{A}(i\xi\omega)$,

$$-\frac{p}{24U}(3L_{1,2}(p) + M_{1,3}(p)) - \frac{1}{4U}L_{0,2}(p) + \frac{1}{48U}(M_{0,3}(p) - M_{2,3}(p))$$

$$= \frac{1}{24U}\int_0^\infty \frac{\mathrm{d}}{\mathrm{d}t}(e^{-pt})(3t^2J_1(t) + t^3J_1'(t))\,\mathrm{d}t - \frac{1}{4U}L_{0,2}(p) + \frac{1}{48U}(M_{0,3}(p) - M_{2,3}(p))$$

$$= -\frac{1}{24U}\int_0^\infty (6tJ_1(t) + 6t^2J_1'(t) + t^3J_1''(t))e^{-pt}\,\mathrm{d}t - \frac{1}{4U}L_{0,2}(p) + \frac{1}{48U}(M_{0,3}(p) - M_{2,3}(p))$$

$$= -\frac{1}{2U}L_{0,2}(p), \tag{C.14}$$

where the last equality follows from noting that $J_0'(x) = -J_1(x)$, applying the Bessel differential equation for $J_0(x)$, and using that $J_0(x) - J_2(x) = 2J_1'(x)$.

After similar simplifications, the stability coefficients take the form

$$\mathscr{A}(i\xi\omega) = \frac{1}{r_0^2}\left[MU^2(n - 1 - \xi^2) + \frac{(n + 1 - \xi^2)}{2U}L_{1,1}(p) - \frac{1}{2U}L_{0,2}(p)\right]$$

$$+ \frac{i\xi}{12Ur_0^3}\left(3L_{0,3}(p) + 2(\xi^2 - 1)L_{1,2}(p)\right) + O\left(\frac{1}{r_0^4}\right), \tag{C.15a}$$

$$\mathscr{B}(i\xi\omega) = \frac{i\xi U}{r_0^2}\left(2MU + \frac{1}{2U^2}L_{0,2}(p)\right) + \frac{\xi^2}{4Ur_0^3}L_{0,3}(p) + O\left(\frac{1}{r_0^4}\right), \tag{C.15b}$$

$$\mathscr{C}(i\xi\omega) = \frac{1}{Ur_0}L_{2,1}(p) + \frac{i\xi U}{r_0^2}\left(2MU + \frac{1}{2U^2}L_{0,2}(p)\right) + O\left(\frac{1}{r_0^3}\right), \tag{C.15c}$$

$$\mathscr{D}(i\xi\omega) = \frac{i\xi}{Ur_0}L_{2,1}(p) + \frac{1}{r_0^2}\left(-MU^2\xi^2 + \frac{1}{U}(-L_{0,2}(p) + L_{1,1}(p))\right) + O\left(\frac{1}{r_0^3}\right). \tag{C.15d}$$

C.2.2 Existence of multiple solutions

We solve for the critical value of M for which $\sigma = 0$. In this limit, we note that $U \to 1$, $L_{0,3}, L_{1,2} \to 0$, $L_{0,2} \to -1$, $L_{1,1} \to 1$, and $L_{2,1} \to 2$. From (4.21),

$$\mathscr{G}_4 = \frac{1}{\xi}\left(\mathscr{A}_2\mathscr{D}_2 + \mathscr{A}_3\mathscr{D}_1 + \mathscr{B}_2\mathscr{C}_2 + \mathscr{B}_3\mathscr{C}_1\right), \tag{C.16}$$

and so we see that the stability condition takes the form

$$\mathscr{G}_4\big|_{\sigma=0} = -\frac{1}{2}(1+n)(1+2M)(1-4M) = 0, \tag{C.17}$$

i.e. $M = \frac{1}{4}$. As seen in figure 4.2, for sufficiently large n, this represents a unified cutoff above which the flat plateaus no longer appear.

To solve for the critical value of n, above which only one solution for σ exists for any value of M, we observe that the limiting case is when the two solutions for σ merge at $\sigma = 0$. Hence, we need to solve the equations

$$\left.\frac{\partial F_4}{\partial \sigma}\right|_{\sigma=0,M=\frac{1}{4}} = 0, \tag{C.18}$$

which, upon substitution into Mathematica, yields

$$\left.\frac{\partial F_4}{\partial \sigma}\right|_{\sigma=0,M=\frac{1}{4}} = -\frac{(1+n)(16-9n)}{8}. \tag{C.19}$$

We conclude that $n = -\frac{9}{16}$ and $M = \frac{1}{4}$. When evaluating $\frac{\partial F_4}{\partial \sigma}$, it must be emphasised that F_4 also depends on σ through U.

C.3 Large argument Bessel function asymptotics

C.3.1 Asymptotic formulation

For $|\nu| \gg |z|$, Heitman *et al.*[54] provides the asymptotic expansions for the Bessel function amplitude, M_ν, and phase, α_ν, which are related to the Bessel J and Y functions via

$$J_\nu(r_0) = M_\nu(r_0)\cos(\alpha_\nu(r_0)), \tag{C.20a}$$

$$Y_\nu(r_0) = M_\nu(z)\sin(\alpha_\nu(r_0)). \tag{C.20b}$$

The expansions for the amplitude M_ν and phase α_ν are given by

$$M_\nu(r_0)^2 \sim \frac{2}{\pi r_0}\left(1 + \sum_{n=1}^{\infty} \frac{t_n}{r_0^{2n}}\right), \tag{C.21a}$$

$$t_n = t_{n-1}\left(\frac{4\nu^2 - (2n-1)^2}{4}\right)\frac{2n-1}{2n}, \tag{C.21b}$$

$$\alpha_\nu'(r_0) = \frac{2}{\pi r_0 M_\nu^2(r_0)} \sim 1 + \sum_{n=1}^{\infty} \frac{s_n}{r_0^{2n}}, \tag{C.21c}$$

$$s_n = -\left(t_n + \sum_{j=1}^{n-1} t_j s_{n-j}\right), \tag{C.21d}$$

$$\alpha_\nu(r_0) = -\frac{\nu\pi}{2} - \frac{\pi}{4} + r_0 - \sum_{n=1}^{\infty} \frac{s_n}{(2n-1)r_0^{2n-1}}. \tag{C.21e}$$

Expressions for products of Bessel functions appearing the analytical evaluation of the stability integrals may thus be written as follows:

$$J_{-\nu}(r_0)J_\nu(r_0) = \frac{1}{2}M_\nu^2(r_0)\Big(\cos(\alpha_{-\nu}(r_0) + \alpha_\nu(r_0)) + \cos(\pi\nu)\Big), \tag{C.22a}$$

$$J_{-\nu}(r_0)J_\nu'(r_0) = \frac{1}{4}\frac{\mathrm{d}M_\nu^2(r_0)}{\mathrm{d}r_0}\Big(\cos(\alpha_{-\nu}(r_0) + \alpha_\nu(r_0)) + \cos(\pi\nu)\Big)$$
$$-\frac{1}{\pi r_0}\Big(\sin(\alpha_{-\nu}(r_0) + \alpha_\nu(r_0)) - \sin(\pi\nu)\Big), \tag{C.22b}$$

$$J_{-\nu}'(r_0)J_\nu'(r_0) = \frac{\pi r_0 \alpha_\nu'(r_0)}{16}\left(\frac{\mathrm{d}M_\nu^2(r_0)}{\mathrm{d}r_0}\right)^2\Big(\cos(\alpha_{-\nu}(r_0) + \alpha_\nu(r_0)) + \cos(\pi\nu)\Big)$$
$$-\frac{\alpha_\nu'(r_0)}{2}\frac{\mathrm{d}M_\nu^2(r_0)}{\mathrm{d}r_0}\sin(\alpha_{-\nu}(r_0) + \alpha_\nu(r_0)) + \frac{\alpha_\nu'(r_0)}{\pi r_0}\Big(\cos(\alpha_{-\nu}(r_0) + \alpha_\nu(r_0)) - \cos(\pi\nu)\Big). \tag{C.22c}$$

In the above equations, we have simplified using the relationships $M_\nu(r_0) = M_{-\nu}(r_0)$ and $\alpha_\nu(r_0) - \alpha_{-\nu}(r_0) = -\pi\nu$, product-to-sum formulas for products of sines and cosines, and equation (C.21c). Using the above expansions, the tangential force balance to eliminate the orbital speed $U = r_0\omega$, the asymptotic relationship $\mathrm{csch}(\pi\beta) = 2e^{-\pi\beta} + O(e^{-2\pi\beta})$ and expanding the arguments of the trigonometric functions in powers of $\frac{1}{r_0}$ about $2r_0 - \frac{\beta^2}{r_0}$ or $2r_0 - \frac{\eta^2}{r_0}$, gives rise to the stability function (4.27) in the main text.

C.3.2   Non-resonant stability problem

We begin by expanding

$$\xi = \xi_0 + \frac{\xi_1}{r_0} + o\left(\frac{1}{r_0}\right), \qquad \xi_0 = \sqrt{n+1}. \tag{C.23}$$

We note that the expansions are slightly simpler if $\frac{U^2\mathscr{F}}{i\xi^2}$ is expanded instead. After significant algebra, the real and imaginary parts of the stability condition are expanded as (4.32).

The equations $\mathrm{Im}\left[\frac{U^2 \mathscr{F}}{i\xi^2}\right] = 0$ and $\mathrm{Re}\left[\frac{U^2 \mathscr{F}}{i\xi^2}\right] = 0$ are very complicated to solve for β and ξ_1. We seek approximations to simplify the system of equations to solve.

The balance $F_{r,1} \sim -F_{r,4}$ prescribes, to leading order, the value of ξ_1. In contrast, the balance $F_{i,1} \sim -F_{i,4}$ prescribes, to leading order, the value of β. The solution process would be greatly simplified if we could ignore ξ_1 from the imaginary part of the stability condition. Note that balancing $F_{r,1} \sim -F_{r,4}$ leads to $\xi_1 = O(r_0^3 e^{-\pi\beta})$. Substituting into $F_{i,5}$ or $F_{i,6}$ leads to terms of order $O\left(\frac{e^{-\pi\beta}}{r_0^2}\right)$, which are the same size as the neglected $F_{i,2}$. Thus, as long as ξ_0 is non-integral, and that the dominant balance involves $F_{i,1}$, we can ignore ξ_1.

Appendix D

Chapter 5 appendices

D.1 Simplifying derivatives of radial force

In this section, we show that $-k+\int_0^\infty \frac{\partial w_r}{\partial x_1}(r_0, r_0, \omega t, t)\,\mathrm{d}t = -M\omega^2+\sigma+\int_0^\infty \mathrm{J}_2\left(2r_0 \sin\left(\frac{\omega t}{2}\right)\right)\cos(\omega t)\mathrm{e}^{-\sigma t}\,\mathrm{d}t$, and then proceed to expand the resulting integral to explain why circular orbits may destabilise at lower memory.

From the definition of w_r in §5.2.1, we see that

$$w_r(r(t), r(s), \theta(t) - \theta(s), t - s) = \frac{\mathrm{J}_1(\mathfrak{D}(t,s))}{\mathfrak{D}(t,s)}[r(t) - r(s)\cos(\theta(t) - \theta(s))]\mathrm{e}^{-\sigma(t-s)}. \quad \text{(D.1)}$$

Differentiating w_r with respect to $r(t)$ and then choosing $r(t) = r(s) = r_0$, we can thus conclude that

$$w_r(r_0, r_0, \omega t, t) = \mathrm{J}_1\left(2r_0 \sin\left(\frac{\omega t}{2}\right)\right)\sin\left(\frac{\omega t}{2}\right)\mathrm{e}^{-\sigma t}, \quad \text{(D.2)}$$

$$\frac{\partial w_r}{\partial x_1}(r_0, r_0, \omega t, t) = \left[\mathrm{J}_1'\left(2r_0 \sin\left(\frac{\omega t}{2}\right)\right)\sin^2\left(\frac{\omega t}{2}\right) + \frac{\mathrm{J}_1\left(2r_0 \sin\left(\frac{\omega t}{2}\right)\right)}{2r_0 \sin\left(\frac{\omega t}{2}\right)}\cos^2\left(\frac{\omega t}{2}\right)\right]\mathrm{e}^{-\sigma t}. \quad \text{(D.3)}$$

(4.4) can be recast in the form

$$-M\omega^2 = -k + \int_0^\infty \frac{w_r(r_0, r_0, \omega t, t)}{r_0}\,\mathrm{d}t. \quad \text{(D.4)}$$

We use the following Bessel function identities,

$$\frac{2\mathrm{J}_n(x)}{x} = \mathrm{J}_{n-1}(x) + \mathrm{J}_{n+1}(x), \quad \text{(D.5a)}$$

$$2\mathrm{J}_n'(x) = \mathrm{J}_{n-1}(x) - \mathrm{J}_{n+1}(x), \quad \text{(D.5b)}$$

to rewrite

$$\frac{\partial w_r}{\partial x_1}(r_0, r_0, \omega t, t) = \frac{1}{2}\left[\mathrm{J}_0\left(2r_0 \sin\left(\frac{\omega t}{2}\right)\right) + \mathrm{J}_2\left(2r_0 \sin\left(\frac{\omega t}{2}\right)\right)\cos\left(\omega t\right)\right]\mathrm{e}^{-\sigma t}. \quad \text{(D.6)}$$

To proceed, we now show how the integrals of the two terms are related.

In accordance with Durey's work on spin states[35], we define

$$C_n = \mathrm{i}^n \int_0^\infty \mathrm{J}_n\left(2r_0 \sin\left(\frac{\omega t}{2}\right)\right) \mathrm{e}^{\frac{\mathrm{i}n\omega t}{2} - \sigma t}\,\mathrm{d}t. \tag{D.7}$$

Using (D.5a),

$$C_n = \mathrm{i}^n \int_0^\infty r_0 \sin\left(\frac{\omega t}{2}\right)\left[\mathrm{J}_{n-1}\left(2r_0 \sin\left(\frac{\omega t}{2}\right)\right) + \mathrm{J}_{n+1}\left(2r_0 \sin\left(\frac{\omega t}{2}\right)\right)\right] \mathrm{e}^{\frac{\mathrm{i}n\omega t}{2} - \sigma t}\,\mathrm{d}t. \tag{D.8}$$

Using (D.5b) and integrating by parts,

$$C_n = \mathrm{i}^n \int_0^\infty \mathrm{J}_n\left(2r_0 \sin\left(\frac{\omega t}{2}\right)\right) \mathrm{e}^{\frac{\mathrm{i}n\omega t}{2}} \frac{\mathrm{d}}{\mathrm{d}t}\left(-\frac{1}{\sigma}\mathrm{e}^{-\sigma t}\right)\mathrm{d}t$$

$$= -\frac{\mathrm{i}^n}{\sigma}\left[\delta_{n0} - \int_0^\infty \left(r_0\omega \cos\left(\frac{\omega t}{2}\right)\mathrm{J}_n'\left(2r_0 \sin\left(\frac{\omega t}{2}\right)\right) + \frac{\mathrm{i}n\omega}{2}\mathrm{J}_n\left(2r_0 \sin\left(\frac{\omega t}{2}\right)\right)\right)\mathrm{e}^{\frac{\mathrm{i}n\omega t}{2}-\sigma t}\,\mathrm{d}t\right]$$

$$= -\frac{\mathrm{i}^n}{\sigma}\left[\delta_{n0} - \int_0^\infty \left(\frac{1}{2}r_0\omega \cos\left(\frac{\omega t}{2}\right)\left(\mathrm{J}_{n-1}\left(2r_0 \sin\left(\frac{\omega t}{2}\right)\right) - \mathrm{J}_{n+1}\left(2r_0 \sin\left(\frac{\omega t}{2}\right)\right)\right)\right.\right.$$

$$\left.\left. + \frac{\mathrm{i}n\omega}{2}\mathrm{J}_n\left(2r_0 \sin\left(\frac{\omega t}{2}\right)\right)\right)\mathrm{e}^{\frac{\mathrm{i}n\omega t}{2}-\sigma t}\,\mathrm{d}t\right], \tag{D.9}$$

where δ_{ij} is the Kronecker delta. For $n \neq 0$, we combine the two expressions for C_n to yield

$$(-\mathrm{i}n\omega + \sigma)C_n - \frac{\mathrm{i}r_0\omega}{2}(C_{n-1} + C_{n+1}) = 0, \tag{D.10}$$

from which we find

$$C_0 = \frac{2(-\mathrm{i}\omega + \sigma)}{\mathrm{i}r_0\omega}C_1 - C_2. \tag{D.11}$$

As C_0 is real, taking real parts of (D.11) and comparing to (4.3) yields

$$C_0 = -\frac{2}{r_0}\mathrm{Re}(C_1) + \frac{2\sigma}{r_0\omega}\mathrm{Im}(C_1) - \mathrm{Re}(C_2). \tag{D.12}$$

Thus, we see that

$$-k + \int_0^\infty \frac{\partial w_r}{\partial x_1}(r_0, r_0, \omega t, t)\,\mathrm{d}t = -M\omega^2 + \sigma + \int_0^\infty \mathrm{J}_2\left(2r_0 \sin\left(\frac{\omega t}{2}\right)\right)\cos(\omega t)\mathrm{e}^{-\sigma t}\,\mathrm{d}t. \tag{D.13}$$

We now proceed to asymptotically expand the integral in the limit of small σ.

D.1.1 Asymptotic expansion of integrals

Using that (D.13) involves a Laplace transform of a periodic function, we write[79]

$$\int_0^\infty J_2\left(2r_0\sin\left(\frac{\omega t}{2}\right)\right)\cos(\omega t)e^{-\sigma t}\,dt = \frac{1}{\omega\left(1-e^{-2\pi\beta}\right)}\int_0^{2\pi} J_2\left(2r_0\sin\left(\frac{t}{2}\right)\right)\cos(t)e^{-\beta t}\,dt$$

$$= \frac{1}{\sigma}\int_0^{2\pi}\left[\frac{1}{2\pi} + \left(\frac{1}{2}-\frac{t}{2\pi}\right)\beta + \left(\frac{\pi}{2}-\frac{t}{2}+\frac{t^2}{4\pi}\right)\beta^2\right]J_2\left(2r_0\sin\left(\frac{t}{2}\right)\right)\cos(t)\,dt + O(\sigma^2),$$

(D.14)

where $\beta = \frac{\sigma}{\omega}$. For any even function g with period T, we note that

$$\Upsilon = \int_0^T tg(t)\,dt = \int_0^T (T-t)g(T-t)\,dt$$

$$= \int_0^T (T-t)g(-t)\,dt = T\int_0^T g(t)\,dt - \Upsilon \tag{D.15}$$

$$\Upsilon = \frac{T}{2}\int_0^T f(t)\,dt \implies \int_0^T \left(\frac{1}{2}-t\right)g(t)\,dt = 0. \tag{D.16}$$

Thus, we see that

$$\int_0^\infty J_2\left(2r_0\sin\left(\frac{\omega t}{2}\right)\right)\cos(\omega t)e^{-\sigma t}\,dt = -\frac{J_0(r_0)J_2(r_0)}{\sigma}$$

$$+\frac{\beta^2}{\sigma}\left[\frac{2\pi^2}{3}J_0(r_0)J_2(r_0) + \frac{1}{4\pi}\int_0^{2\pi} t^2 J_2\left(2r_0\sin\left(\frac{t}{2}\right)\right)\cos(t)\,dt\right] + O\left(\frac{\beta^2}{\sigma}\right). \tag{D.17}$$

While we were unable to demonstrate that the resulting integral is positive for all r_0, we show, in figure D.1, that $\int_0^{2\pi} t^2 J_2\left(2r_0\sin\left(\frac{t}{2}\right)\right)\cos(t)\,dt > 0$ for all $r_0 > 3$. In particular, the integral is approximately bound by $\frac{18\pi}{r_0}$, for sufficiently large r_0. Given that the first quantised orbits occur around the first zero of J_2, which is approximately 5.14, the integral is always positive in the regime of interest. Writing now $\beta = \frac{\sigma}{\omega} = \frac{\sigma r_0}{U} \sim \sigma r_0$, from (5.18), we observe that $\frac{\beta^2}{\sigma} \sim r_0^2\sigma$, and thus

$$\int_0^\infty J_2\left(2r_0\sin\left(\frac{\omega t}{2}\right)\right)\cos(\omega t)e^{-\sigma t}\,dt + \sigma = -\frac{J_0(r_0)J_2(r_0)}{\sigma} + c_1 r_0\sigma + O(\sigma^2), c_1 > 0,$$

(D.18)

where c_1 oscillates with r_0, and satisfies $0 < c_1 < \frac{9}{2}$.
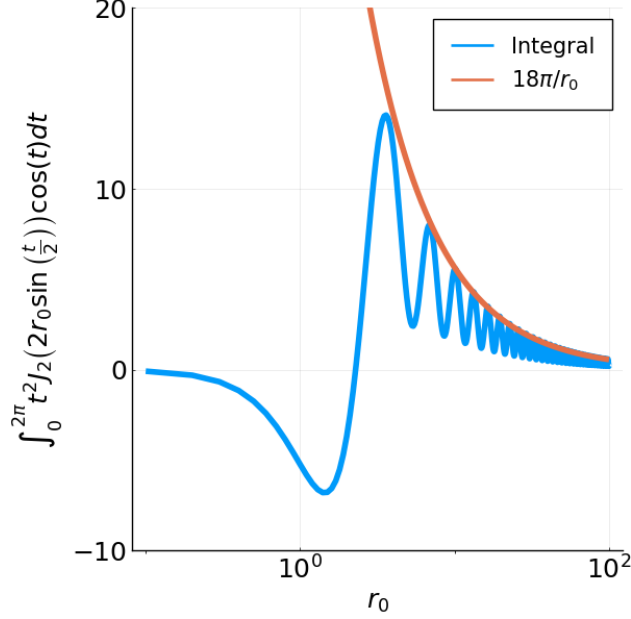
Figure D.1: A plot of $\int_0^{2\pi} t^2 J_2 \left(2r_0 \sin\left(\frac{t}{2}\right)\right) \cos(t) \, dt$ against r_0 to show that c_1 in (D.18) is indeed positive when $J_0(r_0)J_2(r_0)$ is small. This shows that for sufficiently large σ, $\frac{\Delta f_r}{\Delta R}$ in (5.11) is positive, and circular orbits are unstable. The orange line is an approximation for an upper bound of the integral, $18\pi/r_0$.

D.2 Simplification of the stability coefficients

We start from the stability coefficients

$$\mathscr{A} = \frac{2i}{r_0^2 \omega} - \frac{2}{r_0 \omega} f_{01}\left(\frac{\beta_1}{r_0}, r_0\right) - \frac{1}{\omega}\left[f_{00}\left(\frac{\beta_1}{r_0}, r_0\right) - f_{11}(\eta, r_0)\left(1 + \frac{\beta_1 \eta}{r_0^3}\right)\right], \quad \text{(D.19)}$$

$$\mathscr{B} = \frac{\xi\omega}{U^2} + \frac{-\beta_1 f_{01}\left(\frac{\beta_1}{r_0}, r_0\right) + \eta r_0 f_{01}(\eta, r_0)}{U r_0}, \quad \text{(D.20)}$$

$$\mathscr{C} = 2\omega + \frac{\xi\omega}{U^2} + \frac{\beta_1 f_{01}(\beta, r_0) + \eta r_0 f_{01}(\eta, r_0)}{U r_0} \quad \text{(D.21)}$$

$$\mathscr{D} = 2i\xi\omega + \frac{\eta(\beta_1 f_{00}(\beta, r_0) - \eta r_0 f_{00}(\eta, r_0)}{U r_0^2}, \quad \text{(D.22)}$$

and note that $J_0(r_0), J_2(r_0) = O\left(\frac{1}{r_0^{\frac{3}{2}}}\right)$. We aim to discard any terms that are $O\left(\frac{1}{r_0^2}\right)$.

We first now discuss how to expand $f_{01}\left(\frac{\beta_1}{r_0}, r_0\right)$ and $f_{00}\left(\frac{\beta_1}{r_0}, r_0\right)$. Using a quadratic

206

expansion of $J_{-\nu}(r_0)J_\nu(r_0)$ about $\nu = 0$

$$f_{00}\left(\frac{\beta_1}{r_0}, r_0\right) = \pi\,\mathrm{csch}\left(\frac{\pi\beta_1}{r_0}\right) J_{-\frac{i\beta_1}{r_0}}(r_0)J_{\frac{i\beta_1}{r_0}}(r_0)$$

$$= \left[\frac{r_0}{\beta_1} + O\left(\frac{1}{r_0}\right)\right]\left[J_0^2(r_0) - \frac{\beta_1^2}{2r_0^2}\left[-\pi J_0^2(r_0) - \frac{\pi^2}{2}Y_0^2(r_0)\right] + O\left(\frac{1}{r_0^4}\right)\right]$$

$$= \frac{r_0 J_0^2(r_0)}{\beta_1} + \frac{\beta_1\pi^2 Y_0^2(r_0)}{4r_0} + O\left(\frac{1}{r_0^3}\right) = O\left(\frac{1}{r_0^2}\right), \tag{D.23}$$

where $Y_\nu(r_0)$ is the Bessel function of the second kind of order ν and argument r_0, we remark that $\frac{\mathrm{d}}{\mathrm{d}\nu}(J_{-\nu}(r_0)J_\nu(r_0))$ vanishes at $\nu = 0$ as $J_{-\nu}(r_0)J_\nu(r_0)$ is an even function of ν, and that as $J_{-\nu}(r_0)J_\nu(r_0) = O\left(\frac{1}{r_0}\right)$ for fixed ν, we expect its derivatives with respect to ν to scale similarly. We also use the relationship $\frac{\partial}{\partial\nu}(J_\nu(x))|_{\nu=0} = \frac{\pi}{2}Y_0(x)$[1]. Similarly,

$$f_{01}\left(\frac{\beta_1}{r_0}, r_0\right) = \pi\,\mathrm{csch}\left(\frac{\pi\beta_1}{r_0}\right) J_{-\frac{i\beta_1}{r_0}}(r_0)J'_{\frac{i\beta_1}{r_0}}(r_0) = \left[\frac{r_0}{\beta_1} + O\left(\frac{1}{r_0}\right)\right][-J_0(r_0)J_1(r_0)$$

$$+ \frac{i\beta_1}{r_0}\frac{\mathrm{d}}{\mathrm{d}\nu}(J_{-\nu}(r_0)J'_\nu(r_0))|_{\nu=0} + O\left(\frac{1}{r_0^3}\right)]$$

$$= -\frac{r_0 J_0(r_0)J_1(r_0)}{\beta_1} + \frac{i}{r_0} + O\left(\frac{1}{r_0^2}\right) = O\left(\frac{1}{r_0}\right), \tag{D.24}$$

as $J_0(r_0)J_1(r_0) = O\left(\frac{1}{r_0^2}\right)$. We note that

$$\frac{\mathrm{d}}{\mathrm{d}\nu}(J_{-\nu}(r_0)J'_\nu(r_0))|_{\nu=0} = -H_0(r_0)J'_0(r_0) + J_0(r_0)H'_0(r_0)$$

$$= -\frac{\pi}{2}Y_0(r_0)J'_0(r_0) + \frac{\pi}{2}J_0(r_0)Y'_0(r_0) = \frac{1}{r_0}, \tag{D.25}$$

where $H_\nu(r_0) = \frac{\partial J_\nu(r_0)}{\partial\nu}$, and we used the Wronskian relationship between the Bessel functions of the first and second kinds[1].

Finally, we expand the tangential force balance as

$$1 - U^2 = \beta f_{00}(\beta, r_0) = O\left(\frac{1}{r_0^2}\right), \tag{D.26}$$

and thus $U = 1 + O\left(\frac{1}{r_0^2}\right)$. Using all of these expansions, we may now write

$$\mathscr{A} = \frac{r_0^2 J_0(r_0)J_2(r_0)}{\beta_1} - \frac{\pi^2\beta_1 Y_0^2(r_0)}{4} + r_0 f_{11}(\eta, r_0) + O\left(\frac{1}{r_0^2}\right), \tag{D.27a}$$

$$\mathscr{B} = \xi\omega + \eta f_{01}(\eta, r_0) + O\left(\frac{1}{r_0^2}\right), \tag{D.27b}$$

$$\mathscr{C} = 2\omega + \xi\omega + \eta f_{01}(\eta, r_0) + O\left(\frac{1}{r_0^2}\right) \tag{D.27c}$$

$$\mathscr{D} = 2i\xi\omega - \frac{\eta^2 f_{00}(\eta, r_0)}{r_0} + O\left(\frac{1}{r_0^2}\right), \tag{D.27d}$$

which forms the starting point of our asymptotic analysis in §5.3.4.

D.2.1

We show that if $J_0(r_0)J_2(r_0) < 0$, then there exists a large real eigenvalue. From (5.16), if $M = 0$, we see that

$$\mathscr{A}(s) = s + \sigma - \frac{2}{r_0}\frac{\partial \mathcal{I}_0(0)}{\partial r_0} - \mathcal{I}_0(0) + \mathcal{C}_0(s) + \mathcal{I}_1(s). \tag{D.28}$$

As $\mathscr{A}(s) = O\left(\frac{1}{\sigma}\right)$, yet $\mathscr{B}(s), \mathscr{C}(s)$ and $\mathscr{D}(s) = O(1)$ as $\sigma \to 0$, to leading order, the stability condition must satisfy $\mathscr{A}(s) = O(1)$.

For sufficiently small σ, we can approximate

$$\mathscr{A}(s) = s + \sigma + \frac{J_0(r_0)J_2(r_0)}{\sigma} + \mathcal{C}_0(s) + \mathcal{I}_1(s). \tag{D.29}$$

As the Bessel functions are bounded by 1 in magnitude, we can write

$$|\mathcal{C}_0(s)| \leq \frac{1}{2}\left|\int_0^\infty e^{-(\sigma+s)t}\,\mathrm{d}t\right| = \frac{1}{2|\sigma + s|}. \tag{D.30}$$

Thus, if we balance $s + \frac{J_0(r_0)J_2(r_0)}{\sigma} = O(1)$, the integral terms are small. This indicates that

$$s = -\frac{J_0(r_0)J_2(r_0)}{\sigma} + O(1), \tag{D.31}$$

which is real, positive and large if $J_0(r_0)J_2(r_0) < 0$, and so stability is only possible if $J_0(r_0)J_2(r_0) > 0$.

D.3 Derivation of the Bessel function minimisation condition

We seek to simplify the expression for q in (5.30), assuming $\xi \approx r_0$. The main difficulty in simplifying q comes from evaluating $\frac{\partial q_1}{\partial \xi}$, where $q_1 = f_{11}(\mathrm{i}\xi, r_0) + \frac{f_{01}(\mathrm{i}\xi, r_0)}{r_0}$. We note that (5.3.4) allows us to determine the value of q_1, so we aim to relate $\frac{\partial q_1}{\partial \xi}$ with q_1.

We seek a solution of the form $\xi \approx r_0$. The relevant asymptotic expansions for the Bessel functions $J_{\pm\xi}(r_0)$ in this parameter regime are the transition region expansions, which take the form

$$J_\xi\left(\xi + \tau\xi^{\frac{1}{3}}\right) = \left(\frac{2}{\xi}\right)^{\frac{1}{3}}\mathrm{Ai}\left(-2^{\frac{1}{3}}\tau\right) + O\left(\frac{1}{\xi}\right), \tag{D.32a}$$

$$Y_\xi\left(\xi + \tau\xi^{\frac{1}{3}}\right) = -\left(\frac{2}{\xi}\right)^{\frac{1}{3}}\mathrm{Bi}\left(-2^{\frac{1}{3}}\tau\right) + O\left(\frac{1}{\xi}\right), \tag{D.32b}$$

$$J'_\xi\left(\xi + \tau\xi^{\frac{1}{3}}\right) = -\left(\frac{2}{\xi}\right)^{\frac{2}{3}}\mathrm{Ai}'\left(-2^{\frac{1}{3}}\tau\right) + O\left(\frac{1}{\xi}\right), \tag{D.32c}$$

$$Y'_\xi\left(\xi + \tau\xi^{\frac{1}{3}}\right) = \left(\frac{2}{\xi}\right)^{\frac{2}{3}}\mathrm{Bi}'\left(-2^{\frac{1}{3}}\tau\right) + O\left(\frac{1}{\xi}\right), \tag{D.32d}$$

$$J_{-\nu}(x) = J_\nu(x)\cos(\pi\nu) - Y_\nu(x)\sin(\pi\nu), \tag{D.32e}$$

where Ai and Bi are the Airy A and B functions, $r_0 = \xi + \tau \xi^{\frac{1}{3}}, \tau = O(1)$. Using these expansions, we write

$$q_1 = -i\pi \csc(\pi\xi) J'_{-\xi}(r_0) \left[J'_\xi(r_0) + \frac{1}{r_0} J_\xi(r_0) \right]$$

$$= -i\pi \left(\frac{2}{\xi}\right)^{\frac{2}{3}} \left[\text{Ai}' \left(-2^{\frac{1}{3}}\tau\right) \cot(\pi\xi) + O(1) \right] \left[\left(\frac{2}{\xi}\right)^{\frac{2}{3}} \text{Ai}' \left(-2^{\frac{1}{3}}\tau\right) + O\left(\frac{1}{r_0}\right) \right]$$

$$= -i\pi \left(\frac{2}{\xi}\right)^{\frac{4}{3}} \text{Ai}'^2 \left(-2^{\frac{1}{3}}\right) \cot(\pi\xi) + O\left(\left(\frac{1}{r_0}\right)^{\frac{4}{3}}\right). \tag{D.33}$$

To evaluate $\frac{\partial q_1}{\partial \xi}$, we need $\frac{\partial \tau}{\partial \xi}$. As $\frac{\partial r_0}{\partial \xi} = 0$ and $r_0 = \xi + \tau \xi^{\frac{1}{3}}$,

$$\frac{\partial \tau}{\partial \xi} = -\xi^{-\frac{1}{3}} - \frac{1}{3} \xi^{-1} \tau = O\left(\left(\frac{1}{r_0}\right)^{\frac{1}{3}}\right). \tag{D.34}$$

Differentiating q_1 requires the use of the product rule on a product of three terms, two of which decrease when differentiated, and one of which increases when differentiated. It is clear that $\left(\frac{2}{\xi}\right)^{\frac{4}{3}}$ decreases by a factor of $\frac{1}{\xi} \approx \frac{1}{r_0}$ when differentiated. Similarly, $\text{Ai}' \left(-2^{\frac{1}{3}}\tau\right)$ decreases too when differentiated, as $\frac{\partial \tau}{\partial \xi} = O\left(\left(\frac{1}{r_0}\right)^{\frac{1}{3}}\right)$. The only term that does not decrease when differentiated is $\cot(\pi\xi)$; $\frac{\partial}{\partial \xi}(\cot(\pi\xi)) = -\pi \cot(\pi\xi) \csc(\pi\xi) \sec(\pi\xi)$, and $\csc(\pi\xi) = O(r_0^{\frac{1}{3}})$. After substituting in (5.3.4), we write

$$\frac{\partial q_1}{\partial \xi} = q_1 \left(-\pi \csc(\pi\xi) \sec(\pi\xi) + O\left(\left(\frac{1}{r_0}\right)^{\frac{1}{3}}\right) \right)$$

$$= \left(\frac{i\xi}{2r_0^2} + O\left(\frac{1}{r_0^2}\right)\right) \left(-\pi \csc(\pi\xi) \sec(\pi\xi) + O\left(\left(\frac{1}{r_0}\right)^{\frac{1}{3}}\right) \right) = -\frac{i\xi\pi \csc(\pi\xi) \sec(\pi\xi)}{2r_0^2} + O\left(\left(\frac{1}{r_0}\right)^{\frac{4}{3}}\right). \tag{D.35}$$

Thus, we simplify (5.30) for q as,

$$q = \frac{\pi^2 Y_0^2(r_0)}{4} + \frac{2}{2 - \xi\pi \csc(\pi\xi) J_{-\xi}(r_0) J_\xi(r_0)} \left[\frac{\xi\pi \csc(\pi\xi) \sec(\pi\xi)}{2r_0^2} + O\left(\left(\frac{1}{r_0}\right)^{\frac{4}{3}}\right) \right]$$

$$= \frac{\pi^2 Y_0^2(r_0)}{4} + \frac{\xi\pi \sec(\pi\xi)}{r_0^2(2\sin(\pi\xi) - \xi\pi J_{-\xi}(r_0) J_\xi(r_0))} \left[1 + O\left(\left(\frac{1}{r_0}\right)^{\frac{2}{3}}\right) \right]$$

$$= \frac{\pi^2 Y_0^2(r_0)}{4} - \frac{\sec(\pi\xi)}{r_0^2(J_\xi(r_0) \cos(\pi\xi) - Y_\xi(r_0) \sin(\pi\xi)) J_\xi(r_0)} \left[1 + O\left(\left(\frac{1}{r_0}\right)^{\frac{2}{3}}\right) \right]$$

$$= \frac{\pi^2 Y_0^2(r_0)}{4} - \frac{\sec^2(\pi\xi)}{r_0^2 J_\xi^2(r_0)} \left[1 + O\left(\frac{1}{r_0^{\frac{1}{3}}}\right) \right] = \frac{\pi^2 Y_0^2(r_0)}{4} - \frac{1}{r_0^2 J_\xi^2(r_0)} + O\left(\frac{1}{r_0^{\frac{5}{3}}}\right). \tag{D.36}$$

D.4 Memory of instability manipulation

From (5.30), we can write the memory of instability as

$$\beta = \frac{\beta_1}{r_0} + O\left(\frac{1}{r_0^2}\right) = \sqrt{\frac{J_0(r_0)J_2(r_0)}{q}} + O\left(\frac{1}{r_0^2}\right). \tag{D.37}$$

Using Hankel expansions for the Bessel functions[1], $\frac{\pi^2}{4}Y_0^2(r_0) = \frac{\pi}{4r_0}\left(1 - \sin(2r_0)\right) + O\left(\frac{1}{r_0^2}\right)$, and noting that $r_0 \in [j_{2,n}, j_{0,n+1}]$, we can use (5.31) to simplify the expression for q as

$$q = \frac{\pi}{2r_0} - \frac{1}{r_0^2 J_\xi^2(r_0)} + O\left(\frac{1}{r_0^{\frac{5}{3}}}\right) \tag{D.38}$$

Noting that $\xi \approx r_0$, we write []

$$J_\xi(r_0) = \left(\frac{2}{\xi}\right)^{\frac{1}{3}} \mathrm{Ai}\left(-2^{\frac{1}{3}}\tau\right)\left(1 + O\left(\frac{1}{r_0^{\frac{2}{3}}}\right)\right) + \frac{2^{\frac{2}{3}}}{\xi}\mathrm{Ai}'\left(-2^{\frac{1}{3}}\tau\right)\frac{3\tau^2}{10}\left(1 + O\left(\frac{1}{r_0^{\frac{2}{3}}}\right)\right), \tau = \frac{r_0 - \xi}{\xi^{\frac{1}{3}}}. \tag{D.39}$$

As ξ maximises J_ξ, we expect $-2^{\frac{1}{3}}\tau$ to maximise the Airy function, which, for negative argument, takes on a value $A_{\max} \approx 0.53567$. In addition, if $-2^{\frac{1}{3}}\tau$ maximises the Airy function, then $\mathrm{Ai}'\left(-2^{\frac{1}{3}}\tau\right) = 0$. Then, approximating $\frac{2}{\xi} = \frac{2}{r_0} + O\left(\frac{1}{r_0^{\frac{1}{3}}}\right)$, we can write

$$q = \frac{\pi}{2r_0}\left(1 - \frac{2^{\frac{1}{3}}}{\pi A_{\max}^2 r_0^{\frac{1}{3}}}\left[1 + O\left(\frac{1}{r_0^{\frac{1}{3}}}\right)\right]\right) = \frac{\pi}{2r_0}\left(1 - \frac{2^{\frac{1}{3}}}{\pi A_{\max}^2 r_0^{\frac{1}{3}}}\right)\left[1 + O\left(\frac{1}{r_0^{\frac{2}{3}}}\right)\right]. \tag{D.40}$$

Appendix E

Chapter 6 appendices

E.1 Expanding Laplace-type integrals of periodic functions for large memory

E.1.1 Asymptotic expansions

We simplify the form of the Laplace transform for a periodic function f with period T when the decay rate, $\sigma > 0$, approaches zero.[79] For the integral

$$I(\sigma) = \int_0^\infty f(t) e^{-\sigma t}\, dt,$$

we exploit the periodicity of $f(t)$ to write

$$I(\sigma) = \frac{1}{1 - e^{-\sigma T}} \int_0^T f(t) e^{-\sigma t}\, dt.$$

We proceed now to expand $I(\sigma)$ in powers of σ, giving

$$I(\sigma) = \frac{1}{\sigma T} \int_0^T f(t)\, dt + \int_0^T \left[\frac{1}{2} - \frac{t}{T} \right] f(t)\, dt + \sigma \int_0^T \frac{T^2 - 6tT + 6t^2}{12T} f(t)\, dt + O(\sigma^2).$$

$$(E.1)$$

We proceed now to simplify (E.1) in the special case of $f(t)$ being an even function. To achieve these simplifications, we first consider the integral

$$\Upsilon = \int_0^T t f(t)\, dt.$$

By performing the change of variables $t \mapsto T - t$ and exploiting the periodicity and evenness of $f(t)$, we find that

$$\Upsilon = \int_0^T (T - t) f(T - t)\, dt = \int_0^T (T - t) f(-t)\, dt = T \int_0^T f(t)\, dt - \Upsilon. \qquad (E.2)$$

Upon rearranging, we conclude that

$$\int_0^T t f(t)\, \mathrm{d}t = \frac{T}{2}\int_0^T f(t)\, \mathrm{d}t,$$

which we proceed to utilise in equation (E.1) when f is an even function. Notably, the $O(1)$ term in (E.1) vanishes, and the $O(\sigma)$ term can be simplified as

$$\int_0^T \frac{T^2 - 6tT + 6t^2}{12T} f(t)\, \mathrm{d}t = \int_0^T \frac{-T^2 + 3t^2}{6T} f(t)\, \mathrm{d}t. \tag{E.3}$$

In summary, we deduce that for an even periodic function, $f(t)$, with period T, its Laplace tranform may be expanded as

$$\int_0^\infty f(t)\mathrm{e}^{-\sigma t}\, \mathrm{d}t = \frac{1}{\sigma T}\int_0^T f(t)\, \mathrm{d}t + \sigma \int_0^T \frac{-T^2 + 3t^2}{6T} f(t)\, \mathrm{d}t + O(\sigma^2) \tag{E.4}$$

for $0 < \sigma \ll 1$. Equation (E.4) is the higher-order correction to a similar result derived by Oza *et al.*[79].

E.1.2 Proving that the stability integrals are either real or imaginary

We proceed to use symmetry arguments to prove that $\mathcal{I}_{m,1}(\mathrm{i}S)$ and $\mathcal{C}_{m,1}(\mathrm{i}S)$ are both imaginary, whereas $\mathcal{S}_{m,1}(\mathrm{i}S)$ is real. We start from the analytical continuation of these integrals given by equation (6.12), which, for $s = \mathrm{i}S$ with S real, may be expressed

$$\mathcal{I}_{m,1}(\mathrm{i}S) = \frac{1}{2|\omega|\left(1 - \mathrm{e}^{-\frac{2\pi \mathrm{i}S}{|\omega|}}\right)} \int_0^{2\pi} \mathrm{J}_{2m}\left(2r_0 \sin\left(\frac{t}{2}\right)\right) \mathrm{e}^{-\frac{\mathrm{i}St}{|\omega|}}\, \mathrm{d}t, \tag{E.5a}$$

$$\mathcal{C}_{m,1}(\mathrm{i}S) = \frac{1}{2|\omega|\left(1 - \mathrm{e}^{-\frac{2\pi \mathrm{i}S}{|\omega|}}\right)} \int_0^{2\pi} \mathrm{J}_{2m}\left(2r_0 \sin\left(\frac{t}{2}\right)\right) \cos(t)\mathrm{e}^{-\frac{\mathrm{i}St}{|\omega|}}\, \mathrm{d}t, \tag{E.5b}$$

$$\mathcal{S}_{m,1}(\mathrm{i}S) = \frac{1}{2\omega\left(1 - \mathrm{e}^{-\frac{2\pi \mathrm{i}S}{|\omega|}}\right)} \int_0^{2\pi} \mathrm{J}_{2m}\left(2r_0 \sin\left(\frac{t}{2}\right)\right) \sin(t)\mathrm{e}^{-\frac{\mathrm{i}St}{|\omega|}}\, \mathrm{d}t. \tag{E.5c}$$

By making the substitution $t \mapsto 2\pi - t$ for the integral $\mathcal{I}_{m,1}(\mathrm{i}S)$, we obtain

$$\mathcal{I}_{m,1}(\mathrm{i}S) = \frac{1}{2|\omega|\left(1 - \mathrm{e}^{-\frac{2\pi \mathrm{i}S}{|\omega|}}\right)} \int_0^{2\pi} \mathrm{J}_{2m}\left(2r_0 \sin\left(\frac{t}{2}\right)\right) \mathrm{e}^{-\frac{\mathrm{i}S(2\pi - t)}{|\omega|}}\, \mathrm{d}t$$

$$= \frac{\mathrm{e}^{-\frac{2\pi \mathrm{i}S}{|\omega|}}}{2|\omega|\left(1 - \mathrm{e}^{-\frac{2\pi \mathrm{i}S}{|\omega|}}\right)} \int_0^{2\pi} \mathrm{J}_{2m}\left(2r_0 \sin\left(\frac{t}{2}\right)\right) \mathrm{e}^{\frac{\mathrm{i}St}{|\omega|}}\, \mathrm{d}t. \tag{E.6}$$

By comparing this expression with the integral definition in (E.5), we find that

$$\mathcal{I}_{m,1}(\mathrm{i}S) = \frac{1}{2|\omega|\left(1 - \mathrm{e}^{-\frac{2\pi\mathrm{i}S}{|\omega|}}\right)} \int_0^{2\pi} \mathrm{J}_{2m}\left(2r_0\sin\left(\frac{t}{2}\right)\right) \mathrm{e}^{-\frac{\mathrm{i}St}{|\omega|}}\,\mathrm{d}t$$

$$= \frac{\mathrm{e}^{-\frac{2\pi\mathrm{i}S}{|\omega|}}}{2|\omega|\left(1 - \mathrm{e}^{-\frac{2\pi\mathrm{i}S}{|\omega|}}\right)} \int_0^{2\pi} \mathrm{J}_{2m}\left(2r_0\sin\left(\frac{t}{2}\right)\right) \mathrm{e}^{\frac{\mathrm{i}St}{|\omega|}}\,\mathrm{d}t$$

$$= \frac{1}{2|\omega|\left(\mathrm{e}^{\frac{2\pi\mathrm{i}S}{|\omega|}} - 1\right)} \int_0^{2\pi} \mathrm{J}_{2m}\left(2r_0\sin\left(\frac{t}{2}\right)\right) \mathrm{e}^{\frac{\mathrm{i}St}{|\omega|}}\,\mathrm{d}t = -\overline{\mathcal{I}_{m,1}}(\mathrm{i}S), \qquad (\text{E.7})$$

where the over bar denotes the complex conjugate. We thus conclude that $\mathcal{I}_{m,1}(\mathrm{i}S)$ is purely imaginary. We can perform the same calculation to show that $\mathcal{C}_{m,1}(\mathrm{i}S)$ is also imaginary, which follows from the property $\cos(2\pi - t) = \cos(t)$.

To prove that $\mathcal{S}_{m,1}(\mathrm{i}S)$ is real, we likewise employ the substitution $t \mapsto 2\pi - t$. In this calculation, we leverage the relationship $\sin(2\pi - t) = -\sin(t)$, where the additional minus sign contrasts to the corresponding calculations for $\mathcal{I}_{m,1}(\mathrm{i}S)$ and $\mathcal{C}_{m,1}(\mathrm{i}S)$. Specifically, we compute

$$\mathcal{S}_{m,1}(\mathrm{i}S) = \frac{1}{2|\omega|\left(1 - \mathrm{e}^{-\frac{2\pi\mathrm{i}S}{|\omega|}}\right)} \int_0^{2\pi} \mathrm{J}_{2m}\left(2r_0\sin\left(\frac{t}{2}\right)\right) \sin(t)\mathrm{e}^{-\frac{\mathrm{i}St}{|\omega|}}\,\mathrm{d}t$$

$$= -\frac{\mathrm{e}^{-\frac{2\pi\mathrm{i}S}{|\omega|}}}{2|\omega|\left(1 - \mathrm{e}^{-\frac{2\pi\mathrm{i}S}{|\omega|}}\right)} \int_0^{2\pi} \mathrm{J}_{2m}\left(2r_0\sin\left(\frac{t}{2}\right)\right) \sin(t)\mathrm{e}^{\frac{\mathrm{i}St}{|\omega|}}\,\mathrm{d}t$$

$$= -\frac{1}{2|\omega|\left(\mathrm{e}^{\frac{2\pi\mathrm{i}S}{|\omega|}} - 1\right)} \int_0^{2\pi} \mathrm{J}_{2m}\left(2r_0\sin\left(\frac{t}{2}\right)\right) \sin(t)\mathrm{e}^{\frac{\mathrm{i}St}{|\omega|}}\,\mathrm{d}t \qquad (\text{E.8})$$

$$= \overline{\mathcal{S}_{m,1}}(\mathrm{i}S). \qquad (\text{E.9})$$

As $\mathcal{S}_{m,1}(\mathrm{i}S)$ is equal to its complex conjugate, we conclude that it is real.

E.2 Critical rotation for no cyclonic states

The two force balance equations and the complex stability condition total four real equations, which implicitly define M as a function of σ, as plotted in figure 6.4. If we recast the radial and tangential force balance equations in (6.2), and stability conditions $\mathscr{G}(s) = 0$ in (6.6), in the form

$$\mathcal{F}_R(r_0, \omega_0, \sigma, \Omega, M) = 0, \qquad (\text{E.10a})$$

$$\mathcal{F}_T(r_0, \omega_0, \sigma, \Omega, M) = 0, \qquad (\text{E.10b})$$

$$\mathrm{Re}(\mathscr{G}(r_0, \omega_0, \sigma, \Omega, M, \mathrm{i}S_0)) = 0, \qquad (\text{E.10c})$$

$$\mathrm{Im}(\mathscr{G}(r_0, \omega_0, \sigma, \Omega, M, \mathrm{i}S_0)) = 0, \qquad (\text{E.10d})$$

one can differentiate both sides of each equation in (E.10) with respect to σ, as the equations are satisfied for all permissible parameter combinations. For instance,

$$\frac{\mathrm{d}\mathcal{F}_R}{\mathrm{d}\sigma} = \frac{\partial F_{\mathcal{R}}}{\partial \sigma} + \frac{\partial F_{\mathcal{R}}}{\partial r_0}\frac{\mathrm{d}r_0}{\mathrm{d}\sigma} + \frac{\partial F_{\mathcal{R}}}{\partial \omega}\frac{\mathrm{d}\omega}{\mathrm{d}\sigma} + \frac{\partial F_{\mathcal{R}}}{\partial \Omega}\frac{\mathrm{d}\Omega}{\mathrm{d}\sigma} + \frac{\partial F_{\mathcal{R}}}{\partial M}\frac{\mathrm{d}M}{\mathrm{d}\sigma} = 0 \qquad (\text{E.11})$$

Setting $\frac{\mathrm{d}M}{\mathrm{d}\sigma} = 0$ will allow one to solve for the critical value of Ω at which the stability region of the cyclonic state vanishes; the other derivatives, such as $\frac{\mathrm{d}r_0}{\mathrm{d}\sigma}$, also need to be solved numerically. Solving this system of eight real equations yields $\Omega_c = 0.0732$, to four decimal places.

Appendix F

Chapter 7 appendices

A Stationary phase point contributions to stability integrals

We seek the contributions at each critical point for the integral $L_m(\xi)$, defined in equation (7.7). We first consider the contribution to $L_m(\xi)$ near the edges of the integration region, namely $\theta = 0$ and $\theta = 2\pi$, which we denote by $L_{m,0}(\xi)$ and $L_{m,2\pi}(\xi)$, respectively. To determine $L_{m,0}(\xi)$, we approximate $\sin\left(\frac{\theta}{2}\right) \approx \frac{\theta}{2}$ in the argument of the Bessel function, recast the integral as $\int_0^{2\pi} = \int_0^\infty - \int_{2\pi}^\infty$ and evaluate the first integral analytically [1]

$$L_{m,0}(\xi) = \frac{1}{r_0}\left(\frac{\beta + \mathrm{i}\xi}{r_0} + \sqrt{1 + \left(\frac{\beta + \mathrm{i}\xi}{r_0}\right)^2}\right)^{-2m}\left(1 + \left(\frac{\beta + \mathrm{i}\xi}{r_0}\right)^2\right)^{-1/2} - \int_{2\pi}^\infty \mathrm{J}_{2m}(r_0\theta)\mathrm{e}^{-(\beta+\mathrm{i}\xi)\theta}\,\mathrm{d}\theta.$$

It remains now to estimate the size of the remaining integral, $\int_{2\pi}^\infty$. We approximate the integrand by utilising the large-argument Bessel function expansion [1] and noting that $\theta \geq 2\pi$ across the integration domain; then, by evaluating the resultant integral analytically, we obtain the approximate bound

$$\int_{2\pi}^\infty \mathrm{J}_{2m}(r_0\theta)\mathrm{e}^{-(\beta+\mathrm{i}\xi)\theta}\,\mathrm{d}\theta \sim \sqrt{\frac{1}{\pi^2 r_0}} \int_{2\pi}^\infty \cos\left(r_0\theta - \varphi_m\right)\mathrm{e}^{-(\beta+\mathrm{i}\xi)\theta}\,\mathrm{d}\theta = O\left(\frac{\mathrm{e}^{-2\pi\beta}}{r_0\sqrt{r_0}}\right),$$

where $\varphi_m = \frac{1}{4}\pi(1 + 4m)$ is a constant phase shift. Provided that ξ and β are of size at most $O(r_0)$, we see that the contribution to $L_{m,0}$ is dominated by the contribution from the integral $\int_0^\infty$; by neglecting the contribution from the integral $\int_{2\pi}^\infty$, we deduce that $L_{m,0} = O(r_0^{-1})$. By periodicity of the non-exponential portion of the integrand, the contribution near $\theta = 2\pi$ satisfies $L_{m,2\pi}(\xi) = L_{m,0}(\xi)\mathrm{e}^{-2\pi(\beta+\mathrm{i}\xi)}$; the factor $\mathrm{e}^{-2\pi\beta}$ ensures that the contribution $L_{m,2\pi}(\xi)$ is negligible relative to $L_{m,0}(\xi)$ and may henceforth be neglected.

We now determine the contributions arising near points of stationary phase, considering the cases (i) $\xi = O(1)$ as $r_0 \to \infty$ and (ii) $\sigma = \xi/r_0 = O(1)$ as $r_0 \to \infty$ with $0 < \sigma < 1$.

(i) The internal contribution is localised about $\theta = \pi$, where we denote this contribution $L_{m,\pi}(\xi)$. To proceed, we deform the integration region to a small region about $\theta = \pi$,

namely $\pi - \delta < \pi < \theta + \delta$ with $0 < \delta \ll 1$. By applying the large-argument expansion for the Bessel function [1] and utilising the Taylor expansion $\sin\left(\frac{\theta}{2}\right) \approx 1 - \frac{1}{8}(\theta - \pi)^2$, we determine the approximation

$$L_{m,\pi}(S) = \int_{\pi-\delta}^{\pi+\delta} J_{2m}\left(2r_0 \sin\left(\frac{\theta}{2}\right)\right) e^{-(\beta+i\xi)\theta}\, d\theta \sim \frac{e^{-(\beta+i\xi)\pi}}{2\sqrt{\pi r_0}} \sum_{\pm} e^{\pm i\varphi_m} \int_{\pi-\delta}^{\pi+\delta} e^{\mp i2r_0\left(1-\frac{1}{8}(\theta-\pi)^2\right)}\, d\theta.$$

The leading-order form of the resultant integral may be determined using method of stationary phase as $r_0 \to \infty$, giving rise to the contribution

$$L_{m,\pi}(\xi) \sim -\frac{2e^{-\pi(\beta+i\xi)}}{r_0} \cos\left(\varphi_m + 2r_0\right).$$

(ii) We consider the contributions near the stationary points $\theta_\pm = \pi \pm 2\arcsin(\sigma)$, where $\xi = \sigma r_0$ and we assume that $\sigma = O(1)$ with $0 < \sigma < 1$. We proceed similarly by deforming the integration region to two small regions about $\theta = \theta_\pm$, and use the large-argument expansion of the Bessel function [1] to simplify. Specifically, we obtain

$$L_{m,\theta_\pm}(\xi) = \int_{\theta_-\delta}^{\theta_+\delta} J_{2m}\left(2r_0 \sin\left(\frac{\theta}{2}\right)\right) e^{-(\beta+i\xi)\theta}\, d\theta \sim \frac{1}{2\sqrt{\pi r_0}} \sum_{\pm} e^{\pm i\varphi_m} \int_{\theta_\pm-\delta}^{\theta_\pm+\delta} \frac{e^{-ir_0\phi_\pm(\theta)}e^{-\beta\theta}}{\sqrt{\sin\left(\frac{\theta}{2}\right)}}\, d\theta,$$

where $\phi_\pm(\theta) = \sigma\theta \pm 2\sin\frac{\theta}{2}$ is the phase, with $\phi_\pm'(\theta_\pm) = 0$. We proceed to approximate non-highly-oscillatory terms in the integrand by their values at $\theta_\pm$ (corresponding to their leading-order Taylor expansion), and approximate the phase by its quadratic Taylor expansion $\phi_\pm(\theta) \sim \phi_\pm(\theta_\pm) + \frac{1}{2}\phi_\pm''(\theta_\pm)(\theta - \theta_\pm)^2$. By noting that $\phi_\pm''(\theta) = \mp\frac{1}{2}\sin\frac{\theta}{2}$ and $\sin\frac{1}{2}\theta_\pm = \sqrt{1-\sigma^2}$, we obtain

$$L_{m,\theta_\pm}(\xi) \sim \frac{1}{2\sqrt{\pi r_0}\sqrt{1-\sigma^2}} \sum_{\pm} e^{\pm i\varphi_m}e^{-\beta\theta_\pm}e^{-ir_0\phi_\pm(\theta_\pm)} \int_{\theta_\pm-\delta}^{\theta_\pm+\delta} e^{\pm\frac{ir_0}{4}\sqrt{1-\sigma^2}(\theta-\theta_\pm)^2}\, d\theta.$$

By applying the method of stationary phase as $r_0 \to \infty$ and simplifying leads to

$$L_{m,\theta_\pm}(\xi) \sim \frac{2e^{-\pi(\beta+i\xi)}}{r_0} \cos\left(\varphi_m + 2i\beta\arcsin(\sigma) - 2r_0\sqrt{1-\sigma^2} - 2r_0\sigma\arcsin(\sigma)\right).$$

We observe that as $\sigma \to 1$, and for any real a,

$$e^{-\pi\beta}\cos(a + 2i\beta\arcsin(\sigma)) = O\left(e^{-\pi\beta}e^{2\beta\arcsin(\sigma)}\right) = O(1), \qquad (A.0.1)$$

which shows that $L_{m,\theta_\pm} = O\left(r_0^{-1}\right)$. As $L_{m,\theta_\pm}$ and $L_{m,0}$ would be comparable in this case, we cannot neglect the contribution from the interior stationary point. However, as $\sigma \to 1$, we also cannot assume that $2r_0\sin\left(\frac{\theta}{2}\right) \gg 1$, which indicates that we must proceed differently to expand the integrals in this limit.

B Rectilinear expansion: asymptotic formulation

B.1 Integral expansions

We seek an $O\left(r_0^{-4}\right)$ approximation for the following class of integrals I defined in equation (7.8), where we consider the limit as $r_0 \to \infty$, $\omega = O\left(r_0^{-1}\right)$, $U = r_0\omega = O(1)$ and $s = O(1)$, with f and P assumed to be smooth and boundeded. This method is an extension of the method developed by Oza [77], and a variation of the method developed by Liu (flat plateau problem).

The main idea of our method is to approximate the integrand $f\left(2r_0 \sin\left(s/2r_0\right)\right) P\left(s/r_0\right)$ through a series expansion about $r_0 = \infty$. It is possible to let $q = r_0^{-1}$ and differentiate repeatedly with respect to q to derive the series expansion. We present an alternative method, whereby we approximate the argument of f by the first two terms of its series expansion, from which we recognise that

$$f\left(2r_0 \sin\left(\frac{s}{2r_0}\right)\right) \approx f\left(s - \frac{s^3}{24r_0^2}\right) \approx f(s) - \frac{s^3}{24r_0^2}f'(s).$$

We proceed to formalise the above, and show that the product of the individual series expansions for f and for P leads to a satisfactory approximation for $f\left(2r_0 \sin\left(s/2r_0\right)\right) P\left(s/r_0\right)$.

We start by using the generalised mean value theorem to bound the difference between $2r_0 \sin\left(s/2r_0\right)$ and its series expansion to cubic order, giving

$$\left|2r_0 \sin\left(\frac{s}{2r_0}\right) - s + \frac{s^3}{24r_0^2}\right| \leq \frac{s^5}{120r_0^4}\left\|\frac{\mathrm{d}^5}{\mathrm{d}t^5}\left(2\sin\left(\frac{t}{2}\right)\right)\right\|_\infty = \frac{s^5}{1920r_0^4}. \qquad \text{(B.1.2)}$$

By a further application of the mean value theorem, this bound implies that

$$\left|f\left(2r_0 \sin\left(\frac{s}{2r_0}\right)\right) - f\left(s - \frac{s^3}{24r_0^2}\right)\right| \leq \|f'\|_\infty\left|2r_0 \sin\left(\frac{s}{2r_0}\right) - s + \frac{s^3}{24r_0^2}\right| \leq \|f'\|_\infty\frac{s^5}{1920r_0^4}. \tag{B.1.3}$$

Moreover, two additional applications of the mean value theorem give rise to the bounds

$$\left|f\left(s - \frac{s^3}{24r_0^2}\right) - f(s) + \frac{s^3}{24r_0^2}f'(s)\right| \leq \frac{s^6}{1152r_0^4}\|f''\|_\infty \tag{B.1.4}$$

$$\text{and} \quad \left|f\left(2r_0 \sin\left(\frac{s}{2r_0}\right)\right) - f(s) + \frac{s^3}{24r_0^2}f'(s)\right| \leq \frac{s^6}{1152r_0^4}\|f''\|_\infty + \frac{s^5}{1920r_0^4}\|f'\|_\infty. \tag{B.1.5}$$

which leads us to an approximation for $f\left(2r_0 \sin\left(s/2r_0\right)\right)$. We can write Taylor series expansions for $P\left(s/r_0\right)$; it only remains to be seen if we can naively multiply the two approximations to approximate $f\left(2r_0 \sin\left(s/2r_0\right)\right) P\left(s/r_0\right)$.

Suppose we have two approximations, denoted f_0 and P_0, for the functions f and P, respectively, of the form

$$f = f_0 + \epsilon_f \quad \text{and} \quad P = P_0 + \epsilon_P,$$

where ϵ_f and ϵ_P are the errors in the approximations. We can write

$$fP - f_0 P_0 = f_0 \epsilon_P + P_0 \epsilon_f + \epsilon_f \epsilon_P \tag{B.1.6}$$

and so the error incurred by multiplying the product of the two series expansions is $O(\max(f_0 \epsilon_f, P_0 \epsilon_P))$.

We first consider the case where P is even, and may be approximated using a Taylor series:

$$P\left(\frac{s}{r_0}\right) = P(0) + \frac{s^2}{2r_0^2}P''(0) + \epsilon_P, \quad \text{where} \quad |\epsilon_P| \leq \frac{s^4}{24r_0^4}\|P^{(4)}\|_\infty. \tag{B.1.7}$$

We have that $\epsilon_f = O\left(r_0^{-4}\right) = O(\epsilon_P)$, and so after expanding the product of the approximations for f and P and retaining terms to $O\left(r_0^{-2}\right)$, we see that

$$I_{\text{even}}(r_0) = \frac{1}{U}\int_0^\infty \left(P(0)f(s) + \frac{s^2}{2r_0^2}P''(0)f(s) - \frac{s^3 P(0)}{24r_0^2}f'(s)\right)e^{-\nu s/U}\,\mathrm{d}s + O\left(\frac{1}{r_0^4}\right). \tag{B.1.8}$$

Similarly, for the case where P is odd, we now consider the series expansion

$$P\left(\frac{s}{r_0}\right) = \frac{s}{r_0}P'(0) + \frac{s^3}{6r_0^3}P'''(0) + \epsilon_P, \quad \text{where} \quad |\epsilon_P| \leq \frac{s^5}{120r_0^5}\|P^{(5)}\|_\infty. \tag{B.1.9}$$

In a manner similar to the case where P is even, we deduce that

$$I_{\text{odd}}(r_0) = \frac{1}{U}\int_0^\infty \left(\frac{s}{r_0}P'(0)f(s) + \frac{s^3}{6r_0^3}P^{(3)}(0)f(s) - \frac{s^4}{24r_0^3}P'(0)f'(s)\right)e^{-\nu s/U}\,\mathrm{d}s + O\left(\frac{1}{r_0^5}\right). \tag{B.1.10}$$

The fact that successive integral approximation errors decrease by a factor of $O\left(r_0^{-2}\right)$ motivates an expansion in powers of r_0^{-2}.

B.2 Asymptotic equations

Using the expansions in equations (B.1.8) and (B.1.10), we can expand the force balance equations and the stability coefficients.

Force balance equations

We use the notation

$$L_{n,m}(p) = \frac{1}{2}\int_0^\infty t^m \mathrm{J}_n(t)e^{-\mathrm{i}pt}\,\mathrm{d}t \quad \text{and} \quad M_{n,m}(p) = \frac{1}{2}\int_0^\infty t^m \mathrm{J}_n'(t)e^{-\mathrm{i}pt}\,\mathrm{d}t, \tag{B.2.11}$$

where the integrals may be evaluated exactly, but are written in this form for simplicity. The leading order tangential force balance equation take the form

$$U_0^2 = 2L_{1,0}\left(\frac{\sigma_0}{U_0}\right), \tag{B.2.12a}$$

and the first order equation

$$2U_0 U_2 = -2L_{1,1}\left(\frac{\sigma_0}{U_0}\right)\frac{\sigma_2 U_0 - \sigma_0 U_2}{U_0^2} - \frac{1}{4}L_{1,2}\left(\frac{\sigma_0}{U_0}\right) - \frac{1}{12}M_{1,3}\left(\frac{\sigma_0}{U_0}\right). \tag{B.2.13a}$$

Stability functions

We recast $\bar{A} = AU, \bar{B} = BU, \bar{C} = CU, \bar{D} = DU$ to avoid quotient rules in the expansions of the stability coefficients. Expanding σ, U and s in powers of r_0^{-2}, and recognising that $A, D = O(1), B, C = O\left(r_0^{-1}\right)$, we consider the expansions

$$\bar{A} = a_0 + \frac{a_2}{r_0^2} + O\left(\frac{1}{r_0^4}\right), \quad \bar{B} = \frac{b_1}{r_0} + O\left(\frac{1}{r_0^3}\right), \quad \bar{C} = \frac{c_1}{r_0} + O\left(\frac{1}{r_0^3}\right), \quad \bar{D} = d_0 + \frac{d_2}{r_0^2} + O\left(\frac{1}{r_0^4}\right),$$

where the coefficients are summarised as follows: the terms arising at $O(1)$ are, defining $p_i = (\sigma_i + \mathrm{i}s_i)/U_i$,

$$a_0 = -Ms_0^2 U_0 + p_0 U_0^2 + L_{0,0}(p_0) + L_{2,0}(p_0) - 2L_{0,0}\left(\frac{\sigma_0}{U_0}\right),$$

$$d_0 = -MU_0 s_0^2 + U_0(\mathrm{i}s_0 - \sigma_0) + L_{0,0}(p_0) - L_{2,0}(p_0);$$

the terms arising at $O(r_0^{-1})$ are

$$b_1 = \mathrm{i}MU_0^2 s_0 + \frac{\mathrm{i}s_0 - \sigma_0}{U_0} L_{1,1}(p_0) - L_{0,1}(p_0),$$

$$c_1 = \mathrm{i}MU_0^2 s_0 + 2U_0^2 + \frac{\mathrm{i}s_0 + \sigma_0}{U_0} L_{1,1}(p_0) - L_{0,1}(p_0);$$

and the terms arising at $O(r_0^{-2})$ are

$$a_2 = -Ms_0 \left(2U_0 s_2 + U_2 s_0\right) + U_0 U_2(p_0 + p_2) - \frac{2}{U_0} L_{1,1}(p_0)$$
$$- \frac{U_2(p_0 + p_2)}{U_0} \left(L_{0,1}(p_0) + L_{2,1}(p_0)\right) + 2L_{0,1}\left(\frac{\sigma_0}{U_0}\right) \frac{\sigma_2 U_0 - \sigma_0 U_2}{U_0^2}$$
$$+ \frac{1}{24} L_{1,3}(p_0) - \frac{1}{2} L_{0,2}(p_0) - \frac{1}{24} M_{2,3}(p_0) - \frac{1}{12} L_{1,3}\left(\frac{\sigma_0}{U_0}\right)$$

and

$$d_2 = -\kappa_0 s_0 \left(2U_0 s_2 + U_2 s_0\right) + (\mathrm{i}s_2 - \sigma_2)U_0 + (\mathrm{i}s_0 - \sigma_0)U_2 + \frac{1}{24} M_{2,3}(p_0)$$
$$- \frac{(\sigma_2 + \mathrm{i}s_2)U_0 - (\sigma_0 + \mathrm{i}s_0)U_2}{U_0^2} \left(L_{0,1}(p_0) - L_{2,1}(p_0)\right) - \frac{1}{2} L_{0,2}(p_0).$$

C   Resonant quasi-rectilinear regime asymptotics details

C.1   Asymptotic expansions

In order to explore the asymptotic expansions in the near-resonant regime, we utilise the asymptotic expansions valid in the Bessel function transition region, namely [1]

$$
\mathrm{J}_\nu\left(\nu+\tau\nu^{1/3}\right) \sim \frac{2^{\frac{1}{3}}}{\nu^{\frac{1}{3}}}\mathrm{Ai}\left(-2^{\frac{1}{3}}\tau\right) + O\left(\frac{1}{\nu}\right), \quad \mathrm{Y}_\nu\left(\nu+\tau\nu^{1/3}\right) \sim -\frac{2^{\frac{1}{3}}}{\nu^{\frac{1}{3}}}\mathrm{Bi}\left(-2^{\frac{1}{3}}\tau\right) + O\left(\frac{1}{\nu}\right),
$$
(C.1.16)

$$
\mathrm{J}'_\nu\left(\nu+\tau\nu^{1/3}\right) \sim -\frac{2^{\frac{2}{3}}}{\nu^{\frac{2}{3}}}\mathrm{Ai}'\left(-2^{\frac{1}{3}}\tau\right) + O\left(\frac{1}{\nu}\right), \quad \mathrm{Y}'_\nu\left(\nu+\tau\nu^{1/3}\right) \sim \frac{2^{\frac{2}{3}}}{\nu^{\frac{2}{3}}}\mathrm{Bi}'\left(-2^{\frac{1}{3}}\tau\right) + O\left(\frac{1}{\nu}\right),
$$
(C.1.17)

where $\nu \to \infty$ with τ fixed, while Ai, Bi, Ai$'$ and Bi$'$ are the Airy Ai and Bi functions and their derivatives, respectively [1].

C.2   Stability integrals

To greatly simplify the following analysis and avoid catastrophic cancellations in numerical computations, we utilise the following connection identities throughout [1]:

$$
\mathrm{Ai}(z) \mp \mathrm{i}\,\mathrm{Bi}(z) = 2\mathrm{e}^{\mp\frac{\pi\mathrm{i}}{3}}\mathrm{Ai}\left(z\mathrm{e}^{\pm\frac{2\pi\mathrm{i}}{3}}\right) \quad \text{and} \quad \mathrm{Ai}'(z) \mp \mathrm{i}\,\mathrm{Bi}'(z) = 2\mathrm{e}^{\pm\frac{\pi\mathrm{i}}{3}}\mathrm{Ai}'\left(z\mathrm{e}^{\pm\frac{2\pi\mathrm{i}}{3}}\right). \quad \text{(C.2.18)}
$$

By substituting the identities (C.2.18) into the stability coefficients (7.4), we obtain

$$
\mathscr{A} \sim -MS^2 + \sigma + \mathrm{i}S - \frac{1}{U} - \frac{(\beta+\mathrm{i}r_0\sigma)}{r_0^2\omega} + \frac{2\pi}{\omega}\left(\frac{2}{\nu}\right)^{\frac{4}{3}}\mathrm{e}^{\frac{\pi\mathrm{i}}{3}}\mathcal{A}_{11} + o\left(\frac{1}{r_0}\right),
$$

$$
\mathscr{B} \sim \frac{\mathrm{i}MUS}{r_0} + \frac{\beta-\mathrm{i}r_0\sigma}{Ur_0}\left[-\mathrm{csch}(\pi\beta)\cos(2r_0) + \frac{1}{2r_0}\right] - \frac{\mathrm{i}\,(\beta+\mathrm{i}r_0\sigma)}{Ur_0}
$$
$$
- \frac{2\pi\,(\beta+\mathrm{i}r_0\sigma)}{U}\left(\frac{2}{\nu}\right)\mathrm{e}^{\frac{\pi\mathrm{i}}{3}}\mathcal{A}_{01} + o\left(\frac{1}{r_0}\right),
$$

$$
\mathscr{C} \sim \frac{\mathrm{i}MUS}{r_0} + \frac{2U}{r_0} - \frac{\beta+\mathrm{i}r_0\sigma}{Ur_0}\left[-\mathrm{csch}(\pi\beta)\cos(2r_0) + \frac{1}{2r_0}\right]
$$
$$
- \frac{\mathrm{i}\,(\beta+\mathrm{i}r_0\sigma)}{Ur_0} - \frac{2\pi\,(\beta+\mathrm{i}r_0\sigma)}{U}\left(\frac{2}{\nu}\right)\mathrm{e}^{\frac{\pi\mathrm{i}}{3}}\mathcal{A}_{01} + o\left(\frac{1}{r_0}\right),
$$

$$
\mathscr{D} \sim -MS^2 - \sigma + \mathrm{i}S + \frac{(\beta+\mathrm{i}r_0\sigma)}{r_0^2\omega} - \frac{2\,(\beta+\mathrm{i}r_0\sigma)^2\,\pi}{r_0^2\omega}\left(\frac{2}{\nu}\right)^{\frac{2}{3}}\mathrm{e}^{-\frac{\pi\mathrm{i}}{3}}\mathcal{A}_{00} + o\left(\frac{1}{r_0}\right),
$$

where

$$
\nu = -\mathrm{i}\beta + \frac{r_0 S}{U}, \quad \tau = \frac{r_0\,(1-\sigma)+\mathrm{i}\beta}{\nu^{\frac{1}{3}}},
$$

and we denote the products of Airy functions by

$$\mathcal{A}_{00} = \mathrm{Ai}\left(-2^{\frac{1}{3}}\tau\right)\mathrm{Ai}\left(-2^{\frac{1}{3}}\mathrm{e}^{\frac{2\pi\mathrm{i}}{3}}\tau\right), \quad \mathcal{A}_{01} = \mathrm{Ai}\left(-2^{\frac{1}{3}}\tau\right)\mathrm{Ai}'\left(-2^{\frac{1}{3}}\mathrm{e}^{\frac{2\pi\mathrm{i}}{3}}\tau\right),$$

$$\text{and} \quad \mathcal{A}_{11} = \mathrm{Ai}'\left(-2^{\frac{1}{3}}\tau\right)\mathrm{Ai}'\left(-2^{\frac{1}{3}}\mathrm{e}^{\frac{2\pi\mathrm{i}}{3}}\tau\right).$$

For larger κ_0, which is when we expect the near-resonant expansion to be necessary, we see that $\mathscr{A}, \mathscr{D} = O(M)$, but $\mathscr{B}, \mathscr{C} = O(M/r_0) + O(1)$, and thus the stability condition $\mathscr{A}\mathscr{D} + \mathscr{B}\mathscr{C} = 0$ can be approximated by $\mathscr{A}\mathscr{D} = 0$. As $\mathscr{D}$ is the stability coefficient analogous to that of the effect of inline oscillations on a free rectilinear walker, as remarked in section 7.4, it is reasonable to further approximate the stability condition as $\mathscr{D} = 0$, giving

$$-MS^2 + \mathrm{i}S - \sigma + \frac{(\sigma + \mathrm{i}S)}{U^2} - \frac{2r_0(\sigma + \mathrm{i}S)^2\pi}{U^3}\left(\frac{2}{\nu}\right)^{\frac{2}{3}}\mathrm{e}^{-\frac{\pi\mathrm{i}}{3}}\mathcal{A}_{00} = 0. \tag{C.2.19}$$

Choosing $\nu = r_0$ and $\tau = (r_0(1-\sigma) + \mathrm{i}\beta)\nu^{-\frac{1}{3}}$ leads to the approximate near-resonant expansion. The full near-resonant expansion uses the $O(\nu^{-1})$ terms of the asymptotic expansion of $\mathrm{J}_\nu(\nu + \tau\nu^{\frac{1}{3}})$ [1]. In other words,

$$\mathrm{J}_{-\mathrm{i}(\beta + \mathrm{i}r_0\sigma)}(r_0) = \mathrm{J}_\nu\left(\nu + \tau\nu^{\frac{1}{3}}\right) \sim \left(\frac{2}{\nu}\right)^{\frac{1}{3}}\mathrm{Ai}\left(-2^{\frac{1}{3}}\tau\right)\left[1 - \frac{\tau}{5\nu^{\frac{2}{3}}}\right] + \frac{2^{\frac{2}{3}}}{\nu}\frac{3\tau^2}{10}\mathrm{Ai}'(-2^{\frac{1}{3}}\tau), \tag{C.2.20}$$

where

$$\nu = -\mathrm{i}\beta + r_0\sigma \quad \text{and} \quad \tau = \frac{r_0(1-\sigma) + \mathrm{i}\beta}{[-\mathrm{i}\beta + r_0\sigma]^{\frac{1}{3}}}, \tag{C.2.21}$$

and similarly for the other Bessel functions.

C.3 Validity of the near-resonant expansions

Full non-resonant expansions

The full near-resonant expansion hinges on the validity of the asymptotic expansion [1]

$$\mathrm{J}_\nu(\nu + \tau\nu^{1/3}) \sim \left(\frac{2}{\nu}\right)^{\frac{1}{3}}\mathrm{Ai}(-2^{\frac{1}{3}}\tau)\left[1 + \sum_{k=1}^\infty \frac{f_k(\tau)}{\nu^{\frac{2k}{3}}}\right] + \frac{2^{\frac{2}{3}}}{\nu}\mathrm{Ai}'(-2^{\frac{1}{3}}\tau)\sum_{k=0}^\infty \frac{g_k(\tau)}{\nu^{\frac{2k}{3}}}, \tag{C.3.22}$$

where f_k and g_k are polynomials where the degrees increase significantly with k. This expansion is expected to fail, therefore, if τ becomes large. In our system,

$$\nu = -\mathrm{i}\beta + r_0\sigma, \tau = \frac{r_0(1-\sigma) + \mathrm{i}\beta}{[-\mathrm{i}\beta + r_0\sigma]^{\frac{1}{3}}}. \tag{C.3.23}$$

The full near-resonant expansion is only employed if $\sigma \approx 1$. Thus, $\nu = O(r_0)$, and the denominator of τ is $O(r_0^{\frac{1}{3}})$. The expansion then fails if either $\beta = \sigma r_0/U \gg r_0^{\frac{1}{3}}$, or $r_0(1-\sigma) \gg r_0^{\frac{1}{3}}$; this starts to occur when σ no longer decreases significantly with r_0, i.e. the rectilinear regime. We show in figure 7.8 that discrepancies between the near-resonant expansions and the numerical results start to occur when either of these conditions is satisfied.

We now proceed to discuss the validity of the approximate near-resonant expansion, and what happens outside its regime of validity.

Approximate near-resonant expansion

As demonstrated in figure 7.7, the approximate near-resonant expansion qualitatively agrees with the numerical boundary and the rectilinear expansion, and the agreement improves for larger M. To operate when the full near-resonant expansion fails, we assume $\sigma = O(1)$ and demonstrate that the solution of the stability condition derived from the second near-resonant expansion compares favourably to that derived from the free rectilinear state[33, 35].

The parameters of the approximate near-resonant expansion are

$$\nu = r_0 \quad \text{and} \quad \tau = \frac{r_0 \left(1 - \sigma\right) + i\beta}{r_0^{1/3}} = O(r_0^{2/3}). \tag{C.3.24}$$

If $\sigma = O(1)$, then $\beta = O(r_0)$. We also note that, in the rectilinear regime where the near-resonant expansion fails, $1 - \sigma = O(1)$ as $r_0 \to \infty$. Therefore, both the real and imaginary part of τ scale as $r_0^{2/3}$, and thus grow for large orbital radius.

We turn our attention to the product of Airy functions in equation (C.2.19), which is of the form $\mathrm{Ai}\left(-2^{\frac{1}{3}}\tau\right)\mathrm{Ai}\left(-2^{\frac{1}{3}}e^{\frac{2\pi i}{3}}\tau\right)$. For large complex argument z, for z not a negative real number, we use the expansion[1]

$$\mathrm{Ai}(z) \sim \frac{e^{-\frac{2}{3}z^{\frac{3}{2}}}}{2\sqrt{\pi}z^{\frac{1}{4}}}, \quad \text{where} \quad z = -2^{\frac{1}{3}}\tau. \tag{C.3.25}$$

The product of Airy functions then takes the form

$$\mathrm{Ai}(z)\mathrm{Ai}(e^{\frac{2\pi i}{3}}z) \sim \frac{1}{4\pi z^{\frac{1}{4}}(e^{\frac{2\pi i}{3}}z)^{\frac{1}{4}}}e^{-\frac{2}{3}\left(z^{\frac{3}{2}}+(e^{\frac{2\pi i}{3}}z)^{\frac{3}{2}}\right)}. \tag{C.3.26}$$

Choosing $z = -2^{\frac{1}{3}}\tau$, as $\mathrm{Im}(\tau) > 0$, $\mathrm{Im}(z) = \mathrm{Im}\left(-2^{\frac{1}{3}}\tau\right) < 0$, and so $\arg(z) < 0$. This implies that $\arg(e^{\frac{2\pi i}{3}}z) = \arg(z) + \frac{2\pi}{3}$, $\arg\left((ze^{\frac{2\pi i}{3}})^{\frac{3}{2}}\right) = \frac{3}{2}\arg(z) + \pi$ but $\left|(e^{\frac{2\pi i}{3}}z)^{\frac{3}{2}}\right| = \left|z^{\frac{3}{2}}\right|$, so the exponential argument cancels. If we now write $z = -2^{\frac{1}{3}}\tau \equiv 2^{\frac{1}{3}}\gamma r_0^{\frac{2}{3}}$, where we define $\gamma = -(1 - \sigma + i\sigma/U)$, then equation (C.2.19) simplifies to

$$-MS^2 + iS - \sigma + \frac{(\sigma + iS)}{U^2}\left(1 + \left(\frac{2}{U^2}\right)^{\frac{1}{2}}\frac{i(\sigma + iS)}{2\gamma^{\frac{1}{2}}}\right) = 0. \tag{C.3.27}$$

As demonstrated by Durey *et al.* [35], the stability condition for rectilinear walking (which is applicable in the large-radius limit) can be cast as

$$-MS^2 + iS - \sigma + \frac{(\sigma + iS)}{U^2}\left(1 - \frac{\sigma + iS}{\sqrt{(iS + \sigma)^2 + U^2}}\right) = 0, \tag{C.3.28}$$

which is of a similar form to (C.3.27). We thus rewrite the stability conditions for the approximate near-resonant expansion (C.3.27) and the free rectilinear solution (C.3.28) in the combined form

$$-MS^2 + iS - \sigma + \frac{(\sigma + iS)}{U^2}\left(1 + \frac{x_{1,2}(\sigma + iS)}{U}\right) = 0, \tag{C.3.29}$$

where

$$x_1 = \frac{i}{\sqrt{2\gamma}}$$

corresponds to the approximate near-resonant stability condition and

$$x_2 = -\frac{1}{\sqrt{1 + \left(\frac{\sigma + iS}{U}\right)^2}}$$

to the free rectilinear stability condition. Direct computation shows that

$$\frac{1}{x_1^2} - \frac{1}{x_2^2} = -\frac{\sigma^2}{U^2} + (1 - \sigma)\left(1 - \sigma + \frac{2i\sigma}{U}\right). \tag{C.3.30}$$

Durey *et al.* [35] also showed that

$$\sigma \sim \frac{2}{M^3} \quad \text{and} \quad 1 - \sigma \sim 1 - \sqrt{1 - \frac{1}{M^2}} \sim \frac{1}{2M^2} \tag{C.3.31}$$

which implies that

$$\frac{1}{x_1^2} - \frac{1}{x_2^2} \sim \frac{1}{4M^4} + \frac{2i}{UM^5} = O(M^{-4}) \quad \text{for} \quad M \gg 1.$$

To conclude that the simplified near-resonant stability condition approximates the rectilinear stability condition, we would need to show that $x_1 \approx x_2$ and not $x_1 \approx -x_2$. This is accomplished by checking the quadrant of each complex number. Specifically, $\sigma/U > 0$ and $1 - \sigma > 0$ for large M, so γ is in quadrant 3, and its principal-valued square root is in quadrant 4. Hence, $x_1 = \frac{i}{\sqrt{2\gamma}}$ is in quadrant 2. Similarly, $1 + \left(\frac{\sigma + iS}{U}\right)^2 = 1 - \sigma^2 + \frac{\sigma^2}{U^2} + \frac{2i\sigma S}{U^2}$ is in quadrant 1, and its square root is also in quadrant 1. Its negative reciprocal, x_2, is then in quadrant 2.

Let us now find an estimate for $x_2 - x_1$. Firstly, use the known expansions for $1 - \sigma$ and σ in terms of M, and then use linear approximations for large M to approximate x_1. Specifically,

$$x_1 = \frac{i}{\sqrt{-2\left(1 - \sigma + \frac{i\sigma}{U}\right)}} \sim \frac{i}{\sqrt{-2\left(\frac{1}{2M^2} + \frac{2i}{UM^3}\right)}} \sim -M\left(1 - \frac{2i}{MU}\right). \tag{C.3.32}$$

We proceed by manipulating the expansion for $\frac{1}{x_1^2} - \frac{1}{x_2^2}$ to derive an expression for $x_2 - x_1$ in terms of x_1 and x_2, assuming that x_1 and x_2 are approximately equal to leading order in powers of M^{-1}, to show that

$$\frac{1}{x_1^2} - \frac{1}{x_2^2} = \left(\frac{1}{x_1} - \frac{1}{x_2}\right)\left(\frac{1}{x_1} + \frac{1}{x_2}\right) \sim \frac{1}{4M^4}\left(1 + \frac{8i}{MU}\right),$$

$$\frac{1}{x_1} - \frac{1}{x_2} \sim -\frac{1}{8M^3}\left(1 + \frac{6i}{MU}\right),$$

$$x_2 - x_1 = x_1 x_2\left(\frac{1}{x_1} - \frac{1}{x_2}\right) \sim -\frac{1}{8M}\left(1 + \frac{2i}{MU}\right). \tag{C.3.33}$$

This demonstrates that the difference in the rectilinear and second near-resonant stability conditions is $O\left(\frac{1}{M}\right)$ for larger M. We have thus demonstrated why the approximate near-resonant stability condition is more robust than the full near-resonant stability condition for a broader range of r_0. The difference in the two near-resonant stability conditions stems from the neglecting of $i\beta$ when it appears with S.

Ad-hoc resonant quasi-rectilinear regime expansion

We showed that if one takes the approximate resonant expansion outside its regime of validity, the stability condition it solves is $O\left(\frac{1}{M}\right)$ away from the free rectilinear stability problem. This motivates a third ad-hoc resonant expansion, which is constructed so that when $r_0 \to \infty$, the stability coefficient $\mathscr{D}$ approaches that of the free rectilinear stability problem. In our case, we can simply define

$$\mathscr{D} = -M_0 S^2 + iS - \sigma + \frac{(\sigma + iS)}{U^2} - \frac{2r_0(\sigma + iS)^2 \pi}{U^3} \times \left(\frac{2}{r_0}\right)^{\frac{2}{3}} e^{-\frac{\pi i}{3}} \mathrm{Ai}(-2^{\frac{1}{3}}\tau)\mathrm{Ai}(-2^{\frac{1}{3}}e^{\frac{2\pi i}{3}}\tau) + \Delta\mathscr{D} = 0,$$

$$\tag{C.3.34a}$$

$$\Delta\mathscr{D} = \frac{(\sigma + iS)^2}{U^3}(x_2 - x_1), \tag{C.3.34b}$$

which, by construction, produces the correct limiting memory of instability in the limit as $r_0 \to \infty$.

Bibliography

[1] M. Abramowitz and I. A. Stegun. *Handbook of Mathematical Functions with Formulas, Graphs, and Mathematical Tables*, volume 55. US Government printing office, 1948.

[2] J. Arbelaiz, A. U. Oza, and J. W. M. Bush. Promenading pairs of walking droplets: Dynamics and stability. *Phys. Rev. Fluids*, 3(013604), 2018.

[3] G. Bacchiagaluppi and A. Valentini. *Quantum theory at the crossroads: Reconsidering the 1927 Solvay conference.* Cambridge University Press, 2009.

[4] V. Bacot, S. Perrard, M. Labousse, Y. Couder, and E. Fort. Multistable free states of an active particle from a coherent memory dynamics. *Phys. Rev. Lett.*, 122(104303), 2019.

[5] M. Bakker and N. M. Temme. Sum rule for products of Bessel functions: Comments on a paper by Newberger. *J. Math. Phys.*, 25(5):1266–1267, 1984.

[6] T. B. Benjamin and F. Ursell. The stability of the plane free surface of a liquid in vertical periodic motion. *Proc. Roy. Soc. Lond. A.*, 225:505–515, 1954.

[7] Samuel Bernard-Bernardet, Marc Fleury, and Emmanuel Fort. Spontaneous emergence of a spin state for an emitter in a time-varying medium. *The European Physical Journal Plus*, 137(4):1–8, 2022.

[8] N. Bleistein and R. A. Handelsman. *Asymptotic expansions of integrals*. Ardent Media, 1975.

[9] Austin M Blitstein, Rodolfo R Rosales, and Pedro J Sáenz. Minimal quantization model in pilot-wave hydrodynamics. *Physical Review Letters*, 132(10):104003, 2024.

[10] D. Bohm. A suggested interpretation of the quantum theory in terms of hidden variables, i. *Phys. Rev.*, 85:66–179, 1952.

[11] D. Bohm. A suggested interpretation of the quantum theory in terms of hidden variables, ii. *Phys. Rev.*, 85:180–193, 1952.

[12] C. Borghesi, J. Moukhtar, M. Labousse, A. Eddi, E. Fort, and Y. Couder. Interaction of two walkers: Wave-mediated energy and force. *Phys. Rev. E*, 90(063017), 2014.

[13] J. W. M. Bush. Pilot-wave hydrodynamics. *Ann. Rev. Fluid Mech.*, 47, 2015.

[14] J. W. M Bush and A. U. Oza. Hydrodynamic quantum analogs. *Rep. Prog. Phys.*, 84 (017001):1–41, 2020.

[15] J. W. M. Bush, A. U. Oza, and J. Moláček. The wave-induced added mass of walking droplets. *J. Fluid Mech.*, 755(R7), 2014.

[16] M. M. P. Couchman and J. W. M. Bush. Free rings of bouncing droplets: stability and dynamics. *J. Fluid Mech.*, 903(A49), 2020.

[17] M. M. P. Couchman, S. E. Turton, and J. W. M. Bush. Bouncing phase variations in pilot-wave hydrodynamics and the stability of droplet pairs. *J. Fluid Mech.*, 871: 212–243, 2019.

[18] Y. Couder and E. Fort. Single particle diffraction and interference at a macroscopic scale. *Phys. Rev. Lett.*, 97(154101), 2006.

[19] Y. Couder and E. Fort. Probabilities and trajectories in a classical wave-particle duality. *J. Phys.: Conf. Ser.*, 361(012001), 2012.

[20] Y. Couder, E. Fort, C.-H. Gautier, and A. Boudaoud. From bouncing to floating: noncoalescence of drops on a fluid bath. *Phys. Rev. Lett.*, 94(177801), 2005.

[21] Y. Couder, S. Protière, E. Fort, and A. Boudaoud. Walking and orbiting droplets. *Nature*, 437(208), 2005.

[22] T. Cristea-Platon, P. J. Sáenz, and J. W. M. Bush. Walking droplets in a circular corral: Quantisation and chaos. *Chaos*, 28(096116), 2018.

[23] Clinton Davisson and Lester H Germer. Diffraction of electrons by a crystal of nickel. *Physical review*, 30(6):705, 1927.

[24] L. de Broglie. *Ondes et mouvements*. Gautier Villars, Paris, 1926.

[25] L. de Broglie. *An introduction to the study of wave mechanics*. Methuen & Co., London, 1930.

[26] L. de Broglie. Interpretation of quantum mechanics by the double solution theory. *Annales de la Fondation Louis de Broglie*, 12:1–23, 1987.

[27] L. M. Delves and J. N. Lyness. A numerical method for locating the zeros of an analytic function. *Math. Comput.*, 21(100):543–560, 1967.

[28] M. Durey. *Faraday wave-droplet dynamics: a hydrodynamic quantum analogue*. PhD thesis, University of Bath, 2018.

[29] M. Durey. Bifurcations and chaos in a Lorenz-like pilot-wave system. *Chaos*, 30:103115, 2020. doi:10.1063/5.0020775.

[30] M. Durey and J. W. M. Bush. Hydrodynamic quantum field theory: The onset of particle motion and the form of the pilot wave. *Frontiers in Physics*, 8(300), 2020.

[31] M. Durey and J. W. M. Bush. Classical pilot-wave dynamics: the free particle. *Chaos*, 31(033136):1–11, 2021.

[32] M. Durey and P. A. Milewski. Faraday wave-droplet dynamics: Discrete-time analysis. *J. Fluid Mech.*, 821:296–329, 2017.

[33] M. Durey, P. A. Milewski, and J. W. M. Bush. Dynamics, emergent statistics and the mean-pilot-wave potential of walking droplets. *Chaos*, 28(096108), 2018.

[34] M. Durey, P. A. Milewski, and Z. Wang. Faraday pilot-wave dynamics in a circular corral. *J. Fluid Mech.*, 891(A3), 2020.

[35] M. Durey, S. E. Turton, and J. W. M. Bush. Speed oscillations in classical pilot-wave dynamics. *Proc. Roy. Soc. A*, 476(20190884), 2020.

[36] A. Eddi, A. Decelle, E. Fort, and Y. Couder. Archimedean lattices in the bound states of wave interacting particles. *Europhys. Lett.*, 87(56002), 2009.

[37] A. Eddi, E. Fort, F. Moisy, and Y. Couder. Unpredictable tunneling of a classical wave-particle association. *Phys. Rev. Lett.*, 102(240401), 2009.

[38] A. Eddi, E. Sultan, J. Moukhtar, E. Fort, M. Rossi, and Y. Couder. Information stored in Faraday waves: the origin of a path memory. *J. Fluid Mech.*, 674:433–463, 2011.

[39] A. Eddi, J. Moukhtar, S. Perrard, E. Fort, and Y. Couder. Level splitting at a macroscopic scale. *Phys. Rev. Lett.*, 108(264503), 2012.

[40] C. Ellegaard and M. T. Levinsen. Interaction of wave-driven particles with slit structures. *Phys. Rev. E*, 102(023115), 2020.

[41] L. M. Faria. A model for Faraday pilot waves over variable topography. *J. Fluid Mech.*, 811:51–66, 2017.

[42] G. A. Fiete and E. J. Heller. Theory of quantum corrals and quantum mirages. *Rev. Mod. Phys.*, 75:933–948, 2003.

[43] E. Fort, A. Eddi, J. Moukhtar, A. Boudaoud, and Y. Couder. Path-memory induced quantization of classical orbits. *Proc. Natl. Acad. Sci.*, 107(41):17515–17520, 2010.

[44] J. Friedel. Electronic structure of primary solid solutions in metals. *Advances in Physics*, 3(12):446–507, 1954.

[45] C. A. Galeano-Rios, P. A. Milewski, and J.-M. Vanden-Broeck. Non-wetting impact of a sphere onto a bath and its application to bouncing droplets. *J. Fluid Mech.*, 826: 97–127, 2017.

[46] C. A. Galeano-Rios, M. M. P. Couchman, P. Caldairou, and J. W. M. Bush. Ratcheting droplet pairs. *Chaos*, 28(096112), 2018.

[47] C. A. Galeano-Rios, P. A. Milewski, and J.-M. Vanden-Broeck. Quasi-normal free-surface impacts, capillary rebounds and application to Faraday walkers. *J. Fluid Mech.*, 873:856–888, 2019.

[48] T. Gilet. Quantumlike statistics of deterministic wave-particle interactions in a circular cavity. *Phys. Rev. E*, 93(042202), 2016.

[49] H. Goldstein, C.P. Poole, and J.L. Safko. *Classical Mechanics*. Addison Wesley, 2002. ISBN 9780201657029. URL https://books.google.com/books?id=tJCuQgAACAAJ.

[50] I. S. Gradshteyn and I. M. Ryzhik. *Table of integrals, series, and products*. Academic Press, 2014.

[51] D. M. Harris and J. W. M. Bush. The pilot-wave dynamics of walking droplets. *Phys. Fluids*, 25(091112), 2013.

[52] D. M. Harris and J. W. M. Bush. Drops walking in a rotating frame: From quantized orbits to multimodal statistics. *J. Fluid Mech.*, 739:444–464, 2014.

[53] D. M. Harris, J. Moukhtar, E. Fort, Y. Couder, and J. W. M. Bush. Wavelike statistics from pilot-wave dynamics in a circular corral. *Phys. Rev. E*, 88(011001):1–5, 2013.

[54] Zhu Heitman, James Bremer, Vladimir Rokhlin, and Bogdan Vioreanu. On the asymptotics of bessel functions in the fresnel regime. *Applied and Computational Harmonic Analysis*, 39(2):347–356, 2015.

[55] M. Hubert, M. Labousse, and S. Perrard. Self-propulsion and crossing statistics under random initial conditions. *Physical Review E*, 95(062607), 2017.

[56] M. Hubert, M. Labousse, S. Perrard, M. Labousse, N. Vandewalle, and Y. Couder. Tunable bimodal explorations of space from memory-driven deterministic dynamics. *Phys. Rev. E*, 100(032201), 2019.

[57] M. Hubert, S. Perrard, N. Vandewalle, and M. Labousse. Overload wave-memory induces amnesia of a self-propelled particle. *Nat. Comm.*, 13(1):4357, 2022.

[58] K. Kanisawa, M. J. Butcher, H. Yamaguchi, and Y. Hirayama. Imaging of Friedel oscillation patterns of two-dimensionally accumulated electrons at epitaxially grown InAs(111) A surfaces. *Phys. Rev. Lett.*, 86(3384), 2001.

[59] Jun Kondo. Resistance minimum in dilute magnetic alloys. *Progress of theoretical physics*, 32(1):37–49, 1964.

[60] K. M. Kurianski, A. U. Oza, and J. W. M. Bush. Simulations of pilot-wave dynamics in a simple harmonic potential. *Phys. Rev. Fluids*, 2(113602), 2017.

[61] M. Labousse. *Étude d'une dynamique à mémoire de chemin: une expérimentation théorique*. PhD thesis, Université Pierre et Marie Curie UPMC Paris VI, 2014.

[62] M. Labousse and S. Perrard. Non-Hamiltonian features of a classical pilot-wave dynamics. *Physical Review E*, 90(022913), 2014.

[63] M. Labousse, S. Perrard, Y. Couder, and E. Fort. Build-up of macroscopic eigenstates in a memory-based constrained system. *New Journal of Physics*, 16(113027), 2014.

[64] M. Labousse, A. U. Oza, S. Perrard, and J. W. M. Bush. Pilot-wave dynamics in a harmonic potential: Quantization and stability of circular orbits. *Phys. Rev. E*, 93 (033122), 2016.

[65] M. Labousse, S. Perrard, Y. Couder, and E. Fort. Self-attraction into spinning eigenstates of a mobile wave source by its emission back-reaction. *Phys. Rev. E*, 94(042224), 2016.

[66] Nicholas Liu, Matthew Durey, and John WM Bush. Pilot-wave dynamics in a rotating frame: the onset of orbital instability. *Journal of Fluid Mechanics*, 973:A4, 2023.

[67] J. Miles and D. Henderson. Parametrically forced surface waves. *Ann. Rev. Fluid Mech.*, 22:143–165, 1990.

[68] P. Milewski, C. Galeano-Rios, A. Nachbin, and J. W. M. Bush. Faraday pilot-wave dynamics: modelling and computation. *J. Fluid Mech.*, 778:361–388, 2015.

[69] J. Moláček and J. W. M. Bush. Droplets bouncing on a vibrating fluid bath. *J. Fluid Mech.*, 727:582–611, 2013.

[70] J. Moláček and J. W. M. Bush. Drops walking on a vibrating bath: towards a hydrodynamic pilot-wave theory. *J. Fluid Mech.*, 727:612–647, 2013.

[71] C. R. Moon, C. P. Lutz, and H. C. Manoharan. Single-atom gating of quantum-state superpositions. *Nat. Phys.*, 4:454–458, 2008.

[72] A. Nachbin. Walking droplets correlated at a distance. *Chaos*, 28(096110), 2018.

[73] A. Nachbin, P. A. Milewski, and J. W. M. Bush. Tunneling with a hydrodynamic pilot-wave model. *Phys. Rev. Fluids*, 2(034801), 2017.

[74] B. S. Newberger. New sum rule for products of Bessel functions with application to plasma physics. *J. Math. Phys.*, 23(7):1278–1281, 1982.

[75] A. B. Olde Daalhuis and N. M. Temme. Uniform airy-type expansions of integrals. *SIAM Journal on Mathematical Analysis*, 25(2):304–321, 1994.

[76] F. W. J. Olver. Some new asymptotic expansions for bessel functions of large orders. In *Mathematical Proceedings of the Cambridge Philosophical Society*, volume 48, pages 414–427. Cambridge University Press, 1952.

[77] A. U. Oza. *A trajectory equation for walking droplets: hydrodynamic pilot-wave theory*. PhD thesis, Massachusetts Institute of Technology, 2014.

[78] A. U. Oza, R. R. Rosales, and J. W. M. Bush. A trajectory equation for walking droplets: hydrodynamic pilot-wave theory. *J. Fluid Mech.*, 737:552–570, 2013.

[79] A. U. Oza, D. M. Harris, R. R. Rosales, and J. W. M. Bush. Pilot-wave dynamics in a rotating frame: on the emergence of orbital quantization. *J. Fluid Mech.*, 744:404–429, 2014.

[80] A. U. Oza, Ø. Wind-Willassen, D. M Harris, R. R. Rosales, and J. W. M. Bush. Pilot-wave hydrodynamics in a rotating frame: Exotic orbits. *Phys. Fluids*, 26(082101), 2014.

[81] A. U. Oza, E. Siéfert, D. M. Harris, J. Moláček, and J. W. M. Bush. Orbiting pairs of walking droplets: Dynamics and stability. *Phys. Rev. Fluids*, 2(053601), 2017.

[82] A. U. Oza, R. R. Rosales, and J. W. M. Bush. Hydrodynamic spin states. *Chaos*, 28 (096106), 2018.

[83] S. Perrard, M. Labousse, E. Fort, and Y. Couder. Chaos driven by interfering memory. *Phys. Rev. Lett.*, 113(104101), 2014.

[84] S. Perrard, M. Labousse, M. Miskin, E. Fort, and Y. Couder. Self-organization into quantized eigenstates of a classical wave-driven particle. *Nat. Comm.*, 5(3219), 2014.

[85] S. Protière, A. Boudaoud, and Y. Couder. Particle-wave association on a fluid interface. *J. Fluid. Mech.*, 554:85–108, 2006.

[86] G. Pucci, D. M. Harris, L. M. Faria, and J. W. M. Bush. Walking droplets interacting with single and double slits. *J. Fluid Mech.*, 835:1136–1156, 2018.

[87] P. J. Sáenz, T. Cristea-Platon, and J. W. M. Bush. Statistical projection effects in a hydrodynamic pilot-wave system. *Nat. Phys.*, 14:315–319, 2018.

[88] P. J. Sáenz, T. Cristea-Platon, and J. W. M. Bush. A hydrodynamic analog of Friedel oscillations. *Sci. Adv.*, 6(20), 2020.

[89] P. J. Saenz, G. Pucci, S. E. Turton, A. Goujon, R. R. Rosales, J. Dunkel, and J. W. M. Bush. Emergent order in hydrodynamic spin lattices. *Nature*, 596:58–62, 2021. doi:10.1038/s41586-021-03682-1.

[90] Á. Sanz. Atom-diffraction from surfaces with defects: A Fermatian, Newtonian and Bohmian joint view. *Entropy*, 20(451), 2018.

[91] L. Tadrist, J.-B. Shim, T. Gilet, and P. Schlagheck. Faraday instability and subthreshold Faraday waves: surface waves emitted by walkers. *J. Fluid Mech.*, 848:906–945, 2018.

[92] L. Tadrist, T. Gilet, P. Schlagheck, and J. W. M. Bush. Predictability in a hydrodynamic pilot-wave system: Resolution of walker tunneling. *Phys. Rev. E*, 102(013104), 2020.

[93] L. D. Tambasco and J. W. M. Bush. Exploring orbital dynamics and trapping with a generalized pilot-wave framework. *Chaos*, 28(096115), 2018.

[94] L. D. Tambasco, D. M. Harris, A. U. Oza, R. R. Rosales, and J. W. M. Bush. The onset of chaos in orbital pilot-wave dynamics. *Chaos*, 26(103107), 2016.

[95] Geoffrey Ingram Taylor. Interference fringes with feeble light. In *Proceedings of the Cambridge Philosophical Society*, volume 15, pages 114–115, 1909.

[96] S. J. Thomson, M. Durey, and R. R. Rosales. Collective vibrations of a hydrodynamic active lattice. *Proc. Roy. Soc. A*, 476(20200155), 2020.

[97] S. E. Turton. *Theoretical modeling of pilot-wave hydrodynamics*. PhD thesis, Massachusetts Institute of Technology, 2020.

[98] S. E. Turton, M. M. P. Couchman, and J. W. M. Bush. A review of the theoretical modeling of walking droplets: towards a generalized pilot-wave framework. *Chaos*, 28 (096111), 2018.

[99] R. Valani, A. C. Slim, D. M. Paganin, T. P. Simula, and T. Vo. Unsteady dynamics of a classical particle-wave entity. *Phys. Rev. E*, 104(015106), 2021.

[100] George Neville Watson. *A treatise on the theory of Bessel functions*. Cambridge university press, 1995.